

NASA/CR-2012-217330



# Electromagnetic Nondestructive Evaluation of Wire Insulation and Models of Insulation Material Properties

*Nicola Bowler, Michael R. Kessler, Li Li, Peter R. Hondred, and Tianming Chen  
Iowa State University, Ames, Iowa*

---

January 2012

## NASA STI Program . . . in Profile

Since its founding, NASA has been dedicated to the advancement of aeronautics and space science. The NASA scientific and technical information (STI) program plays a key part in helping NASA maintain this important role.

The NASA STI program operates under the auspices of the Agency Chief Information Officer. It collects, organizes, provides for archiving, and disseminates NASA's STI. The NASA STI program provides access to the NASA Aeronautics and Space Database and its public interface, the NASA Technical Report Server, thus providing one of the largest collections of aeronautical and space science STI in the world. Results are published in both non-NASA channels and by NASA in the NASA STI Report Series, which includes the following report types:

- **TECHNICAL PUBLICATION.** Reports of completed research or a major significant phase of research that present the results of NASA programs and include extensive data or theoretical analysis. Includes compilations of significant scientific and technical data and information deemed to be of continuing reference value. NASA counterpart of peer-reviewed formal professional papers, but having less stringent limitations on manuscript length and extent of graphic presentations.
- **TECHNICAL MEMORANDUM.** Scientific and technical findings that are preliminary or of specialized interest, e.g., quick release reports, working papers, and bibliographies that contain minimal annotation. Does not contain extensive analysis.
- **CONTRACTOR REPORT.** Scientific and technical findings by NASA-sponsored contractors and grantees.
- **CONFERENCE PUBLICATION.** Collected papers from scientific and technical conferences, symposia, seminars, or other meetings sponsored or co-sponsored by NASA.
- **SPECIAL PUBLICATION.** Scientific, technical, or historical information from NASA programs, projects, and missions, often concerned with subjects having substantial public interest.
- **TECHNICAL TRANSLATION.** English-language translations of foreign scientific and technical material pertinent to NASA's mission.

Specialized services also include creating custom thesauri, building customized databases, and organizing and publishing research results.

For more information about the NASA STI program, see the following:

- Access the NASA STI program home page at <http://www.sti.nasa.gov>
- E-mail your question via the Internet to [help@sti.nasa.gov](mailto:help@sti.nasa.gov)
- Fax your question to the NASA STI Help Desk at 443-757-5803
- Phone the NASA STI Help Desk at 443-757-5802
- Write to:  
NASA STI Help Desk  
NASA Center for AeroSpace Information  
7115 Standard Drive  
Hanover, MD 21076-1320

NASA/CR-2012-217330



# Electromagnetic Nondestructive Evaluation of Wire Insulation and Models of Insulation Material Properties

*Nicola Bowler, Michael R. Kessler, Li Li, Peter R. Hondred, and Tianming Chen  
Iowa State University, Ames, Iowa*

National Aeronautics and  
Space Administration

Langley Research Center  
Hampton, Virginia 23681-2199

Prepared for Langley Research Center  
under Cooperative Agreement NNX07AU54A

January 2012

The use of trademarks or names of manufacturers in this report is for accurate reporting and does not constitute an official endorsement, either expressed or implied, of such products or manufacturers by the National Aeronautics and Space Administration.

Available from:

NASA Center for AeroSpace Information  
7115 Standard Drive  
Hanover, MD 21076-1320  
443-757-5802

## Table of Contents

LIST OF FIGURES .....	v
LIST OF TABLES .....	x
LIST OF PUBLICATIONS AND PRESENTATIONS RESULTING FROM THIS WORK	xi
Chapter I. Introduction.....	1
1. Motivation .....	1
2. History of wiring insulation.....	2
3. Technical approach.....	2
Permittivity .....	2
Breakdown voltage .....	2
Thermal exposure .....	3
Water and saline exposure .....	3
Mechanical stress.....	3
Material characterization .....	4
4. NDE of wire insulation.....	4
Motivation .....	5
Causes of failure and aging in aircraft wiring.....	5
Inspection techniques.....	5
Chapter II. Polyimide .....	8
1. Introduction .....	8
2. Sample material.....	9
3. Thermal degradation.....	12
Thermal degradation kinetics.....	12
Effect of thermal degradation on permittivity.....	25
Effect of thermal degradation on electrical breakdown behavior .....	31
Lifetime prediction under electrothermal multi-stress .....	37
4. Water/saline exposure .....	43
Effect of water/saline exposure on permittivity .....	43
Effect of water exposure on electrical breakdown behavior .....	49
5. Summary .....	53
Chapter III. Polytetrafluoroethylene (PTFE) .....	54
1. Introduction .....	54
2. Sample material.....	55

3. Thermal degradation.....	59
Thermal degradation kinetics.....	59
Effect of thermal exposure on permittivity.....	65
4. Effect of tensile strain on permittivity.....	67
Experiment.....	67
Results and discussion.....	69
5. Summary.....	72
<b>Chapter IV. Ethylene-tetrafluoroethylene (ETFE).....</b>	<b>73</b>
1. Introduction.....	73
2. Sample material.....	74
3. Thermal degradation.....	78
Thermal degradation kinetics.....	78
Effect of thermal exposure on permittivity.....	85
4. Summary.....	88
<b>Chapter V. Development of a Capacitive Sensor for Nondestructive Evaluation of Wiring Insulation 89</b>	
1. Analysis of a capacitive sensor for the evaluation of circular dielectric cylinders.....	89
Introduction.....	89
Modeling.....	92
Derivation of Green's function in cylindrical coordinates.....	93
Numerical implementation.....	96
Experimental verification.....	101
Summary.....	105
2. Analysis of a capacitive sensor for the evaluation of circular cylinders with a conductive core.....	105
Introduction.....	106
Modeling.....	108
Derivation of Green's function in cylindrical coordinates.....	109
Numerical implementation.....	112
Experiment.....	117
Summary.....	123
3. A Capacitive Probe for Quantitative Nondestructive Evaluation of Wiring Insulation.....	124
Introduction.....	124
Summary of the physical model.....	126
Probe and measurement system.....	127

Measurement system and uncertainty analysis .....	129
Parameters of the wire under test.....	130
Case study: evaluation of polyimide-coated wires after thermal and hydrolytic exposure.....	132
Results and discussion .....	133
4. Summary .....	138
Chapter VI. Conclusion.....	140
Bibliography .....	142

THIS PAGE INTENTIONALLY LEFT BLANK

## LIST OF FIGURES

Figure 1 Chemical Structure of Kapton® Polyimide. ....	8
Figure 2 Results of dynamic mechanical analysis on dried PI. ....	10
Figure 3 Percentage weight loss of PI as a function of temperature measured at 30 °C/min heating rate .....	11
Figure 4 The real permittivity (a) and loss factor (b) of dry PI over frequency range 1 Hz to 1 MHz and temperature range –140 to 180 °C. ....	12
Figure 5 Friedman plot for a single step (A) normal reaction, (B) accelerated reaction, and (C) retarded reaction. ....	17
Figure 6 TG curves broaden as the rate increases from 2 to 30 Kmin <sup>-1</sup> . ....	18
Figure 7 DTG curves for the data shown in Figure 6. ....	18
Figure 8 Friedman plot from the data shown in Figure 6. ....	19
Figure 9 Activation energy plot for air atmosphere from (a) Friedman Analysis and (b) Ozawa-Flynn- Wall Analysis. ....	22
Figure 10 Schematic representation of the multistep reaction. ....	22
Figure 11 Best fit model of the TG data for the four-step reaction models in Fig. 6, with parameters given in Table 3. The curves represent the model and the symbols represent the experimental data. .	23
Figure 12 TG isothermal curves of experimental data and model prediction. ....	23
Figure 13 3-dimensional FTIR data for exit gases of a 30 K·min-1 ramp rate TG on degradation onset. .....	24
Figure 14 FTIR data for exit gases of a 30 Kmin-1 ramp rate TG on degradation onset for four different spectral ranges. Peak intensities are only proportional within each range and should not be compared from range to range. ....	25
Figure 15 MS data for exit gases of a 30 Kmin-1 ramp rate TG. ....	25
Figure 16 The loss factor of PI degraded at 475 °C for 3 hr, measured over frequency from 1 Hz to 1 MHz and temperature from –140 to 180 °C. ....	27
Figure 17 The loss factor of dry PI and PI degraded at 475 °C for 3 hr as a function of frequency at room temperature. ....	27
Figure 18 Effect of thermal degradation time and temperature on $\epsilon'$ of PI at 1 kHz. Error bars indicate the standard deviation in measurements on three nominally-identical samples. ....	28
Figure 19 Arrhenius plot for $\beta$ - and $\gamma$ - relaxations of dry PI and PI degraded at 475 °C for 3 hr. ....	29
Figure 20 Pyrolysis process of imide groups of PI during heating [29]. ....	30
Figure 21 FTIR spectra of Kapton polyimide at 30, 400, 450 and 480 °C. ....	30
Figure 22 The cumulative distribution function of the measured dielectric strength of PI samples heated at 475 °C for up to 4 hours. Symbols represent experimental data and lines are obtained by least-squares fitting to the data. ....	35
Figure 23 As for Figure 41 but for PI samples heated for 4 hours at various temperatures from 450 to 480 °C. ....	36
Figure 24 The Weibull-statistical scale parameter ( $\alpha$ ) and the shape parameter ( $\beta$ ) as functions of heating time. ....	36

Figure 25 The Weibull-statistical scale parameter ( $\alpha$ ) and the shape parameter ( $\beta$ ) as functions of heating temperature for 4 hr heating time. ....	37
Figure 26 Measured voltage breakdown of degraded Kapton Film (symbols) with best linear fit (solid line).....	41
Figure 27 Predicted time to failure at 12 and 14.7 kV and for isothermal temperatures ranging from 250 to 400 °C. ....	42
Figure 28 The real permittivity (a) and loss factor (b) of PI immersed in water and saline solutions, measured at 1 kHz. Error bars indicate the standard deviation in measurements on three nominally-identical samples. ....	45
Figure 29 The real permittivity (a) and loss factor (b) of PI following immersion in distilled water. .	46
Figure 30 The real permittivity (a) and loss factor (b) of PI following immersion in 80 g/l saline. ....	47
Figure 31 Effect of dissolved sodium chloride on the real permittivity (a) and loss factor (b) of PI, measured at 1 kHz. ....	48
Figure 32 Chain scission mechanism of PI hydrolysis through interaction of H <sub>2</sub> O with the carbonyl groups [54]. ....	49
Figure 33 The cumulative distribution function of the measured dielectric strength of PI samples immersed in water for 0, 4, 8, 16 and 24 hours. ....	51
Figure 34 The Weibull-statistical scale parameter ( $\alpha$ ) and the shape parameter ( $\beta$ ) as functions of time of PI immersion in distilled water. ....	51
Figure 35 The cumulative distribution function of the measured dielectric strength of PI samples immersed in water for 24, 48, 72 and 96 hours. ....	52
Figure 36 Temperature-pressure phase diagram of crystalline PTFE with the inter- and intra-polymer chain crystalline structures. ....	55
Figure 37 PTFE (a) below the melting temperature 327 °C; and (b) above the melting temperature. ....	56
Figure 38 Results of dynamic mechanical analysis on as-received PTFE. ....	56
Figure 39 Real permittivity of as-received PTFE as function of frequency at room temperature. ....	58
Figure 40 Real permittivity of as-received PTFE as a function of frequency and temperature. ....	58
Figure 41 Real permittivity of as-received PTFE as a function of temperature at 1.15 kHz. (a): -150 to 300 °C; (b): -10 to 50 °C. ....	59
Figure 42 TG curves for PTFE.....	62
Figure 43 DTG curves for PTFE. ....	62
Figure 44 Friedman Analysis for PTFE. ....	63
Figure 45 PTFE activation energy from (a) Friedman Analysis and (b) Ozawa-Flynn-Wall Analysis. ....	63
Figure 46 Model of the best fit TG data for a single-step reaction model in air for PTFE. In the plot, the curves represent the model and the shapes represent the modeled experimental data. ....	64
Figure 47 Real permittivity of PTFE as a function of thermal exposure time at 340 °C in air. ....	66
Figure 48 Experimental arrangement for permittivity measurement while the sample is under tensile strain, using an Agilent E4980A LCR meter and Test Resources, Inc. tensile load frame Model 150Q250. ....	68
Figure 49 Engineering stress-strain curve of PTFE.....	69

Figure 50 The change in the real relative permittivity of PTFE as a function of tensile strain. Note, $\epsilon_r = 2.076$ at 0% strain.....	71
Figure 51 The difference between the real relative permittivity of PTFE under strain (solid symbol) and of released PTFE (open symbol), compared with untreated PTFE. ....	71
Figure 52 Homogeneity of extruded ETFE by (a) DSC; (b) DMA.....	75
Figure 53 Results of dynamic mechanical analysis on extruded ETFE. ....	76
Figure 54 Real permittivity (a) and loss factor (b) of extruded ETFE as a function of frequency and temperature.....	77
Figure 55 Real permittivity and dissipation factor of extruded ETFE as a function of temperature at 1.15 kHz. ....	78
Figure 56 TG curves for ETFE.....	81
Figure 57 DTG curves for ETFE.....	81
Figure 58 Friedman Analysis for ETFE. ....	82
Figure 59 Activation energy from (a) Friedman Analysis and (b) Ozawa-Flynn-Wall Analysis. ....	82
Figure 60 Two-step consecutive model fits to (a) the two slowest heating rates and (b) the two fastest heating rates.....	83
Figure 61 DTG model fit of the two slowest heating rates for ETFE. ....	84
Figure 62 Model of the best fit TG data for the three-step reaction models air atmospheres. In the plots, the curves represent the model, the data point shapes represent the modeled experimental data, and the + represents the un-modeled experimental data.....	84
Figure 63 Real permittivity and dissipation factor of extruded and annealed ETFE as a function of frequency at room temperature.....	87
Figure 64 Real permittivity of ETFE as a function of thermal exposure time at 160 °C. ....	87
Figure 65 Dissipation factor of ETFE as a function of thermal exposure time at 160 °C.....	88
Figure 66 Mid-IR spectra of annealed ETFE and ETFE thermally exposed at 160 °C for 96 hr.....	88
Figure 67 Arc-electrode capacitive sensor. The radii of the sensor electrodes and the cylindrical dielectric rod are denoted $\rho_0$ and $a$ , respectively. The arc-angle of each sensor electrode is $\phi_0$ (rad). The length of each electrode in the vertical direction is $l$ and the width in the horizontal direction is $w = \phi_0 \times \rho_0$ . ....	93
Figure 68 Point source outside of a dielectric rod, assumed infinitely long.....	93
Figure 69 Discretization of the arc-electrode surfaces into $M \times N$ elements of assumed constant surface charge density. ....	98
Figure 70 Calculated sensor output capacitance as a function of electrode length $l$ and arc-angle $\phi_0$ . The dielectric rod is in free space, with a relative permittivity of 2.5 and a radius of 9.525 mm. ....	99
Figure 71 Calculated sensor output capacitance $C$ as a function of the ratio of dielectric rod radius $a$ to electrode radius $\rho_0$ . The electrode radius, arc-angle, and length are $\rho_0 = 9.525$ mm, $\phi_0 = 174.44^\circ$ , and $l = 4$ mm, respectively. ....	100

Figure 72 Calculated sensor output capacitance as a function of dielectric rod relative permittivity. $a/\rho_0 = 1$ , $l = 4$ cm and $\phi_0 = 174.44^\circ$ except where indicated. All the sensor electrodes have fixed radius $\rho_0 = 9.525$ mm. ....	101
Figure 73 Agilent E4980A precision LCR meter and Agilent probe test fixture 16095A used for sensor capacitance measurements. Subfigure: photography of the flexible rectangular planar electrodes fabricated using photolithography. ....	102
Figure 74 Measured and calculated $C$ for various sensor configurations (see Table 18) in contact with different dielectric test-pieces. Measurement results and error bars are denoted by the black symbol. ....	104
Figure 75 Curved patch capacitive sensor. The radii of the sensor electrodes, the conductor, and the cylindrical test-piece are denoted $\rho_0$ , $a$ , and $b$ , respectively. The arc-angle of each sensor electrode is $\phi_0$ (rad). The length of each electrode in the vertical direction is $l$ and the width in the horizontal direction is $w = \phi_0 \times \rho_0$ . ....	109
Figure 76 Point source outside of an infinitely long dielectric-coated conductor. ....	110
Figure 77 Curved patch capacitive sensor is divided into $M \times N$ elements on each electrode, each with assumed constant surface charge density. ....	113
Figure 78 Calculated sensor output capacitance as a function of electrode length $l$ and arc-angle $\phi_0$ . The rod is in free space with conductor radius $a = 8$ mm, dielectric radius $b = \rho_0 = 9$ mm and dielectric permittivity $\epsilon_{r2}' = 2.5$ . ....	114
Figure 79 Calculated sensor output capacitance $C$ as a function of the ratio of cylindrical test-piece outer radius $b$ to electrode radius $\rho_0$ and the ratio of conductive core $a$ to cylindrical test-piece outer radius $b$ . The electrode radius, arc-angle and length are 9 mm, $174^\circ$ and 4 cm, respectively. ....	115
Figure 80 Calculated sensor capacitance and dissipation factor as a function of the dielectric coating real permittivity $\epsilon_{r2}'$ and imaginary permittivity $\epsilon_{r2}''$ . Sensor configuration: $\rho_0 = 9$ mm, $a/b = 0.8$ , $b/\rho_0 = 1$ , $l = 4$ cm and $\phi_0 = 170^\circ$ except where indicated in other lines. $\epsilon_{r2}''$ and the material dissipation factor are assumed to be zero in a). $\epsilon_{r2}' = 2$ in b). ....	116
Figure 81 Agilent E4980A precision LCR meter and Agilent probe test fixture 16095A used for sensor capacitance measurements. Subfigure: photography of the flexible rectangular planar electrodes fabricated using photolithography. ....	118
Figure 82 Photograph of fabricated capacitive probe with curved patch electrodes. Subfigure: capacitive probe holding a wire sample under test. ....	128
Figure 83 Algorithm for determination of the effective electrode arc-angle $\phi_0$ . ....	129
Figure 84 Schematic diagram of fluorinated ethylene propylene (FEP)-coated polyimide 150FWN019 film. Nominal thicknesses of each layer of polyimide 150FWN019 film, FEP fluoropolymer film, and the liquid H lacquer film are $25 \mu\text{m}$ , $13 \mu\text{m}$ , and $129 \mu\text{m}$ , respectively. The FEP provides adhesion between the layers of polyimide. $D_c = 2.09$ mm, $D_w = 2.50$ mm (nominal). ....	131
Figure 85 Algorithm for determination of the imaginary permittivity $\epsilon''$ for the virgin wires. ....	132

Figure 86 Left: muffle furnace used for thermal exposure. Upper right: wire samples after heat exposure (brown) and a control wire (yellow). The samples are 4 cm long. Lower right: For hydrolytic exposure, both ends of the sample are sealed with wax. ....	133
Figure 87 a) measured capacitance and b) dissipation factor for heat exposed wires. Uncertainties derive from the standard deviation of measurements on three separate samples. Physical degradation of the sample heated beyond 2 hours at 475 °C prevented accurate capacitance measurement for those conditions. ....	134
Figure 88 Inferred real permittivity $\epsilon'$ of the thermally exposed wires in comparison with that of polyimide HN film (Chapter II). a) 400 and 425 °C; b) 450 and 475 °C. ....	135
Figure 89 Inferred imaginary permittivity $\epsilon''$ of the thermally exposed wires. ....	136
Figure 90 As for Figure 87 but for hydrolytically exposed wires. ....	137
Figure 91 Inferred complex permittivity, a) real part and b) imaginary part, of the hydrolytically exposed wires in comparison with that of polyimide HN film (Chapter II). ....	138

## LIST OF TABLES

Table 1 History of wiring insulation used in commercial aircraft.....	3
Table 2 Selected properties of 125 $\mu\text{m}$ thick Kapton®HN film.....	9
Table 3 Parameters used in the kinetic model.....	24
Table 4 Correlated coefficient of 2-parameter and 3-parameter Weibull distribution of dielectric strength of PI heated at 475 $^{\circ}\text{C}$ .....	35
Table 5 Weight loss of PI samples heated at 475 $^{\circ}\text{C}$ for up to 4 hours.....	37
Table 6 Weight loss of PI samples heated for 4 hours at various temperatures from 450 to 480 $^{\circ}\text{C}$ ..	37
Table 7 Parameters values used to obtain the calculated lifelines shown in Figure 27.....	42
Table 8 Weight gain of PI samples immersed in distilled water for up to 96 hours.....	52
Table 9 The Weibull-statistical scale parameter ( $\alpha$ ) and the shape parameter ( $\beta$ ) of dry PI.....	52
Table 10 Properties of PTFE and PE.....	55
Table 11 Kinetic Parameters for the single step autocatalytic model for PTFE.....	64
Table 12 Kinetic Models in comparison for PTFE*.....	64
Table 13 Crystallinity of PTFE for various values of tensile strain, measured by X-ray diffraction immediately upon removing the sample from the tensile tester.....	70
Table 14 Properties of ETFE.....	73
Table 15 Reaction parameters for two-step consecutive model fits for ETFE.....	83
Table 16 Reaction parameters for the three-step consecutive model fit.....	85
Table 17 F-Test statistical analysis of the model fits for three-step reactions for ETFE*.....	85
Table 18 Parameters of the dielectric test-pieces and the arc-electrode sensors used in benchmark experiments. The areas of the two sets of sensor electrodes are $29 \times 20 \text{ mm}^2$ and $29 \times 40 \text{ mm}^2$ , respectively.....	103
Table 19 Comparison of test-piece permittivity values between independently measured ones and inversely determined ones from measured capacitance using the arc-electrode sensors.....	104
Table 20 Measured complex permittivity values of the dielectric coating materials.....	120
Table 21 Parameters of the test-pieces and the capacitive sensors used in benchmark experiments. The three copper rods used as the conductive cores in the cylindrical test-pieces had a uniform diameter of $15.90 \pm 0.01 \text{ mm}$ .....	120
Table 22 Measured and calculated capacitance for various sensor configurations in contact with different cylindrical test-pieces.....	121
Table 23 Probe parameters, Figure 82.....	129

## LIST OF PUBLICATIONS AND PRESENTATIONS RESULTING FROM THIS WORK

### Articles in Journals (in print or accepted)

- 1 L. Li, N. Bowler, M. R. Kessler and S.-H. Yoon, Dielectric Response of PTFE and ETFE Wiring Insulation to Thermal Exposure, *IEEE Trans. Dielectr. Electr. Insul.*, 17, 1234-1241, 2010.
- 2 L. Li, N. Bowler, P. R. Hondred, and M.R. Kessler, Influence of Thermal Degradation and Saline Exposure on Dielectric Permittivity of Polyimide, *J. Phys. Chem. Solids*. 72, 875-881, 2011.
- 3 P. R. Hondred, S. Yoon, N. Bowler, E. Moukhina and M. R. Kessler, Degradation Kinetics of Polyimide Film, *High Performance Polymers*, 23, 335-342, 2011.
- 4 T. Chen, N. Bowler and J. R. Bowler, Analysis of Arc-electrode Capacitive Sensors for Characterization of Dielectric Cylindrical Rods, *IEEE Trans. Instrumentation Meas.*, DOI: [10.1109/TIM.2011.2157573](https://doi.org/10.1109/TIM.2011.2157573).
- 5 L. Li, N. Bowler, P. R. Hondred and M. R. Kessler, Statistical Analysis of Electrical Breakdown Behavior of Polyimide Following Degrading Processes, *IEEE Trans. Dielectr. Electr. Insul.*, 18, 1955-1962, 2011.

### Bulletins, Reports, or Conference Proceedings That Have Undergone Stringent Editorial Review by Peers (in print or accepted)

- 1 S.-H. Yoon, N. Bowler and M. R. Kessler, Thermal Analysis Properties of PTFE Electrical Wiring Insulation Material, Proceedings of the North American Thermal Analysis Society Annual Conference (NATAS 2008). Aug. 18-20, 2008. Atlanta, GA. CD-ROM. Pages: 9.
- 2 L. Li, N. Bowler, S.-H. Yoon and M. R. Kessler, Dielectric Properties of PTFE Wiring Insulation Materials as a Function of Thermal Exposure, *2008 Annual Report: Conference on Electrical Insulation and Dielectric Phenomena*, IEEE Dielectrics and Electrical Insulation Society, 95-98.
- 3 L. Li, N. Bowler, S.-H. Yoon and M. R. Kessler, Dielectric Properties of ETFE Wiring Insulation as a Function of Thermal Exposure, *2009 Annual Report: Conference on Electrical Insulation and Dielectric Phenomena*, IEEE Dielectrics and Electrical Insulation Society. CD-ROM. Pages: 4.
- 4 P. R. Hondred, S.-H. Yoon, N. Bowler and M. R. Kessler, Onset Degradation Kinetics of Poly(ethylene-alt-tetrafluoroethylene), Proceedings of the 37th North American Thermal Analysis Society Annual Conference (NATAS 2009). Sep. 20-23, 2009. Lubbock, TX. CD-ROM. Pages: 9.
- 5 P. R. Hondred, S.-H. Yoon, N. Bowler and M. R. Kessler, A Comparison of Degradation Kinetics for Aerospace Wire Insulation Materials, Proceedings of the 38th North American Thermal Analysis Society Annual Conference (NATAS 2010). Aug. 15-18, 2010. University of Pennsylvania, PA. CD-ROM. Pages: 7.
- 6 Li Li, N. Bowler, P. R. Hondred and M.R. Kessler, Dielectric Response of Polyimide to Thermal and Saline Degradation, *2010 Annual Report: Conference on Electrical Insulation and Dielectric Phenomena*, IEEE Dielectrics and Electrical Insulation Society. CD-ROM. Pages: 4.

Bulletins, Reports, or Conference Proceedings That Have Not Undergone Stringent Editorial Review by Peers (in print or accepted)

- <sup>1</sup> T. Chen and N. Bowler, Cylindrical Capacitive Sensor for the Evaluation of Wire Insulation and Cable Degradation, Aircraft Airworthiness and Sustainment Conference, Austin, TX, 10-13 May 2010. <http://www.airworthiness2010.com>. Pages: 7.
- 2 L. Li, N. Bowler, S.-H. Yoon and M. R. Kessler, Dielectric Response of PTFE Wiring Insulation to Thermal Exposure, Aircraft Airworthiness and Sustainment Conference, Austin, TX, 10-13 May 2010. <http://www.airworthiness2010.com>. Pages: 11.
- 3 P. R. Hondred, S.-H. Yoon, N. Bowler and M. R. Kessler, Degradation Kinetics of Polyimide Insulation Material, Aircraft Airworthiness and Sustainment Conference, Austin, TX, 10-13 May 2010. <http://www.airworthiness2010.com>. Pages: 5.

Abstracts (in print or accepted) and Technical Presentations

- 1 N. Bowler, L. Li, S.-H. Yoon and M. R. Kessler, Dielectric and Thermal Analysis Properties of PTFE Wiring Insulation for Nondestructive Evaluation and Lifetime Prediction, NASA Aviation Safety Technical Conference, Denver, CO, October 21-23, 2008
- 2 N. Bowler, L. Li, P. R. Hondred, T. Chen and M. R. Kessler, Investigation of Dielectric and Thermal Properties of Wire Insulating Polymers for Development of Capacitive Nondestructive Evaluation, NASA Aviation Safety Technical Conference, McLean, VA, November 17-19, 2009.
- 3 P. R. Hondred, L. Li, T. Chen, S.-H. Yoon, N. Bowler and M. R. Kessler, Modeling and Nondestructive Evaluation of Wire Insulation, Interagency Wiring Group Meeting, Kennedy Space Center, December 8-10, 2009.
- 4 P. R. Hondred, S.-H. Yoon, N. Bowler and M. R. Kessler, Degradation Kinetics of Aerospace Wire Insulation Material, Society of Engineering Science 47th Annual Technical Meeting, Iowa State University, October 4-6, 2010.
- 5 N. Bowler and T. Chen, A Capacitive Sensor for Inspecting Wiring Insulation, The 2011 Aircraft Airworthiness and Sustainment Conference, San Diego, CA, April 18-21, 2011.
- 6 N. Bowler and T. Chen, Capacitive Sensors for Measuring Complex Permittivity of Planar and Cylindrical Test Pieces, 12th International Symposium on Nondestructive Characterization of Materials, Blacksburg, VA, June 19-24, 2011.
- 7 N. Bowler, L. Li, P. R. Hondred, T. Chen and M. R. Kessler, Dielectric Properties of Wiring Insulation Polymers in Response to Thermal, Hydrolytic and Mechanical Aging, and a Capacitive Sensor for Inspecting Wiring Insulation, NASA Langley Research Center Nondestructive Evaluation Sciences Branch, Hampton, VA, June 2011.

Publications and Creative Works Submitted but Not Accepted

1. P. Hondred, N. Bowler and M. R. Kessler, Electrothermal Lifetime Prediction of Polyimide Wire Insulation with Application to Aircraft, *IEEE Trans. Dielectr. Electr. Insul.*, submitted September 2011.
2. T. Chen and N. Bowler, Analysis of a Capacitive Sensor for the Evaluation of Circular Cylinders with a Conductive Core, *Meas. Sci. Technol.*, submitted September 2011.

## Chapter I. Introduction

Polymers have been widely used as wiring electrical insulation materials in space/air-craft. The dielectric properties of insulation polymers can change over time, however, due to various aging processes such as exposure to heat, humidity and mechanical stress. Therefore, the study of polymers used in electrical insulation of wiring is important to the aerospace industry due to potential loss of life and aircraft in the event of an electrical fire caused by breakdown of wiring insulation.

Part of this research is focused on studying the mechanisms of various environmental aging process of the polymers used in electrical wiring insulation and the ways in which their dielectric properties change as the material is subject to the aging processes. The other part of the project is to determine the feasibility of a new capacitive nondestructive testing method to indicate degradation in the wiring insulation, by measuring its permittivity.

### 1. *Motivation*

Dielectric wiring insulation is used to separate electrical conductors by preventing the flow of charge between wires. Insulation materials function to maintain a continuous and specified value of permittivity over a specified range of electromagnetic field frequency and strength. Another essential property of wiring insulation is the dielectric strength, a field at which the material fails to resist the flow of current and arcing occurs. The dielectric properties of potential wiring insulation materials are always carefully considered to guarantee that the selected materials satisfy requirements of the operating environment.

Both the dielectric permittivity and dielectric strength of wire insulation may change over time, however, due to various degradation processes such as thermal aging, moisture exposure and mechanical degradation. For example, wiring may be improperly installed and maintained, increasing the risk of damage due to heat, moisture and chafing [1]. Such damage mechanisms may act acutely, or act to 'age' the insulation material over many cycles of aircraft operation. These mechanisms by which wire systems insulation may be degraded produce what are known as a 'soft' faults, which act to modify the impedance of the affected region of the coated wire structure, when viewed as a transmission line, rather than a 'hard' fault such as an open or short in the conductor itself. It has been reported [2] that aircraft suffer from undiagnosed wiring degradation which may cause short-circuiting, fire and loss of control function. According to Captain Jim Shaw, manager of the in-flight fire project for the United States Air Line Pilots Association (ALPA), there are on average three fire and smoke events in jet transport aircraft each day in USA and Canada alone, and the vast majority are electrical. It was presented in Air Safety Week, 2001, that aircraft were making emergency landings, suffering fire damage to the point of being written off etc,

at the rate of more than one a month based on the experience of the previous few months. These issues remain a concern for new aircraft.

Motivated by these concerns, the contribution of this work is to explore and record change in dielectric properties of wire insulation due to various degradation processes.

## 2. *History of wiring insulation*

Table 1 shows wiring insulation materials applied in commercial aircraft since the 1960s [1]. PVC (polyvinyl chloride) and Nylon were the main insulation materials from the 1960s to the 1980s. However, in the next decades, PI (polyimide) was almost the only wiring insulation polymer used in the listed airplanes. After the 1990s, another two materials, TKT<sup>1</sup> (Teflon -Kapton -Teflon) and Tefzel® ETFE (ethylene-tetrafluoroethylene), have been widely used. This work focuses on three polymers: PI, PTFE and ETFE. More detailed information about these polymers will be introduced in Chapters II, section 3.

## 3. *Technical approach*

### **Permittivity**

The permittivity is a parameter that indicates the relative charge storage capability of dielectrics in the presence of an electric field. In general, permittivity is complex, denoted  $\epsilon^* = \epsilon' - j\epsilon''$ . Complex permittivity measurements have been made on the sample materials investigated here, before and after degradation, to explore the changes in permittivity and dielectric relaxations in response to degradation. Two instruments were employed to measure complex permittivity of the polymers. The first one is a Novocontrol Spectrometer, which is capable of measurement over frequency range from 1  $\mu$ Hz to 3 GHz. A temperature-controlled sample cell also permits measurements at temperatures from -200 °C to 400 °C. The other one is an Agilent E4980A LCR meter coupled with a 16451 dielectric test fixture, which is available from 20 Hz to 2 MHz at room temperature.

### **Breakdown voltage**

Another essential property of dielectric insulators is the dielectric breakdown voltage, the point at which the applied voltage causes current flow in a device (transistor, capacitor etc) to increase uncontrollably. Breakdown in a capacitor results in the replacement of a reactive insulating component by either a low-resistance short circuit or open circuit, usually with disastrous consequences as far as the overall circuit function is concerned. The probability of its occurrence must therefore be kept to an

---

<sup>1</sup> Teflon is a trade name for PTFE (polytetrafluoroethylene) and Kapton is a trade name for polyimide.

absolute minimum. Dielectric breakdown of insulation polymers before and after degradation processes have been measured by a DIELECTRIC RIGIDITY 6135 which can supply voltage up to 60 kV..

### Thermal exposure

Thermal exposure can significantly influence properties of polymers by changing microstructure, phase morphology, chemical composition, etc. The effect of thermal exposure in air on the permittivity of PI, PTFE and PI has been explored, which will be discussed in Chapters II, III, and IV, respectively.

**Table 1** History of wiring insulation used in commercial aircraft.

<b>Wiring insulation material</b>	<b>Applied years</b>	<b>Applied aircraft</b>
PVC/ Nylon	1960-1980	707, 727, 737, and DC-8
Slash 6	1965-1985	DC-9
Poly-X and Stilan	1970-1980	747, DC-10/MD-11
PI	1970 later	727, 737, 757, 767, MD-80/-90, DC-10/MD-11, Lockheed L-1011, Airbus
Tefzel	1975 later	727, 737, 757, 767, MD-80/-90, DC-10/MD-11
Tefzel/PI	1980-1990c	747
TKT	1990 later	737, 757, MD-80/-90, DC-10/MD-11

### Water and saline exposure

There are several physical consequences of water absorption to wire insulation material including plasticization, swelling, and changes in dielectric properties. Even though polyimide has very good electrical and physical properties, it is very susceptible to humidity, which can give rise to cracks in the insulation and cause electrical malfunctions. In response to the concern that aircraft which serve in navy are exposed to sea water, the effect of water and saline exposure on dielectric properties of polyimide has been studied. Effect of saline exposure on insulating properties of PI will be presented in Chapter II.

### Mechanical stress

During cycles of aircraft operation and due to improper installation, wiring insulation materials may be exposed to mechanical stress, which can result in structural changes and consequently influence the dielectric properties of the insulation. Given this concern, the influence of mechanical strain on the

permittivity of PTFE is investigated in Chapter III. A system capable of measuring dielectric permittivity while a polymer sample is simultaneously under tensile strain is designed and applied.

### **Material characterization**

Thermal analysis instruments, such as a TGA (thermogravimetric analyzer) Q50 instrument, a DMA (dynamic mechanical analyzer) Q800 instrument and a DSC (differential scanning calorimeter) Q20 instrument, are used to investigate thermal properties of the polymers. TGA uses heat to induce chemical and physical changes in materials and performs a corresponding measurement of mass change as a function of temperature or time. In some advanced instruments, residual gases released from materials can be analyzed using TGA-tandem instruments, such as TGA-FTIR or TGA-Mass Spectrometry, to determine the identity of the released gas and give insight into the weight loss mechanism. DMA measures the mechanical properties of polymer material as function of temperature and frequency, which reveals molecular relaxations in polymers. DSC is used to measure temperatures and heat flow during thermal transitions (glass transition, crystallization and melting) in polymeric materials. The degree of crystallinity of semi-crystalline polymers can also be obtained from the crystallization exotherm. Those methods have been applied to investigate thermal properties of the three polymers, which will be presented in Chapters II, III and IV.

X-ray diffraction (XRD) and Infrared (IR) spectroscopy are also utilized. Both of these analysis methods are widely used to determine properties of polymers. XRD turns out to be a convenient and reliable method to investigate crystalline structure. The degree of crystallinity of polymers, which plays an important part in determining their dielectric properties, has been measured by XRD. IR spectroscopy is one of the most common spectroscopic methods applied to analyze organic compositions. It utilizes a Michelson interferometer and is based on IR absorption by dipolar molecules as they undergo vibrational and rotational transitions. Each peak in an IR spectrum indicates characteristic absorption regions for some commonly observed bond strength and bending deformations. It has been used to detect signs of oxidation due to thermal exposure of PI and ETFE.

#### **4. *NDE of wire insulation***

The theme of this research is focused on evaluating wiring insulation status through capacitive methods. Insulation status can be characterized by its dielectric properties. Model-based capacitive methods developed in this research relate quantitatively the measurable capacitance to the dielectric properties of wires under test, and therefore allow for effective determination of wire insulation status. Experimental studies on realistic aircraft wires showed that dielectric property changes in wiring insulation due to

thermal and hydrolytic exposures can be successfully detected using the capacitive methods developed in this research, for wire type MIL-W-81381/12.

### **Motivation**

This work is motivated by the effective evaluation of degradation status of air- and space-craft wiring insulation. Degradation in electrical wiring insulation has the potential to cause aviation catastrophe due to consequent short-circuiting or loss of control function [88]. Different wire inspection techniques have been developed over the past decade, for the purpose of replacing the traditional visual inspection method.

### **Causes of failure and aging in aircraft wiring**

In [89], causes and modes of failure in legacy aircraft wiring have been categorized. These causes include chemical degradation such as corrosion of current carriers and hydrolytic scission of polymer chains, electrical degradation of wiring insulation that may be due to concentrated electric fields at sites of electrical stress and different kinds of arcing, and mechanical degradation due to vibration, over bending and other kinds of mechanical stress.

### **Inspection techniques**

Visual inspection is probably the most widely used method for aircraft wire inspection. It is highly laborious while giving little quantitative information about the condition of the wires. Different physics-based wire inspection techniques have been developed over the past decade to replace this traditional inspection method, of which a summary is given here.

#### *Methods that can be applied for wiring conductor inspection*

These wire inspections methods can qualitatively determine if the wiring is faulty but are not suitable for inspection of aging aircraft wiring. Resistance measurement methods differentiate broken wires from good ones by measuring the end-to-end cable resistance. High resistance indicates broken wires (open circuit) while low resistance means the wiring is healthy (short circuit). The low-voltage resistance tests and dielectric-withstand-voltage tests can detect faults but are not suitable for miniaturization or pinpointing the fault [90].

One of the most commonly used physics-based techniques for aircraft wiring testing is reflectometry, in which a high frequency electrical signal is sent down the wire and any impedance discontinuities in the testing wire results in reflected signals. The location of the fault can be determined from the time or phase delay between the incident and reflected signals whereas the impedance of the discontinuity is obtained from the magnitude of the reflection coefficient. An excellent review paper that compares different reflectometry methods is [91]. Reflectometry, however, is not capable of inspecting the insulation conditions. Reflectometry methods are distinguished by the types of incident voltage used. Time domain

reflectometry (TDR) uses a short rise time voltage step as the incident voltage. This method is susceptible to noises and is not optimal for live wire testing [92] [93] [94]. Frequency domain reflectometry (FDR) uses a set of stepped-frequency sine waves as the incident voltage. A conceptual design of a "smart wiring system" based on FDR methods that can be used for on-board testing of aging aircraft wiring has been described in [90]. Phase-detection frequency-domain reflectometer (PD-FDR) has also been applied for locating open and short circuits in a Navy F-18 flight control harness [95]. Sequence time domain reflectometry (STDR) and spread spectrum time domain reflectometry (SSTDR) use pseudo noise sequence and sine wave modulated pseudo noise code as the incident voltage, respectively. Testing systems based on these two techniques are capable of testing live wires and therefore have the potential to be used on energized aircraft to locate intermittent faults. The parameters that control the accuracy, latency, and signal to noise ratio for SSTDR in locating defects on live cables has been examined in [96], and the feasibility of spread spectrum sensors for locating arcs on realistic aircraft cables and live wire networks has been demonstrated in [97] and [98].

In [99], linear relationships between the capacitance/inductance of open-/short- circuited wires (parallel insulated round wires, twisted-pair wires, and coaxial cables) and their length have been demonstrated and enables the determination of cable length from measured capacitance/inductance values.

#### *Methods that can be applied for wiring insulation inspection*

Infrared thermography systems and pulsed X-radiography systems have been developed as nondestructive testing methods of aircraft wiring [100]. Infrared thermography has the benefits of rapidly examining large areas of wiring and can serve as a global testing method, whereas a portable pulsed X-ray system can be used to obtain a radiographic image of the portion of the wire or cable.

Ultrasonic methods have also been developed to obtain quantitative information about aircraft wire insulation [101]. These methods, by modeling insulated wires as cylindrical waveguides, have been able to relate extensional wave phase velocity to heat damage or exposure in wire insulation and thus provide quantitative information about the insulation condition.

Acoustic and impedance testing methods aiming at locating intermittent faults in aircraft wires and the widely used Mil-Std-1553 data bus system have been reported in [102]. Micro-fabricated current sensors that could be located in key areas of the electrical wiring and interconnects systems have been reported in [103]. Partial discharge (PD) analysis methods for diagnosing aircraft wiring faults are explored in [104], where a simulation of PD signal based on high-voltage insulation testing standard [105] has been detailed, followed by wavelet based analysis to de-noise the PD signals.

*Capacitance methods developed in this research*

Deficiencies of the above methods suitable for wiring insulation inspection include the need of complex instruments in the measurement and not being able to provide quantitative information about the insulation condition at specific locations. A favorable solution to these deficiencies is capacitive methods, from which quantitative information about the permittivity of wiring insulation at specific locations can be obtained using not so complicated equipment.

A curved patch capacitive sensor, with electrodes that conform to cylindrical test-piece surfaces, has been developed for wiring insulation evaluation. Numerical models have been developed and verified for both the homogeneous dielectric cylinder structure and the cylindrical structure of dielectric-coated conductors. Experimental studies on realistic aircraft wires showed that dielectric property changes in wiring insulation due to thermal and hydrolytic exposures can be successfully detected using the curved patch capacitive sensors, for wire type MIL-W-81381/12.

## Chapter II. Polyimide

Polyimide (PI) is widely used as an insulation material for machines and wiring, and is effective at temperatures up to 400 °C. Given the fact that polyimide may be exposed to extreme temperatures during unusual events in service, its thermal degradation kinetics and the effect of thermal degradation on its permittivity and electrical breakdown behavior have been studied. The lifetime of polyimide under electrothermal multi-stress is predicted by using a short term technique. As polyimide is commonly immersed in salt water while serving in navy aircraft, effect of water/saline exposure on its permittivity and electrical breakdown behavior is also investigated in this chapter.

### 1. Introduction

Kapton HN is a polyimide film developed by DuPont which has been successfully used as electrical insulation in a wide range of temperatures, from -269 °C to +400 °C (4 K - 673 K) [3]. The chemical name for Kapton HN is poly (4,4'-oxydiphenylene-pyromellitimide), and its chemical structure is shown in Figure 1. Kapton® Polyimide is produced from the condensation of pyromellitic dianhydride and 4,4'-oxydiphenylamine. In addition to its very light weight and advanced mechanical properties compared to other insulator types, Kapton HN polyimide has good dielectric properties, such as high breakdown field, low dielectric constant and low loss factor. Selected properties of 125 µm thick Kapton HN film are listed in Table 2 [3]. However, polyimide is very susceptible to hydrolytic degradation, which can give rise to cracks in the insulation and cause electrical malfunctions [4].

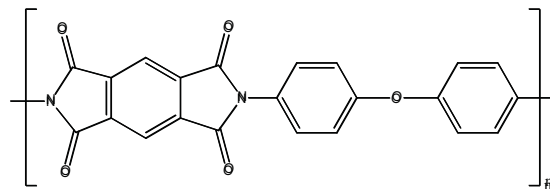


**Figure 1** Chemical Structure of Kapton® Polyimide.

Melcher et al [5] explored the effect of moisture on the complex permittivity of polyimide film in a temperature range from 80 to 325 K. It is presented that the imaginary part  $\epsilon''$  measured for a film which was dried for two days shows only one maximum in the temperature range (the lowest curve). Absorption of water alters this behavior for different water contents at fixed frequency 10 kHz. The peak height increases with water content and an additional smaller loss peak appears at its lower temperature shoulder.

The shape of the larger peak, which is notified as the high-temperature peak, is the same for all film. The influence of the high-temperature peak can be subtracted because its shape is essentially independent

of the water content. But the height of the peak increases with higher water content. The second peak, the low-temperature peak, is considered to be strongly overlapped by the high-temperature peak. According to a statement in [6], since the high-temperature peak is present even at low humidity levels, it is proposed to be associated with water absorbed at the carbonyl groups. And the low-temperature peak is only visible at higher humidity, it is likely caused by water absorbed at the ether linkage. As the two loss peaks can be removed by drying the film, it is concluded that the water dipole causes this relaxation process and not an intrinsic dipole of the polyimide chain.

It is also presented in reference [5] that the increase of the real part  $\epsilon'$  near room temperature correlates to the peaks in  $\epsilon''$ .

Thermal exposure of polyimide has also been explored [7] [8] [9] [10]. No significant changes in the dielectric properties of polyimide were observed after thermal exposure in air or  $N_2$  from 200 to 350 °C for up to 5000 hours.

**Table 2** Selected properties of 125  $\mu\text{m}$  thick Kapton®HN film.

Property	Value
Dielectric strength	154 kV/mm at 60 Hz, 23 °C and 50% RH
Dielectric constant	3.5 at 1kHz, 23 °C and 50% RH
Dissipation factor	0.0026 at 1kHz, 23 °C and 50% RH
Melting point	none
Glass transition	360 to 410 °C
$\beta$ -transition	60 to 127 °C
$\gamma$ -transition	-118 to -28 °C
Ultimate tensile strength	231 MPa at 23 °C
Impact strength	78 N cm at 23 °C
Yield point at 3%	69 MPa at 23 °C

## 2. *Sample material*

All the PI samples under investigation in this chapter were cut from large sheets of 125- $\mu\text{m}$ -thick Kapton® HN PI film obtained from Dupont.

The storage modulus  $E'$ , loss modulus  $E''$  and  $\tan \delta$  of PI film were measured from -150 to 180 °C at 1 Hz by DMA and analyzed by the software 'TA Universal Analysis' which can estimate values of peaks and shoulders in the curve to a tenth of a degree, as shown in Figure 2. The  $\tan \delta$  curve reveals two molecular relaxations at approximately 60°C and 350 °C. The relaxation at 350 °C is attributed to the glass transition that occurs in the amorphous phase [3], while the relaxation at approximately 60 °C is associated with the  $\beta$ -transition, which is a sub- $T_g$  relaxation that takes place at temperatures between 60 and 127 °C [11]. It is considered to be a result of torsional oscillations of the phenylene ring, involving

imide groups of PI [12]. In addition, PI exhibits  $\gamma$ -transition in temperature range between -118 and -28 °C [11] due to increase in the vibration of aromatic groups as intra- and intermolecular interactions decrease in the presence of absorbed moisture [12].

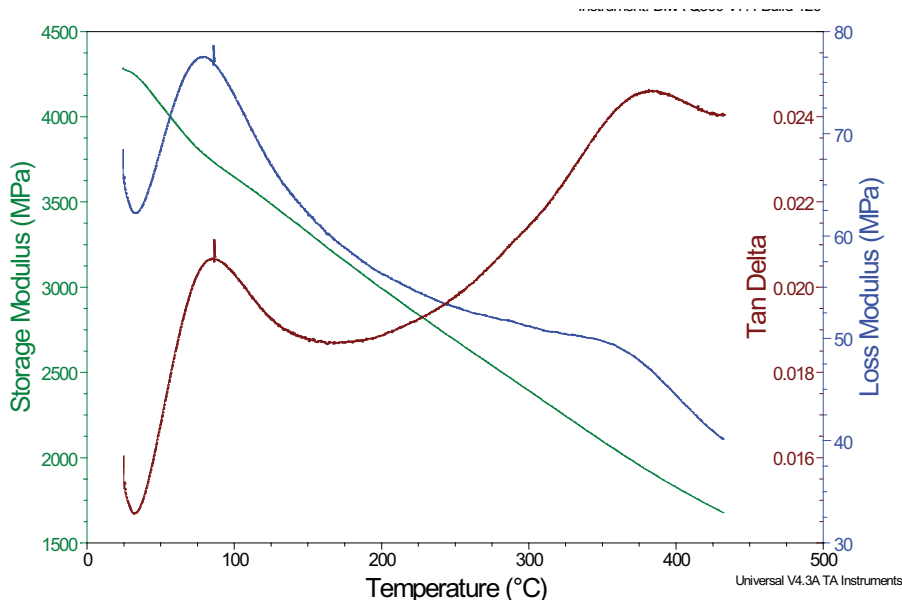


**Figure 2** Results of dynamic mechanical analysis on dried PI.

Since the permittivity and electrical breakdown strength of Kapton PI film changes significantly with moisture content [13], dry samples are needed in order to obtain baseline (control) values of dielectric strength for comparing with those obtained following thermal exposure and immersion in water. In order to determine a heating temperature to effectively remove water from PI, weight loss of a PI sample was monitored by thermogravimetric analysis (TGA) while it was heated from 30 to 900 °C in air at 30 °C/min. As shown in Figure 3, an initial weight loss of 1% was observed at approximately 200 °C, which is attributed to loss of water from the sample during the heating process. Therefore, PI samples for baseline breakdown measurement were dried by heating at 200 °C for 1 hr, which, moreover, cannot give rise to degradation of PI.

One dry PI control sample was coated with gold paint immediately upon removal from the isothermal furnace. Its complex permittivity was measured at frequencies from 1 Hz to 1 MHz over temperatures increasing from -140 °C to 180 °C in increments of 10 °C, by using a Novocontrol Dielectric Spectrometer with temperature-controlled standard sample cell. The real permittivity,  $\epsilon'$ , and loss factor,  $\tan \delta$ , of the dry PI control sample over the whole temperature and frequency ranges are plotted as surface plots in Figures 4a and 4b, respectively. Below approximately 0 °C,  $\epsilon'$  increases with temperature; while it decreases with increasing temperature at higher temperatures. Given that polyimide is a polar polymer,

the dependence of its real permittivity on temperature is determined by how much its intra- and intermolecular interactions change with temperature [13]. If intra- and intermolecular interactions are independent of temperature, the permittivity would decrease with temperature. However, if intra- and intermolecular interactions change significantly with temperature, the dependence of permittivity on temperature would be governed by the change in intra- and intermolecular interactions and  $\epsilon'$  would increase with temperature. Therefore, it is speculated here that the intra- and intermolecular interactions of polyimide change significantly with temperature below 0 °C, while at higher temperatures their change with temperature is reduced. It can also be seen that  $\epsilon'$  decreases with frequency at each temperature; while  $\tan \delta$  as a function of temperature reveals two peaks. The higher-temperature peak corresponds to the  $\beta$ -relaxation of PI. On the other hand, the lower-temperature peak can be ascribed to the  $\gamma$ -relaxation of PI. The highest values of  $\tan \delta$  observed at low frequencies and high temperatures are considered as a result of electrode polarization [14].

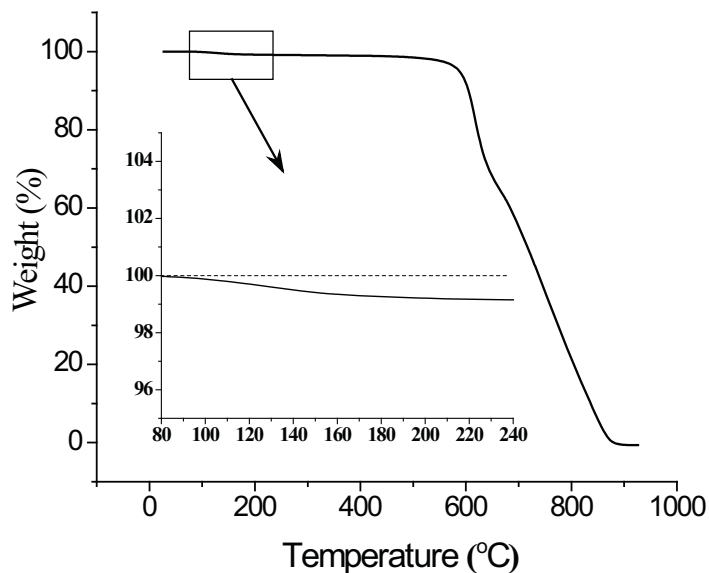


**Figure 3** Percentage weight loss of PI as a function of temperature measured at 30 °C/min heating rate

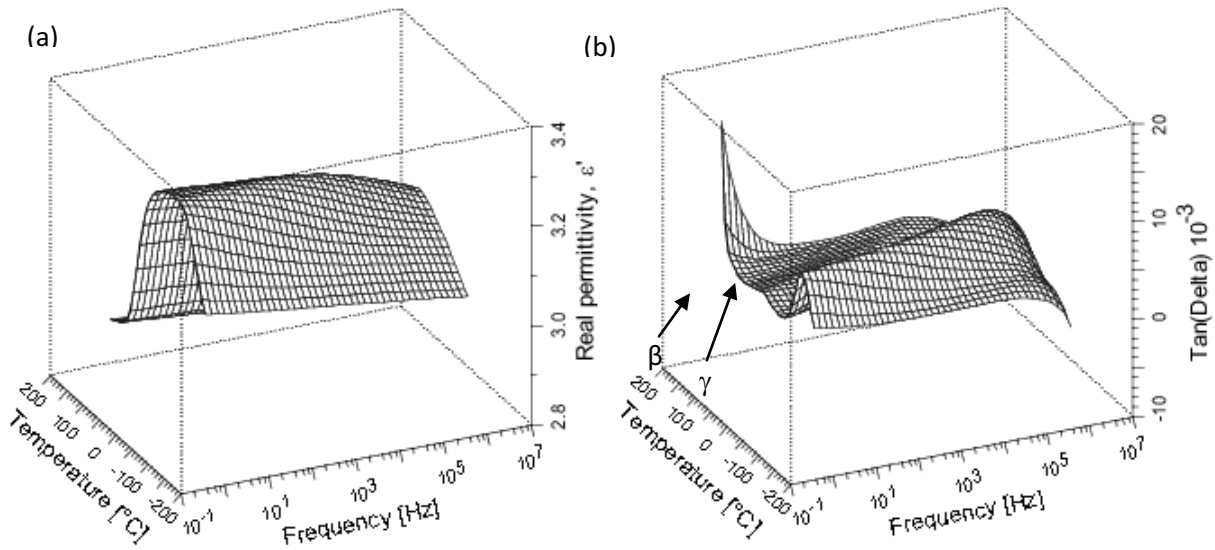


**Figure 4** The real permittivity (a) and loss factor (b) of dry PI over frequency range 1 Hz to 1 MHz and temperature range  $-140$  to  $180$  °C.

### 3. *Thermal degradation*

#### **Thermal degradation kinetics**

##### *Method and experiment*

The most common tool for analyzing polymer degradation is thermogravimetry (TG). TG measures the degree of degradation (as measured by mass loss) with respect to time ( $t$ ) and temperature ( $T$ ) [15]. The degree of degradation ( $\alpha$ ) for the case of total decomposition with zero rest mass can be defined as:

$$\alpha = f(t, T) = 1 - \frac{wt\%}{100} \quad (1)$$

where  $wt\%$  is the relative mass obtained directly from the TG experiment.

TG experiments capturing the polymer degradation at different heating rates provide data that can be used to obtain degradation kinetic parameters, such as activation energy, for various reaction models. In this work, Kapton is analyzed by TG in an air environment to investigate the degradation in oxidative environments. Through the use of isoconversional kinetics, the advanced model mechanisms are identified. A mathematical model representing degradation is developed with an excellent statistical fit to the experimental TG data and is used to compare isothermal data. Finally, Fourier Transformed Infrared (FTIR) analysis and Mass Spectroscopy (MS) analysis of the exit gases identifies the breakdown components of Kapton to verify the complex degradation of Kapton.

A thermogravimetric (TG) analyzer, model Q50 from TA Instruments (New Castle, DE), was used for all of the TG experiments. The experiments were conducted from room temperature to 900 °C at five separate ramp rates: 2, 5, 10, 20, and 30 Kmin<sup>-1</sup>. Under the controlled environment of the TG instrument, the samples were degraded in an air atmosphere using a balanced purge gas flow rate of 40 mL/min and a sample purge gas flow rate of 60 mL/min. Samples were placed on a platinum pan during the degradation process. Kinetic analysis was performed with the Netzsch Thermokinetics 2 program (version 2004.05) and standard statistical and plotting programs. Further study was conducted through evolved gas analysis, a technique utilizing MS and FTIR on exit gases from the TG experiments, to verify the degradation breakdown components and paths. Each test sample was punched out of the film using a circular punch, 5 mm in diameter, ensuring reproducible sample weight and shape. The sample masses were 3.6 ± 0.5 mg.

#### *Kinetic modeling*

In degradation kinetics, the degree of degradation (Eqn. 1) varies from 0 (no mass loss) to 1 (complete mass loss). When modeling, two separate functions are assumed;  $K(T)$  and  $f(\alpha)$ , such that the governing differential equation has the following form:

$$\frac{d\alpha}{dt} = K(T)f(\alpha) \quad (2)$$

where  $da/dt$  is the rate of degradation,  $K(T)$  is the temperature-dependent rate constant, and  $f(\alpha)$  corresponds to the reaction model [16]. The temperature-dependent rate constant is commonly described by the Arrhenius equation:

$$K(T) = A e^{-E/RT} \quad (3)$$

where  $R$  is the universal gas constant,  $E$  is the activation energy, and  $A$  is a pre-exponential factor [17].

When heating at a constant rate, Eqn. 2 can be redefined to eliminate the time-dependence by dividing through by the heating rate:

$$\frac{d\alpha}{dT} = \frac{A}{\beta} f(\alpha) e^{-E/RT} \quad (4)$$

where  $\beta = dT/dt$  is the heating rate.

Through linear transformation, the kinetic parameters ( $A$  and  $E$ ) can be obtained by the time-independent rate equation:

$$\ln\left(\frac{d\alpha/dT}{f(\alpha)}\right) = \ln\left(\frac{A}{\beta}\right) - \frac{E}{RT} \quad (5)$$

Eqn. 5 follows the linear form  $y = a_0 + a_1x$  (with  $x = 1/T$ ) and optimal fit of the kinetic parameters is determined using linear regression. By calculating these parameters through linear regression at several different mass losses, the variation in the kinetic parameters as a function mass loss is determined.

In one approach for kinetic degradation modeling, constant activation energy and pre-exponential factors are assumed [17]. The model-free isoconversional method allows for varying kinetic parameters by assuming both the activation energy and pre-exponential factor are a function of the degree of degradation [18]. Friedman's method, a well-known technique, obtains the activation energy by plotting the logarithmic form of the rate equation for each heating rate:

$$\ln \left[ \beta_i \left( \frac{d\alpha}{dT} \right)_{\alpha,i} \right] = \ln(A_\alpha f(\alpha)) - \frac{E_\alpha}{RT_{\alpha,i}} \quad (6)$$

where the subscripts  $\alpha$  and  $i$  represent the value at a particular degree of degradation and the data from the given heating rate experiment, respectively [17]. The activation energy at each degree of degradation is calculated with linear regression from a plot of  $\ln[\beta_i (d\alpha/dT)_{\alpha,i}]$  versus  $1/T_{\alpha,i}$  across all of the heating rates tested. The Friedman plot not only provides confirmation of the multi-step processes during the reaction but also provides insight into the type of reaction steps. The type of reaction can be determined by comparing the slope of the constant fractional mass loss trend line to the slope of the constant heating rate data at each peak. The peak slope specifically refers to the slope of the linear portion to the right side of each peak. Comparing the relative magnitude of each negative slope, three types of reactions are defined: normal, accelerated, and retarded. A normal reaction corresponds to slopes of equal magnitude in both the fractional mass loss trend line and the peak slope of the constant heating rate data—Figure 5A. An accelerated reaction corresponds to a steeper peak slope in the constant heating rate data compared to the fractional mass loss trend line—Figure 5B. A retarded reaction corresponds to a steeper fractional mass loss trend line compared to the peak slope in the constant heating rate data—Figure 5C. Similar to the Friedman method, kinetic parameters can also be calculated by the Ozawa and Flynn-Wall integral isoconversional method [19] [20].

Expanding the kinetic analysis from a single-step reaction to a multistep reaction, the differential equations are separated based on each step of the reaction. The overall degree of degradation is constructed as follows:

$$\alpha = 1 - \sum_j w_j a_j \quad (7)$$

where  $\alpha$  is the total fractional mass loss,  $a_j$  is fractional mass loss of a specific reaction step,  $w_j$  is the contribution of a specific reaction step into total mass loss, and  $j$  represents the given reaction step [21]. The sum of the contributions of all steps is equal to 1:

$$\sum_j w_j = 1 \quad (8)$$

Each fractional mass loss of a specific reaction step can be written as an individual differential equation modeling the degradation of the reaction step such as [22]:

$$\frac{d(a_j \rightarrow a_{j+1})}{dt} = A_j e^{-E_j/RT} f(a_j, a_{j+1}) \quad (9)$$

The rate of reaction for a degradation from A  $\rightarrow$  B (step 1) is given by  $d(a_1 \rightarrow a_2)/dt$ . The rate of reaction for the degradation from B  $\rightarrow$  C (step 2) is given by  $d(a_2 \rightarrow a_3)/dt$ . The rate of reaction for the degradation from C  $\rightarrow$  D (step 3) is given by  $d(a_3 \rightarrow a_4)/dt$ . In this format of differential equations the values  $a_1, a_2, a_3$  and  $a_4$  are the formal concentrations of the formal substances A, B, C, and D. A is the educt, B is the product of the first step and educt for the second step, C is the product of the second step and the educt for the third step, and D is the product of the third step which is the final product of the whole process. Each value of  $a_i$  changes from 0 to 1. The initial state corresponds to  $a_1=1, a_2=0, a_3=0$  and  $a_4=0$ , and final state D corresponds to  $a_1=a_2=a_3=0$ , and  $a_4=1$ . If the reaction steps are completely separated, then the intermediate state after the first step corresponds to  $a_1=0, a_2=1$  and  $a_3=a_4=0$  and the intermediate state right after the second step corresponds to  $a_1=a_2=0, a_3=1$  and  $a_4=0$ . The degradation continues to follow the analogy of chemical kinetics, where step 2 follows step 1, step 3 follows step 2, but may occur before complete conversion of A to B.

### *Results and discussion*

The TG scans for five different heating rates began at room temperature and the data can be seen in Figure 6. Like most polyimides, Kapton is extremely stable at intermediate temperatures [23]. The onset of degradation increases with increasing heating rate and involves a rapid and complete degradation. The derivative of the weight with respect to temperature provides better insight into the mechanism of degradation. For a specific heating rate, the number of peaks in the derivative thermograms (DTG) represents the minimum number of reaction steps involved. By varying the heating rates, the degradation steps can be separated and isolated. At higher heating rates, for Kapton, the reaction mechanisms can be separated for better kinetic model understanding. Figure 7 shows the DTG curves. The peaks of the DTG help to determine the reaction steps. Based on the DTG curves below, heating at 30 K $\cdot$ min $^{-1}$ , a minimum of three reaction steps, or three peaks, can be seen.

The Friedman plot for Kapton can be found in Figure 8. A multi-step reaction is again evident from the curvature of the plot. For each heating rate, there are separate reaction peaks. This indicates the probability of a multiple step reaction. Model-free analysis shows a complex process with three peaks for curves 30 Kmin $^{-1}$  and 20 Kmin $^{-1}$  and only two peaks for 2, 5, and 10 Kmin $^{-1}$ . The fluctuation in the number of peaks indicates that the mechanism of the decomposition changes with heating rate.

Furthermore, the type of reaction can be determined by comparing the fractional mass loss trend lines discussed previously with Figure 8. The fractional mass loss trend lines are the solid linear curves in Figure 8, and are found from linear regression at specific values of  $\alpha$  ranging from 0.2 to 0.8. In all cases for Kapton, the peak slope is steeper than the fractional mass loss trend line indicating an accelerated reaction, probably autocatalysis. For autocatalysis, the generic governing differential equation, presented in Eqn. 2, defines the reaction model,  $f(a_j)$ , such that:

$$f(a_j) = (1 - a_j)^n (1 + K_{cat} a_j) \quad (10)$$

where  $n$  represents the reaction order and  $K_{cat}$  represents the autocatalysis constant.

The Friedman analysis is used to calculate the activation energy ( $E_\alpha$ ) and the pre-exponential factor ( $A_\alpha$ ) from the slope and the y-intercept of the fractional mass loss trend lines, respectively [18] [19] [20]. The activation energy and pre-exponential factor are shown in Figure 9 and presents activation energies from 20 kJ/mol to 190 kJ/mol. The plot of the activation energy with respect to the amount of degradation again confirms the multistep reaction by presenting non-constant activation energy throughout the entire degradation process. The fluctuating activation energy indicates an overlap of multiple reactions. As the reaction begins, the activation energy is about 190 kJ/mol and then shifts to 40 kJ/mol for a fractional mass loss of about 0.35. The activation energy increases to 60 kJ/mol for a fractional mass loss of 0.45, and then decreases to 20 kJ/mol for mass loss 0.8, and finishes by trending upward in the final moments of decomposition. The error bars show that the activation energy for the beginning of the reaction can be well-defined. For the last steps at the fractional mass loss 0.7 the error bar of activation energy is much higher and the lower value can reach almost zero kJ/mol. The error bars are calculated using standard error from the linear regressions defined by the Friedman Analysis.

A physical meaning for the mass loss dependent activation energy from the Friedman Analysis is difficult to identify with confidence because of the independence of overlapping degradation mechanisms. Rather, the Friedman Analysis is useful in identifying multistep reactions. Given the complexity of backbone structure in polyimide, the chemical structure can rearrange in tandem with the degradation through aroyl migration or hydrolysis of the imido group. Dine-Hart et al. have proposed possible degradation pathways in their studies of polyimide film [24] [25].

An integral isoconversional method called Ozawa-Flynn-Wall Analysis was also used to calculate the activation energy as a function of fractional mass loss [19] [20]. Similar to the differential method used in the Friedman Analysis, the activation energy can be extracted using isoconversional trend lines. The benefit of comparing these two methods for activation energy provides insight into the type of reaction step to best model the degradation. Since the integral method for calculating activation energy cannot

utilize separation of variables, degradation kinetics involving competitive reactions show variations between the activation energies between the Friedman and Ozawa-Flynn-Wall Analysis. In conjunction with DTG peaks, the experimental data suggests a minimum of three steps with a combination of competitive and consecutive steps.

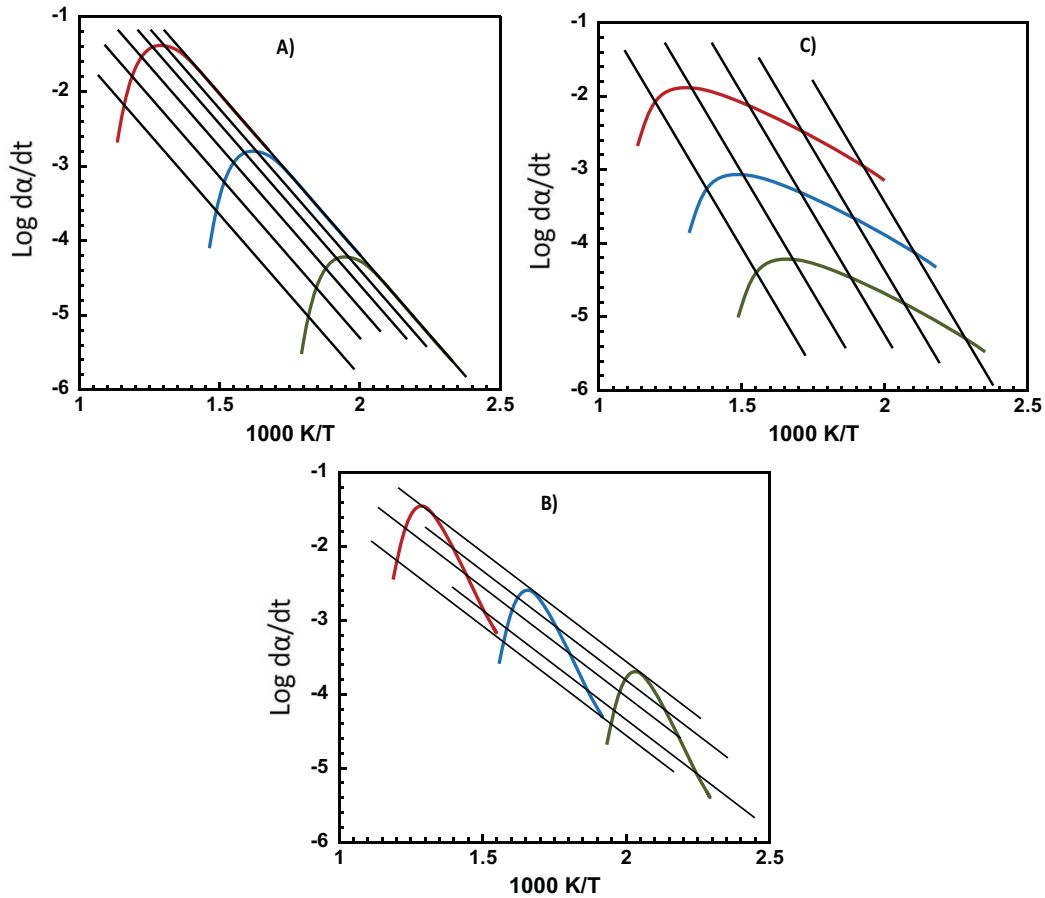


**Figure 5** Friedman plot for a single step (A) normal reaction, (B) accelerated reaction, and (C) retarded reaction.

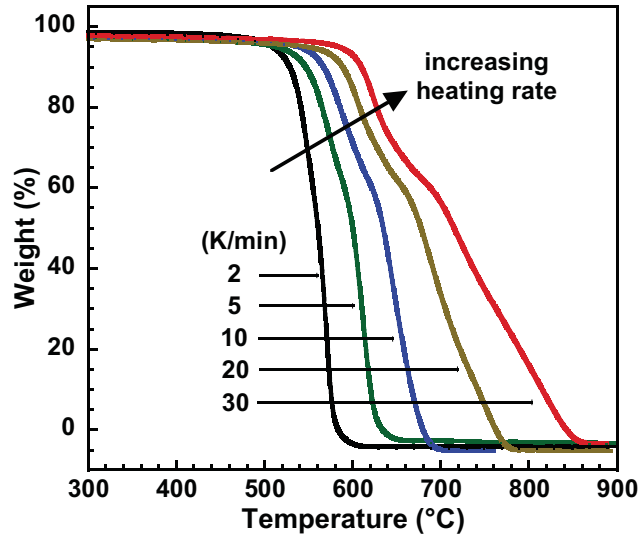


Figure 6 TG curves broaden as the rate increases from 2 to 30 Kmin<sup>-1</sup>.

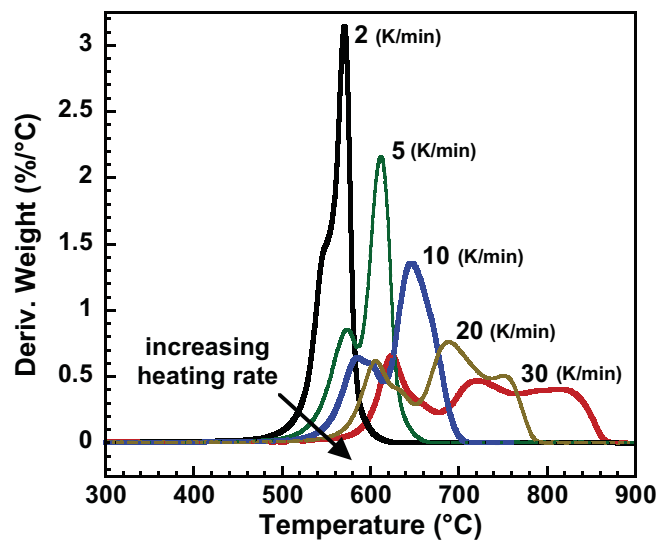


Figure 7 DTG curves for the data shown in Figure 6.

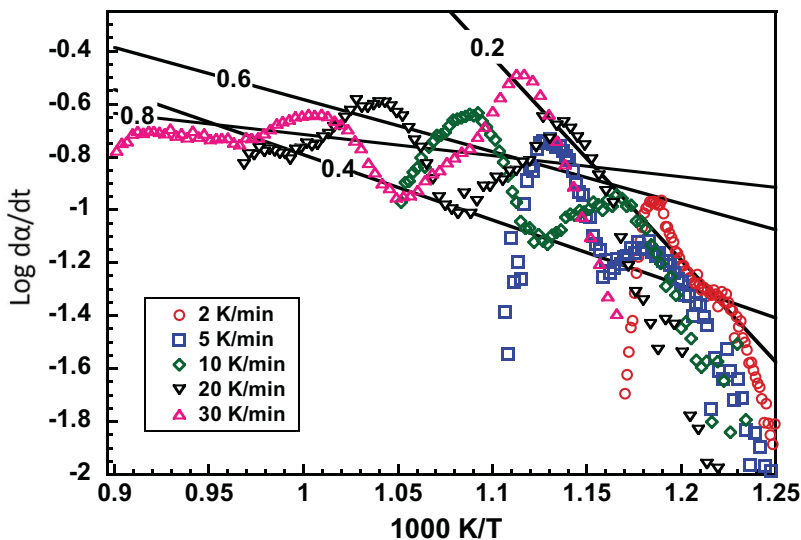


Figure 8 Friedman plot from the data shown in Figure 6.

For the simulation, a model of three parts was used. The schematic representation of the mechanisms can be seen in Figure 10. The first part is the process from reactant A to reactant B, which proceeds along two different paths 1 and 2. The second part is the one elementary reaction from reactant B to reactant C, and the third part is the process from C to D, which also follows two parallel paths. Two different paths for the third part of the model are necessary because the experimental data, Figures 5 and 6 show that the decomposition mechanism for the last 60% mass loss depends on the heating rate. A multivariate version of the Borchardt and Daniels method was used to determine the optimal fit of the kinetic parameters by multiple linear regression [26]. The results of the model fit can be seen in Figure 11, with parameters given in Table 3.

These parameters come from the combination of Eqn. 2 with the autocatalytic reaction model found in Eqn. 10 for each step of the reaction diagrammed in Figure 10. The Arrhenius parameters,  $E$  and  $A$ , are related to the temperature sensitivity of the reaction [27]. The reaction order and autocatalytic constant provide additional description of the chemical and physical reactions. The autocatalytic constant describes the extent in which the degradation reaction itself acts as a catalyst for that reaction. In thermodynamics of gases and liquids, the reaction order is an integer of stoichiometric equivalence. However, if the reaction takes place in the solid-solid, solid-liquid, and solid-gaseous phases, physical processes influence the reaction rate such as diffusion, phase-boundary reactions, or nucleation. Therefore, the direct evaluation of experimental data with unknown reaction order gives non-integer values. With respect to the first 3 steps, the effects are minimal and an approximate reaction order of  $n = 1$  can be used without effecting the model drastically. Yet, in the final two steps, there are significant variations to the reaction

order that cannot be approximated away. Therefore, the physical processes influencing the degradation of the final competitive reaction steps differ from the stoichiometric coefficients and play a significant role in the degradation.

From a statistical perspective, the model follows the data with an  $r^2$  value of 0.99991. The large activation energies of the initial steps and very small values of activation energies for the last steps are in agreement with results of Friedman analysis, if the error bars are taken into account.

The kinetic parameters obtained for the multi-step model were then used to develop an isothermal model that would represent degradation across a 4-hour isothermal exposure for an air atmosphere, also obtained by TG analysis. We modeled a temperature spread of 425 to 475°C in 25°C increments. Figure 12 shows a comparison of the isothermal experimental data and the mathematical models. Isothermal tests intrinsically have significant uncertainty because of the variability to achieve the set temperature. While the isothermal data and the model prediction differ by up to ~16%, the model captures the general trend and magnitude of weight loss shown in the experimental data. This error is within the bounds of a typical isothermal test, but could be brought down with improvements to isothermal experimental environment such as tighter temperature control and gradients. However, the isothermal model was able to accurately capture the general trend of the mass loss.

To further explore the degradation process, evolved gas analysis was conducted during the TG experiments. This coupled FTIR and MS analysis involved monitoring the exit gases as a function of time during the TG experiments at different heating ramp rates. The 3-dimensional FTIR data can be seen in Figure 13 and the 2-dimensional FTIR data constructed for analysis is shown in Figure 14. The MS data is shown in Figure 15.

There are four peak groups of interest as seen in the four sections in the FTIR figure. The first major group of peaks revolves around the 3500 to 3800  $\text{cm}^{-1}$  wavenumber range. These peaks indicate the bond stretching of functional groups with removable hydrogen (bonds such as  $\text{NH}_2$ ,  $\text{NH}$ ,  $\text{COOH}$ , and  $\text{OH}$ ) [28]. The second major group of peaks occurs in the wavenumber range 2100 to 2400  $\text{cm}^{-1}$ . These peaks carry the largest intensity and indicate bonds such as  $\text{CO}$  and  $\text{CO}_2$  [28]. This is to be expected since carbon dioxide and carbon monoxide are dominant products of degradation. The third set of peaks appears at wavenumbers around 1000 to 2000  $\text{cm}^{-1}$ . Since these fall close to the “fingerprint region” it is difficult to claim specifically what these peaks indicate. However, this peak area signifies bonds such as  $\text{N}=\text{O}$ ,  $\text{N}=\text{C}$ ,  $\text{NO}_2$ , and fragmented aromatic rings [28]. The final set of peaks are found at around 720  $\text{cm}^{-1}$  and indicates nitro and nitroso compounds ( $\text{NO}$  bonds) [28]. These conclusions correspond well to typical breakdown mechanisms proposed for Kapton. Dine-Hart showed that under oxidative degradation, Kapton initially evolves  $\text{CO}_2$  through hydrolysis of the imido group followed by the decarboxylation of the resulting acid group, evolves  $\text{CO}_2$  through an aroyl migration, and  $\text{CO}$  through extrusion of the imido

group [24] [29]. Blumenfeld also shows the evolution of CO<sub>2</sub>, CO, and H<sub>2</sub>O through the initial oxidative degradation of the aryl ether groups while leaving behind the diimide group [30]. Further degradation at elevated temperatures cleaves the diimide residual into its nitrogen compounds [30].

The mass spectroscopy data corresponds closely to the FTIR data as well. The first major peak identified is mass number 44. This peak, which spreads across the whole TG degradation curve, corresponds to carbon dioxide, which was shown in the FTIR data to be a major exit gas contributor [28]. Peaks 17 and 18 correspond to water and more generally to the removable hydrogen of the functional groups also found in the FTIR data above [28]. Peak 22 is the double ionized peak for carbon dioxide and therefore is overshadowed by the first carbon dioxide peak [28]. Peaks 30, 45, and 46 are indicative of the nitro and nitroso compounds correlating to the FTIR peak in the 720 cm<sup>-1</sup> range [28]. One peak not shown, mass number 28, is the mass number for carbon monoxide [28]. While the FTIR data indicates evolution of carbon monoxide, the mass number also corresponds to nitrogen in its diatomic form and consequently the nitrogen in the air environment overshadows the carbon dioxide emission.

Both the MS and 3-dimensional FTIR data validate the multistep reaction by presenting multiple peaks in the exit gas analysis. The 3-dimensional FTIR data, shown in Figure 13, clearly shows three peaks along the time axis, at around 2400 cm<sup>-1</sup> wavenumber. In addition, the MS data indicates overlapping peaks, shown in Figure 15, as the reaction progresses providing support for the multistep reaction chosen in Figure 10.

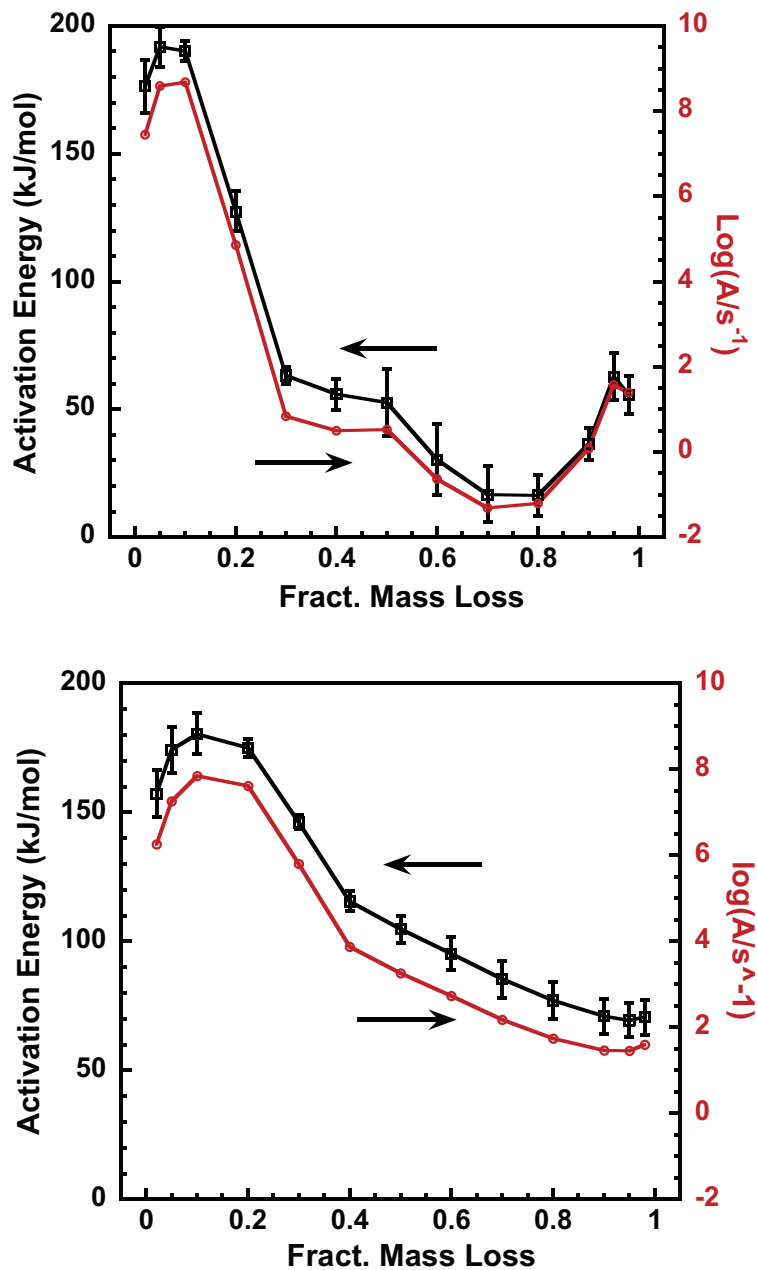


Figure 9 Activation energy plot for air atmosphere from (a) Friedman Analysis and (b) Ozawa-Flynn-Wall Analysis.

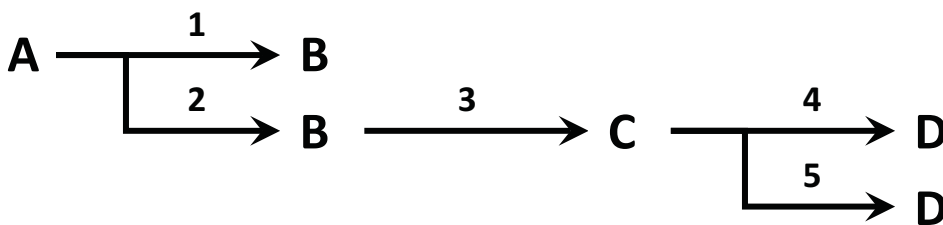
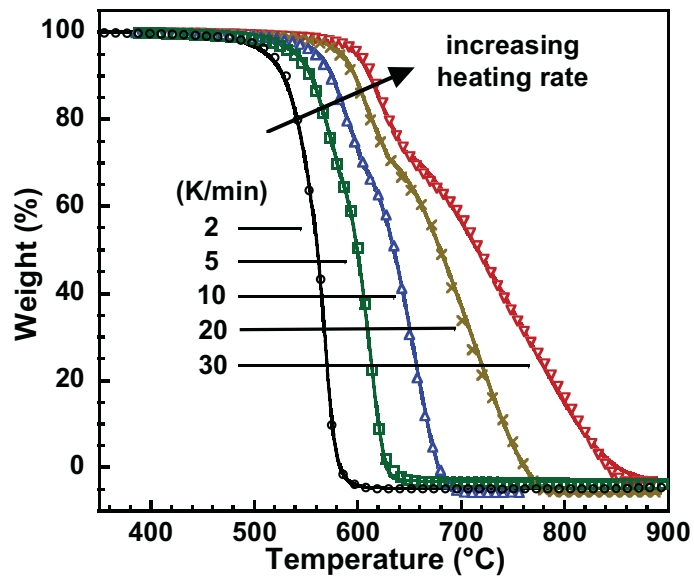
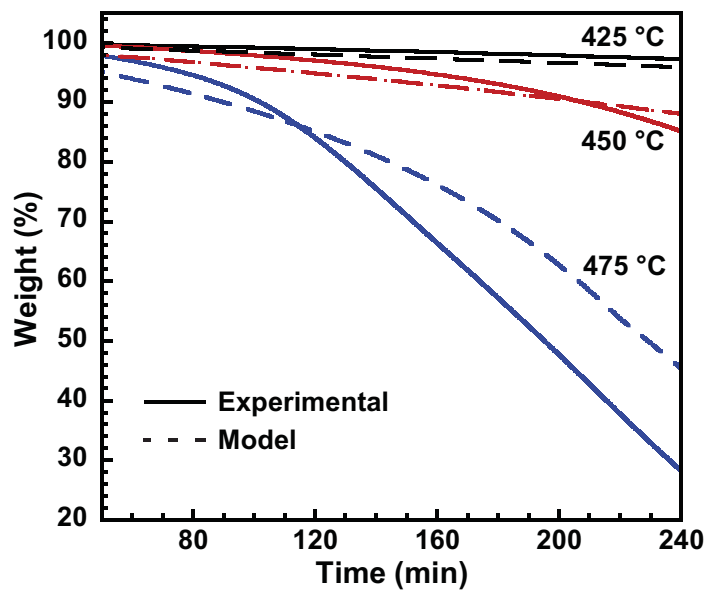


Figure 10 Schematic representation of the multistep reaction.



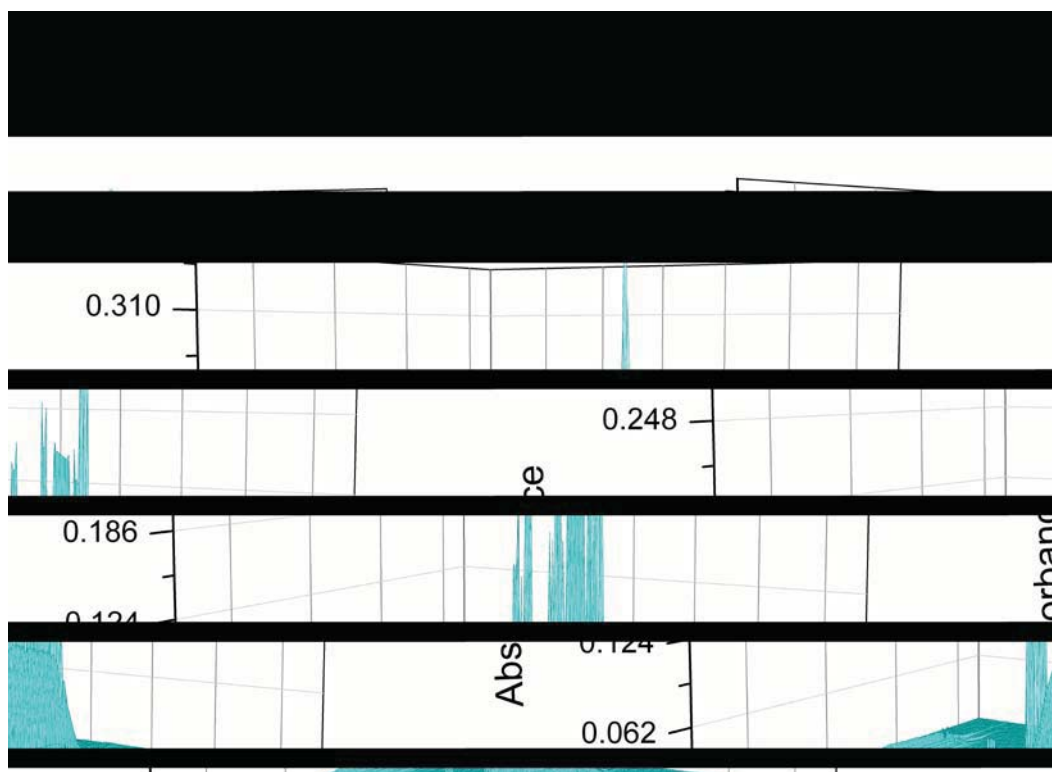
**Figure 11** Best fit model of the TG data for the four-step reaction models in Fig. 6, with parameters given in Table 3. The curves represent the model and the symbols represent the experimental data.



**Figure 12** TG isothermal curves of experimental data and model prediction.

**Table 3** Parameters used in the kinetic model.

	Activation Energy (kJ/mol)	Log ( $A_1/s^{-1}$ )	Reaction Order	Log ( $K_{cat}$ )
<b>Step 1</b>	189.62	8.40	0.77	0.94
<b>Step 2</b>	189.48	8.38	0.75	0.93
<b>Step 3</b>	168.73	7.73	0.89	0.09
<b>Step 4</b>	0.10	-3.43	3.17	1.65
<b>Step 5</b>	9.79	-3.17	0.40	1.38

**Figure 13** 3-dimensional FTIR data for exit gases of a 30 K·min<sup>-1</sup> ramp rate TG on degradation onset.

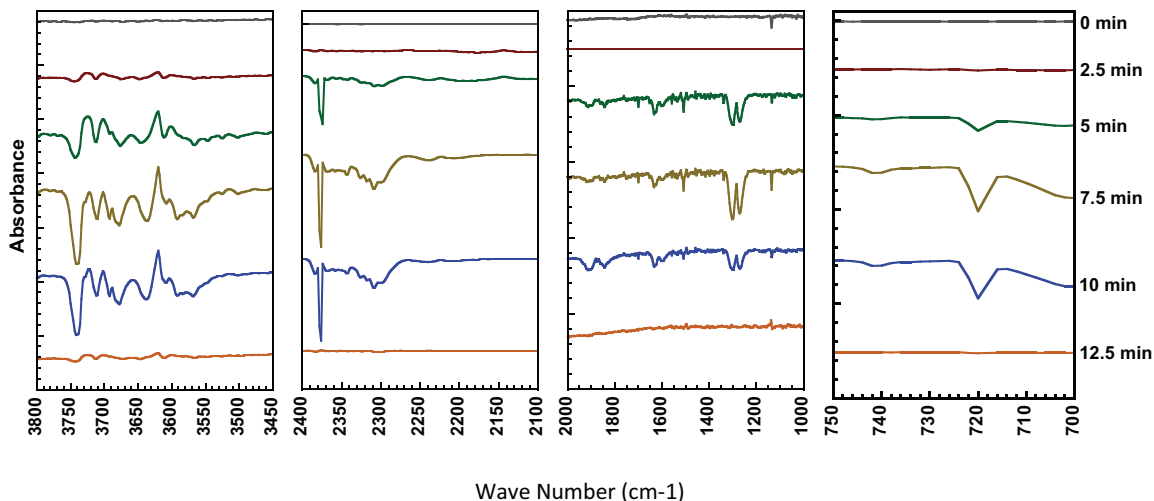


**Figure 14** FTIR data for exit gases of a 30 Kmin-1 ramp rate TG on degradation onset for four different spectral ranges. Peak intensities are only proportional within each range and should not be compared from range to range.

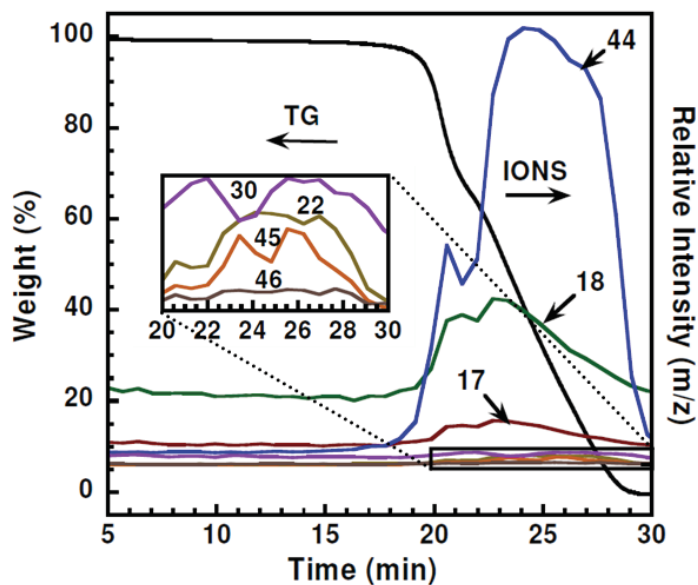


**Figure 15** MS data for exit gases of a 30 Kmin-1 ramp rate TG.

### Effect of thermal degradation on permittivity

It has been presented previously in the literature that dielectric properties of PI are not changed significantly by heating at temperatures up to 350 °C for as long as 5000 hours either in air or N<sub>2</sub> [7] [8] [9] [10]. However, given the fact that electrical wiring insulation still has to work under extreme temperatures, such as may occur in the vicinity of extreme events during service, it is also valuable to explore the effect of thermal degradation at higher temperatures in air on the dielectric permittivity of PI.

The Kapton PI film was sectioned into 3 cm by 10 cm rectangular samples, which were heated at 400, 425, 450 and 475 °C for 1, 2, 3, 4 and 5 hours in an isothermal muffle furnace. In order to eliminate possible distortion of the samples during the heating process, the two shorter edges of each PI sample were stabilized by a pair of mirror-finish stainless steel plates. Consequently, the majority of each sample was exposed to oxygen and eligible for permittivity measurement. After heating, the PI samples were removed from the furnace and cooled in air. With higher temperatures or longer heating times, the samples became more brittle, darker and thicker, which can be associated with the formation of oxidized layers on the sample surfaces during the initial degradation of PI [24] [29]. Thermal degradation at temperatures higher than 475 °C or for exposure times longer than 5 hr was not conducted because the PI became so badly deformed that its permittivity could not be measured successfully.

The thickness of all treated samples was measured by using a micrometer with uncertainty of 1  $\mu\text{m}$  after cooling. Directly following thickness measurement, the samples were coated with silver paint, serving both as film electrodes for permittivity measurement and to prevent significant moisture exchange between the samples and air. The silver paint dries quickly at room temperature, but requires curing for 16 hr at room temperature to achieve a volume resistivity as low as  $5 \times 10^{-6}$  to  $1.25 \times 10^{-5}$   $\Omega \cdot \text{m}$ . When the silver paint was totally cured, each sample was cut into three smaller samples for permittivity measurement. The permittivity of all treated samples was measured from 1 kHz to 2 MHz at room temperature, using the Agilent E4980A LCR meter coupled with a 16451 test fixture. The three identically degraded samples under all degrading conditions revealed highly similar values of  $\epsilon'$  and  $\tan \delta$ , the standard deviation measured for both is less than 1%.

Figure 16 shows the loss factor of PI degraded at 475 °C for 3 hr as a function of temperature and frequency. Compared with Figure 4b, the height of the  $\beta$ -relaxation peak is substantially increased, indicating tremendous increase in the intensity of the  $\beta$ -relaxation [31]. The  $\beta$ -relaxation cannot be observed at frequencies higher than 500 Hz after thermal degradation. To explore the effect of thermal degradation on the  $\gamma$ -relaxation, the frequency dependence of  $\tan \delta$  at room temperature for the degraded PI is plotted and compared with that of the dry PI in Figure 17. Even though the intensity of the  $\gamma$ -relaxation is not obviously changed, the peak for  $\gamma$ -relaxation moves to higher frequencies after the thermal degradation.

As shown in Figure 18, the real permittivity of PI measured at 1 kHz increases with time and temperature of thermal degradation in air. The real permittivity of the PI sample heated at 475 °C for 3 hours is 4.15, versus 3.77 for the sample heated at 450 °C for 5 hours and 3.24 for the control sample. PI samples degraded at 475 °C for 4 and 5 hours were highly brittle and wrinkled, which meant that it was not possible to measure their permittivity successfully. On the other hand,  $\tan \delta$  of PI reveals little change after thermal degradation at 400, 425 or 450 °C and is not shown here. After thermal degradation at

475 °C for 3 hr, however,  $\tan \delta$  of PI as function of frequency is changed significantly, as shown in Figure 17.

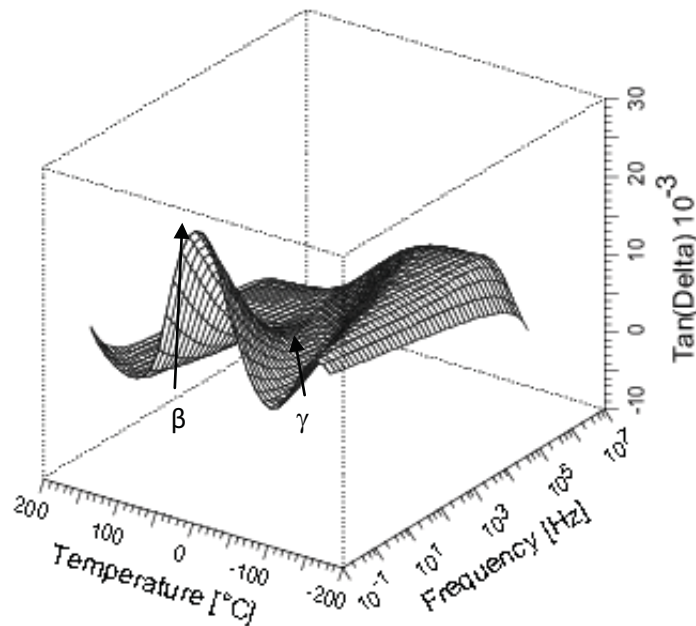


**Figure 16** The loss factor of PI degraded at 475 °C for 3 hr, measured over frequency from 1 Hz to 1 MHz and temperature from -140 to 180 °C.

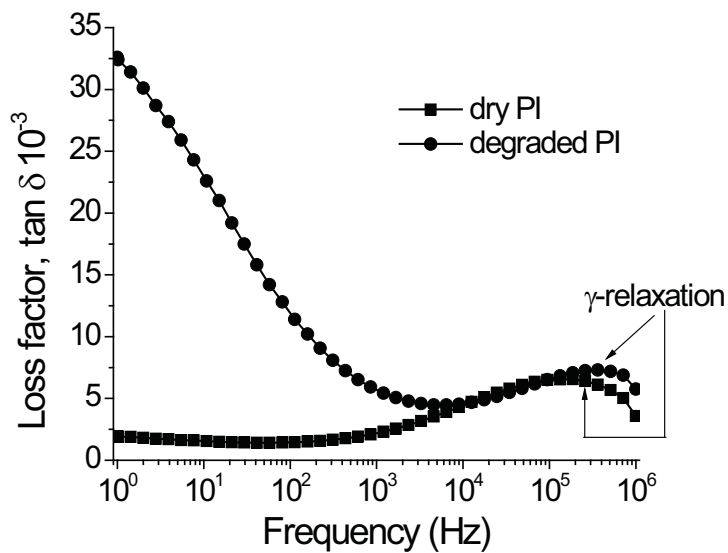


**Figure 17** The loss factor of dry PI and PI degraded at 475 °C for 3 hr as a function of frequency at room temperature.

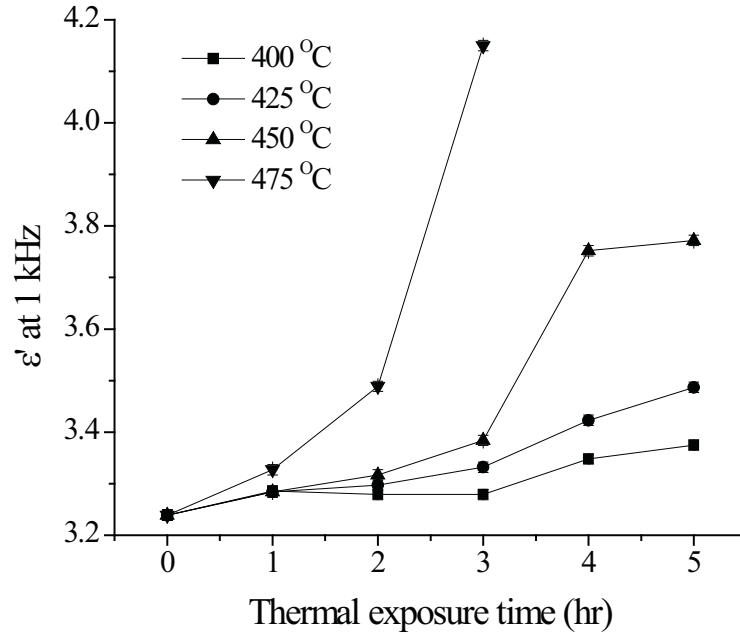


**Figure 18** Effect of thermal degradation time and temperature on  $\epsilon'$  of PI at 1 kHz. Error bars indicate the standard deviation in measurements on three nominally-identical samples.

The activation energy for the  $\beta$ - and  $\gamma$ -relaxations can be calculated from the Arrhenius equation:

$$E = k \ln \left( \frac{f_2}{f_1} \right) \left( \frac{1}{T_1} - \frac{1}{T_2} \right)^{-1} \quad (11)$$

where  $E$  is the activation energy of molecular relaxation;  $k$  is the Boltzmann constant;  $T_1$  and  $T_2$  are the absolute temperatures of transition at frequencies  $f_1$  and  $f_2$ , respectively. The equation can be rewritten as a linear function relating  $1/T$  and  $\ln \omega$ :

$$\ln f = -\frac{E}{k} \frac{1}{T} + C \quad (12)$$

where  $C$  is a constant. By plotting the dependence of  $\ln f$  on  $1/T$ , the activation energy can be obtained from slope of the line. Based on the measured complex dielectric spectra as shown in Figures 4b and 16, the Arrhenius plots of both  $\beta$ - and  $\gamma$ -relaxations of the dry and degraded PI (at 475 °C for 3 hr) are given in Figure 19. For the dry PI, the activation energy is determined to be  $0.48 \pm 0.02$  eV for the  $\gamma$ -relaxation and  $0.85 \pm 0.05$  eV for the  $\beta$ -relaxation. The uncertainties arise from estimated uncertainty in the slopes obtained via linear regression. Those values of activation energy determined here agree, to within experimental uncertainty, with values presented in the literature: 0.47 eV for the  $\gamma$ -relaxation [32], and 0.87 eV for the  $\beta$ -relaxation [33] [11]. However,  $\beta$ -relaxation of the degraded PI is only observed below

500 Hz and reveals no variation as function of temperature. Therefore, the Arrhenius plot for  $\beta$ -relaxation is a vertical line as shown in Figure 19, and its activation energy could not be determined. On the other hand, the activation energy of the  $\gamma$ -relaxation is determined to be  $0.46 \pm 0.02$  eV for degraded PI, which is not influenced by thermal degradation at 475 °C for 3 hr, despite the shift of the  $\gamma$ -relaxation to higher frequency.

Dine-Hart et al have studied the process of oxidative thermal degradation of PI for a short period in air by thermal analysis methods, saponification testing and infrared spectroscopy [24] [29]. It was observed that the chemical structure of PI film was significantly changed by thermal degradation [24]. Figure 20 demonstrates pyrolysis process of imide groups during oxidative thermal degradation of PI, which gives rise to  $\text{CO}_2$  and  $\text{CO}$ , breaks chemical bonding in imide groups and forms free radicals [29]. Thus, we hypothesize that the significant increases in  $\epsilon'$  of PI following oxidative thermal degradation at 400 to 475 °C could arise from the formation of free radicals, which enhance electrical polarization in PI. Moreover, due to scission in chemical bonding in imide groups, the torsional oscillations of the phenylene ring become much easier, increasing the intensity of the  $\beta$ -relaxation. As discussed in section 3.1, release of gas was detected while a Kapton PI sample was heated from 30 °C to 900 °C with heating rate 30 °C/min. Extracting data from Figure 13, Figure 21 shows the FTIR spectra of the PI sample at 30, 400, 450 and 480 °C. Compared with the spectrum at 30 °C, the FTIR spectra at 400, 450 and 480 °C reveal new absorbance peaks at 2170, 2320 and 2370  $\text{cm}^{-1}$ , corresponding to chemical bonds of  $\text{CO}$  and  $\text{CO}_2$  [24]. The mass also confirmed the release of  $\text{CO}_2$  and  $\text{CO}$  at temperatures above 400 °C; and consequently endorse the degradation path of PI shown in Figure 20. Thus, we can conclude that the significant increase in the real permittivity and intensity of the  $\beta$ -relaxation are results of pyrolysis of imide groups of PI during oxidative thermal degradation.

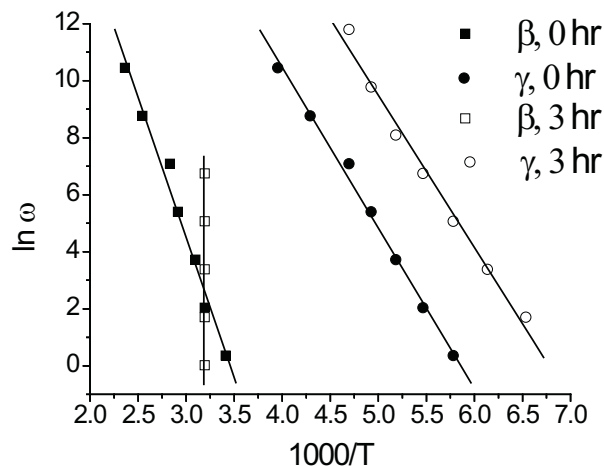


**Figure 19** Arrhenius plot for  $\beta$ - and  $\gamma$ -relaxations of dry PI and PI degraded at 475 °C for 3 hr.

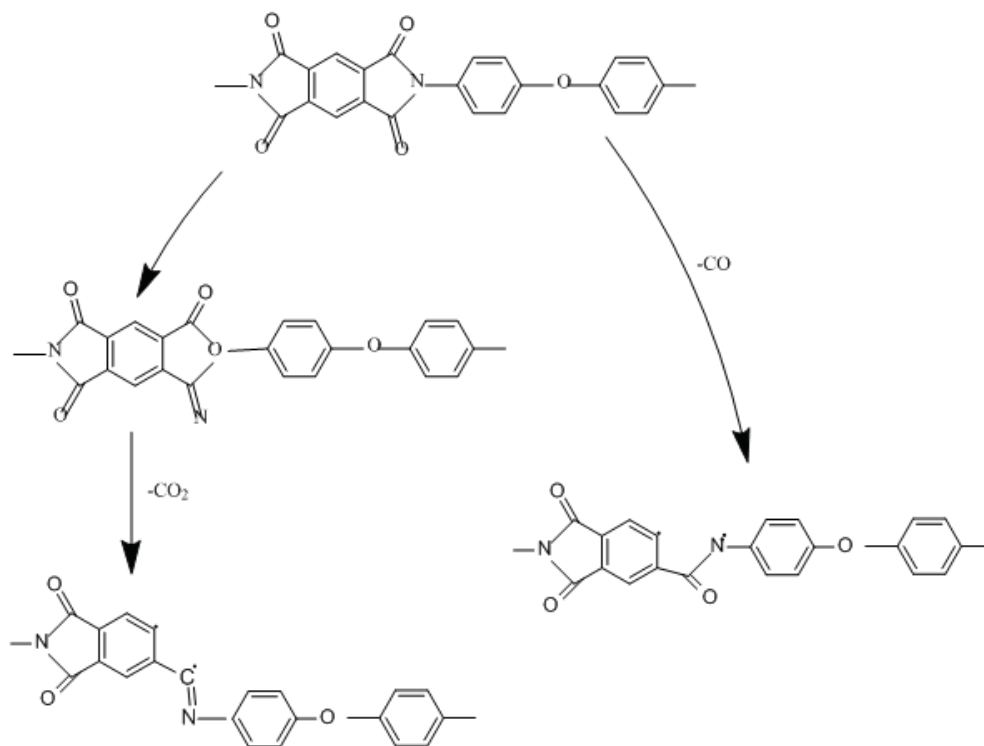


**Figure 20** Pyrolysis process of imide groups of PI during heating [29].

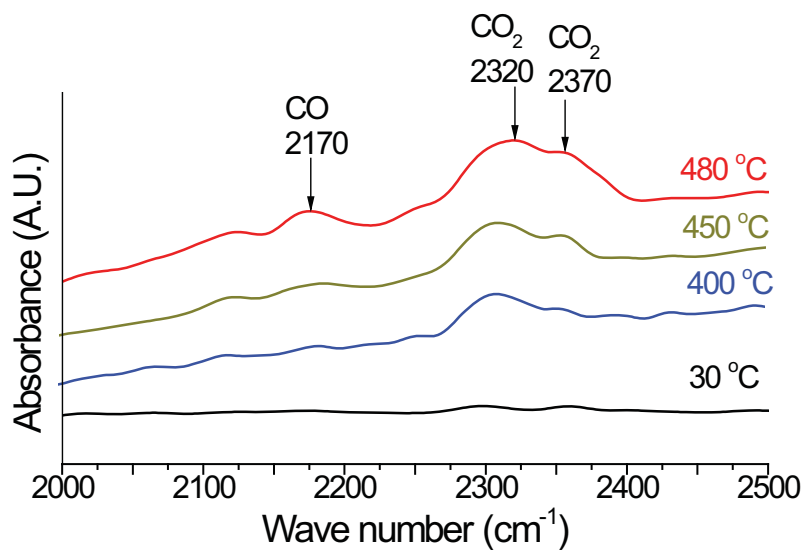


**Figure 21** FTIR spectra of Kapton polyimide at 30, 400, 450 and 480 °C.

### Effect of thermal degradation on electrical breakdown behavior

The effect of heating at temperatures up to 400 °C on electrical breakdown behavior of PI has been studied previously. In reference [34], decreases in both AC and DC dielectric strength of Kapton PI as the testing temperature increased from 20 to 250 °C were presented. Diahm et al [35], who tested at temperatures up to 400 °C, also observed a decrease in DC dielectric strength of PI film with increasing temperature. In contrast, it has been stated in references [7] and [9] that the dielectric strength of PI was enhanced after heat treatment below 350 °C for up to 300 hours.

However, considering that PI as electrical insulation often has to function at even higher temperatures, such as in spacecraft [36] or in the vicinity of extreme events during service [37], it is also valuable to study changes in its breakdown behavior due to thermal exposure at higher temperatures. In this paper, the influence of short-period thermal exposure at 450 to 480 °C in air on AC dielectric strength of PI is presented. Since none of the papers mentioned above have explored the reason why dielectric strength was changed by the heating processes, the relationship between thermal exposure mechanisms and electrical breakdown of PI is explored here.

#### *Weibull distribution*

Given the random distribution of electrical weak points in insulation material, a different dielectric strength can be measured on nominally identical samples [38]. As a result of this behavior, statistical distribution analysis has been adopted to analyze the breakdown behavior of PI. Several statistical distribution methods are available for the description of electrical breakdown behavior, including Weibull, Gumbel, log-normal and recently proposed empirical failure probability methods [39], among which the Weibull method is the most commonly used for solid insulation materials [38]. The cumulative distribution function (CDF) [40] for two-parameter Weibull distribution is shown in the following equation [38]:

$$F(E; \alpha, \beta) = 1 - \exp \left[ - \left( \frac{E}{\alpha} \right)^\beta \right] \quad (13)$$

where  $F$  is the probability of failure at an electrical field up to  $E$ ,  $E$  is the measured breakdown strength of insulation,  $\alpha$  is the scale parameter, and  $\beta$  is the shape parameter, which is a measure of the dispersion of  $E$  and decreases with increasing scatter. Both  $\alpha$  and  $\beta$  are always positive and obtained through least-squares regression in this work. In the least-squares regression method [38],  $Y_i$  and  $X_i$  values are assigned by the following equations:

$$Y_i = \ln(E_i) \quad (14)$$

$$X_i = \ln \left\{ -\ln [1 - F(i, N)] \right\} \quad (15)$$

Then,  $Y_i$  is a linear function of  $X_i$ ,

$$Y_i = mX_i + c \quad (16)$$

in which the slope,  $m$ , and intercept,  $c$  are given by the following equations:

$$m = \frac{\sum_i^N (X_i - \bar{X})(Y_i - \bar{Y})}{\sum_i^N (X_i - \bar{X})^2}, \quad c = \bar{Y} - m\bar{X}. \quad (17)$$

Parameters  $\beta$  and  $\alpha$  are estimated from  $m$  and  $c$ , respectively:

$$\beta = \frac{1}{m}, \text{ and } \alpha = \exp(c). \quad (18)$$

The CDF function as described in equation (34) is supposed to create a reasonably straight line in a typical Weibull plot, where logarithmic dielectric strength,  $E$ , is plotted on the horizontal axis; and the failure probability,  $F$ , is plotted on the vertical axis. (For example, see Figure 22 later.)

Two-parameter Weibull distribution is a special case of three-parameter Weibull distribution, as shown in the following equation, where the local parameter  $\gamma$  is zero.

$$F(E; \alpha, \beta) = 1 - \exp \left[ - \left( \frac{E}{\alpha} \right)^\beta \right] \quad (19)$$

Weibull firstly employed mean ranks to estimate the probability of failure in 1951 [41], but later he recognized Benard's approximation for median rank, which assigns the CDF of failure  $F(i, N)$ ,

$$F(i, N) = \frac{i - 0.3}{N + 0.4} \quad (20)$$

where  $N$  is the total number of measured dielectric strength values and  $i$  is the assigned rank when the dielectric strengths are listed in order from smallest to largest. Benard's approximation is considered to be of good accuracy for plotting the Weibull distribution and estimating  $\alpha$  and  $\beta$ ; its uncertainty is only 0.1% for  $N = 50$  and 1% for  $N = 5$  [38]. The goodness of fit can be represented by a simple correlation

coefficient,  $P$ , which is a number between -1 and 1. As dielectric strength always gives a linear fit with positive slope, the  $P$  in this study locates between 0 and 1. The closer the  $P$  to 1, the better the fit is.

$$P = \frac{\sum_{i=1}^N (X_i - \bar{X})(Y_i - \bar{Y})}{\sqrt{[\sum_{i=1}^N (X_i - \bar{X})^2][\sum_{i=1}^N (Y_i - \bar{Y})^2]}} \quad (21)$$

In this paper, the two-parameter Weibull distribution is applied to statistically analyze the influence of thermal exposure and immersion in water on the electrical breakdown behavior of PI. As stated in reference [38], 20 measured values of breakdown strength for each sample under test is considered sufficient to provide meaningful results. Here, breakdown tests were conducted at 20 different points on each sample.

### *Experiment*

The samples were cut into 6 cm by 10 cm sheets, large enough to measure dielectric strength 20 times at different points. The mass of each sample was measured using a balance with uncertainty 0.01 mg. The thickness of the samples was measured using a micrometer with uncertainty 1  $\mu\text{m}$ . The PI samples for thermal exposure were heated at 475 °C for 1, 2, 3 and 4 hours in an isothermal muffle furnace to investigate the effect of thermal exposure time; and at 450, 460, 465 and 480 °C for 4 hours to study the effect of temperature. Thermal exposure for longer times or at higher temperatures was not conducted as the PI was so brittle and wrinkled that its dielectric strength could not be measured successfully. Directly after thermal exposure, the samples were removed from the furnace and cooled to room temperature. It was observed that the PI samples became more brittle, darker and thicker with increasing thermal exposure times or temperatures. Directly after cooling, the mass of the samples was measured again and compared with the value obtained before thermal exposure.

Breakdown voltage was measured using a Dielectric Rigidity 6135.054 instrument designed according to standards ASTM D-149 [42] and D-876. The Dielectric Rigidity instrument consists of an oil-insulated transformer, capable of supplying AC voltage up to 60 kV, and a shut-proof resistant test chamber, which houses a bath for insulating liquid and a mobile support for electrodes with diameter of 6.34 mm. In this work, Envirotemp® FR3® fluid, a vegetable oil with antioxidant additive, cold flow additive and colorant, was applied as an insulating and cooling medium. During the measurement process, the voltage across the PI samples was increased from zero at a rate of 0.5 kV/s and stopped at a value where the sample failed, which was recorded as its breakdown voltage,  $E_{BD}$ . Twenty measurements of dielectric strength were made on each sample.

### *Results and discussion*

The two-parameter Weibull cumulative distribution function of dry PI and the samples heated at 475 °C for 1 to 4 hours is plotted in Figure 22. The symbols represent experimentally measured dielectric strengths and the solid lines represent a linear fit to the 20 data points, for each exposure condition. Since the symbols in Figure 22 reveal “S” shape curves around their linear fit, it is hypothesized that three-parameter Weibull distribution could give a better fit [40]. The correlated coefficients of two-parameter and three-parameter Weibull distributions for the experimentally measured dielectric strengths have been calculated and are compared in Table 4. It is observed that for each thermal exposure condition, the highest correlation coefficients of the three-parameter Weibull distribution are very similar or even lower than those of two-parameter Weibull distribution. For 0 hr and 3 hr, the local parameters are negative, which is physically unreasonable as dielectric strength is always a positive number. As stated in reference [16], the correlated coefficient of the three-parameter Weibull distribution should be much higher than that of the two-parameter Weibull distribution to be an equally good fit. Therefore, it is concluded that three-parameter Weibull distribution cannot give a better fit than two-parameter Weibull distribution, and statistical analysis of electrical breakdown behavior of all PI samples investigated in this study will be conducted by using two-parameter Weibull distribution.

The CDF of two-parameter Weibull distribution of the samples heated at 450 to 480 °C for 4 hours is compared with that of dried PI in Figure 23. The dielectric strength values measured for dry PI (0 hr) are in the range from 130 to 160 kV/mm, agreeing well with values for PI films with equivalent thickness presented in references [35] [43] [44]: 100 to 200 kV/mm.

With longer heating time or higher temperature, the linear fits to the measured data shift towards lower dielectric strength and reveal decreasing slope, indicating greater dispersity in the measured dielectric strength values. The scale parameter ( $\alpha$ ) and the shape parameter ( $\beta$ ), obtained through least-squares regression, are applied here to quantitatively analyze the effect of thermal exposure on breakdown behavior of PI. The dependence of  $\alpha$  and  $\beta$  on heating time and temperature is plotted in Figures 24 and 25, respectively. Both  $\alpha$  and  $\beta$  decrease with increasing heating time or temperature. Statistically, the short-period thermal exposure at 450 to 480 °C significantly decreases the dielectric strength of the PI samples and gives rise to much more randomly dispersed weak points in PI film.

It has been stated previously [45] [46] that low-level degradation in polymers due to thermal exposure, such as chemical aging and physical aging, increases probability of electrical breakdown of the material. The chemical aging of PI during thermal exposure, which gives rise to pyrolysis process of imide groups and release of CO<sub>2</sub> and CO gases, has been discussed in section 2. On the other hand, as listed in Tables 5 and 6, weight loss in PI increases with heating time or temperature. It is 2.90% for the sample heated at 450 °C for 4 hr, and 21.78% for the one heated at 480 °C for 4 hr. The large weight loss following

thermal exposure of PI further supports the occurrence of chemical aging of PI during thermal exposure. To explore the possibility of physical aging during thermal exposure, enthalpic relaxation measurement on a PI sample heated at 480 °C for 4 hr was conducted by using DSC. However, no endothermic peak was observed on the DSC curve, revealing no sign of physical degradation in the degraded PI. Therefore, the increased susceptibility of PI film to electrical breakdown following the heat treatment is considered to be a result of consequential chemical aging of PI, which gives rise to free radicals, as shown in Figure 20.

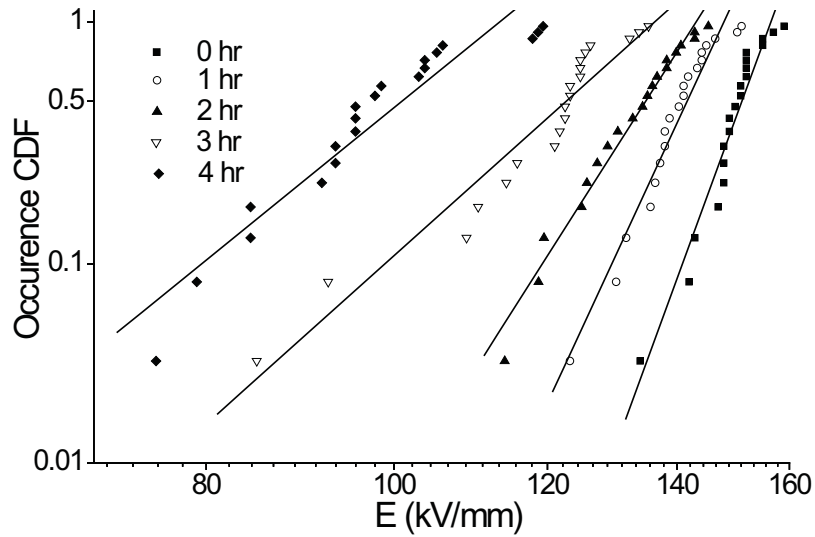


**Figure 22** The cumulative distribution function of the measured dielectric strength of PI samples heated at 475 °C for up to 4 hours. Symbols represent experimental data and lines are obtained by least-squares fitting to the data.

**Table 4** Correlated coefficient of 2-parameter and 3-parameter Weibull distribution of dielectric strength of PI heated at 475 °C

Time of heating at 475 °C	Correlation coefficient, $P$	
	Two-parameter Weibull	Three-parameter Weibull
0 hr	0.9876	0.9876, $\gamma$ is negative
1 hr	0.9903	0.9902
2 hr	0.9938	0.9933
3 hr	0.9451	0.9602, but $\gamma$ is negative
4 hr	0.9770	0.9862

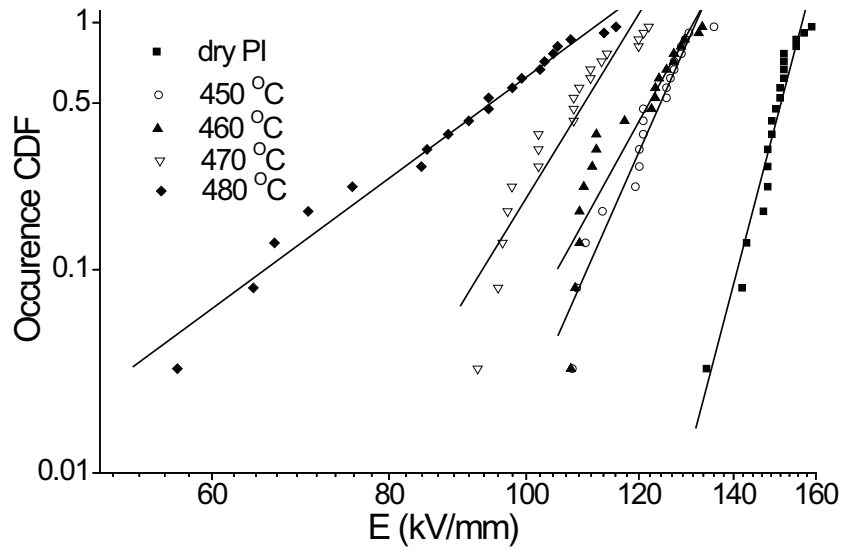


**Figure 23** As for Figure 41 but for PI samples heated for 4 hours at various temperatures from 450 to 480 °C.

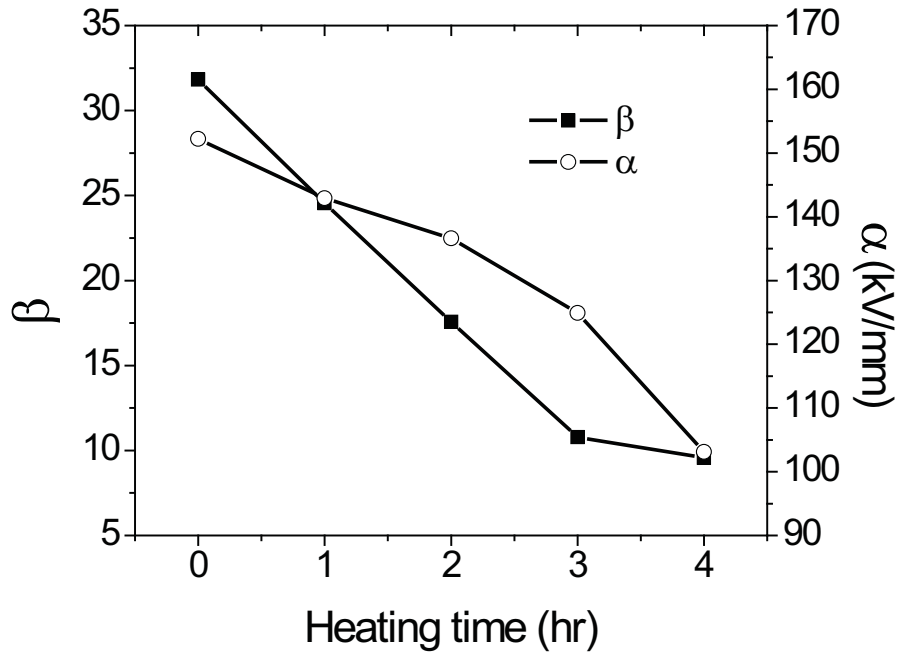


**Figure 24** The Weibull-statistical scale parameter ( $\alpha$ ) and the shape parameter ( $\beta$ ) as functions of heating time.

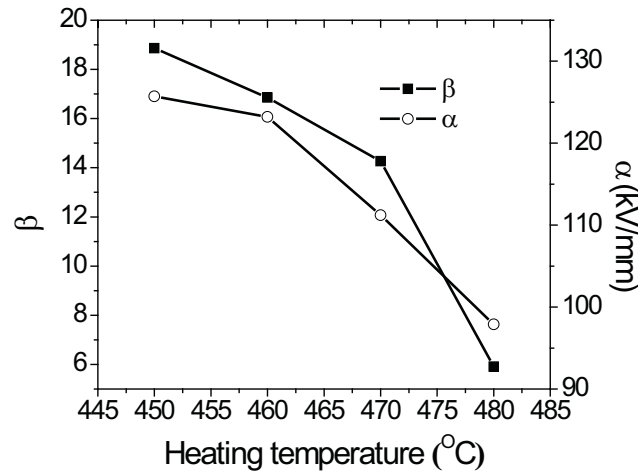


**Figure 25** The Weibull-statistical scale parameter ( $\alpha$ ) and the shape parameter ( $\beta$ ) as functions of heating temperature for 4 hr heating time.

**Table 5** Weight loss of PI samples heated at 475 °C for up to 4 hours.

Heating time (hr)	Weight loss (%)
1	1.39
2	3.04
3	7.08
4	14.51

**Table 6** Weight loss of PI samples heated for 4 hours at various temperatures from 450 to 480 °C.

Heating temperature (°C)	Weight loss (%)
450	2.90
460	4.18
470	8.21
480	21.78

## Lifetime prediction under electrothermal multi-stress

### *Theory and method*

The concept of using thermogravimetric analysis in conjunction with electrical stress testing to predict lifetime of insulation material was first proposed in 1971 by Toop [47]. The lifetime model relates electrical life theory to kinetic decomposition theory through TG analysis. Toop's model is not applicable for all wire insulation materials, in particular these with extremely complex decomposition mechanisms. However, Toop has shown that the lifetime of a material such as Formvar, wire enamel with a simple thermogram, can be described as accurately from his proposed electrothermal model as it can by

following the failure criteria and test procedures given in ASTM D2307. This ASTM standard is developed for testing relative thermal endurance of film-insulated round magnet wire.

Toop's work is built on the chemical rate theory devised by Dakin, which provides a relationship between the material's degree of degradation and physical properties [48]. More recently, Montanari and Simoni have further explored the aging, degradation, and modeling with regards to electrical insulating materials including models such as tree-growth [49], multi and space charge [49] which again build on the chemical rate theory of Dakin [50] [51].

In the calculation of electrothermal lifetime, the degree of degradation is linked to electrical breakdown voltage. By an empirical correlation, mathematical modeling of the kinetics of degradation can be combined with knowledge of the electrical breakdown voltage to obtain a single lifetime prediction.

Now replacing  $\alpha$  in equation (2) by electrical breakdown voltage  $V$  means that  $f(V)$  is the reaction model dependent on the breakdown voltage mechanism of the material. The function  $f(V)$  embodies the chemical and physical effects of applied voltage  $V$  on the test piece. The rate of change in voltage breakdown is constrained by the general differential equation for a changing material property,

$$\frac{dV}{dt} = K(T)f(V) \quad (22)$$

such that  $dV/dt$  is the change in electrical voltage breakdown and  $f(V)$  is the reaction model dependent on the voltage breakdown mechanism of the material.

Rearranging and integrating the governing equation with  $r$  replaced by  $V$  gives:

$$\int_{V_0}^{V_f} \frac{dV}{f(V)} = K(T) \int_0^{t_f} dt \quad (23)$$

where limits  $V_0$  and  $V_f$  are the breakdown voltages corresponding to the pristine and the failed samples respectively, and  $t_f$  is the time for the breakdown voltage to reach the failure criterion. Taking equation (23) and applying these limits, another function of the breakdown voltage can be realized:

$$\left[ \int \frac{dV}{f(V)} \right]_{V_0}^{V_f} = [g(V)]_{V_0}^{V_f} = K(T)t_f \quad (24)$$

and substituting the Arrhenius function for  $K(T)$  gives:

$$g(V_f) - g(V_0) = At_f e^{-E/RT} \quad (25)$$

from which:

$$t_f = \frac{e^{E/RT}}{A} [g(V_f) - g(V_0)]. \quad (26)$$

Similar to the development given in equations (22) through (26) for electrical breakdown voltage, the generalized differential equation, equation (2), is also a starting point from which to develop  $g(\alpha)$ , a

function of degradation analogous to  $g(V)$ . By taking the rearrangement in (4), and defining the parameter  $x = E/RT$ , the separation of variables procedure isolates the temperature and mass loss in the function to give:

$$\frac{\beta}{A}g(\alpha) = -\frac{E}{R}\int e^{-x}x^{-2}dx + C. \quad (27)$$

The initial and final conditions are  $T_0$ ,  $x_0$ , and  $\alpha_0$  and  $T'$ ,  $x'$ , and  $\alpha'$  respectively. Ultimately, at failure,  $T' = T_f$ . Therefore, equation (27) can be written as:

$$\frac{\beta}{A}[g(\alpha') - g(\alpha_0)] = \frac{E}{R}[p(x') - p(x_0)] \quad (28)$$

where:

$$p(x) = \frac{e^{-x'}}{x'} - \int_{x'}^{\infty} \frac{e^{-x}}{x} dx. \quad (29)$$

As seen in [47], when taking the logarithm of (26) the y-intercept is equivalent to the y-intercept of the logarithm of (28). Consequently, these equations can be assimilated as follows:

$$\log(t_f) = \frac{E}{2.303RT} + \log \frac{Ep(x)}{\beta R}. \quad (30)$$

With the correlation found through  $p(x)$ , the temperature,  $T$ , in equation (30) is defined as the failure temperature of the thermogram,  $T_f$  [47]. Since  $p(x)$  correlates back to the mass loss in equation (4), the failure temperature is defined as the temperature at which a corresponding mass loss intersects the slowest heating thermogram. See Figure 6 for  $T_f$ .

A thermogravimetric analyzer, model Q50 from TA Instruments (New Castle, DE), was used for the TG experiments. The TG experiments were conducted in an oxidative environment with a nitrogen balance purge gas flow rate of 40 mL/min and an air sample purge gas flow rate of 60 mL/min. The tests were performed over a temperature range of 35 to 900°C at five different heating ramp rates: 2, 5, 10, 20, and 30 Kmin<sup>-1</sup>. Kinetic analysis was performed with the Netzsch Thermokinetics 2 program (version 2004.05).

Samples for electrical breakdown testing were isothermally heated at 425, 450, 460, 465, 470, 475, and 480 °C for up to 5 hr in an isothermal muffle furnace. These temperatures were chosen to provide uniform sample degradation because Kapton is thermally stable below 400 °C. Prior to degradation, the samples were all dried in a standard convection oven for 1 hour at 150 °C. A simple isothermal TG analysis of Kapton HN at 150 °C for 1 hour shows 2-3% mass loss and then stabilizes with no additional mass loss; indicating the removal of water from the sample. The samples were then placed in a sealed, pre-weighed,

plastic bag. The dried Kapton was weighed to obtain initial weight and then placed in the muffle furnace for degradation. On completion of isothermal heating the samples were again placed in the pre-weighed bag and weighed again to obtain their mass loss. After that, the breakdown voltage of the samples was measured.

A 60 kV dielectric rigidity device (Ceast part number 6135.053 /6135.054) was used for breakdown voltage testing. The experiments were conducted at room temperature in a flame-resistant bio-oil liquid (Envirotemp® FR3TM Fluid) insulation bath. The tests were conducted in accordance with ASTM Standard D149–09 “Standard Test Method for Dielectric Breakdown Voltage and Dielectric Strength of Solid Electrical Insulating Materials at Commercial Power Frequencies.” Breakdown voltage was measured at twenty separate locations, evenly distributed across each 60 x 90 mm<sup>2</sup> specimen, and the values were averaged for each specimen.

#### *Experiment, results and discussion*

The kinetic pathway for the thermal degradation of Kapton was shown in our earlier work to fit a five step model with both competitive and consecutive reaction steps [21]. The activation energy shown in this work is the overall activation energy for the complete degradation of Kapton. When the activation energies for the individual steps are separated, five different constant activation energies are obtained. The initial reaction steps, a competitive model, contain activation energy of 189 kJ/mol [21]. Since the degradation for the electrical breakdown analysis is from the initial degradation steps, this activation energy is used for calculating the lifetime prediction for Kapton.

Measured breakdown voltage of degraded Kapton is plotted in Figure 26. A linear fit of the breakdown voltage as a function of degradation is used to represent the trend of the data. This trend line is useful in calculating the lifetime to electrical failure. Each data point in the figure represents the average of twenty test measurements on a degraded sample sheet. The error bars represent the standard error with a 95% confidence interval between the twenty test values.

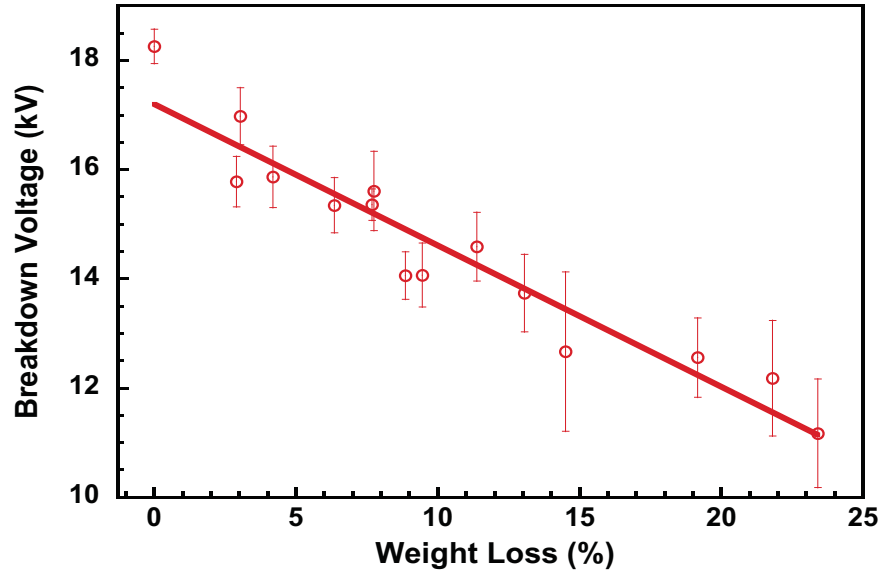


**Figure 26** Measured voltage breakdown of degraded Kapton Film (symbols) with best linear fit (solid line).

In the electrothermal lifetime prediction model of (30), time to failure,  $t_f$ , is calculated from test temperature and voltage, TG analysis parameters  $E$  and  $T_f$ , and the breakdown voltage value. First, a breakdown voltage value is selected (e.g. 12kV) and the relevant fractional mass loss is read from Figure 5 (20%).

This fractional mass loss defines failure temperature,  $T_f$ , from Figure 6—the temperature of the slowest thermogram corresponding to the relevant fractional mass loss (541 °C or 814 K). The failure temperature along with the activation energy of 189 kJ/mol are then utilized in (29) to calculate the correlation fitting parameter  $p(x)$ .

Using equation (30), the lifelines shown in Figure 27 are calculated based on two particular sets of environmental conditions; voltages of 12 and 14.7 kV (10 and 20% mass loss respectively) and a temperature range from 250 to 400 °C. Lifelines for other sets of conditions can also be obtained but these two are chosen for demonstration here. The values of  $T_f$ ,  $\alpha$ ,  $V_f$ , and  $E$  used are found in Table 7.

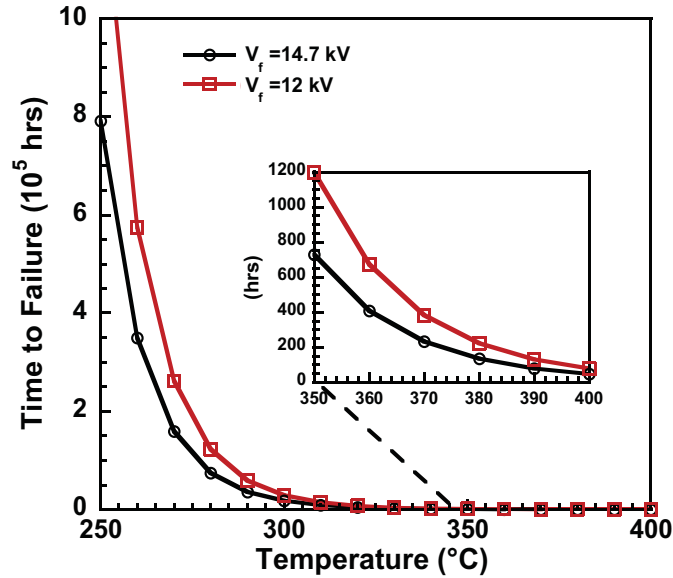


**Figure 27** Predicted time to failure at 12 and 14.7 kV and for isothermal temperatures ranging from 250 to 400 °C.

**Table 7** Parameters values used to obtain the calculated lifelines shown in Figure 27.

$V_f$ (kV)	$\alpha$ (%)	$T_f$ (K)	$E$ (kJ/mol)	$\beta$ K/hr	$t_f$ at 350°C (hr)
12	20	814	189	120	1200
14.7	10	801	189	120	729

As stated previously [21], the model presented in this work is not applicable to all materials; specifically those with extremely complex degradation mechanisms. The Kapton film studied here may, however, be treated in this way by considering only the initial part of the weight loss curves (within the first 25%) where a simple mechanism is responsible for degradation. Further, the thermogram for Kapton is no more complex than the thermogram for Formvar, treated in [21], in which a polyimide film was also treated.

Within the first 25% of weight loss, Kapton remains functional as wire insulation. Beyond 25% weight loss, the thin film failed to maintain the mechanical properties required for standard wire insulation and it was not possible to collect breakdown voltage data. At the elevated temperatures of this degradation study, the the surface of the Kapton film oxidizes. The oxidative layer can be seen on the surface of the material as darkening of the material color and alligator cracking of the surface. The oxidation causes the material to become brittle and deformed as the size of the oxidative layer expands—causing the material to fold over on itself.

Beyond 25% weight loss, the breakdown voltage is expected to drop rapidly, showing a large decrease in breakdown voltage for minor weight losses. This expectation comes from the loss of material

properties due to the extensive oxidation of Kapton. In fact, beyond 25% weight loss, there are indications that the Kapton polymer backbone is degraded enough that most of the linear chains are broken. The change in activation energy seen in Figure 9 for the first 25% weight loss indicates the rupture of the Kapton backbone—the sharp drop in activation energy is related to the breaking of the stable covalent bonds. When the linear chain is ruptured repeatedly, commonly through aroyl migration or hydrolysis of the imido group, the free radicals, mobile molecules, and oxygen molecules provide pathways for continued degradation at lower activation energies as observed between 30 and 100% weight loss [21]. These types of new pathways have been observed in the mass spectroscopy data from TG experiments in which the peak indicating carbon dioxide emission clearly indicates two unique mechanisms. The first mechanism (backbone rupture) endures for the first 25% of degradation and the second unique mechanism (new pathway) appears at around 25% weight loss [21]. Additionally, the nitrogen compounds have distinguishable mechanisms that again indicate a transition at 25% weight loss from the rupture of the major chain to the breaking of subcomponents.

To summarize, Kapton film may be treated by electrothermal analysis based on the criteria used in [47], provided that the lifetime prediction stays within the bounds of Kapton's functional mechanical properties, i.e. within 25% weight loss. In this 25% weight loss, electrical breakdown characteristics and physical changes are related through free volume and free radicals. Beyond the 25% threshold, the mechanical properties are destroyed through the rupturing of the stable covalent bonds in the polymer backbone. This is seen through observing the physical appearance of the degraded Kapton, the reduction in activation energy around 25%, and through the evolved gas analysis reported in [21].

#### 4. *Water/saline exposure*

##### **Effect of water/saline exposure on permittivity**

All PI samples for saline exposure experiments were cut into strips 3 cm wide by 9 cm long and immersed in distilled water or saline solutions for various times, including 0.5, 1, 2, 4, 6, 12 and 24 days. Saline solutions with three different concentrations were made by mixing distilled water with sodium chloride: 0.45 g/l, 6 g/l and 80 g/l, with conductivities 1 mS/cm, 10 mS/cm and 100 mS/cm [52], respectively. Immediately after removal from water or saline solutions, the samples were wiped to remove water on their surfaces, their thickness was measured by using the micrometer, and the samples were coated with silver paint introduced in section 2. When the silver paint was totally cured, each sample was cut into three smaller samples for permittivity measurement. The permittivity of all treated samples was measured from 1 kHz to 2 MHz at room temperature, using the Agilent E4980A LCR meter coupled with

a 16451 test fixture. The three identically degraded samples under all degrading conditions revealed highly similar values of  $\epsilon'$  and  $\tan \delta$ , the standard deviation measured for both is less than 1%.

Figure 28 shows the real permittivity and loss factor measured at 1 kHz as a function of sample immersion time in water and saline solutions. In the case of both water and saline, the real permittivity and loss factor of PI exhibit rapid increases in the first 4 days, but neither of them changes obviously after 6 days. Figures 29 and 30 show how  $\epsilon'$  and  $\tan \delta$  of PI behave as a function of frequency from 1 kHz to 2 MHz and immersion time, in water and 80 g/l saline, over 4 days.  $\epsilon'$  and  $\tan \delta$  of PI immersed in water are increased by approximately 11% and 40%, respectively; and by 12% and 40% for the sample immersed in 80 g/l saline. As shown in Figures 29b and 30b, the intensity of the  $\gamma$ -relaxation increases with time of immersion, because the PI samples absorb more moisture with longer time of immersion. This observation agrees well with the findings by mechanical testing methods [32]. The frequency of the  $\gamma$ -relaxation, however, is not changed as a function of immersion time.

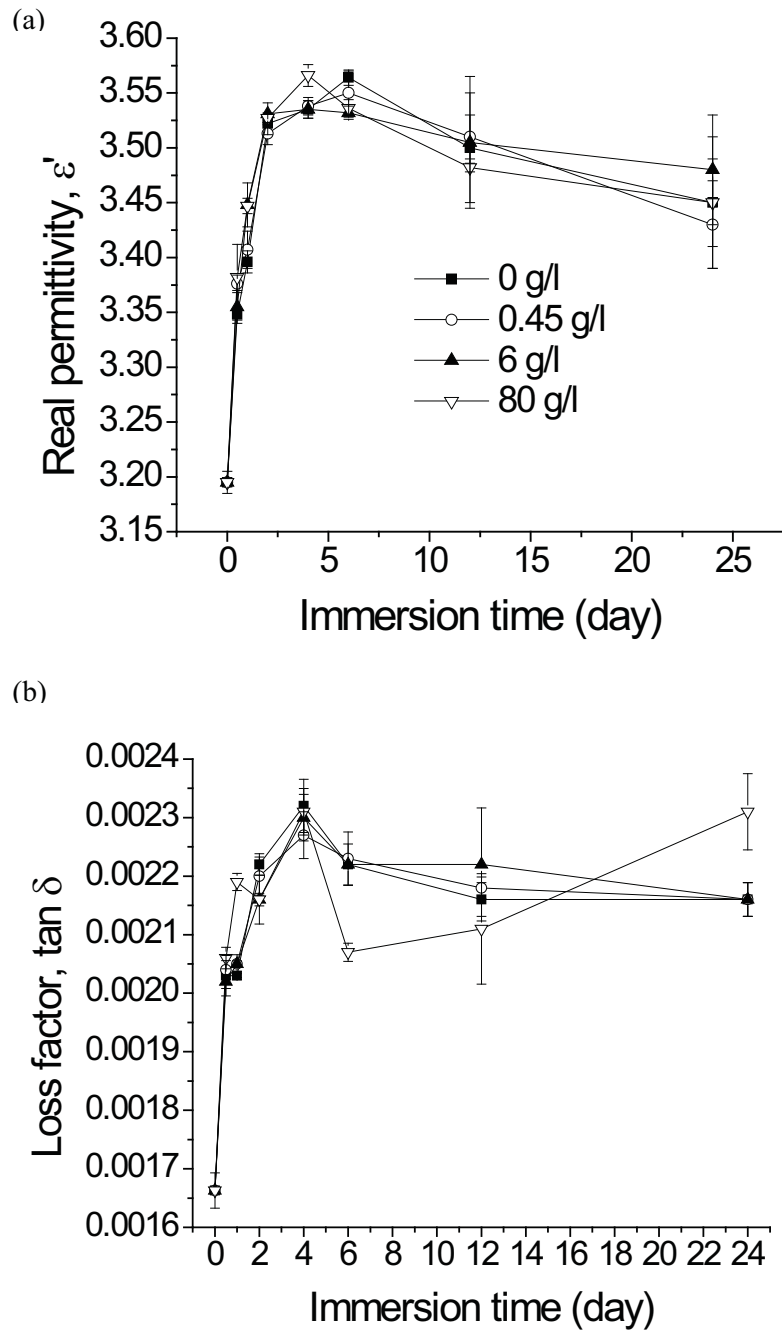


**Figure 28** The real permittivity (a) and loss factor (b) of PI immersed in water and saline solutions, measured at 1 kHz. Error bars indicate the standard deviation in measurements on three nominally-identical samples.

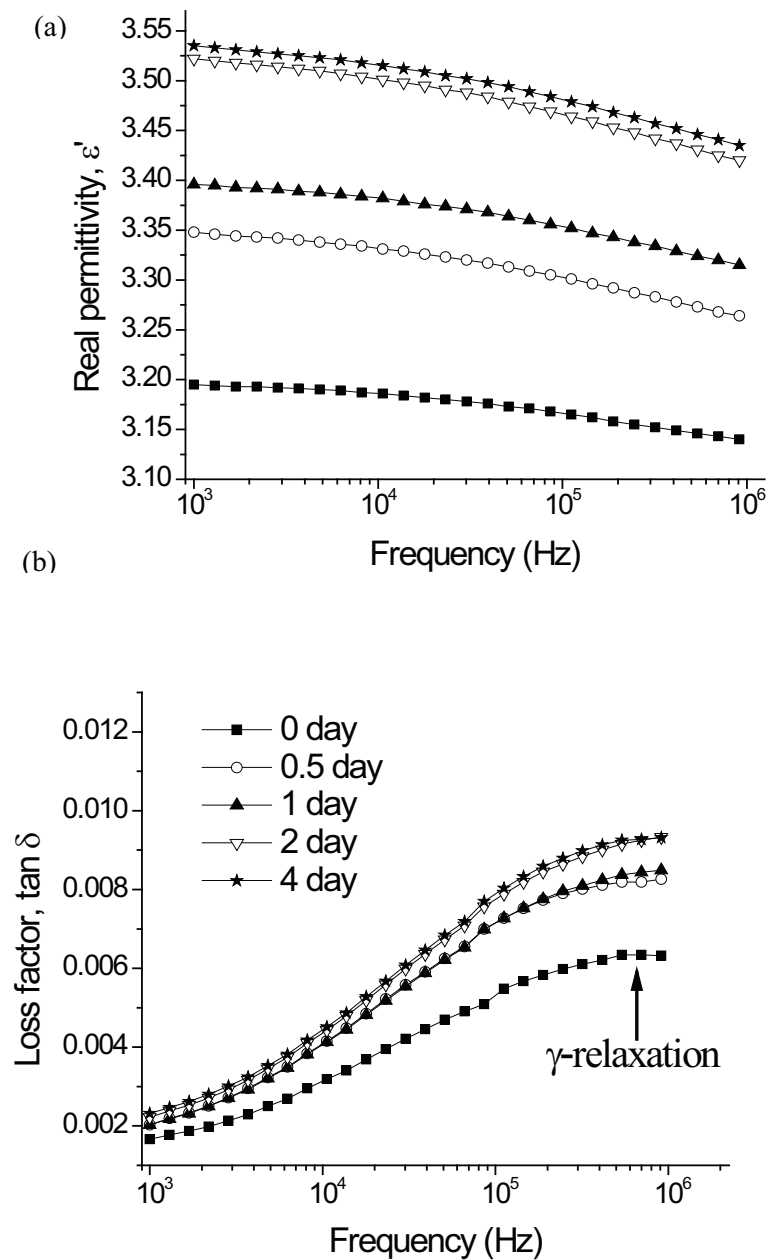


**Figure 29** The real permittivity (a) and loss factor (b) of PI following immersion in distilled water.

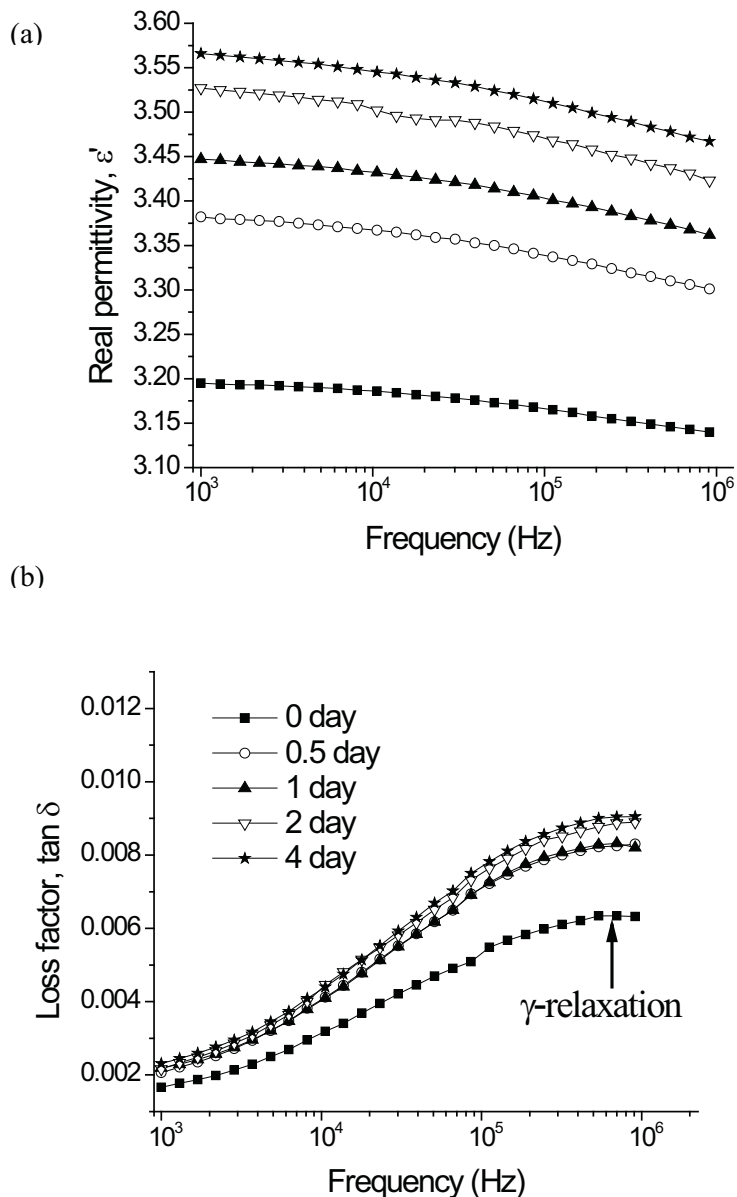


**Figure 30** The real permittivity (a) and loss factor (b) of PI following immersion in 80 g/l saline.

In order to further explore the effect of dissolved sodium chloride on the complex permittivity of PI, the differences in  $\epsilon'$  and  $\tan \delta$  between the samples immersed in water and those immersed in saline are plotted as function of immersion time in Figure 31. It can be concluded that the variation in salinity does not change complex permittivity of PI significantly and that the increases in  $\epsilon'$  and  $\tan \delta$  are as a result of moisture absorption.

The reason for the increase in real permittivity and loss factor of PI by moisture absorption can be attributed to the formation of polar groups and chain scission during hydrolytic degradation. Deiasi and Russell [53] observed a decrease in number-average molecular weight of PI caused by chain scission due to a chemical reaction between water and imperfections in the polymer chain. The chain scission mechanism is shown schematically in Figure 32 [54], which agrees with the statement in reference [6] that water molecules can bond to the carbonyl groups of PI. It has also been stated that the chemical reaction is rapid in the early stages of aging, and then slows as the number of susceptible sites in the polymer chain decrease [55]. This explains why the real permittivity and loss factor of PI are increased significantly during the first 4 days of immersion, after which there is little further change.

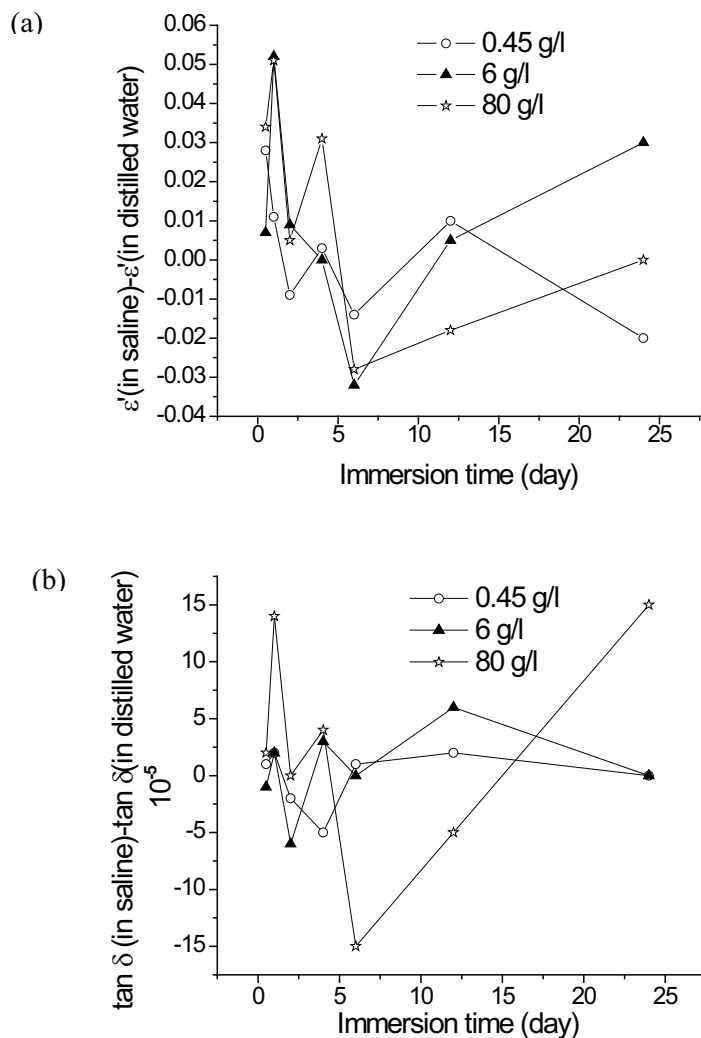


**Figure 31** Effect of dissolved sodium chloride on the real permittivity (a) and loss factor (b) of PI, measured at 1 kHz.

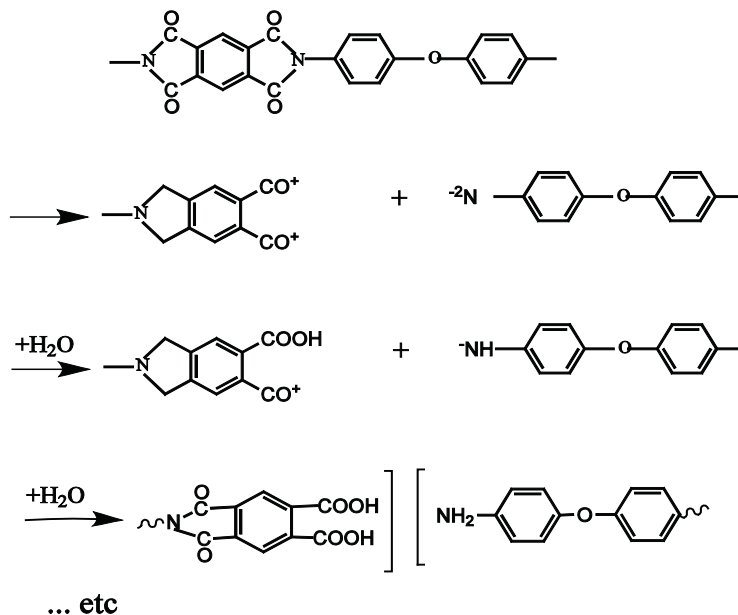


**Figure 32** Chain scission mechanism of PI hydrolysis through interaction of H<sub>2</sub>O with the carbonyl groups [54].

### Effect of water exposure on electrical breakdown behavior

PI is susceptible to moisture absorption. It has been reported that, while a MIL-W-81381 wire was undergoing accelerated aging in a humidity chamber, cracks propagated from the PI insulation tape to the conductor, acting as a current leakage path, and finally caused destructive failure in the circuit [4]. Increases in both the dielectric constant and the loss factor of PI with increasing water uptake have been observed [5]. However, even though Dupont has reported linear decrease in AC dielectric strength of PI as a function of humidity [3], few have statistically studied the effect of moisture absorption on breakdown behavior of PI. This paper statistically analyzes how AC dielectric strength of PI changes as the material is immersed in water for up to 96 hours by using Weibull distribution analysis.

As concluded in section 3.2 that the effect of dissolved sodium chloride on permittivity of PI immersed in salt water is minor, it is speculated that electrical breakdown behavior could not be influenced by variation in salinity significantly either. Thus, study of electrical breakdown behavior of PI after saline exposure is not investigated here.

### Experiment

The samples were cut into 6 cm by 10 cm sheets, large enough to measure dielectric strength 20 times at different points. The mass of each sample was measured using a balance with uncertainty 0.01 mg. The

thickness of the samples was measured using a micrometer with uncertainty 1  $\mu\text{m}$ . The PI samples were immersed in distilled water at room temperature for 4, 8, 16, 24, 48, 72 and 96 hours. The surfaces of the samples were wiped dry after they were removed from the water. Directly after wiping, the mass of the samples was measured again and compared with the value obtained before immersion in water. Twenty measurements of dielectric strength were made on each sample by using the Dielectric Rigidity 6135.054 instrument.

### *Results and discussion*

The Weibull cumulative distribution function of the PI immersed in water for 0, 4, 8, 16 and 24 hours is shown in Figure 33. The straight line fit to each data set moves towards lower values of dielectric strength with increasing immersion time. Moreover, slopes of the lines decrease as immersion time increases. As described in section 4.2,  $\alpha$  and  $\beta$  parameters are obtained via least-squares regression. Figure 34 shows how  $\alpha$  and  $\beta$  decrease with longer PI immersion in water.

As shown in Table 7 and Figure 35, no significant further change in either weight gain or dielectric strength of PI was observed after immersion in water for more than 24 hours. This observation is in line with the statement in reference [5] that PI is saturated with moisture after immersion in water for 25 hours.

Formation of side ionic groups due to dissociation of polymer chains is considered to be the reason why the insulation capability of PI film is deteriorated due to water uptake. Figure 32 shows the hydrolysis scheme for PI, in which polymer chains are broken and chemical composition is changed. OH<sup>-</sup> from water molecules bonds to either of the four carbonyl groups and H<sup>+</sup> bonds to the amine groups, generating ionic groups at sides of the new polymer chain [4] [6] [53]. The side ionic groups can greatly promote charge transport in PI insulation, which is termed as “intrinsic ionic conduction” in reference [45]. Consequently, electrical failure of the PI film is significantly accelerated.

It has been stated that chemical changes in PI due to moisture absorption are fully reversible by annealing for 1 hour [56]. Thus, in order to investigate whether physical degradation occurred in PI during immersion in water as well as chemical degradation, a sample immersed in distilled water for 24 hours was dried again by heating at 200 °C for 1 hour in order to eliminate the influence of ionic side group formation on dielectric strength of PI. The Weibull plot of breakdown for the annealed sample (not shown here) revealed no obvious change when compared with that of the control sample. As listed in Table 8, the scale parameter,  $\alpha$ , of the sample is not significantly changed. Therefore, it is concluded that immersion in water did not give rise to significant physical degradation of the PI film. The change in the shape parameter,  $\beta$ , could be a result of variation in dispersity of electrical weak points in the two samples.

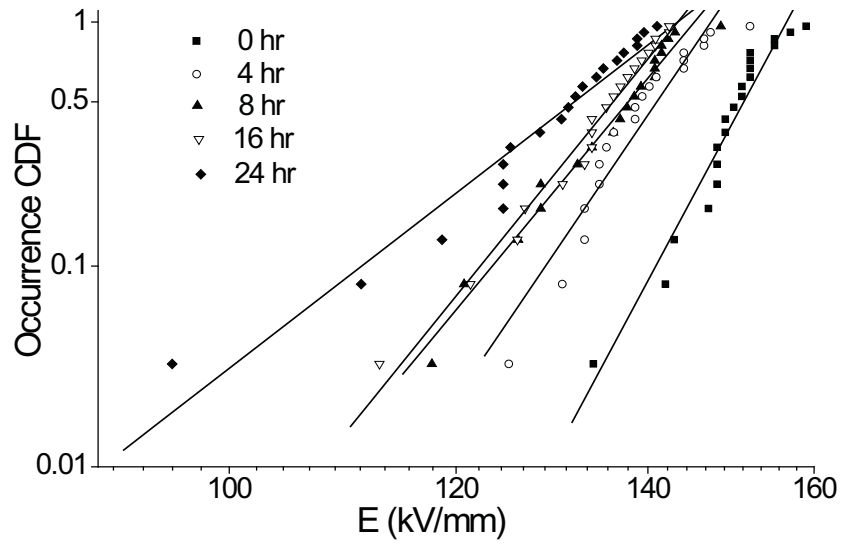


**Figure 33** The cumulative distribution function of the measured dielectric strength of PI samples immersed in water for 0, 4, 8, 16 and 24 hours.

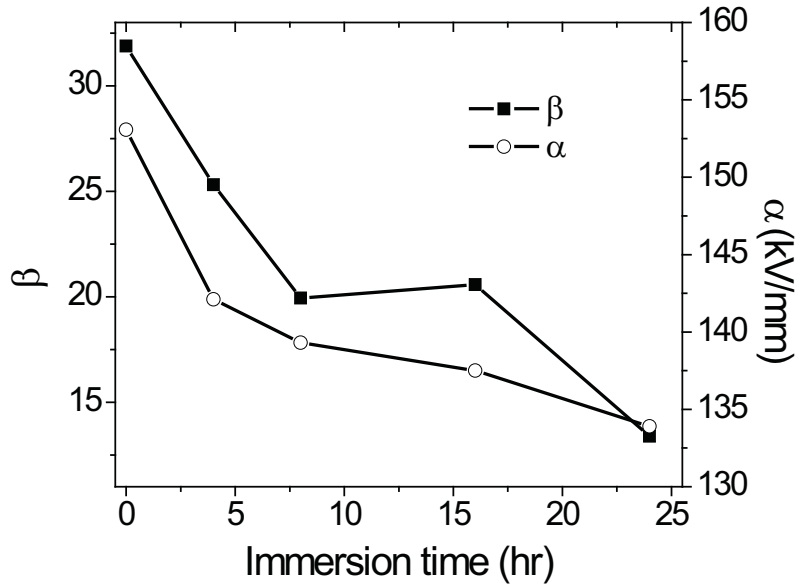


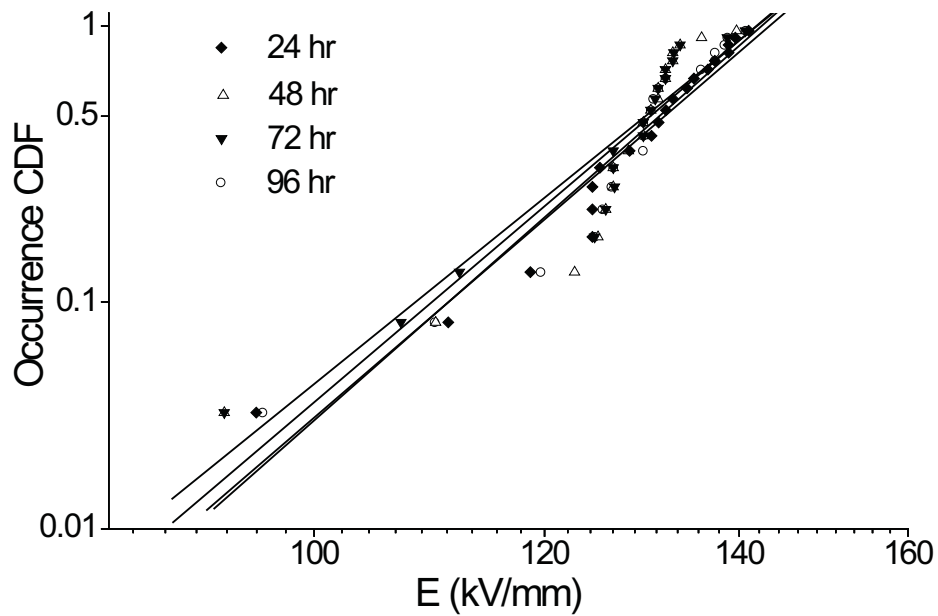
**Figure 34** The Weibull-statistical scale parameter ( $\alpha$ ) and the shape parameter ( $\beta$ ) as functions of time of PI immersion in distilled water.

**Table 8** Weight gain of PI samples immersed in distilled water for up to 96 hours.

Immersion time (hr)	Weight gain (%)
4	0.87
8	1.32
16	1.75
24	1.80
48	1.80
72	1.81
96	1.80

**Table 9** The Weibull-statistical scale parameter ( $\alpha$ ) and the shape parameter ( $\beta$ ) of dry PI.

sample	$\alpha$ (kV/mm)	$\beta$
The original dry PI	$152.2 \pm 0.3$	$32 \pm 2$
2 <sup>nd</sup> dry PI	$154.4 \pm 0.2$	$40 \pm 2$

**Figure 35** The cumulative distribution function of the measured dielectric strength of PI samples immersed in water for 24, 48, 72 and 96 hours.

## 5. *Summary*

This chapter investigates the effects thermal degradation in air and immersion in water/saline on the insulating performances of Kapton PI film. FTIR and MS exit gas analysis verified the degradation components and the multistep degradation process of Kapton. After either the heating process or immersion in water, the real permittivity and loss factor of PI are increased substantially. Intensity of the  $\beta$ -relaxation is substantially increased due to scission of chemical bonding in imide groups during thermal degradation at 475 °C for 3 hr. As PI samples absorbed more moisture with longer time of immersion in water or saline, the intensity of  $\gamma$ -relaxation following saline exposure is increased. On the other hand, using statistical analysis by two-parameter Weibull distribution, we observed that the dielectric strength of PI is greatly decreased and individual measurements of breakdown voltage are much more randomly distributed, with increasing time or temperature of thermal exposure and increasing time of immersion in water. The deterioration of insulating properties of PI after the degrading processes is explained in terms of chemical degradation due to pyrolysis of imide groups during thermal exposure and formation of ionic side groups during the hydrolysis process of PI while immersed in water. However, dissolved sodium chloride shows minor influence on dielectric properties of PI immersed in saline solutions. A short term technique based on thermal analysis and electrical breakdown measurement is verified to be a good solution to predict lifetime of PI under electrothermal multi-stress.

### Chapter III. Polytetrafluoroethylene (PTFE)

Due to its excellent dielectric properties and hydrophobicity, PTFE (polytetrafluoroethylene) is widely used as an outer coating material for wiring insulation [1]. Therefore, it is always exposed to heat and mechanical stress during service. In this chapter, the effect of thermal exposure and tensile strain on permittivity of PTFE is investigated.

#### 1. Introduction

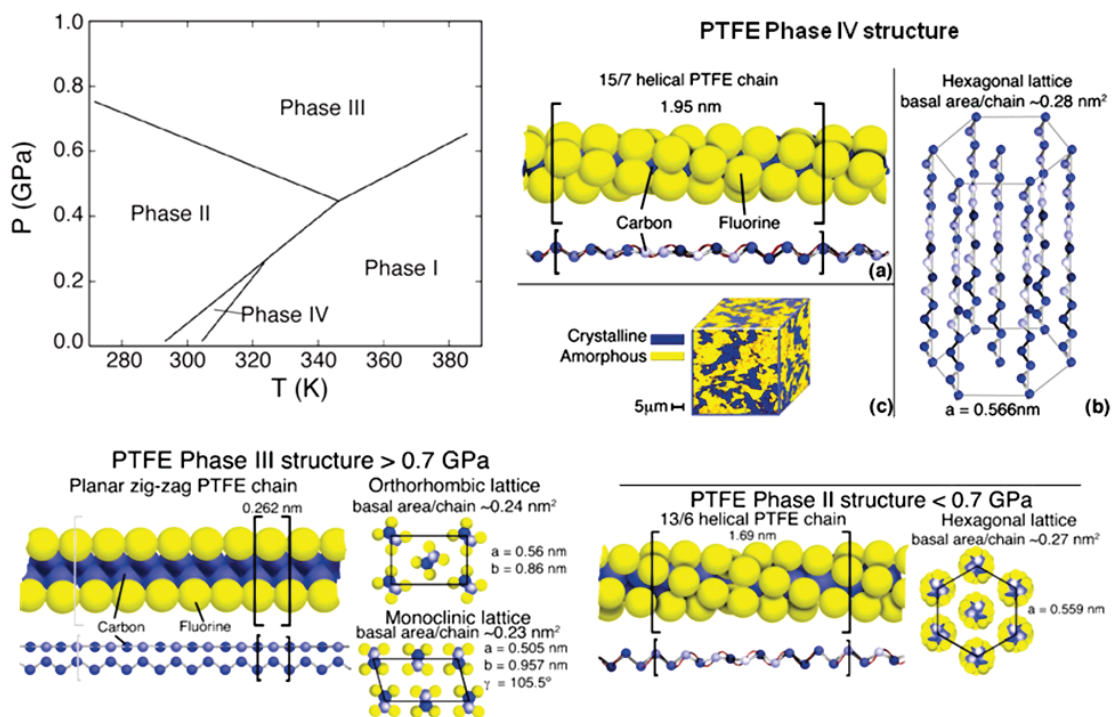
PTFE,  $(-\text{CF}_2-)_n$ , is a fluorocarbon polymer, typically with a very high molecular weight. The substitution of fluorine for hydrogen causes the material to exhibit extreme properties. Due to the C-F bonds, it exhibits special properties surpassing those of most polymers due to the substitution of fluorine for hydrogen, such as very high melting temperature and good chemical resistance. The main physical and chemical properties of PTFE are compared with those of polyethylene (PE) in Table 9 [57].

In PTFE, closed connected amorphous and crystalline phases coexist due to its extremely high molecular weight ( $\sim 1 \times 10^6$ ) [58]. The temperature-pressure phase behavior of crystalline PTFE is shown in Figure 36 [59, 60]. At atmospheric pressure, the room temperature crystalline structure of PTFE (phase IV) transfers to phase II below 19 °C [61] and to phase I above 31 °C [62]. The first-order transition at 19 °C from phase II triclinic to phase IV hexagonal reflects an untwisting in the helical conformation from 13 atom/180 degree turn [63] [64] to 15 atoms/turn [63] [65] [66] and an increase in the hexagonal lattice spacing. Above 31 °C the individual polymer chains lose their well defined helical repeat unit [63] [67]. Further rotational disordering and untwisting of the helices produces a pseudo-hexagonal structure. At room temperature, phase II transfers to phase III orthorhombic above  $\sim 0.65$  GPa [68]. Amorphous PTFE has the same repeat atomic structure as the crystalline domains but without significant order [60].

PTFE has excellent electrical insulating properties due to its low relative permittivity (2.0-2.2 [69]), low dielectric loss ( $< 0.0002-0.0005$  [70]), good frequency stability in a wide spectral range (up to 10 GHz), and high breakdown strength (19.2 kV/mm [70]). Reference [71] shows the complex permittivity of PTFE as a function of temperature at microwave frequencies  $f \approx 11.5$  GHz. The real permittivity of PTFE decreases from 2.12 to 2.01 as temperature increases from -151 to 102 °C and the dissipation factor is less than  $10^{-3}$  even at high temperatures. As presented in reference [72], the real permittivity of PTFE decreases from 2.35 to 2.09 as temperature increases from -150 to 250 °C at 10 kHz. Additionally, because of its good mechanical and thermal stability over temperatures up to 260 °C [73], PTFE has been extensively applied as wire insulation material in air- and spacecraft.

**Table 10** Properties of PTFE and PE.

Property	PTFE	Polyethelyne
Density (g/cm <sup>3</sup> )	2.2-2.3	0.92-1
Melting Temperature (°C)	342±10 (1st) 327±10 (2nd)	105-140
T <sub>g</sub> (α-PTFE) (°C)	126	-
T <sub>g</sub> (β-PTFE) (°C)	30	-
T <sub>g</sub> (γ-PTFE) (°C)	80	-
Surface Energy (dynes/g)	18	33
Resistance to Solvents and Chemicals	Excellent, no known solvent.	Susceptible to hot hydrocarbons.

**Figure 36** Temperature-pressure phase diagram of crystalline PTFE with the inter- and intra-polymer chain crystalline structures.

## 2. Sample material

In this work, all PTFE samples were cut from the same large sheet supplied by Fluoro-Plastics, which is nominally  $610 \times 610 \times 1 \text{ mm}^3$ . The melting point of as-received PTFE was determined to be  $327 \text{ }^\circ\text{C}$  by a DSC (differential scanning calorimetry) test. The PTFE sample appears opaque white and relatively hard

below its melting temperature, as shown in Figure 37a; while turned to be translucent and very easily pierced with a needle above the melting temperature, Figure 37b.



**Figure 37** PTFE (a) below the melting temperature 327 °C; and (b) above the melting temperature.

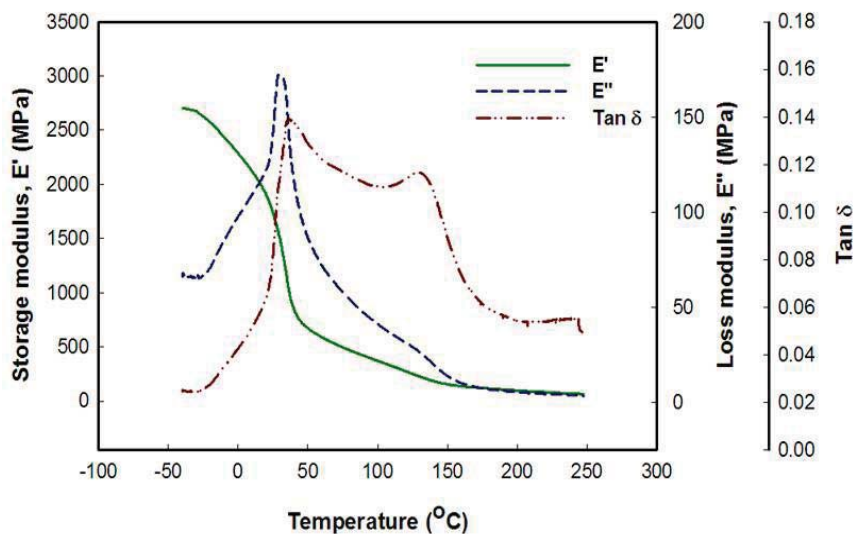


**Figure 38** Results of dynamic mechanical analysis on as-received PTFE.

Figure 38 reveals the storage modulus  $E'$ , loss modulus  $E''$  and  $\tan \delta = E''/E'$  of an as-received PTFE sample as a function of temperature, which was measured by DMA (dynamic mechanical analysis) at 1 Hz. The shape and intensity of peaks in the  $\tan \delta$  curve, as well as the magnitude of the storage modulus, are determined by the degree of crystallinity in the PTFE. Thermal transitions at 36.1 °C ( $\beta$  transition) and 129.3 °C (primary  $\alpha$  transition) can be observed according to peaks of  $\tan \delta$  analyzed by the software 'TA Universal Analysis' which can estimate values of peaks and shoulders in the curve to a tenth of a degree. These peaks correspond to 29.2 °C and 120.0 °C in the loss modulus curve. The above values are close to the data listed in Table 9 and are discussed more fully in reference [19]. Due to limitation in the temperature range of the DMA measurement, the  $\gamma$ -transition at around -80 °C is not shown.

The real permittivity of as-received PTFE was measured over frequency range from 1 Hz to 1 MHz at room temperature by Novocontrol spectrometer, as shown in Figure 39. The error bar was given by the Novocontrol spectrometer, which includes the accuracy of the used impedance analyzer and the influences of cables and sample holders. The error bar also strongly depends on frequency of measurement and the actual sample impedance. As expected, the permittivity of PTFE is extremely stable over the whole frequency range. The mean value and standard deviation of the data points in Figure 39 are  $2.214 \pm 0.001$ . Since the dissipation factor of PTFE is so small that it is beyond the measurement accuracy of this spectrometer over most of the frequency range, the measured values of loss factor are not shown here.

To explore dielectric performance of PTFE at extreme temperatures, the permittivity was also measured over temperature range -150 to 300 °C at frequency from 1 Hz to 1 MHz. During measurements, the whole sample cell was housed in a temperature-controlled container, in which the temperature was gradually increased in 10 °C increments. Figure 40 shows the real permittivity of as-received PTFE as functions of both frequency and temperature. Drawn with data points from Figure 40, Figure 41a shows the real permittivity as a function of temperature at 1.15 kHz. At this frequency,  $\epsilon'$  decreases from 2.287 to 1.968 as temperature increases from -150 °C to 300 °C. A probable explanation of this behavior is that, as a nonpolar polymer, the polarization of PTFE is mainly electronic. In that case, the Clausius-Mossotti equation can be applied, as stated in [13].

$$\frac{N\alpha_e}{3\epsilon_0} = \frac{(\epsilon-1)M}{(\epsilon+2)\rho} \quad (43)$$

where  $N$  is the number of polarizable entities per unit volume,  $\alpha_e$  is electronic polarizability,  $\epsilon_0$  is the permittivity of free space,  $\epsilon$  is the relative permittivity of PTFE,  $M$  is molar weight and  $\rho$  is mass density. Rearranging the above equation gives

$$\epsilon = \frac{3M\epsilon_0}{M\epsilon_0 - N\alpha_E\rho} \quad (44)$$

Since density decreases as the temperature increases, it can be postulated from the above equation that  $\epsilon'$  should decrease slightly with temperature, as the measurements show in Figure 41a).

Focusing on the temperature range  $-10\text{ }^{\circ}\text{C}$  to  $50\text{ }^{\circ}\text{C}$  in Figure 41b, two step-like decreases in  $\epsilon'$  are observed near  $19\text{ }^{\circ}\text{C}$  and  $31\text{ }^{\circ}\text{C}$ , which can be associated with structural first-order phase transitions at these two temperatures [72]. The room-temperature crystalline structure of PTFE (phase IV hexagonal) transfers to phase II triclinic below  $19\text{ }^{\circ}\text{C}$  by angular displacement [61] and to phase I pseudo-hexagonal above  $31\text{ }^{\circ}\text{C}$  by crystal disorder [62], which are both accompanied by step-like changes of the specific volume. Due to the thermal expansion of the sample capacitor,  $\epsilon'$  of PTFE shows two step-like decreases in the vicinity of the phase transition temperatures.

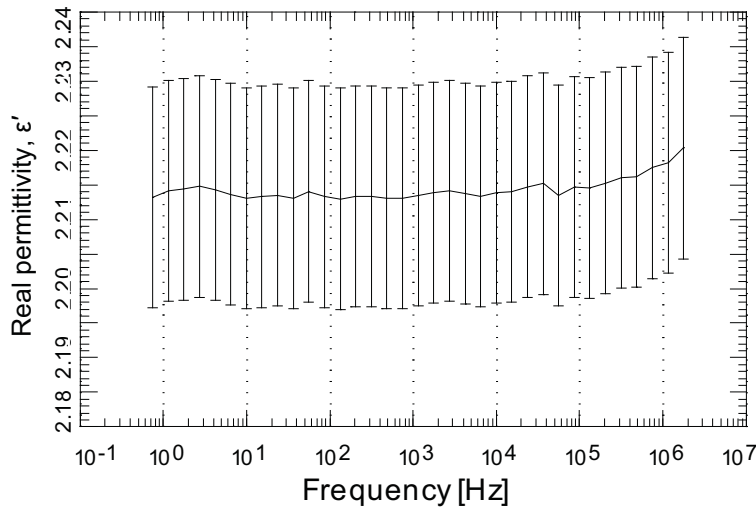


**Figure 39** Real permittivity of as-received PTFE as function of frequency at room temperature.

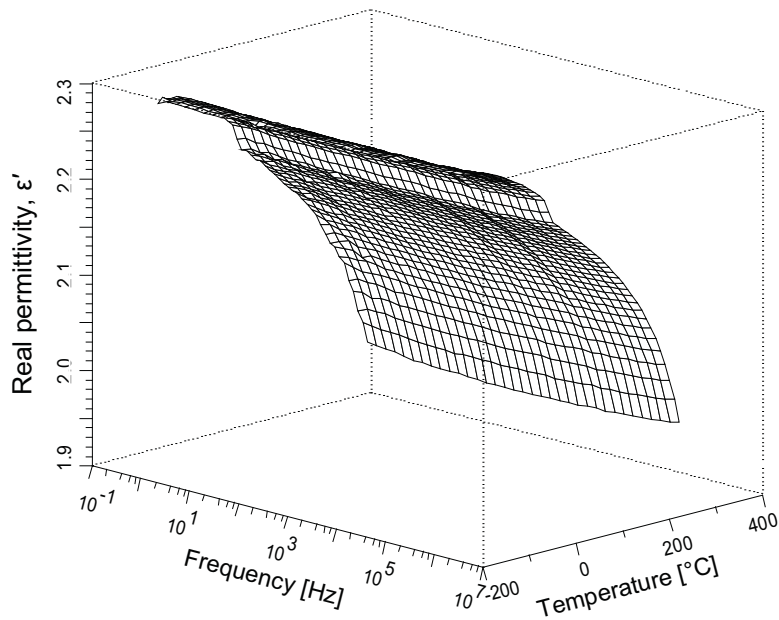


**Figure 40** Real permittivity of as-received PTFE as a function of frequency and temperature.

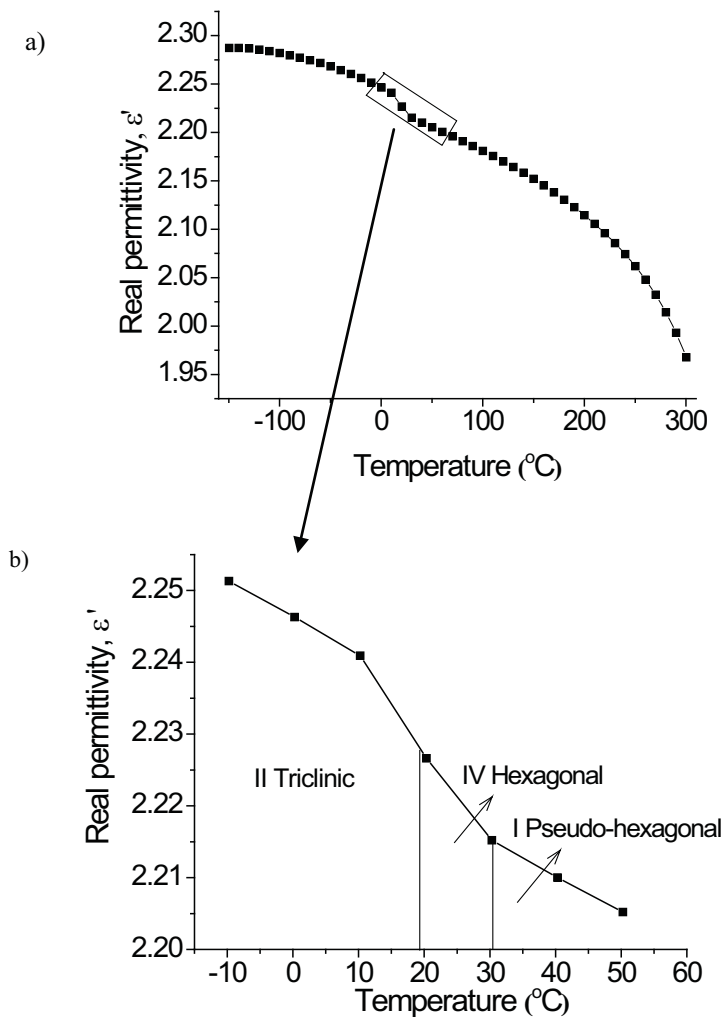


**Figure 41** Real permittivity of as-received PTFE as a function of temperature at 1.15 kHz. a): -150 to 300  $^{\circ}\text{C}$ ; b): -10 to 50  $^{\circ}\text{C}$ .

### 3. *Thermal degradation*

#### **Thermal degradation kinetics**

##### *Method and experiments*

A thermogravimetric analyzer, model Q50 from TA Instruments (New Castle, DE), was used for all of the TG experiments. Experiments involving PTFE were conducted from room temperature to 700  $^{\circ}\text{C}$  at five separate ramp rates: 2, 5, 10, 20, and 30  $\text{Kmin}^{-1}$ . Under the controlled environments of the TG instrument, the samples were degraded in an air atmosphere using a balanced purge gas flow rate of 40  $\text{mL}/\text{min}$  and a sample purge gas flow rate of 60  $\text{mL}/\text{min}$ . Samples were placed on a platinum pan during the degradation process. Kinetic analysis was performed with the Netzsch Thermokinetics 2 program

(version 2004.05) and standard statistical and plotting programs. The same kinetic modeling was used as studying thermal degradation kinetics of polyimide, as described in Chapter II.

### *Results and discussion*

The TG scans for PTFE began at room temperature, and degradation was not observed until elevated temperatures were reached. The high temperature TG data is given in Figure 42. Like most fluoropolymers, PTFE is extremely stable at intermediate temperatures. The onset of degradation increases with increasing heating rate and involves a rapid and complete degradation. From the TG curves, the variation between the temperatures of the degradation onset points provides insight into the reaction model. The uniform temperature spread of the onset point for the PTFE degradation curves indicates a single step for the degradation.

The derivative of the weight with respect to temperature provides better insight into the mechanism of degradation. For a specific heating rate, the number of peaks in the derivative thermogram (DTG) represents the minimum number of reaction steps involved. By varying the heating rates, the degradation steps can be separated and isolated. Figure 43 shows the DTG curves of PTFE. Notably, only one peak is observed for the five heating rates. Based on the single DTG peak, a single step reaction can be seen.

Once initial observations of the thermograms have been made, a Friedman analysis based on equation (6) provides information about multi-step processes during the reaction and also offers insight into the type of reaction step. Similar to the DTG plots, the number of peaks indicates the minimum number of reaction steps in the degradation. For PTFE there is one single peak as seen in Figure 44. Therefore a single step reaction is again evident from the curvature of the plot for PTFE.

The type of the reaction can also be determined by comparing the slope of the constant fractional mass loss trend line to the slope of each peak at the beginning of the reaction step [21]. For PTFE, the first peaks have in all cases the acceleration, probably autocatalysis. For autocatalysis, the generic governing differential equation, presented in equation 2, defines the reaction model,  $f(\alpha)$ , such that:

$$f(\alpha) = (1 - \alpha)^n(1 + K_{cat}X) \quad (45)$$

where  $\alpha$  represents the degree of degradation,  $n$  represents the reaction order,  $K_{cat}$  represents the autocatalysis constant, and  $X$  represents the step of the reaction.

From the Friedman analysis as well as the Ozawa-Flynn-Wall analysis, activation energy as a function of fractional mass loss can be obtained [18] [19] [27]. For PTFE, the plot of the activation energy with respect to the amount of degradation again confirms the single step autocatalytic reaction by presenting linearly declining activation energy seen in Figure 45. Activation energy developed from Friedman analysis presents activation energies between 130 kJ/mol and 70 kJ/mol.

From the TG curves, DTG curves, Freidman Analysis, and activation energies, a single step autocatalytic kinetic model was deemed the best model to represent the PTFE degradation. The model fitted data can be seen in Figure 46 and the kinetic parameters can be seen in Table 11. Several other reactions were tested in order to validate the single step autocatalytic reaction. These reactions included alternative single step reactions as well as a few multiple step reactions. The closest fitting alternative models can be seen in Table 12.

Comparing the single step autocatalytic reaction with the other reactions, an F-test shows that the chosen reaction fits the data best. See Table 12 for an F-test comparison and a schematic representation of the different models. The F-test is a statistical test used to compare models that have been fit to experimental data sets. The F-test identifies the best model fit of the population for which the data was sampled by testing the residual variances of the individual models against one another. The equation is as follows:

$$F_{exp}(f_1, f_r) = \frac{\sum_{j=1}^S \sum_{k=1}^{N_s} (Y_{jk} - \hat{Y}_{jk}(\text{model}_1))^2 / f_1}{\sum_{j=1}^S \sum_{k=1}^{N_s} (Y_{jk} - \hat{Y}_{jk}(\text{model}_r))^2 / f_r} \quad (46)$$

or:

$$F - test = \frac{\text{lack-of-fit sum of squares/degrees of freedom}}{\text{pure-error sum of squares/degrees of freedom}} \quad (47)$$

where  $f_1$  is the degree of freedom for model 1 and  $f_r$  is the degree of freedom for the reference model. Typically, the model with the lowest deviation, the best fit, is chosen as the reference model and therefore  $F_{exp} = 1$ . Based on the standard 5% significance level,  $F_{critical}$  is determined from the F-distribution, the null distribution for the test.

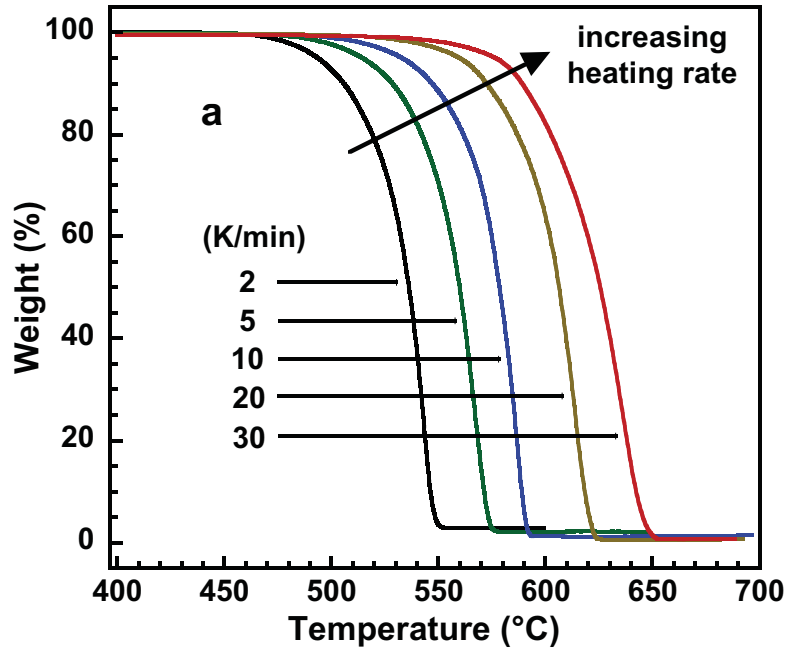


Figure 42 TG curves for PTFE.

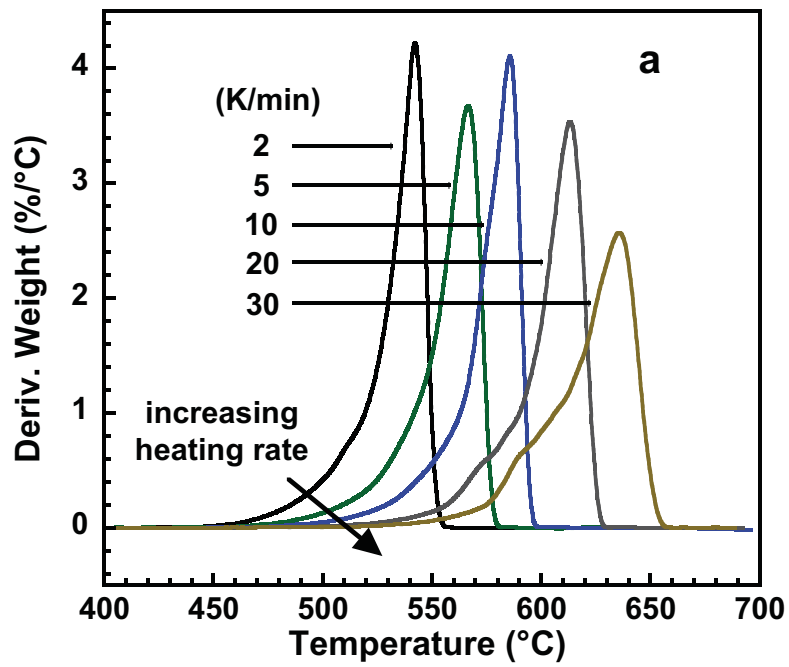


Figure 43 DTG curves for PTFE.

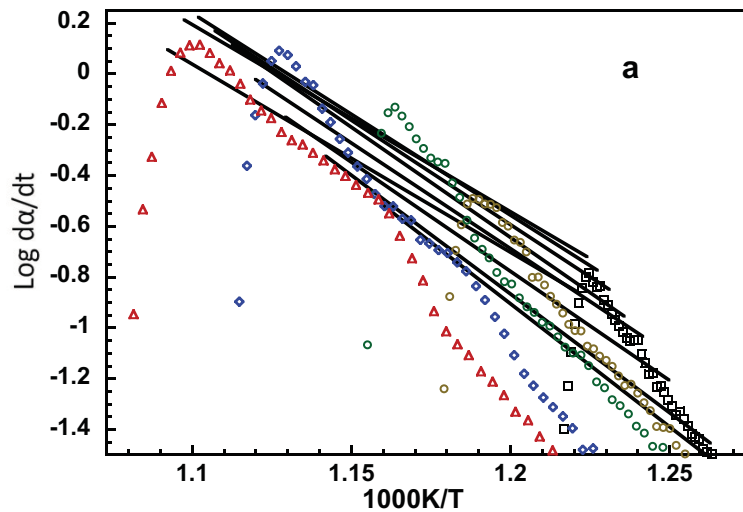


Figure 44 Friedman Analysis for PTFE.

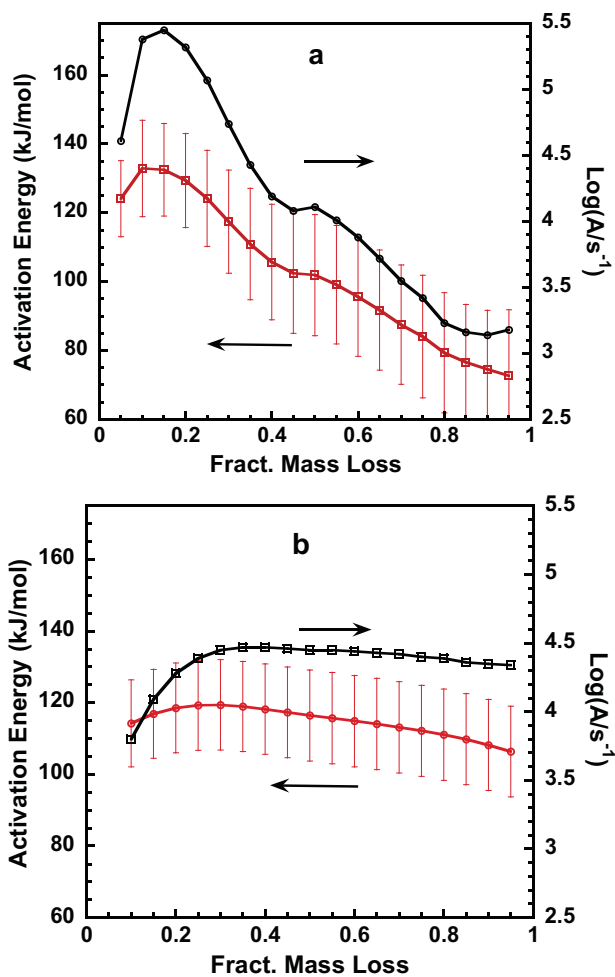
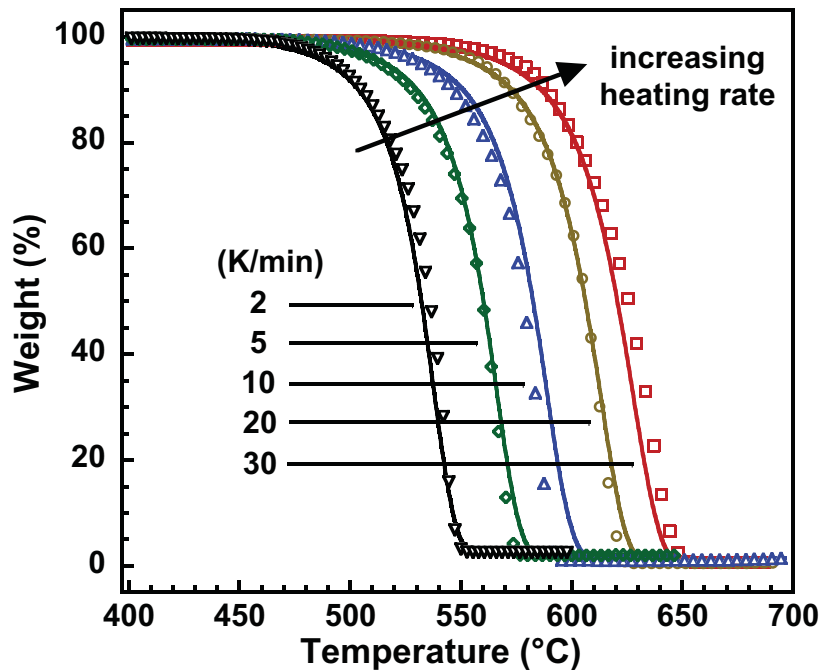


Figure 45 PTFE activation energy from (a) Friedman Analysis and (b) Ozawa-Flynn-Wall Analysis.



**Figure 46** Model of the best fit TG data for a single-step reaction model in air for PTFE. In the plot, the curves represent the model and the shapes represent the modeled experimental data.

**Table 11** Kinetic Parameters for the single step autocatalytic model for PTFE.

Activation Energy (kJ/mol)	Log (A1/s-1)	Reaction Order	Log (Kcat)
169.0	7.25	0.74	1.16

**Table 12** Comparison of kinetic models for PTFE\*.

Reaction Model	Model Designation	$f(\alpha)$	$F_{exp}$
First Order	F1	$(1 - \alpha)$	7.21
Second Order	F2	$(1 - \alpha)^2$	19.34
$n$ th Order	Fn	$(1 - \alpha)^n$	1.17
$n$ th Order with Autocatalysis	Cn-X	$(1 - \alpha)^n(1 + K_{cat}X)$	1.0

\* $F_{critical} = 1.10$

## Effect of thermal exposure on permittivity

### *Experiment*

For the thermal exposure experiment, rectangular PTFE samples approximately  $100 \times 80 \times 1 \text{ mm}^3$  were cut from the large PTFE sheet. Each sample was large enough to provide three smaller samples for subsequent permittivity measurements. The PTFE was heated isothermally at  $340 \pm 3 \text{ }^\circ\text{C}$ , a temperature above the melting point, in an isotherm muffle furnace for 2, 6, 12, 24, 36, 48, 60, 72, 84 and 96 hr.

The PTFE samples for all exposure times were allowed to cool naturally in situ after the furnaces were turned off. Doors of the furnaces were not opened during the cooling process. While in the furnace the samples were sandwiched between two stainless-steel plates with mirror finish, to inhibit distortion. Once the samples were completely cool, after 48 hr, their permittivity was measured at room temperature over the frequency range 1 kHz to 2 MHz. Permittivity of as-received PTFE was also measured as baseline data.

### *Result and discussion*

Figure 47 shows the way in which  $\epsilon'$  of PTFE increases as thermal exposure time increases, at four frequencies. Thermal exposure at  $340 \text{ }^\circ\text{C}$  for 96 hr increases  $\epsilon'$  of PTFE by approximately 2%, which is significantly larger than the standard deviation between measurements on three nominally identical samples, which is less than 0.1%.

The increase in real permittivity of PTFE after thermal exposure at  $340 \text{ }^\circ\text{C}$  is attributed to enhancement of crystallinity following the heating and cooling processes. In semicrystalline polymers, motion of charge carriers, such as degenerated monomer molecules, can be blocked at the crystalline/amorphous phase boundaries and generate interfacial (Maxwell-Wagner-Sillars) polarization [74]. If the crystalline phase grows, the interfacial polarization may be enhanced, causing an increase in  $\epsilon'$ . To investigate this hypothesis, X-ray diffraction (XRD) measurements were conducted on as-received PTFE and PTFE thermally exposed at  $340 \text{ }^\circ\text{C}$  for 48 hr and 96 hr. After thermal exposure, three samples were allowed to cool slowly in situ as described in before. Three other samples were quenched in liquid  $\text{N}_2$  to inhibit crystallization. While the XRD patterns of the PTFE samples all suggest a hexagonal crystal structure is present regardless of thermal history, the degree of crystallinity (as measured by peak area) in quickly-quenched PTFE was found to be  $0.24 \pm 0.01$ , versus  $0.29 \pm 0.01$  in as-received PTFE,  $0.32 \pm 0.01$  in PTFE slowly cooled after isothermal heating at  $340 \text{ }^\circ\text{C}$  for 48 hr and  $0.35 \pm 0.01$  in PTFE slowly cooled after isothermal heating at  $340 \text{ }^\circ\text{C}$  for 96 hr. Hence the increase in  $\epsilon'$  as a function of thermal exposure time, shown in Figure 47, can be attributed to increasing crystallinity. The uncertainties derive from the standard deviation of measurements on three nominally identical samples.

The increase in crystallinity observed in slow-cooled thermally-exposed PTFE compared with as-received samples supports the observation that  $\epsilon'$  increases following thermal exposure at  $340 \text{ }^\circ\text{C}$  (which

is higher than the melting point 327 °C) with slow cooling (Figure 47). On the other hand, the reduction in crystallinity of quickly-quenched, thermally-exposed PTFE compared with as-received samples accompanied a reduction in  $\epsilon'$  of approximately 2%, much larger than the standard deviation between measurements of three nominally identical samples (0.2%). This observation further supports the hypothesis that increase in crystallinity is accompanied by an increase in  $\epsilon'$  for the range of conditions studied here.

An alternative explanation for the increase in  $\epsilon'$  with increasing crystallinity of PTFE can be framed in terms of a charge carrier diffusion model. In reference [75] it is suggested that development of a heterogeneous structure such as exists in a semicrystalline polymer leads to an increase in permittivity of the polymer approaching the formation of a percolating network of the conducting amorphous phase.

The two proposed models offer similar features since the time to explore the percolation structure by the charge carriers is equivalent to the time to transfer charges to the micro-capacitors formed by semicrystalline structure in the interfacial polarization model.

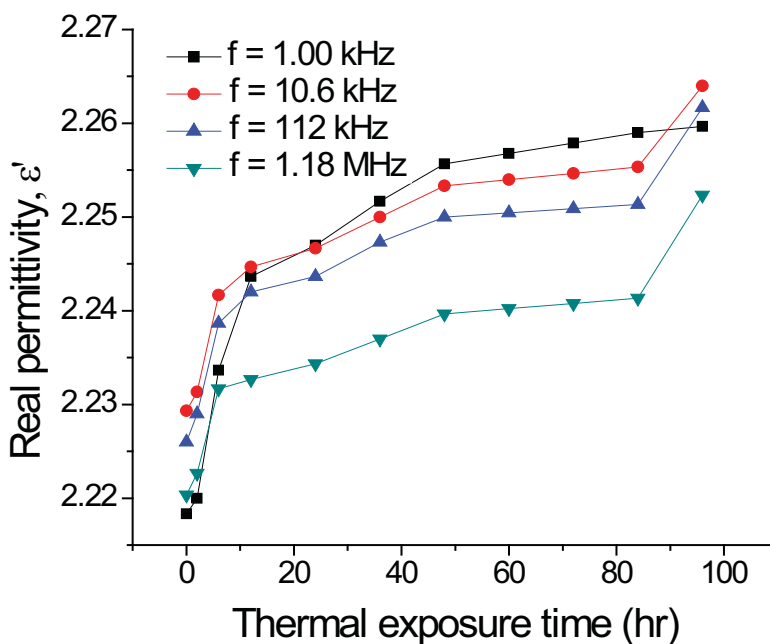


**Figure 47** Real permittivity of PTFE as a function of thermal exposure time at 340 °C in air.

#### 4. *Effect of tensile strain on permittivity*

##### **Experiment**

The dielectric permittivity of untreated PTFE was firstly measured over the frequency range from 1 Hz to 1 MHz at room temperature using a Novocontrol Dielectric Spectrometer. As shown in Figure 39, the real permittivity of PTFE is approximately constant over this frequency range, with average value  $\epsilon_r' = 2.076 \pm 0.002$ . For this reason, subsequent permittivity measurement of all samples in this study was conducted only at 100 kHz. The imaginary permittivity of PTFE is too small to be accurately measured by the dielectric spectrometer, so is not included in this discussion.

In order to effectively study the influence of tensile strain on the permittivity of PTFE, a system capable of in-situ measurement of the permittivity of a polymer sample while under tensile strain was employed. This avoids the difficulty that once the polymer sample is removed from a tensile loading frame, the polymer chains may recover to some extent, changing the permittivity. As shown in Figure 48, the test fixture of an Agilent E4980A LCR meter fits in between the two clamps of a tensile loading frame (TestResources Inc., Model 150Q250) in order to measure the capacitance of the sample while it is stretched. For this reason, the accessible length of the sample was initially 75 cm or longer. Note that this configuration applies longitudinal stress while permittivity is measured orthogonally to the direction of the applied stress. The thickness of the samples was measured to uncertainty 1  $\mu\text{m}$  by using a micrometer tipped with flat, parallel discs with diameter of approximately 5 mm that contact the sample. The diameter of the discs was selected to be similar to that of the capacitor electrodes with diameter of 5 mm, so that the thickness was measured over an area at least as small as the sample area.

All the PTFE samples investigated in this study were cut from a single sheet supplied by Fluoro-Plastics Inc.. The dimension of each sample was approximately  $90 \times 40 \times 0.39 \text{ mm}^3$ . An engineering stress-strain curve of one sample, shown in Figure 49, was measured in order to guide the selection of strains for simultaneous permittivity measurement. Engineering stress is defined as the ratio of the internal force with the original area of the sample surface on which the internal force acts on, in this case the cross-sectional area of the sample strip. The sample reveals elastic mechanical behavior below 18 MPa load, and fails at approximately 31 MPa load, at which the engineering strain is approximately 190%. In order to ensure successful measurement without failure of the PTFE sample, mechanical strains of 25, 50, 75, 100, 125 and 150% were selected for simultaneous permittivity measurement..

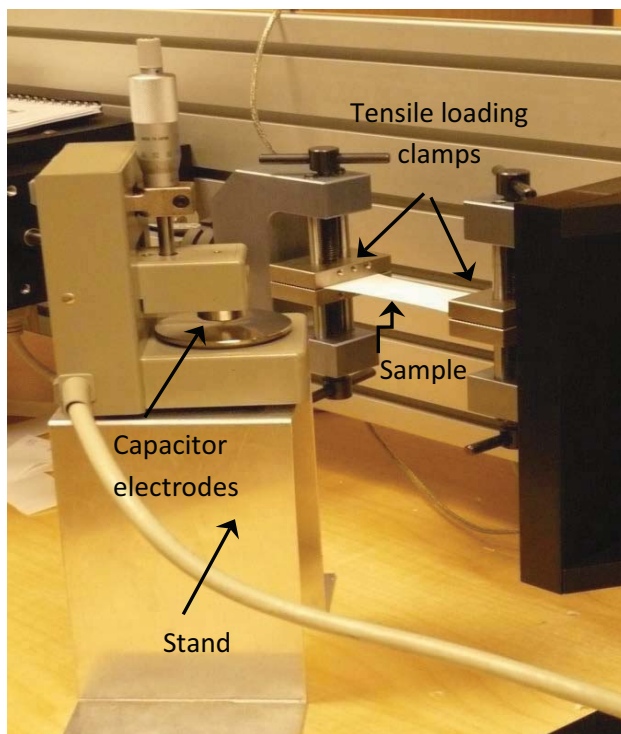


**Figure 48** Experimental arrangement for permittivity measurement while the sample is under tensile strain, using an Agilent E4980A LCR meter and Test Resources, Inc. tensile load frame Model 150Q250.

To explore the potential effect of strain rate, strains of 50, 100, and 150% were achieved by strain rates of 12.7 and 25.4 mm/min, respectively. Other strains studied were achieved by strain rate 25.4 mm/min. Once the assigned strains were reached, dielectric permittivity of all stretched samples was measured at their centers, at which they were most reliably stretched to the desired strain with assigned strain rate. The initial dielectric permittivity of each sample was measured at 100 kHz prior to application of tensile strain.

Additionally, to study the effect of stress relief, samples with strains of 50, 100, and 150% were held in the tensile loading frame for up to 24 hours, and their in-situ permittivity was measured at times  $t = 1, 2, 4, 6,$  and 24 hours, respectively. Finally, the load was released and permittivity of all the samples was immediately measured again, to explore the effect of recovery of the polymer chains.

X-ray Diffraction (XRD) was conducted to examine possible structural changes in PTFE as a consequence of tensile strain, in order to explore the mechanism by which mechanical strain influences the permittivity of PTFE.

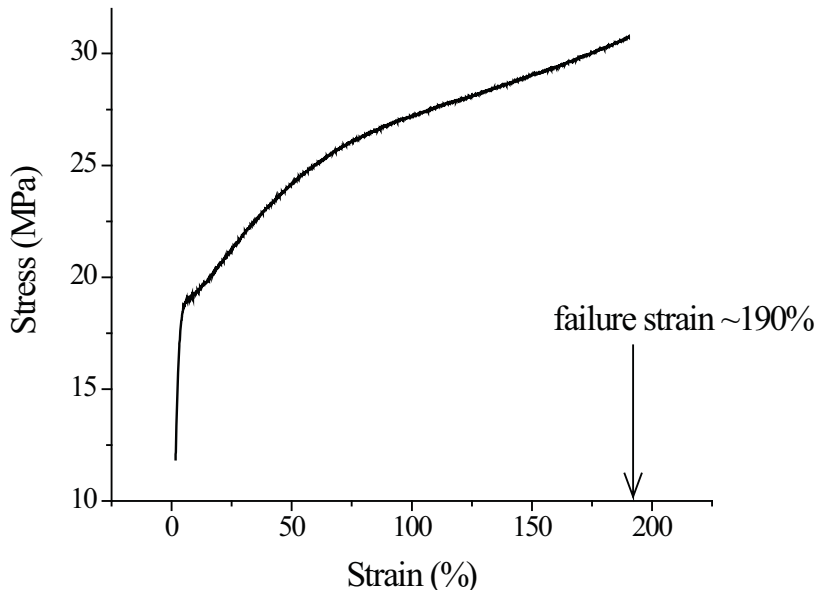


**Figure 49** Engineering stress-strain curve of PTFE.

## Results and discussion

Figure 50 shows the difference between the real relative permittivity of strained and unstrained PTFE,  $\Delta\epsilon_r$ , as a function of mechanical strain. The real permittivity of PTFE decreases with increasing tensile strain, e.g. by approximately 19% for 150% strain. As stated in Chapter II, a dielectric material exhibits some or all of the four polarization mechanisms: atomic, ionic, dipolar and interfacial polarization [74]. Given that PTFE is a non-polar semicrystalline polymer, its real permittivity is associated with only two polarization mechanisms: atomic polarization due to a shift of the electron clouds in each atom under the influence of the applied electric field and interfacial polarization due to accumulation of free charges at interfaces between the amorphous and crystalline polymer phases [74]. The observed decreases in the real permittivity of PTFE therefore may in principal be as a result of decrease in either atomic polarization or interfacial polarization, or both. Atomic polarization as defined above, however, cannot be influenced by mechanical strain. On the other hand, according to the Fringed Micelle Model [76], the chains of a polymer under mechanical load increase their alignment along the direction in which the load is applied, hence increasing the degree of alignment in the amorphous phase and producing a greater degree of crystallinity. Thus, it is hypothesized here that the interfacial polarization of PTFE declines under mechanical strain due to decreased mobility of free charges, as a result of increased ordering of the polymer chains.

To investigate this hypothesis, the degree of crystallinity of samples with tensile strains of 50, 100 and 150% was determined by XRD, immediately upon removal of the polymer samples from the load frame. It was observed that the degree of crystallinity increases, overall, with mechanical strain, as listed in Table 13. The XRD spectra also revealed that the crystal structure of strained PTFE at room temperature is hexagonal, the same as that of un-strained PTFE [64].

After the samples were released from the tensile loading frame, their permittivity was immediately measured and observed to recover somewhat, increasing by up to 8% as shown in Figure 51, suggesting partial recovery of the polymer chains. It is reasonable to conclude that the decrease in the real permittivity of PTFE is associated with increased ordering of the polymer chains in the presence of mechanical strain.

The potential effect of stress relief was investigated by measuring permittivity on samples strained to 50, 100 and 150% for 24 hours. Permittivity was measured at times  $t = 1, 2, 4, 6,$  and 24 hours. No significant change in measured permittivity was observed as a function of time up to 24 hours. Finally, the permittivity of PTFE stretched with strain rate of 25.4 mm/min was observed to be quantitatively similar to that of PTFE stretched to the same strain with half the strain rate, 12.7 mm/min. Thus, within the range of stresses and strains studied here, it is concluded that there is no obvious influence of stress relief and strain rate on the permittivity of strained PTFE.

**Table 13** Crystallinity of PTFE for various values of tensile strain, measured by X-ray diffraction immediately upon removing the sample from the tensile tester.

<b>Tensile strain (%)</b>	<b>Degree of crystallinity (%)</b>
0	$36 \pm 3$
50	$42 \pm 3$
100	$42 \pm 3$
150	$47 \pm 3$

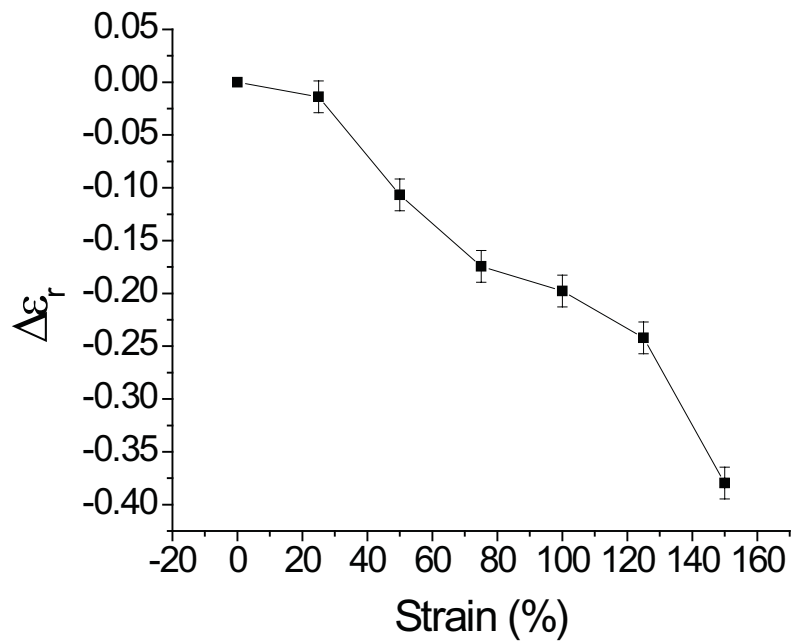


**Figure 50** The change in the real relative permittivity of PTFE as a function of tensile strain. Note,  $\epsilon_r = 2.076$  at 0% strain.

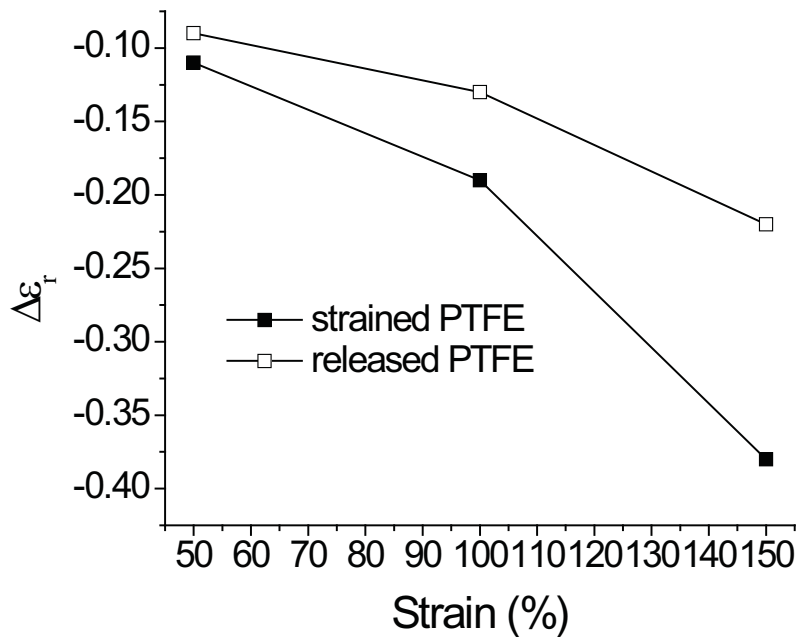


**Figure 51** The difference between the real relative permittivity of PTFE under strain (solid symbol) and of released PTFE (open symbol), compared with untreated PTFE.

## 5. *Summary*

Thermal degradation of PTFE is considered as a single step autocatalytic reaction. Thermal exposure studies on PTFE show increase in real permittivity by approximately 2% following isothermal heating at 340 °C for 96 hr. This observation is associated with increase in crystallinity (from 29% in an as-received sample to 35% in a sample isothermally heated at 340 °C for 96 hr) that enhances the interfacial polarization between the amorphous phase and crystal phase of the polymer. On the other hand, in the presence of mechanical loading, polymer chains of PTFE are oriented along the direction of loading, which limits motion of free charges and thereby weakens the interfacial polarization. Consequently, the real permittivity of PTFE measured transverse to the direction of the applied load was observed to decrease with applied load; by approximately 19% for engineering strain of 150%. An associated increase in the degree of crystallinity with increasing tensile strain was measured (from 36% in an as-received sample to 47% in a sample with engineering strain 150%), supporting the hypothesis that limited motion of free charge carriers is responsible for the observed reduction in permittivity transverse to the applied load direction. Upon removal from the load frame, the oriented polymer chains of PTFE recovered to some extent, as indicated by an associated increase in the permittivity by up to 8%. On the other hand, the strain rate by which the PTFE samples were stretched to various strains and the stress relief process investigated while the PTFE samples were held at constant strain for up to 24 hr did not change the real permittivity of PTFE significantly.

It is interesting that, in the case of thermal exposure, an increase in crystallinity of approximately 6% is observed along with a modest *increase* in permittivity (up to 2%) in thermally exposed samples for the conditions studied whereas, for strained samples, an increase in crystallinity of approximately 11% is observed along with a larger (up to 19%) *reduction* in permittivity. It should be noted that value of crystallinity is not the primary factor in determining interfacial polarization relaxation intensity (and therefore permittivity). For example, a study on poly(ether ether ketone) [77] concluded that the nature and degree of perfection in the crystallized regions play a more dominant role in determining the dielectric properties of the polymer. The degradation mechanisms studied here (thermal exposure and mechanical stress) likely give rise to crystallizations that are significantly different from each other in nature and degree of perfection. Thus, the trends in the measured values of crystallinity and in the permittivity for each of the degradation mechanisms described above are likely not in conflict but rather explained by significant differences in the crystal nature of those samples.

## Chapter IV. Ethylene-tetrafluoroethylene (ETFE)

ETFE (ethylene-tetrafluoroethylene) has been applied as the only wiring insulation material in Boeing 747, 767 and 777 aircraft since the 1990s. This chapter describes an investigation of the way in which the real permittivity and loss factor of ETFE change after thermal exposure in air for up to 96 hours.

### 1. Introduction

Ethylene-tetrafluoroethylene (1:1 ratio) alternating copolymer  $(-\text{CH}_2\text{CH}_2\text{CF}_2\text{CF}_2-)_n$  is a fluoroplastic material. At room temperature, it has a molecular conformation in which extended zigzag chains are packed in orthorhombic cells with cell dimensions  $a = 0.96$  nm,  $b = 0$  nm,  $c = 0.50$  nm and  $\gamma = 96^\circ$  [57]. Each molecule is adjacent to four other molecules in which the  $-\text{CH}_2-$  groups of a chain are positioned next to the  $-\text{CF}_2-$  groups of the next chain [78]. Essentially, the bulky  $-\text{CF}_2-$  groups nestle into the space above the smaller  $-\text{CH}_2-$  groups of an adjacent chain [79], interlocking the chains as a result. Due to this special chain conformation, ETFE has desirable properties such as a stable dielectric constant, low dissipation factor, high melting temperature and high elastic modulus. Selected physical and electrical properties of ETFE taken from the literature are listed in Table 14.

Reference [57] has presented the dielectric constant of ETFE over the frequency range from 1 kHz to 10 GHz at 22 °C and 150 °C. At room temperature, the dielectric constant of ETFE is between 2.5 and 2.6 below 10 MHz and decreases to approximately 2.3 at 10 GHz. Change in dielectric constant due to temperature can also be observed, especially at high frequencies. The dissipation factor of ETFE is less than 0.001 below 10 kHz, increasing to 0.023 at 100 MHz and decreasing at higher frequencies [57].

Table 14 Properties of ETFE.

Property	Value	Property	Value
Density (g/cm <sup>3</sup> )	1.75-1.79	Dielectric constant	2.5-2.6 below 10 MHz
Melting Temperature (°C)	255-280	Dissipation factor	Less than 0.007 below 1 MHz
Molecular relaxation temperatures (°C)	~ 110 ( $\alpha$ ) 0-100 ( $\alpha'$ ) ~ -87 ( $\gamma$ )	Dielectric strength (kV/mm)	64 (254 $\mu\text{m}$ film)

## 2. *Sample material*

The ETFE samples studied here were discs nominally 1 mm thick and 63 mm in diameter, which were extruded from Tefzel 750® ETFE pellets supplied by Dupont. The heat flow and storage modulus as a function of temperature on samples cut from different spots of the extruded discs were measured by DSC (Differential Scanning Calorimeter) and DMA (Dynamic Mechanical Analysis), respectively. Good homogeneity in thermal and mechanical properties of the extruded samples was verified, as shown in Figures 52a and 52b.

The storage modulus  $E'$ , loss modulus  $E''$  and  $\tan \delta$  of extruded ETFE from -150 °C to 180 °C at 1 Hz was measured by DMA, as shown in Figure 53. The storage modulus is 868 MPa at 25 °C, and 57.5 MPa at 150 °C. The  $\tan \delta$  curve reveals three molecular relaxations at 86.0, approximately 50, and -98.1 °C, analyzed by the software 'TA Universal Analysis'. The relaxation at 86.0 °C is the  $\alpha$ -relaxation, which has been attributed to the glass transition that occurs in the amorphous phase [17]. The relaxation at approximately 50 °C is attributed to the  $\alpha'$ -transition that is related to a reversible crystal transformation from the orthorhombic to the hexagonal lattices. This transformation occurs gradually over a broad temperature range (0 to 100 °C). In some ETFE, this transition is ill-defined and can be better described as a transition from pseudo-hexagonal to a hexagonal crystal phase [12]. The peak at -98.1 °C is associated with the  $\gamma$ -transition.

The real permittivity and loss factor of extruded ETFE was measured over the frequency range 1 Hz to 1 MHz and the temperature range -150 °C to 210 °C by the Novocontrol Dielectric Spectrometer. Three dimensional dependences of  $\epsilon'$  and  $\tan \delta$  are shown in Figures 54a and 54b, respectively. The highest values of  $\epsilon'$  and  $\tan \delta$ , observed at low frequency (below ~10 Hz) and high temperature (above ~200 °C) may be due to one or more extrinsic or intrinsic electrical phenomena, such as electrode polarization, interfacial polarization and conductivity effects [80].

Extracting data from Figure 54, the dependence of  $\epsilon'$  and  $\tan \delta$  on temperature at 1.15 kHz are shown in Figure 55. Two peaks in the loss factor of ETFE at -80 °C and 92 °C are observed. These are associated with  $\gamma$ - and  $\alpha$ -transitions respectively [81]. The two peak temperatures are close to the transition temperatures listed in Table 14, -87 °C and 110 °C. The differences in these values are likely due to measurement of different material properties by different equipment on slightly different samples.

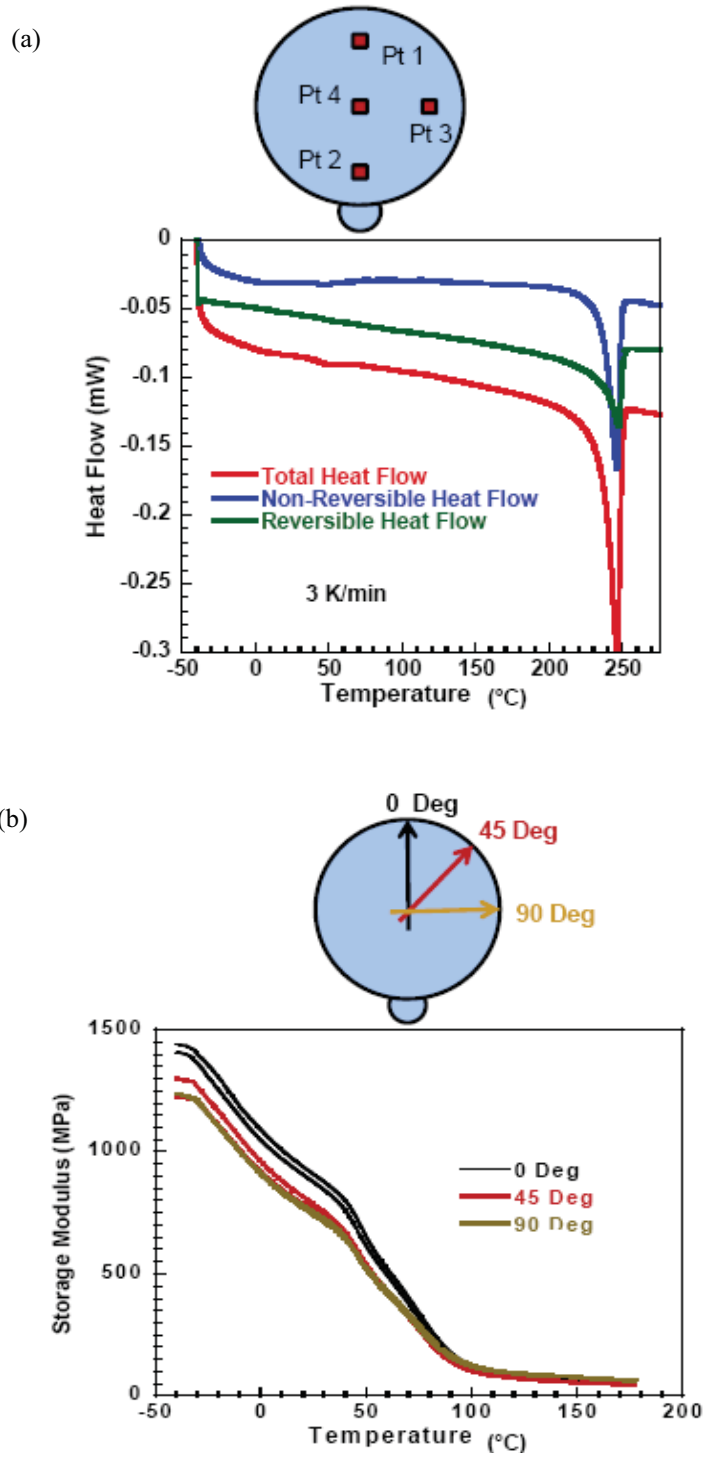
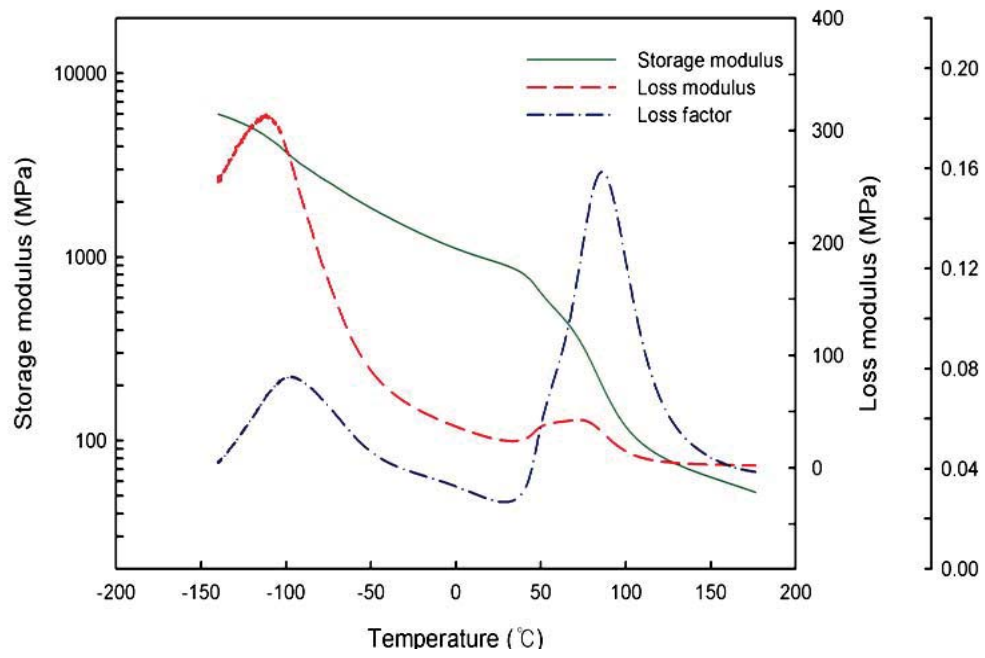
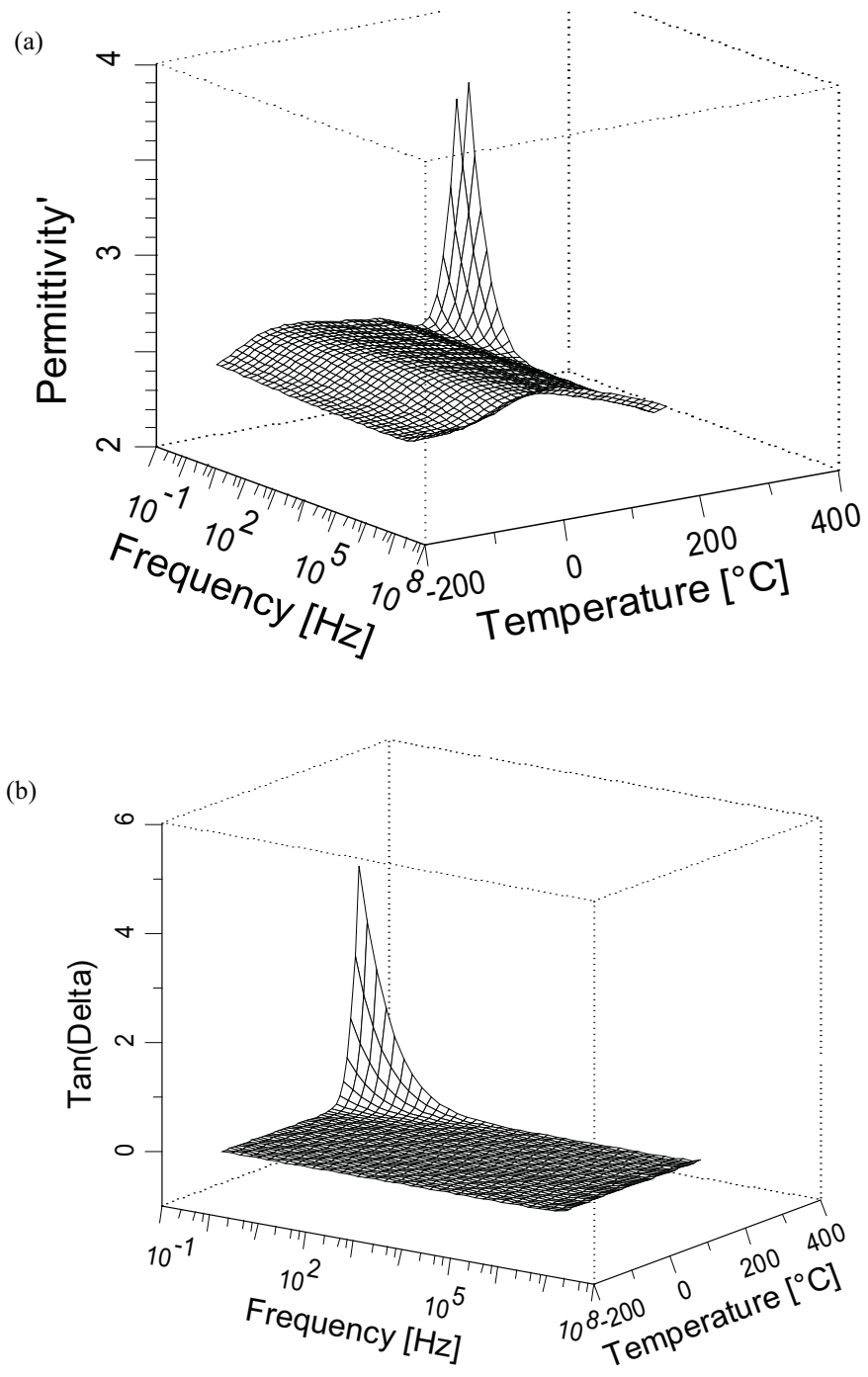


Figure 52 Homogeneity of extruded ETFE by (a) DSC; (b) DMA.



**Figure 53** Results of dynamic mechanical analysis on extruded ETFE.



**Figure 54** Real permittivity (a) and loss factor (b) of extruded ETFE as a function of frequency and temperature.

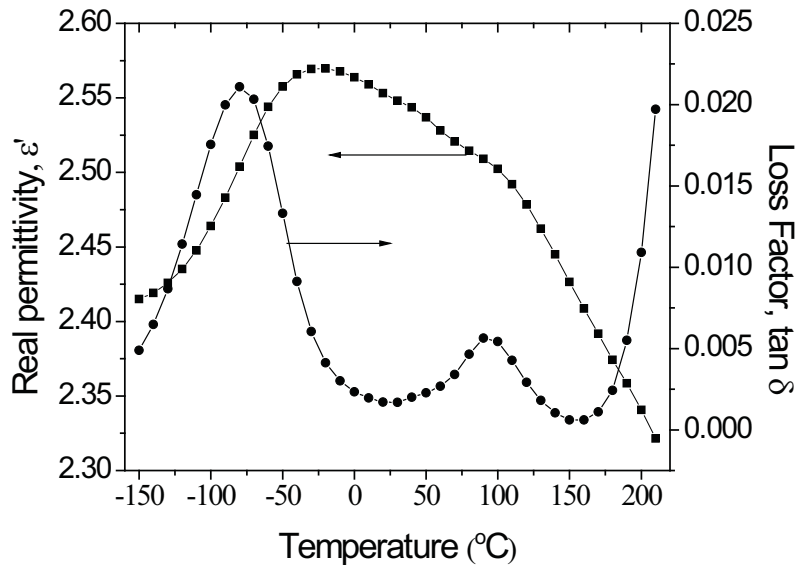


Figure 55 Real permittivity and dissipation factor of extruded ETFE as a function of temperature at 1.15 kHz.

### 3. Thermal degradation

#### Thermal degradation kinetics

##### Method and experiment

The kinetics of thermal degradation of ETFE was studied by using the method for studying PTFE. The extruded ETFE was cleaned prior to experimental testing with a Kim Wipe and ethanol to remove any oils or dusts on the sample that might affect the weight and degradation of the material. Each test sample was removed from the disk through a circular punch ensuring reproducible sample weight and shape. The sample masses were  $8.7 \pm 0.2$  mg. To reduce sample variability, the samples were chosen from the lower third of the extruded disk.

Expounding the kinetic analysis from a single-step reaction (described in Chapter III) to a consecutive multistep reaction, the differential equations are as follows:

$$\frac{da}{dt} = -f(a, b)A_1e^{-E_1/RT} \quad (48)$$

$$\frac{db}{dt} = -\frac{da}{dt} - f(b, c)A_2e^{-E_2/RT} \quad (49)$$

$$c = 1 - a - b = \alpha \quad (50)$$

where the reaction follows an  $A \rightarrow B \rightarrow C$  model [82] [83]. The rate of reaction for the degradation from  $A \rightarrow B$  (step 1) is given by  $da/dt$ . The rate of reaction for the degradation from  $B \rightarrow C$  (step 2) is given by  $db/dt$ . In this format of differential equations  $a$ ,  $b$ , and  $c$  are analogous to concentrations in chemical kinetics and  $A$ ,  $B$  and  $C$  represent degradation states; where state  $A$  corresponds to  $a = 1$ ,  $b = 0$  and  $c = 0$ , state  $B$  corresponds to  $a = 0$ ,  $b = 1$  and  $c = 0$ , and state  $C$  corresponds to  $a = 0$ ,  $b = 0$  and  $c = 1$ . The degradation continues to follow the analogy of chemical kinetics, where step 2 follows step 1, but may occur before complete conversion of  $a$  to  $b$ .

### *Results and discussion*

The TG scans for ETFE began at room temperature, and degradation was not observed in either system until elevated temperatures were reached. The high temperature TG data is given in Figure 56. Like most fluoropolymers, ETFE is extremely stable at intermediate temperatures. The onset of degradation increases with increasing heating rate and involves a rapid and complete degradation. From the TG curves, the variation between the temperatures of the degradation onset points provides insight into the reaction model. For ETFE, the separation between the temperatures of the degradation onset points increases between curves as the heating rate increases. This indicates a consecutive step reaction model. Whereas, a decreasing separation between the degradation onset points as the heating rate increases indicates a competitive model.

The derivative of the weight with respect to temperature provides better insight into the mechanism of degradation. For a specific heating rate, the number of peaks in the derivative thermogram (DTG) represents the minimum number of reaction steps involved. For ETFE, it is clearly seen at  $2 \text{ Kmin}^{-1}$  that there are two distinct peaks. At slow heating rates, the reaction is dominated by a specific mechanism; however, as the heating rate increases, this dominating mechanism is replaced with an alternative mechanism at higher heating rates. Figure 57 shows the two mechanisms in the DTG curves. Based on the DTG curves below, heating at  $2 \text{ Kmin}^{-1}$ , a minimum of two reaction steps, or two peaks, can be seen.

Once initial observations of the thermograms have been made, a Friedman analysis based on equation 6 provides information about multi-step processes during the reaction and also offers insight into the type of reaction step. Similar to the DTG plots, the number of peaks indicates the minimum number of reaction steps in the degradation. For ETFE there are two distinct overlapping peaks seen in Figure 58. Therefore a multi-step reaction is again evident from the curvature of the plot for ETFE.

The type of the reaction can also be determined by comparing the slope of the constant fractional mass loss trend line to the slope of each peak at the beginning of the reaction step [21]. For ETFE, the first peaks have in all cases the acceleration, probably autocatalysis. For autocatalysis, the generic governing differential equation, presented in equation 2, defines the reaction model,  $f(\alpha)$ , such that:

$$f(\alpha) = (1 - \alpha)^n(1 + K_{\text{cat}}X) \quad (51)$$

where  $\alpha$  represents the degree of degradation,  $n$  represents the reaction order,  $K_{\text{cat}}$  represents the autocatalysis constant, and  $X$  represents the step of the reaction.

From the Friedman analysis as well as the Ozawa-Flynn-Wall analysis, activation energy as a function of fractional mass loss can be obtained [18] [19] [27]. The plot of the activation energy for ETFE with respect to the amount of degradation again confirms the multistep reaction by presenting fluctuating activation energy seen in Figure 59. This indicates an overlap of multiple reactions. Activation energy developed from Friedman analysis presents activation energies between 140 kJ/mol and 210 kJ/mol.

To verify the two-step model the TG curves, DTG curves, Friedman Analysis, and activation energies suggested, a two-step consecutive model was introduced to (a) the two slowest heating rates and (b) the two fastest heating rates—seen in Figure 60. Table 15 presents the corresponding model parameters. The difference between the parameters, primarily the activation energies, indicates the two-step model is an insufficient model for predicting thermal degradation and indicates another step must be involved. Additionally, the model fit of the slow heating rate DTG seen in Figure 61 identifies a poor fit at the end of the reaction and this difference between model and experimental data indicates an additional step required.

Consequently, a three-step consecutive model was used. The model fit is presented in Figure 62. Table 16 presents the corresponding model fitting parameters. The activation energy for the first step in the final model is the same as the activation for the two-step fit of the slow thermograms. This means that the first step of the final model is the deciding step for the initial part of the degradation reaction. The second step is a secondary process for that deciding step. This secondary process is responsible for large temperature separation of the degradation onset points at high heating rates in Figure 56. This second step, a coupling step, should not be considered separately from the first step. The third step in the three-step consecutive model is responsible for the second DTG peak, or the final stages of the degradation process for both the slow and fast heating rates.

However, comparing the three step consecutive reaction to three-step competitive reactions, an F-test shows that the consecutive reaction fits the data better. See Table 17 for F-test comparison and a schematic representation of the different models.

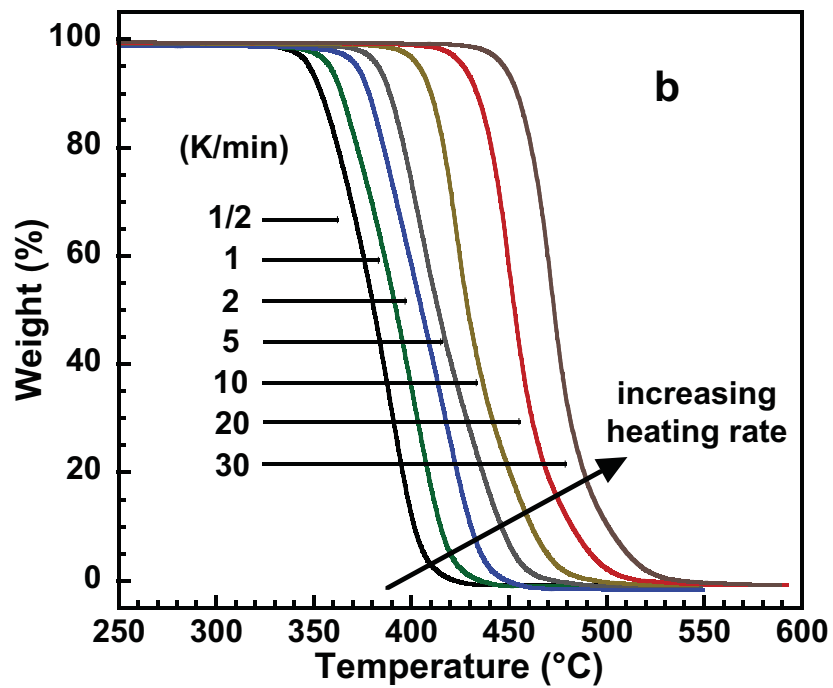


Figure 56 TG curves for ETFE.

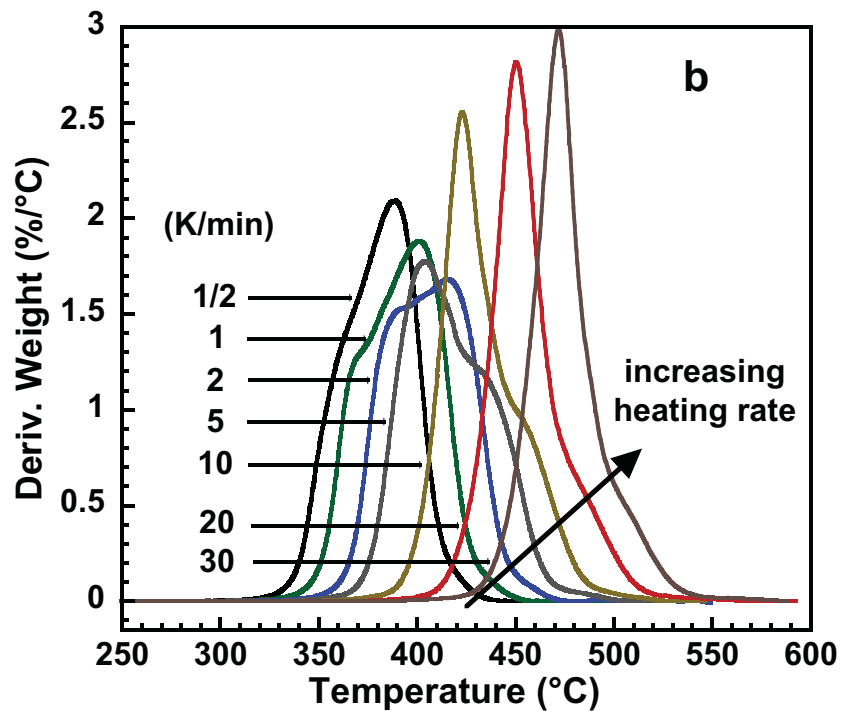


Figure 57 DTG curves for ETFE.

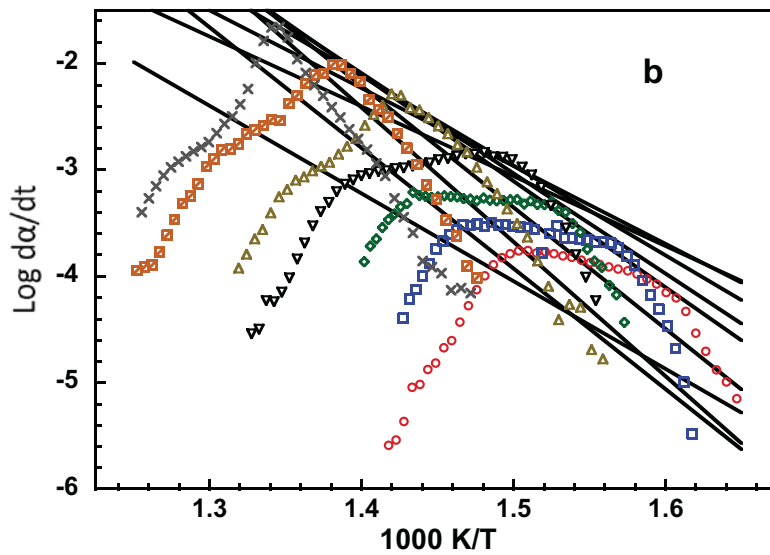


Figure 58 Friedman Analysis for ETFE.

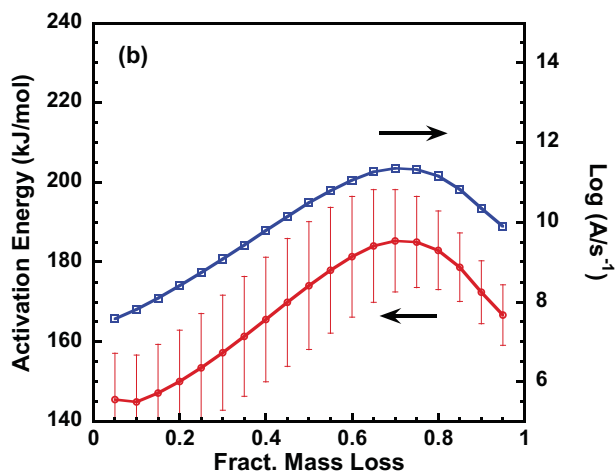
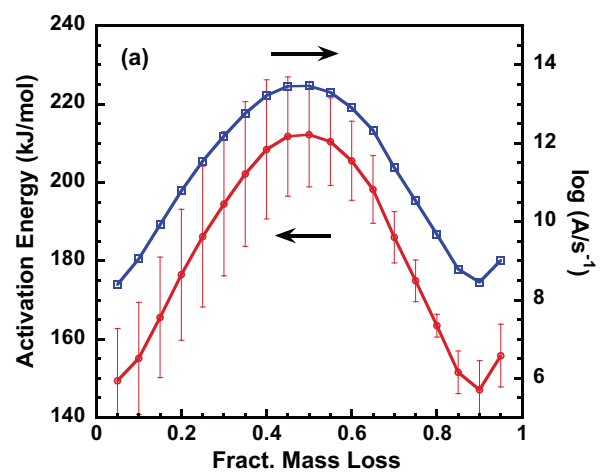


Figure 59 Activation energy from (a) Friedman Analysis and (b) Ozawa-Flynn-Wall Analysis.

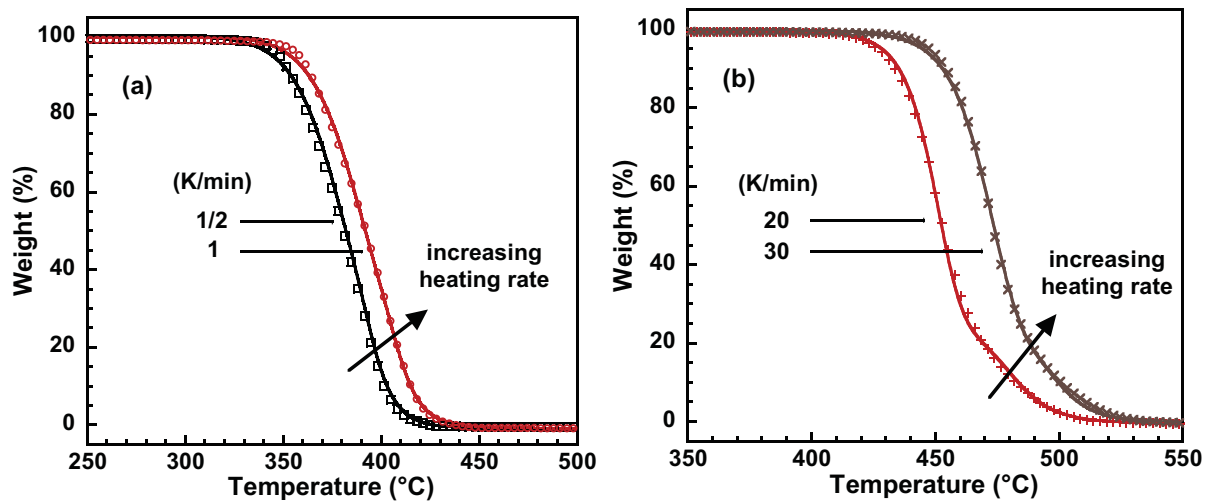


Figure 60 Two-step consecutive model fits to (a) the two slowest heating rates and (b) the two fastest heating rates.

Table 15 Reaction parameters for two-step consecutive model fits for ETFE.

		Activation Energy (kJ/mol)	Log (A1/s-1)	Reaction Order	Log (Kcat)
Slow Heating	Step 1	246.26	16.47	1.97	1.26
	Step 2	181.84	11.02	0.96	-0.56
Fast Heating	Step 1	79.30	1.34	0.71	3.15
	Step 2	103.52	5.48	1.02	-4.00

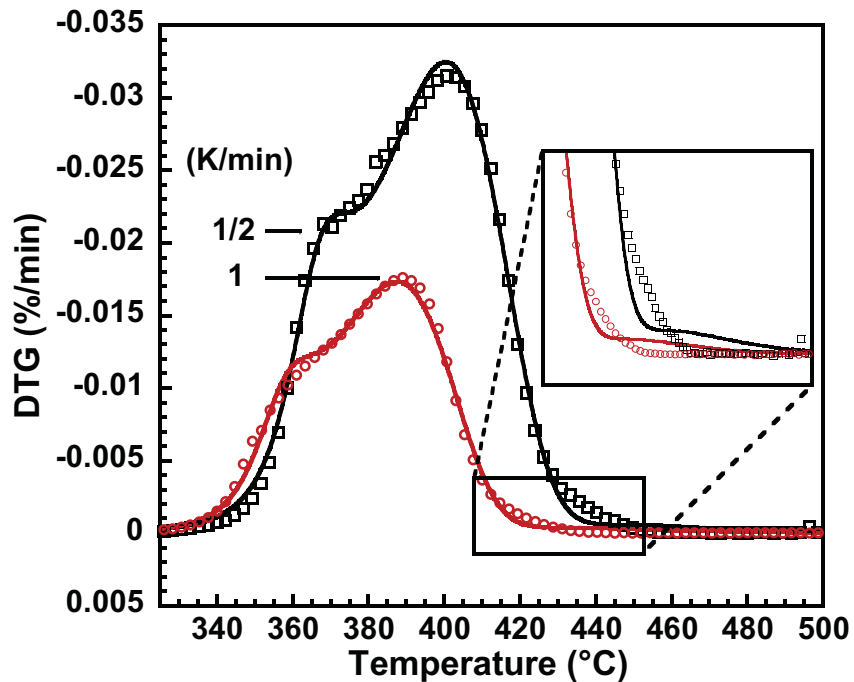


Figure 61 DTG model fit of the two slowest heating rates for ETFE.

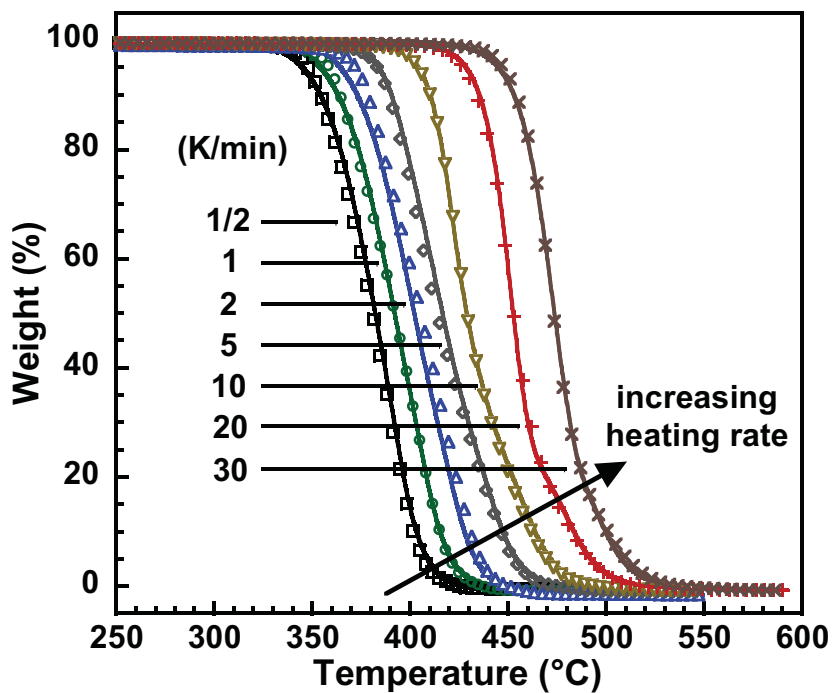


Figure 62 Model of the best fit TG data for the three-step reaction models in air atmospheres. In the plots, the curves represent the model, the data point shapes represent the modeled experimental data, and the + represents the un-modeled experimental data.

**Table 16** Reaction parameters for the three-step consecutive model fit.

	Activation Energy (kJ/mol)	Log (A1/s-1)	Reaction Order	Log (K <sub>cat</sub> )
<b>Step 1</b>	247.25	16.55	1.48	-0.59
<b>Step 2</b>	0.03	-3.50	0.74	2.34
<b>Step 3</b>	123.03	6.38	1.37	0.63

**Table 17** F-Test statistical analysis of the model fits for three-step reactions for ETFE\*.

Consecutive Reaction	Competitive Reaction 1	Competitive Reaction 2	Competitive Reaction 3
A → B → C → D	A → B → C ↓ D	A → B ↓ C ↓ D	A → B ↓ C → D
1.0	1.78	11.69	57.24

\* F<sub>critical</sub> = 1.02

### Effect of thermal exposure on permittivity

#### Experiment

Prior to thermal exposure, extruded ETFE discs were annealed isothermally at 60 °C in another isotemp muffle furnace for 2 hr prior to thermal exposure. The annealing was done in order to relieve residual stress that resulted from the extrusion process and flatten the samples for permittivity measurement. When cooled completely, annealed discs were subjected to thermal exposure at 160 ± 2 °C for 2, 6, 12, 24, 36, 48, 60, 72, 84 and 96 hr. The temperature 160 °C, much lower than the melting temperature of 245 °C, was chosen due to significant sample deformation after thermal exposure at higher temperatures that prevented successful permittivity measurement. Three discs were exposed for each exposure time.

During the exposure process, all the samples were sandwiched between two stainless-steel plates with mirror finish, to inhibit distortion. After the furnace was turned off, doors of the furnaces were not opened until all exposed ETFE samples were naturally cooled down in situ. Once the samples were completely cool, after 48 hr, their permittivity was measured at room temperature over the frequency range 1 kHz to 2 MHz. Permittivity of as-extruded ETFE and annealed ETFE samples were also measured to provide comparative data.

#### Result and discussion

Values for  $\epsilon'$  and  $\tan \delta$  of both extruded and annealed ETFE samples are compared in Figure 63. The  $\epsilon'$  of extruded ETFE decreases from 2.599 to 2.539 as frequency increases from 1 kHz to 2 MHz. Loss

factor,  $\tan \delta$ , increases over this frequency range but is small (below 0.007) even at 2 MHz. These results agree with the values listed in Table 13. It can be observed that  $\epsilon'$  of extruded ETFE and annealed ETFE are similar over the frequency range measured and  $\tan \delta$  overlaps closely until above 1 MHz. (The separation below 20 kHz is due to large uncertainty in the measurements for low frequencies.) It can be concluded that the annealing process at 60 °C for 2 hr does not influence the dielectric properties of ETFE significantly and it is reasonable to anneal the samples prior to thermal exposure at 160 °C for up to 96 hr, for the purpose of relieving residual stress.

Figures 64 and 65 show how thermal exposure duration influences  $\epsilon'$  and  $\tan \delta$ , respectively, of ETFE at four frequencies. Since the measurement uncertainty in  $\tan \delta$  is quite large below 20 kHz,  $\tan \delta$  at 1.00 and 10.6 kHz are not shown in Figure 65. Figure 64 shows how thermal exposure time influences  $\epsilon'$  of ETFE at four frequencies. As exposure time increases up to 96 hr,  $\epsilon'$  increases by 0.05 (approximately 2%, which is significantly larger than the standard deviation between measurements on three nominally identical samples, 0.5%). From Figure 65,  $\tan \delta$  is not changed significantly by thermal exposure at 112 kHz. At 1.18 MHz, however,  $\tan \delta$  decreases by 11% after thermal exposure for 96 hr.

XRD tests conducted on annealed ETFE and ETFE thermally exposed at 160 °C for both 48 hr and 96 hr indicated that the degree of crystallinity,  $0.65 \pm 0.01$ , was not changed by thermal exposure. This is in accordance with results presented in reference [84].

On the other hand, mid-infrared (IR) analysis on annealed ETFE and ETFE thermally exposed at 160 °C for 96 hr has revealed chemical changes in ETFE following thermal exposure. The absorbance spectra are shown in Figure 66. Similar peaks corresponding to the presence of  $\text{CF}_2$  at  $1460 \text{ cm}^{-1}$ , and C–H at  $2850 \text{ cm}^{-1}$  and  $2890 \text{ cm}^{-1}$  are observed in both spectra. However, the spectrum of thermally-exposed ETFE contains an extra peak at  $1680 \text{ cm}^{-1}$ , corresponding to the C=O group, and a much higher and broader –OH peak at  $3450 \text{ cm}^{-1}$ . These indicate that chemical changes occurred during thermal exposure of ETFE, including oxidation and dehydrofluorination [85]. Oxidant thermal exposure accompanied by chain breakage and polar group formation can increase dielectric permittivity of polymers by enhancing their charge carrier mobility. It has been reported [86] that chain breakage can decrease polymer viscosity by reducing average molecular weight, which increases the charge carrier mobility. The formation of polar groups can also promote the charge carrier mobility in ETFE. The decrease in  $\tan \delta$  at 1.18 MHz, shown in Figure 65, is also attributed to the additional polar groups formed during thermal exposure [87].

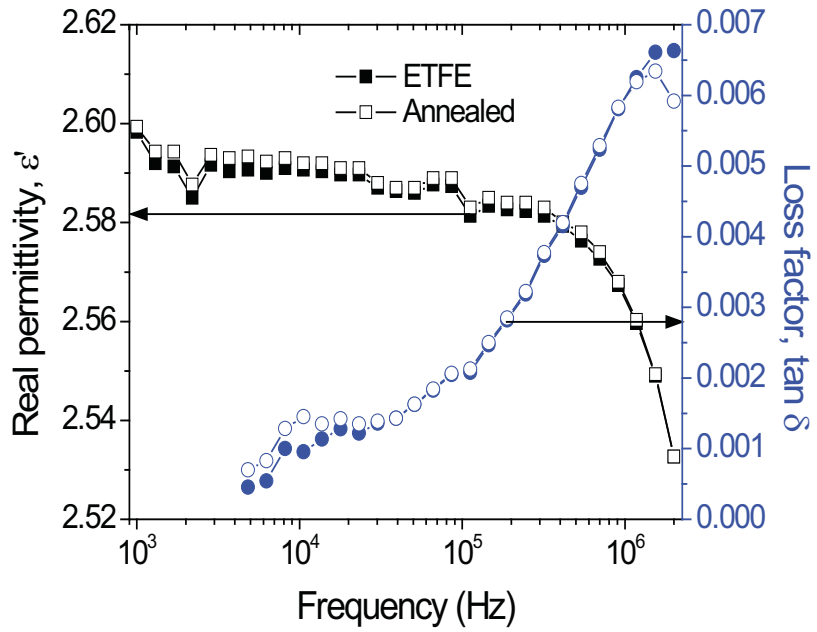


**Figure 63** Real permittivity and dissipation factor of extruded and annealed ETFE as a function of frequency at room temperature.

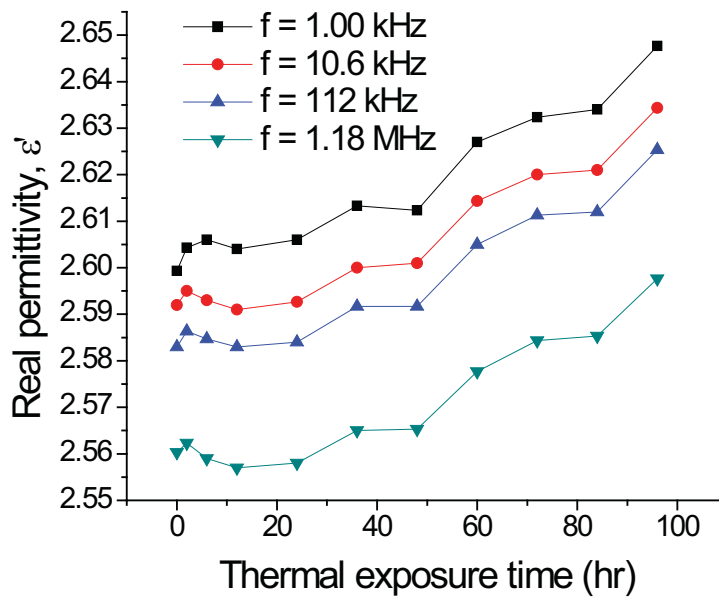


**Figure 64** Real permittivity of ETFE as a function of thermal exposure time at 160 °C.

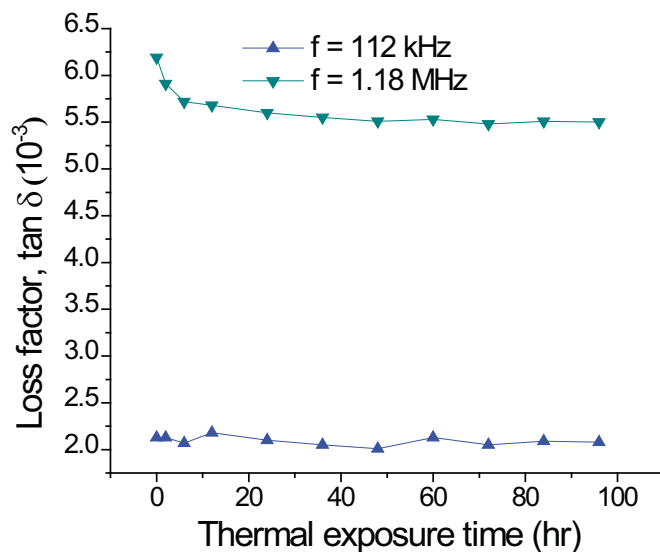


**Figure 65** Dissipation factor of ETFE as a function of thermal exposure time at 160 °C.

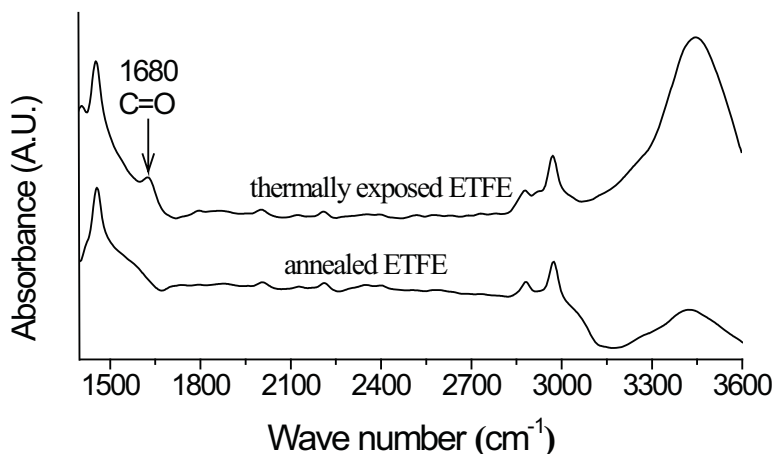


**Figure 66** Mid-IR spectra of annealed ETFE and ETFE thermally exposed at 160 °C for 96 hr.

#### 4. *Summary*

The thermal degradation of ETFE is considered as a three-step consecutive reaction model with each step governed by an autocatalysis reaction model. After thermal exposure at 160 °C for 96 hr in air, approximately 2% increase in the real permittivity and 11% decrease in the loss factor of ETFE are observed. These observations are considered as a result of oxidation and dehydrofluorination during the heating process, which give rise to formation of polar groups.

## **Chapter V. Development of a Capacitive Sensor for Nondestructive Evaluation of Wiring Insulation**

Curved patch capacitive sensors have been developed to evaluate the material dielectric properties of cylindrical structures. These sensors consist of two curved patch electrodes that are coaxial with and exterior to the cylindrical test-piece. Description on the development of capacitive NDE sensor in this chapter is divided into three parts. In part 1, a numerical model that relates the permittivity of a homogeneous dielectric rod to the capacitance of a curved patch sensor is described. Experimental results that verify the validity of the numerical model are provided. In part 2, a numerical model that relates the permittivity of a cylindrical dielectric-coated conductor to the capacitance of a curved patch sensor is described, together with benchmark experiment results that verify the theory. In the last part of this chapter, a prototype capacitive sensor has been fabricated and applied for dielectric property measurements of aircraft wires (wire type MIL-W-81381/12). Groups of wires have been exposed to different thermal and hydrolytic environments. Experimental studies using the prototype capacitive sensor showed that, thermal and hydrolytic exposure induced dielectric property changes in this type of wire insulation have been successfully detected.

### ***1. Analysis of a capacitive sensor for the evaluation of circular dielectric cylinders***

An arc-electrode capacitive sensor has been developed for the quantitative characterization of permittivity of cylindrical dielectric rods. The material property of the cylindrical test-piece can be inversely determined from the sensor output capacitance based on a theoretical model. For the modeling process, the electrostatic Green's function due to a point source exterior to a dielectric rod is derived. The sensor output capacitance is calculated numerically using the method of moments (MoM), in which the integral equation is set up based on the electrostatic Green's function. Numerical calculations on sensor configuration optimization are performed. Calculations also demonstrate the quantitative relationship between the sensor output capacitance and the test-piece dielectric and structural properties. Capacitance measurements on different dielectric rods with different sensor configurations have been performed to verify the validity of the numerical model. Very good agreement (to within 3%) between theoretical calculations and measurement results is observed.

### **Introduction**

Increasing demands for dielectric measurements have been observed over the past decade, with new applications of advanced composites in modern aircraft, automobiles, and shipbuilding. Specifically,

dielectric measurements are important for the characterization of thin films, substrates, circuit boards, printed-wiring boards, bulk materials, powders, liquids and semisolids.

Capacitance methods, because of their simplicity, relatively low cost, and high accuracy, have been applied to characterize the dielectric properties of many different materials. Over the past 100 years, closed-form solutions for capacitances due to various canonically shaped electrodes have been found, by mapping out the electrostatic field in the vicinity of the conductors. Canonical electrode shapes are those formed from surfaces easy to describe in standard coordinates, including strips, circular discs, annular rings, cylindrical arcs, spherical caps, etc.

It is convenient to solve capacitance problems associated with electrified strips using Cartesian coordinates. The capacitances for two parallel and coplanar infinite strips [106], as well as charged thin-strip quadrupoles [107], have been solved using the triple integral equations. In addition, the potential associated with a physically more realistic strip of finite length, the potential due to polygonal plates, and the potential due to a charged elliptical plate have been derived using dual integral equations in Cartesian coordinates [107].

Using cylindrical coordinates, the solution to dual integral equations has been applied to obtain the surface charge distribution of a charged disc in free space, and also to obtain the potential due to a circular disc placed between two parallel earthed planes [106]. The solution of the Fredholm equation has been applied to solve for the capacitance of an electrified disc situated inside an earthed coaxial infinitely long hollow cylinder. Also, the field due to two equal coplanar electrified discs has been solved by the method of Kobayashi potentials, while the capacitance between two identical, parallel and coaxial discs has been obtained by solving Love's integral equation. These solutions are available in the classic book written by Sneddon [106]. Furthermore, an axisymmetric problem of several charged coaxial discs has been considered by the dual integral equation method, and the solution has been obtained for the case when the distance between neighboring discs is large compared to their radii [108]. The potential of a system of  $N$  charged, arbitrarily located, circular discs has also been considered in [108]. Aside from classic problems associated with discs, Cooke's solution of a set of triple integral equations has been applied to solve for the field due to a charged annular ring of finite width in free space [106], while the solution to the integro-series equations has been applied to obtain the total charge for a capacitor that consists of a coupled disc and spherical cap [107].

Another set of canonical capacitance problems discussed in the literature are infinitely long axially slotted open cylinders. In [107], the capacitance generated by a pair of charged symmetrically or asymmetrically placed circular arcs has been calculated in circular cylindrical coordinates, whereas the capacitance due to a pair of charged symmetrically placed elliptic arcs has been solved in elliptic cylinder coordinates [107].

The canonical capacitance problems, mentioned above, are all discussed in free space situations, and need further modifications to be applicable for characterization of material dielectric properties. Other semi-analytical and numerical capacitive solutions have been developed over the past decade to keep pace with new applications of dielectric materials. For example, interdigital dielectrometry has been applied for material dielectric property characterization as one of the most commonly used capacitance sensors. An excellent review paper on interdigital sensors is [109], in which sensor modeling, fabrication, measurement setup, and applications are discussed in detail. In addition to a widely-used effective semi-analytical approach, called the continuum model [110], conformal mapping techniques have also been applied to obtain closed-form solutions for the capacitance of interdigital sensors in surface contact with multi-layered dielectric structures [111]. Examples of practical applications of interdigital sensors include estimation of meat fat content [112] and insulation damage detection in power system cables [113]. Multichannel fringing electric field sensors, designed by finite-element (FE) method calculations for sensor modeling, optimization and performance evaluation, have been used for material property measurements [114]. Cylindrical geometry electroquasistatic dielectrometry sensors have been developed using semi-analytical models to quantitatively relate the dielectric properties of multi-layered test-pieces to sensor output transcapacitance [115]. Concentric coplanar capacitive sensors for nondestructive evaluation of multi-layered dielectric structures have been developed in [116], and can be applied to detect water ingress and inhomogeneities in aircraft radome structures. In addition, rectangular coplanar capacitance sensors have been developed to detect water intrusion in composite materials [117] and for damage detection in laminated composite plates [118]. Rectangular capacitive array sensors that detect surface and subsurface features of dielectric materials have been developed in [119]. In [99], approaches of determining the length of open-circuited aircraft wires through capacitance measurements have been presented.

In this research, a model-based capacitive method is developed for the quantitative dielectric property characterization of circular cylindrical dielectric rods. The work is motivated by testing of cylindrical components such as wiring insulation or polymeric tubing, and will be developed to deal with those cases in future. The capacitance sensor consists of two arc-shaped patch electrodes that are located exterior to and coaxially with the cylindrical test-piece. These two sensor electrodes exhibit a measurable capacitance whose value depends on both the dielectric and geometrical properties of the dielectric rod. The arc-electrode configuration offers a nondestructive and convenient way of determining the dielectric constant of cylindrical test-pieces, compared to cutting a slice from the test-piece for a conventional parallel-plate capacitance measurement. A numerical method, the method of moments (MoM), is employed in the numerical calculations. First, the Green's function for a point source over the surface of a dielectric rod is derived in cylindrical coordinates, in the form of modified Bessel functions of the first

and second kinds of integer order  $n$ :  $I_n(z)$  and  $K_n(z)$ . This Green's function then serves as the integration kernel in MoM calculations, from which the sensor surface charge distribution is obtained. Once the sensor surface charge distribution is known, one can easily calculate the sensor output capacitance  $C$  through  $C = Q/V$ , where  $Q$  is the total charge on one electrode and  $V$  is the potential difference between the two sensor electrodes. Validation of numerical results by benchmark experiments has been performed, and very good agreement (to within 3%) between theoretical calculations and measurements is observed. The advantage of the arc-electrode capacitive sensor reported in this study, compared to existing planar capacitive sensors, is that the arc electrodes conform to the surface of a cylindrical test-piece and concentrate the electric field in the material under test. In addition, the physics-based model developed in this report allows inverse determination of test-piece permittivity from measured arc-electrode capacitance.

### **Modeling**

Figure 67 shows the configuration of the arc-electrode capacitive sensor. The capacitive sensor consists of two identical arc-electrodes coaxial with a cylindrical dielectric rod, and exhibits a measurable capacitance  $C$  that is quantitatively related to the permittivity and diameter of the material under test. In the theoretical modeling, the cylindrical dielectric rod is assumed to be infinitely long while the arc-electrodes are infinitesimally thin. The more general case in which the electrodes and the test-piece have different radii, as shown in Figure 67, is considered theoretically. However, in order to achieve maximum output capacitance, it is more desirable to have the sensor electrodes in tight contact with the cylindrical test-piece in measurements. One practical approach to achieving tight surface contact between the electrode and the test-piece is to deposit the sensor electrodes on a compressible dielectric material used as the sensor substrate, and press the substrate against the test-piece to conform the arc electrodes to the test-piece surface. This approach will be attempted in a future version of the sensor.

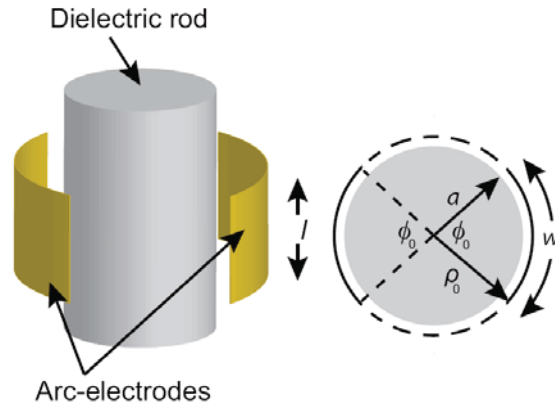


**Figure 67** Arc-electrode capacitive sensor. The radii of the sensor electrodes and the cylindrical dielectric rod are denoted  $\rho_0$  and  $a$ , respectively. The arc-angle of each sensor electrode is  $\phi_0$  (rad). The length of each electrode in the vertical direction is  $l$  and the width in the horizontal direction is  $w = \phi_0 \times \rho_0$ .

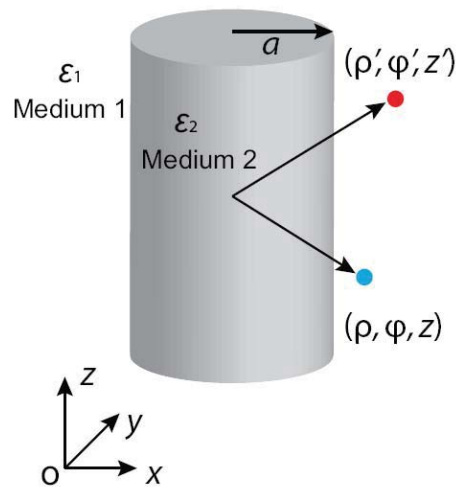


**Figure 68** Point source outside of a dielectric rod, assumed infinitely long.

### Derivation of Green's function in cylindrical coordinates

The electrostatic Green's function due to a point charge outside of an infinitely long dielectric rod is derived in cylindrical coordinates, to form the integral equations later used in MoM calculations. Figure 68 shows a point charge placed at  $(\rho', \phi', z')$  exterior to a cylindrical dielectric rod of radius  $a$  and dielectric constant  $\epsilon_2$ . Without loss of generality, the dielectric constant for the medium exterior to the dielectric rod is assumed to be  $\epsilon_1$ . The resulting potential  $\Psi(\rho, \phi, z)$  due to such a point charge satisfies the Laplace equation in each homogeneous region:

$$\left[ \frac{1}{\rho} \frac{\partial}{\partial \rho} \left( \rho \frac{\partial}{\partial \rho} \right) + \frac{1}{\rho^2} \frac{\partial^2}{\partial \phi^2} + \frac{\partial^2}{\partial z^2} \right] \Psi(\rho, \phi, z) = -\frac{1}{\rho} \delta(\rho - \rho') \delta(\phi - \phi') \delta(z - z'), \quad (52)$$

and is subject to the interface conditions at the surface defined by  $\rho = a$ :

$$\Psi^{(1)} = \Psi^{(2)} \quad \text{and} \quad \varepsilon_1 \frac{\partial}{\partial \rho} \Psi^{(1)} = \varepsilon_2 \frac{\partial}{\partial \rho} \Psi^{(2)} \quad (53)$$

where superscripts (52) and (53) correspond to the regions defined by  $\rho > a$  and  $0 < \rho < a$ , respectively.

To find a suitable solution, one starts with the fundamental solution of the Laplace equation in free space:

$$G_0(\mathbf{r} | \mathbf{r}') = \frac{1}{4\pi |\mathbf{r} - \mathbf{r}'|}, \quad (54)$$

where  $\mathbf{r}$  corresponds to the observation point at  $(\rho, \phi, z)$  and  $\mathbf{r}'$  corresponds to the source point at  $(\rho', \phi', z')$ . Using the integral [120]

$$\frac{1}{r} = \frac{2}{\pi} \int_0^\infty K_0(\kappa \rho) \cos(\kappa z) d\kappa, \quad (55)$$

where  $r = \sqrt{\rho^2 + z^2}$  and  $K_0(\kappa \rho)$  is the modified Bessel function of the second kind of order zero, one can rewrite the fundamental solution in cylindrical coordinates, which is convenient considering the cylindrical boundary surfaces of the problem. By using the addition theorem [120]

$$K_0(\kappa \xi) = I_0(\kappa \rho_<) K_0(\kappa \rho_>) + 2 \sum_{t=1}^{\infty} \cos[t(\phi - \phi')] I_t(\kappa \rho_<) K_t(\kappa \rho_>), \quad (56)$$

where  $\xi = \sqrt{\rho^2 + \rho'^2 - 2\rho\rho' \cos(\phi - \phi')}$ ,  $\rho_<$  is the lesser of  $\rho$  and  $\rho'$ , and  $\rho_>$  is the greater, (55) is transformed to an arbitrary coordinate system. The potential at an observation point  $(\rho, \phi, z)$  due to a source point at  $(\rho', \phi', z')$  in free space is expressed as

$$G_0(\mathbf{r} | \mathbf{r}') = \frac{1}{2\pi^2} \times \left\{ \int_0^\infty \tilde{G}_0(\rho, \rho', \kappa) \cos[\kappa(z - z')] d\kappa + 2 \sum_{t=1}^{\infty} \cos[t(\phi - \phi')] \int_0^\infty \tilde{G}_t(\rho, \rho', \kappa) \cos[\kappa(z - z')] d\kappa \right\}, \quad (57)$$

where

$$\tilde{G}_t(\rho, \rho', \kappa) = I_t(\kappa \rho_<) K_t(\kappa \rho_>) \quad t = 0, 1, 2, \dots, \quad (58)$$

and  $I_t(\kappa\rho_<)$  is the modified Bessel function of the first kind of order  $t$ . It is noted that the difference between the Green's function due to a point charge in free space and that due to a point charge exterior to an infinitely long dielectric rod lies in the interface conditions at a surface  $\rho = \text{constant}$ . To find the Green's function due to a point charge outside of a dielectric rod, one needs only to modify the integral kernel  $\tilde{G}_t(\rho, \rho', \kappa)$  in (57) so that the interface conditions in (53) are satisfied:

$$\tilde{G}_t^{(1)}(\rho, \rho', \kappa) = \tilde{G}_t^{(2)}(\rho, \rho', \kappa), \quad (59)$$

and

$$\varepsilon_1 \frac{\partial}{\partial \rho} \tilde{G}_t^{(1)}(\rho, \rho', \kappa) = \varepsilon_2 \frac{\partial}{\partial \rho} \tilde{G}_t^{(2)}(\rho, \rho', \kappa) \quad (60)$$

To create a kernel that satisfies (59) and (60), define

$$\tilde{G}_t^{(1)}(\rho, \rho', \kappa) = I_t(\kappa\rho_<)K_t(\kappa\rho_>) + A(\kappa)K_t(\kappa\rho)K_t(\kappa\rho'), \quad (61)$$

and

$$\tilde{G}_t^{(2)}(\rho, \rho', \kappa) = B(\kappa)I_t(\kappa\rho)K_t(\kappa\rho'). \quad (62)$$

The first term in (61) represents the primary field due to the point source, while the second term represents the reflected field with a reflection coefficient  $A(\kappa)$ . In the region  $0 < \rho < a$  there exists only the transmitted field and  $B(\kappa)$  in (62) is the transmission coefficient. Substitute (61) and (62) into (59) and (60) to find that the coefficient  $A(\kappa)$  is expressed as

$$A(\kappa) = -\frac{(\varepsilon_2 - \varepsilon_1)I_t(\kappa a)I_t'(\kappa a)}{\varepsilon_2 I_t'(\kappa a)K_t(\kappa a) - \varepsilon_1 I_t(\kappa a)K_t'(\kappa a)}, \quad (63)$$

where  $I_t'(z_0) = dI_t(z)/dz|_{z=z_0}$  and similarly for  $K_t'(z_0)$ . Now the potential  $G^{(1)}(\mathbf{r}|\mathbf{r}')$  at an observation point exterior to the dielectric cylinder due to a point charge also outside of the cylinder is expressed as

$$G^{(1)}(\mathbf{r}|\mathbf{r}') = \frac{1}{2\pi^2} \times \left\{ \int_0^\infty \tilde{G}_0^{(1)}(\rho, \rho', \kappa) \cos[\kappa(z-z')] d\kappa + 2 \sum_{t=1}^\infty \cos[t(\phi-\phi')] \int_0^\infty \tilde{G}_t^{(1)}(\rho, \rho', \kappa) \cos[\kappa(z-z')] d\kappa \right\}. \quad (64)$$

The derived Green's function, dependent on the permittivity and radius of the dielectric rod under test, is used later to calculate the capacitance of the arc-electrode sensor.

*Note on the choice of the Bessel function kernel*

Instead of using the identity in (55), one can also express  $1/r$  in terms of the of Bessel function of the first kind of order zero  $J_0(\kappa\rho)$  [121]:

$$\frac{1}{r} = \int_0^\infty J_0(\kappa\rho)e^{-\kappa z} d\kappa, \quad (65)$$

and express the Green's function  $G_j^{(1)}(\mathbf{r}|\mathbf{r}')$  in the form of Bessel functions of the first and the second kind

$$G_j^{(1)}(\mathbf{r}|\mathbf{r}') = \frac{1}{4\pi} \times \left\{ \int_0^\infty \tilde{K}_0^{(1)}(\rho, \rho', \kappa) e^{-\kappa|z-z'|} d\kappa + 2 \sum_{t=1}^\infty \cos[t(\phi-\phi')] \int_0^\infty \tilde{K}_t^{(1)}(\rho, \rho', \kappa) e^{-\kappa|z-z'|} d\kappa \right\}, \quad (66)$$

where

$$\tilde{K}_t^{(1)}(\rho, \rho', \kappa) = J_t(\kappa\rho)J_t(\kappa\rho') + A_j(\kappa)Y_t(\kappa\rho)J_t(\kappa\rho') \quad t = 0, 1, \dots, \quad (67)$$

$$A_j(\kappa) = -\frac{(\varepsilon_2 - \varepsilon_1)J_t(\kappa a)J_t'(\kappa a)}{\varepsilon_2 J_t'(\kappa a)Y_t(\kappa a) - \varepsilon_1 J_t(\kappa a)Y_t'(\kappa a)}, \quad (68)$$

$J_t'(\kappa a) = dJ_t(\kappa\rho)/d(\kappa\rho)|_{\rho \rightarrow a}$  and  $Y_t'(\kappa a) = dY_t(\kappa\rho)/d(\kappa\rho)|_{\rho \rightarrow a}$ . However, the denominator in (68) contains an infinite number of zeros for  $\kappa$  from 0 to  $\infty$ , and increases the complexity in MoM numerical implementations. Therefore, the Green's function in the form of modified Bessel functions, (64), is a better choice here for calculating the sensor output capacitance.

### Numerical implementation

The capacitance  $C$  between the two arc-electrodes is calculated numerically as follows. The Green's function derived above is used to set up the integral equation in MoM calculations, which leads to the solution for the surface charge density on each electrode. The two electrodes are oppositely charged in the numerical calculations. Because of the axisymmetry of the problem, it is only necessary to calculate the surface charge density on one of the electrodes. The output capacitance  $C$  is then calculated from

$$C = \frac{Q}{V}, \quad (69)$$

where the total charge  $Q$  on each electrode is obtained by integrating the surface charge density over the electrode surface and  $V$  is the potential difference between the electrodes.

### Calculation method

Figure 69 shows the discretization of the arc-electrode surfaces into  $M \times N$  elements of assumed constant surface charge density. Each electrode is discretized into  $M$  elements in the  $\phi$  direction and  $N$

elements in the  $z$  direction. Denote the surface charge density on the left electrode as  $\sigma_s(\phi', z')$  and that on the right electrode as  $\sigma_s(\phi' + \pi, z')$ . The potential at the observation point  $\mathbf{r} = (\rho_0, \phi, z)$  on the electrode surface due to the charged arc-electrodes can be expressed by integrating (64) over the electrode surfaces:

$$\begin{aligned} \Psi(\phi, z) = & \frac{1}{\epsilon_0} \iint_{\text{Left electrode}} G^{(1)}(\mathbf{r} | \mathbf{r}') \sigma_s(\phi', z') \rho_0 d\phi' dz' \\ & - \frac{1}{\epsilon_0} \iint_{\text{Right electrode}} G^{(1)}(\mathbf{r} | \mathbf{r}') \sigma_s(\phi' + \pi, z') \rho_0 d\phi' dz' \end{aligned} \quad (70)$$

In the MoM calculations, the following expansion is used to approximate the continuous function  $\sigma_s(\phi', z')$ :

$$\sigma_s(\phi', z') = \sum_{j=1}^{MN} \sigma_j b_j(\phi', z'), \quad (71)$$

where  $\sigma_j$  is the unknown constant surface charge density on element  $j$  and  $b_j(\phi', z')$  is the pulse basis function

$$b_j(\phi', z') = \begin{cases} 1 & \text{on element } j \\ 0 & \text{elsewhere.} \end{cases} \quad (72)$$

To solve for the  $MN$  unknown coefficients  $\sigma_j$ , weighting (or testing) functions  $w_i(\phi, z)$  are introduced to force that the boundary condition for the potential in (70) is satisfied for each element on the sensor surface. The point-matching method is used, in which the weighting functions are Dirac delta functions:

$$w_i(\phi, z) = \delta(\phi - \phi_i) \delta(z - z_i) \quad \text{on element } i, \quad (73)$$

where  $i = 1, 2, \dots, MN$ . Discretizing the integral equation using weighting functions in each of the  $MN$  elements, (70) is expressed as the following matrix equation:

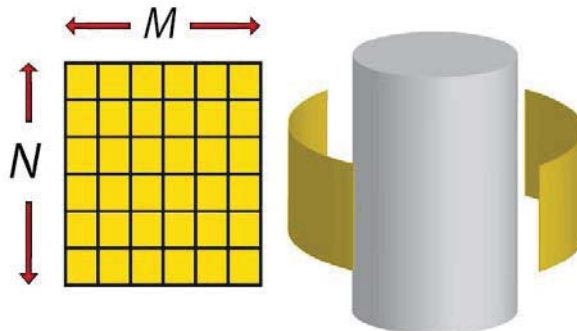


**Figure 69** Discretization of the arc-electrode surfaces into  $M \times N$  elements of assumed constant surface charge density.

$$\begin{bmatrix} G_{11} & G_{12} & \cdots & G_{1L} \\ G_{21} & G_{22} & \cdots & G_{2L} \\ \vdots & \vdots & \ddots & \vdots \\ G_{L1} & G_{L2} & \cdots & G_{LL} \end{bmatrix} \times \begin{bmatrix} \sigma_1 \\ \sigma_2 \\ \vdots \\ \sigma_L \end{bmatrix} = \bar{\mathbf{V}} \quad (74)$$

where  $L = MN$  and

$$G_{ij} = \frac{1}{\varepsilon_0} \iint_{\text{element } j} G^{(1)}(\mathbf{r}_i | \mathbf{r}'_j) b_j(\phi', z') \rho_0 d\phi' dz' \quad (75)$$

All the elements in  $\bar{\mathbf{V}}$  share the same potential  $v$  that is the potential applied to one of the electrodes. The other electrode has potential  $-v$ . From (75) the surface charge density  $\sigma_s(\phi', z')$  on one of the electrodes is solved, and that for the other electrode is simply  $-\sigma_s(\phi' + \pi, z')$ . The total charge  $Q$  on each electrode can be found by integrating  $\sigma_s(\phi', z')$  over the electrode surface. The sensor output capacitance  $C$  is ultimately calculated through (69).

#### *Example calculations*

When numerically calculating the matrix element given in (75), the zero to infinity summation and integral in  $G^{(1)}(\mathbf{r} | \mathbf{r}')$  (see (64)) need to be truncated. The convergence of the Green's function depends on values of  $\varepsilon_2/\varepsilon_1$ ,  $a/\rho$  and  $\phi_0$ . When these values are large, large truncation ranges for the summation and integral in (64) are needed. It is found that, for the case  $\varepsilon_2/\varepsilon_1=5$ ,  $a/\rho=1$ ,  $\phi_0 = 177^\circ$  and  $l = 4$  cm, if one truncates the summation in  $G^{(1)}(\mathbf{r} | \mathbf{r}')$  with 40 terms and the integral with the range from 0 to 2000 for the off-diagonal components in (75), and the summation with 300 terms and the integral with the range from 0 to 2000 for the diagonal components, accuracy to three significant figures can be achieved in the final calculated sensor output capacitance  $C$ . The cases calculated in Figure 70 to Figure 72 and Figure 74 have smaller  $\varepsilon_2/\varepsilon_1$ ,  $a/\rho$  and  $\phi_0$  values than those in the case calculated above. The truncation standard used here is adopted in all numerical calculations of sensor capacitance value in this section. It guarantees achieving convergence with accuracy to the third significant digit in all the cases discussed below.

The dependence of sensor output capacitance on the electrode configuration is investigated as follows. In Figure 70, sensor output capacitance  $C$  is plotted as a function of the electrode length  $l$  and the arc-

angle  $\phi_0$ . In this example calculation, the infinitely long dielectric rod is assumed to be in free space, with relative permittivity  $\epsilon_r=2.5$  and radius  $a = 9.525$  mm (chosen to be similar to the radii of the rods used for experiments described later.) The arc-electrodes share the same radius as the cylindrical rod. It is seen from Figure 70 that for any fixed electrode arc-angle  $\phi_0$ , there exists a linear relationship between the sensor capacitance  $C$  and the electrode length  $l$ . On the other hand, for any given electrode length  $l$ , the sensor output capacitance  $C$  increases as the electrode arc-angle  $\phi_0$  increases, and tends to infinity as  $\phi_0$  tends to  $180^\circ$ . This is explained by the fact that the output capacitance  $C$  results from interaction between the sensor electrodes. The charge density on the electrodes is highest at the electrode edges, and increases as the electrode edges come closer together. As  $\phi_0$  tends to  $180^\circ$ , the gaps between the edges of the two electrodes become infinitesimally small and therefore the resulting capacitance tends to infinity, in accordance with the singular behavior of the charge density at the electrode edges. Figure 70 shows that in order to achieve maximum sensor output signal, the ideal sensor electrodes would be as long as practically possible and with large arc-angle  $\phi_0$ .

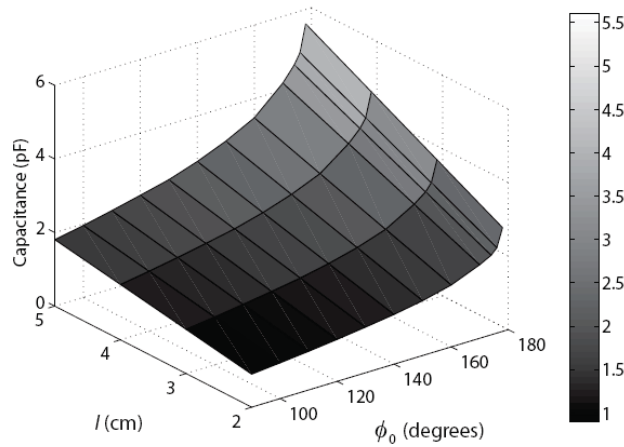


**Figure 70** Calculated sensor output capacitance as a function of electrode length  $l$  and arc-angle  $\phi_0$ . The dielectric rod is in free space, with a relative permittivity of 2.5 and a radius of 9.525 mm.

Figure 71 shows an example of the sensor output capacitance  $C$  as a function of the ratio  $a/\rho_0$  (see Figure 67). Rod parameters are as for Figure 70. The arc-electrodes each have fixed radius  $\rho_0 = 9.525$  mm, arc-angle  $\phi_0 = 174.44^\circ$  and length  $l = 4$  cm. In other words, Figure 71 shows the dependence of sensor capacitance on the cylindrical test-piece diameter, for a fixed arc-electrode sensor configuration. It is seen from Figure 71 that as the ratio  $a/\rho_0$  increases, sensor output capacitance increases dramatically,

especially when this ratio tends to 1. This is because as  $a/\rho_0$  increases, the average permittivity interior to the arc-electrodes increases and therefore  $C$  increases. On the other hand, the sensor's most sensitive area lies in the region close to the gaps between the two electrodes. As  $a/\rho_0$  tends to 1, the arc-electrodes are more likely to detect increases in the average permittivity surrounding the sensor. This is why the sensor output capacitance  $C$  changes more rapidly as the ratio  $a/\rho_0$  approaches 1. The theoretical calculation in Figure 71 demonstrates that, during measurements, unidentified small air gaps existing between the arc electrodes and the dielectric rod under test can introduce relatively large uncertainty in the measured  $C$ , especially as  $a \rightarrow \rho_0$ . Therefore, in order to achieve the strongest sensor output signal and the smallest uncertainty due to possible air gaps between the electrodes and test-piece, it is desirable to have the arc-electrodes in tight surface contact with the test-piece.

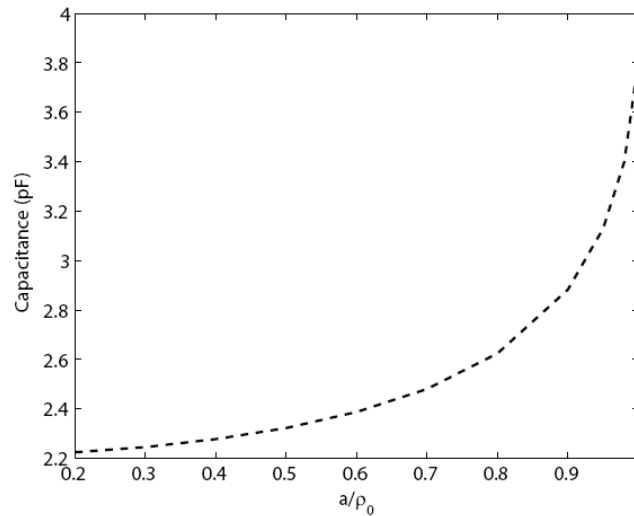


**Figure 71** Calculated sensor output capacitance  $C$  as a function of the ratio of dielectric rod radius  $a$  to electrode radius  $\rho_0$ . The electrode radius, arc-angle, and length are  $\rho_0 = 9.525$  mm,  $\phi_0 = 174.44^\circ$ , and  $l = 4$  mm, respectively.

The sensor output capacitance  $C$  as a function of dielectric rod relative permittivity  $\epsilon_{r2}$  is plotted in Figure 72, in which different sensor configurations are considered. A linear relationship between the sensor output capacitance and the test-piece permittivity is observed and has been verified numerically, by computation of a sufficient number of data points (seven in this case). It is seen that the slope of sensor output capacitance versus rod permittivity depends on both the sensor configuration and the ratio  $a/\rho_0$ . For a given  $a/\rho_0$ , the value of the slope increases as the electrode length  $l$  and arc-angle  $\phi_0$  increase. This is because the value of the slope represents changes in the absolute values of the capacitance for any

rod permittivity increment. These absolute value changes in capacitance are most obvious for sensors with large electrode length  $l$  and arc-angle  $\phi_0$  values. This also explains why the value of the slope, for fixed  $l$  and  $\phi_0$  values, increases as  $a/\rho_0$  increases. However, it is worth pointing out that for fixed electrode radius  $\rho$ , arc-angle  $\phi_0$ , and  $a/\rho_0$  values, although increasing electrode length  $l$  increases the value of the slope, relative changes in capacitance as  $\epsilon_{r2}$  changes stay the same, because of the linear relationship between the sensor output capacitance  $C$  and electrode length  $l$  (see Figure 70).

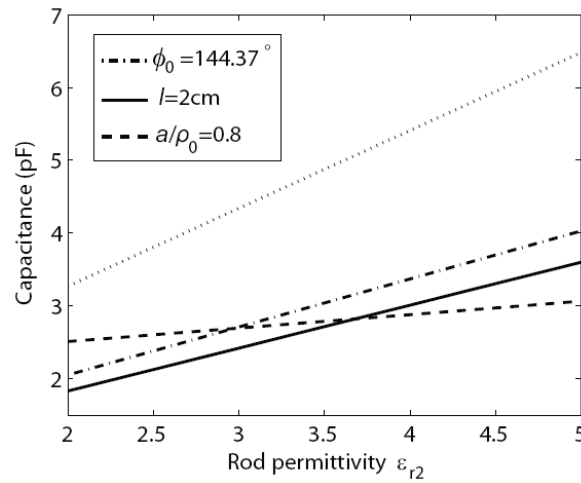


**Figure 72** Calculated sensor output capacitance as a function of dielectric rod relative permittivity.  $a/\rho_0 = 1$ ,  $l = 4$  cm and  $\phi_0 = 174.44^\circ$  except where indicated. All the sensor electrodes have fixed radius  $\rho_0 = 9.525$  mm.

### Experimental verification

Capacitance experiments were performed to verify the validity of the developed theory. Two sets of rectangular planar electrodes (shown in Figure 73) were fabricated using photolithography by American Standard Circuits Inc.. The sensor shape was achieved by selectively etching a  $18 \mu\text{m}$  thick copper cladding (14 mL standard) off a flat  $25.4 \mu\text{m}$  thick Kapton<sup>®</sup> type 100 CR polyimide film. These flexible electrodes were fixed onto different cylindrical dielectric test-pieces later to form the arc-electrode capacitance sensors. The sensor dimensions are  $w=29$  mm and  $l=20$  mm for one set and  $w=29$  mm and  $l=40$  mm for the other (see Figure 67). A Nikon EPIPHOT 200 microscope was used to independently measure the fabricated sensor dimensions, for the purpose of checking the difference between the fabricated dimensions and the specified ones, and therefore the accuracy of the fabrication process. The “traveling microscope” measurement method, with accuracy of 0.01 mm, was used to measure the relatively large sensor electrode dimensions. It was found that the measured dimensions of the fabricated electrodes are identical with the nominal values under such measurement accuracy.

Three 304.8-mm-long dielectric rods are used in the measurements to simulate the infinitely long cylindrical dielectric rod. The dielectric rods are long compared with the electrode lengths (factors of approximately 8 and 15 longer), and the edge effect due to finite rod length can be neglected if the sensor electrodes are placed at the center of the rods. The rod materials are Acetal Copolymer (Tecaform™), Cast Acrylic, and Virgin Electrical Grade Teflon® PTFE. A digital caliper, with accuracy of  $\pm 0.01$  mm, was used to independently measure the diameter of each rod. The permittivity of each rod was independently determined by cutting a slice from the end of each rod, and then measuring the permittivity of each slice using a Novocontrol Alpha Dielectric Spectrometer at 1 MHz. In the Novocontrol measurements, both sides of each slice were brushed with silver paint to form the measuring electrodes.

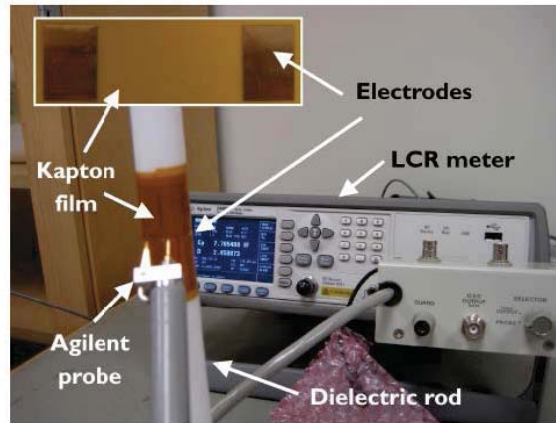


**Figure 73** Agilent E4980A precision LCR meter and Agilent probe test fixture 16095A used for sensor capacitance measurements. Subfigure: photography of the flexible rectangular planar electrodes fabricated using photolithography.

The rectangular planar electrodes were attached to each dielectric rod by taping the thin Kapton® sensor substrate tightly against the rod material, as shown in Figure 73. The electrodes were aligned carefully so that the upper and lower edges of the two electrodes were at the same height, the vertical edges of both electrodes were in parallel, and the two vertical gaps between the two electrodes were of the same size, as assumed in the theoretical model. Another layer of 25.4- $\mu\text{m}$ -thick Kapton® film was wrapped tightly onto the outsides of the electrodes in order to minimize the air gap between the electrodes and the dielectric rod. Because the Kapton® films used were quite thin, influences from their permittivity on the measurement signal were negligible.

For each dielectric test-piece used in the benchmark experiments, the test-piece material, test-piece diameter, independently measured test-piece relative permittivity, electrode radius  $\rho_0$ , and electrode arc-angle  $\phi_0$  are listed in Table 18. The electrode radius  $\rho_0$  for each rod is obtained by summing the dielectric rod radius and the Kapton® substrate thickness. The electrode arc-angle  $\phi_0$  in Table 18 is

different for each test-piece because of the fact that the diameter of each rod is different while the electrode width  $w$  is the same. The parameters shown in the table were used as the inputs in the numerical calculations.

An Agilent E4980A precision LCR meter was used to measure the sensor output capacitance. The LCR meter operating frequency was set as 1 MHz, so that the measurement error from the LCR meter was less than 0.3% for a 1 pF capacitance while at the same time being a good approximation for the electrostatic assumption in the numerical model (results of the calculation do not depend on frequency). A static model can be applied for this configuration even at  $f = 1$  MHz because, at this frequency, the corresponding wavelength  $\lambda = 300$  m. The diagonal dimensions of the electrodes in the measurement are smaller than 5 cm, which means the maximum phase change over the electrode surfaces is less than  $0.06^\circ$  and the effect of scattering is therefore negligible. A  $0.06^\circ$  phase change is not detectable here, being below the measurement sensitivity of the Novocontrol dielectric spectrometer and the LCR meter. If a lower operating frequency is desired for practical capacitance measurements, an impedance measurement instrument with higher accuracy when measuring large impedance values should be used. (According to the relationship  $Z = 1 / j2\pi fC$ , the impedance  $Z$  resulting from measuring a given capacitance  $C$  under a lower frequency  $f$  will be larger).

**Table 18** Parameters of the dielectric test-pieces and the arc-electrode sensors used in benchmark experiments. The areas of the two sets of sensor electrodes are  $29 \times 20 \text{ mm}^2$  and  $29 \times 40 \text{ mm}^2$ , respectively.

Test-piece material	Test-piece diameter (mm)	Measured test-piece permittivity	Electrode radius $\rho_0$ (mm)	Electrode arc-angle $\phi_0$
Tecaform™	$19.08 \pm 0.01$	$3.77 \pm 0.05$	$9.565 \pm 0.005$	$173.71^\circ \pm 0.10^\circ$
Cast Acrylic	$19.03 \pm 0.01$	$2.88 \pm 0.05$	$9.540 \pm 0.005$	$174.17^\circ \pm 0.09^\circ$
Teflon®	$19.10 \pm 0.01$	$2.23 \pm 0.05$	$9.575 \pm 0.005$	$173.53^\circ \pm 0.09^\circ$

Sensor output capacitance  $C$  was measured by placing the probe of an Agilent probe test fixture 16095A across the two sensor electrodes, as shown in Figure 73. The parts on the electrodes where the probe is in surface contact were not covered by Kapton® films. This probe test fixture was connected to the LCR meter and the measured capacitance was read from the LCR meter screen. Figure 74 shows the comparison between the calculated and measured sensor output capacitance for each test-piece material and the two different electrode configurations. Experimental data show excellent agreement with numerical results (to within 3%), and the maximum absolute difference in capacitance is less than 0.1 pF. It is worth pointing out that even if Kapton® films are tightly wrapped around the electrodes to attempt to

eliminate the air gaps between electrodes and the test-piece, small gaps still exist. In particular, the vertical edges of the electrodes tend to bend up, giving rise to small air gaps, where the sensor is most sensitive. This points to the fact that the ideal way to achieve best agreement between theory and measurements is to deposit the arc-electrodes directly onto the cylindrical test-pieces. Thus errors coming from the misalignment of sensor electrodes and the existence of air gaps will be eliminated. On the other hand, deposition of electrodes directly onto the test-piece is costly, time-consuming and undesirable for most practical purposes.

One purpose for these arc-electrode sensors is the inverse determination of the permittivity of materials under test from measured sensor capacitance. Comparisons are made in Table 19 to assess the capability and accuracy of the arc-electrode sensors in material dielectric property characterization. The sample permittivities inferred from measured capacitance values shown in Figure 74 are compared with those

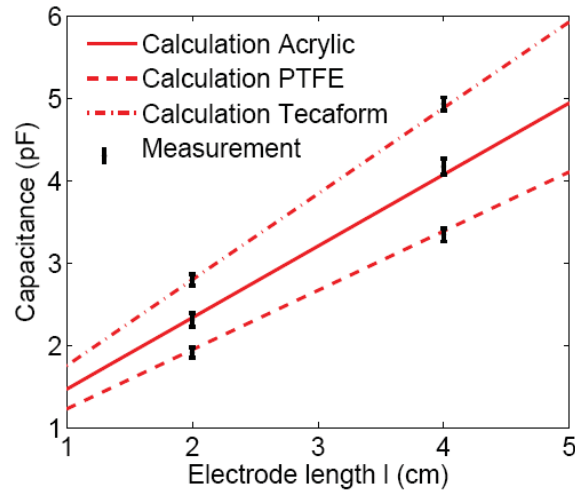


**Figure 74** Measured and calculated  $C$  for various sensor configurations (see Table 18) in contact with different dielectric test-pieces. Measurement results and error bars are denoted by the black symbol.

**Table 19** Comparison of test-piece permittivity values between independently measured ones and inversely determined ones from measured capacitance using the arc-electrode sensors.

Test-piece material	Independently measured permittivity	Electrode length (mm)	Inversely determined permittivity	Relative difference (%)
Tecaform™	$3.77 \pm 0.05$	20	$3.76 \pm 0.07$	0.3
		40	$3.82 \pm 0.08$	1.3
Cast Acrylic	$2.88 \pm 0.05$	20	$2.88 \pm 0.01$	0.0
		40	$2.89 \pm 0.01$	0.3
Teflon®	$2.23 \pm 0.05$	20	$2.16 \pm 0.11$	3.1
		40	$2.18 \pm 0.09$	2.2

measured by a Novocontrol dielectric spectrometer, in the manner discussed in the second paragraph in Section 1.4. Again, excellent agreement between inferred and independently measured test-piece permittivities is obtained. Table 19 demonstrates the great potential of using the arc-electrode capacitive sensors for accurate and convenient permittivity measurements of cylindrical dielectric materials.

### **Summary**

A numerical model, based on the electrostatic Green's function due to a point source exterior to an infinitely long cylindrical dielectric, has been developed to quantitatively evaluate the dielectric property of cylindrical dielectric test-pieces. The quantitative dependence of the sensor output capacitance on the test-piece permittivity and radius has been demonstrated numerically and verified experimentally. The permittivity of various cylindrical test-pieces has been inferred from measured capacitance to within 1% accuracy, on average.

### **2. *Analysis of a capacitive sensor for the evaluation of circular cylinders with a conductive core***

A capacitive sensor has been developed for the purpose of measuring the permittivity of a cylindrical dielectric that coats a conductive core cylinder. The capacitive sensor consists of two identical curved patch electrodes that are exterior to and coaxial with the cylindrical test-piece. The permittivity of the cylinder is determined from measurements of capacitance by means of a physics-based model. In the model, an electroquasistatic Green's function due to a point source exterior to a dielectric-coated conductor is derived, in which the permittivity of the dielectric material may take complex values. The Green's function is then used to set up integral equations that relate the unknown sensor surface charge density to the imposed potentials on the electrode surfaces. The method of moments is utilized to discretize the integral equation into a matrix equation that is solved for the sensor surface charge density and eventually the sensor output capacitance. This model enables the complex permittivity of the dielectric coating material, or the geometry of the cylindrical test-piece, to be inferred from the measured sensor capacitance and dissipation factor. Experimental validation of the numerical model has been performed on three different cylindrical test-pieces for two different electrode configurations. Each of the test-pieces has the structure of a dielectric coated brass rod. Good agreement between measured and calculated sensor capacitance (to an average of 7.4%) and dissipation factor (to within 0.002) was observed. Main sources of uncertainty in the measurement include variations in the test-piece geometry, misalignment of sensor electrodes, strain-induced variation in the test-piece permittivity, and the existence of unintended air gaps between electrodes and the test-piece. To demonstrate the effectiveness

of the sensor, measurements of capacitance have been made on aircraft wires and the permittivity of the insulation inferred. A significant change in permittivity was observed for thermally degraded wires.

## **Introduction**

This part of the report describes development and benchmark testing of a model-based capacitive method for complex permittivity measurement of a cylindrical dielectric that coats a conductive core cylinder. The work is motivated by the effective evaluation of degradation status of air- and space-craft wiring insulation. Degradation in electrical wiring insulation has the potential to cause aviation catastrophe due to consequent short-circuiting or loss of control function [88]. One effective approach of evaluating insulation degradation state is through permittivity measurements, which can be achieved using capacitive methods.

Capacitive methods offer a favorable solution to the accurate characterization of material dielectric properties at low costs. For example, model-based interdigital sensors allow the inverse determination of test-piece material properties from measured sensor output capacitance [109]. Applications of interdigital sensors include humidity and moisture sensing, electrical insulation properties sensing, chemical sensing, biosensing, and others. Rectangular coplanar capacitive sensors have been developed to detect water intrusion in composite materials, on the physical basis that changes in material dielectric properties lead to variations in the sensor capacitance [117]. Rectangular capacitance sensors also find application in damage detection in laminated composite plates [118], evaluation of moisture content in reinforced concrete covers [122], and rain sensing [123]. Rectangular capacitive sensor arrays have been reported in [119], and shown to be capable of detecting surface and subsurface features of dielectrics. Circular shaped capacitive sensors have also been developed for the quantitative characterization of material properties. Multichannel fringing electric field sensors [114], cylindrical geometry electroquasistatic dielectrometry sensors [115] and concentric coplanar capacitive sensors [116] are some examples of these. In addition, parallel plate capacitors formed by two circular discs with coplanar guard electrodes have been used to detect strength-limiting defects (large voids) in cellular glasses [124]. Capacitive techniques that have the potential to be integrated into aircraft wiring test systems are presented in [125] to [99]. Arc-electrode capacitive sensors have been developed to characterize material and structural properties of cylindrical dielectric rods [125]. A so-called 'meander' coil and a quarter-circular interdigital sensor have been used in detection of cable insulation damage [113]. In [99], linear relationships between the capacitance of open-circuited aircraft wires and their length have been demonstrated and enable the determination of wiring conductor length from measured capacitance values. Further references on capacitive methods can be found in [116] and [125].

In addition to capacitive techniques, other electrical testing methods have been developed to evaluate the wiring conductor condition. Reflectometry is one of the most commonly used techniques for aircraft wiring testing, in which a high frequency electrical signal is transmitted along the wire and any impedance discontinuities result in reflected signals whose interpretation may give an estimate of the flaw position. An excellent review paper that compares different reflectometry methods is [91]. Low-voltage resistance tests and dielectric-withstand-voltage tests are two qualitative methods that can detect faults, but are not suitable for inspection of aging aircraft wiring because of the difficulty of miniaturization and pinpointing the fault [90].

The fundamental relationships between the capacitance of a curved patch capacitive sensor and the dielectric property of its test-piece are presented. The test-piece discussed here has the structure of a dielectric-coated conductor. The sensor consists of two identical and symmetric curved patch electrodes, which are located exterior to and coaxially with the cylindrical test-piece. For the modeling, an electroquasistatic Green's function due to a point source exterior to a cylindrical dielectric-coated conductor is derived in cylindrical coordinates, in which the permittivity of the dielectric material may take complex values, Section 2.2. The Green's function is then used to set up integral equations that relate the unknown sensor surface charge density to the predetermined electric potentials on the sensor electrodes. The method of moments (MoM) is utilized to discretize the integral equation into a matrix equation that is solved for the sensor surface charge density, Section 2.3. The total charge  $Q$  on each electrode is then calculated and the capacitance between the two curved patch electrodes is obtained through  $C = Q/V$ , in which  $V$  is the potential difference between the two electrodes. Large-scale experimental verification of the theory has been carried out on copper rods coated with different dielectric materials, for two different electrode configurations, Section 2.4. Measured and numerically calculated sensor capacitance values agree to an average of 7.4%, whereas the dissipation factors agree to within 0.002. Major factors contributing to the measurement uncertainty are variations in the test-piece geometry, misalignment of sensor electrodes, strain induced variation in the test-piece permittivity, and the existence of unintended air gaps between the sensor electrodes and cylindrical test-pieces. These are discussed in detail in Section 2.4.

This part of Chapter V is focused on the development and verification of a physics-based measurement method. In related research that will be published in a later article, a prototype capacitive probe has been built based on the method presented in this section [126]. This probe has been applied for quantitative characterization of insulation degradation on actual aircraft wires. Changes in the insulation complex permittivity, induced by thermal and hydrolytic exposures, have been clearly detected. One of these results is shown here, Section 2.5, in order to demonstrate the feasibility of quantitative evaluation of wiring insulation permittivity using the model described in this section. The capacitance technique

developed in this section has the potential to be built into smart embedded wiring test systems of the future. It is complementary to large-scale inspection techniques. For instance, two ultrasonic transducers can be used in a pitch/catch configuration to generate and receive an ultrasonic guided wave in a wire, and obtain an overall indication of the wire insulation condition [101]. When faults are indicated by such system-level inspection techniques, high accuracy local inspections using the curved patch capacitive sensors may follow.

### **Modeling**

The method of moments (MoM) is utilized in the modeling process instead of the finite element method. The adopted numerical method has the advantage of only needing to discretize surfaces, rather than the volume, to obtain the sensor capacitance. The number of unknowns to solve is proportional to  $N^2$ , where  $N$  is the number of unknowns in one dimension. Most commercially available finite element tools, however, have to discretize a truncated space, in which the number of unknowns to solve is proportional to  $N^3$ . This means using the MoM in the modeling significantly reduces the number of unknowns to solve and therefore the required computation time and computer memory. This feature is important in quantitative evaluation of wiring insulation permittivity using the capacitive method. Because the insulation permittivity is determined inversely based on measured capacitance through the numerical model, faster numerical models can significantly reduce the amount of time needed during this process.

### *Sensor configuration*

The configuration of the curved patch capacitive sensor is shown in Figure 75. The two identical and symmetric curved sensor electrodes are assumed in the theory to be infinitesimally thin. The cylindrical test-piece is modeled as an infinitely long dielectric-coated perfect conductor. The conductor is kept at ground potential in the modeling and the patch electrodes are held at equal and opposite potentials,  $\pm V/2$ . The sensor output capacitance is calculated in the electroquasistatic regime, in which the permittivity of the dielectric coating may take complex values while the resulting potential still satisfies the Laplace equation.

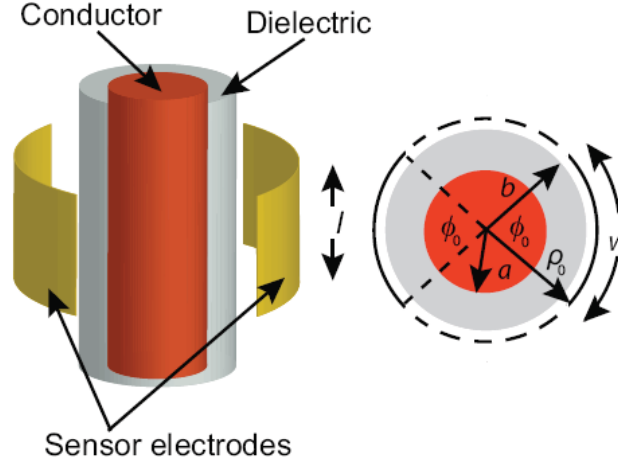


**Figure 75** Curved patch capacitive sensor. The radii of the sensor electrodes, the conductor, and the cylindrical test-piece are denoted  $\rho_0$ ,  $a$ , and  $b$ , respectively. The arc-angle of each sensor electrode is  $\phi_0$  (rad). The length of each electrode in the vertical direction is  $l$  and the width in the horizontal direction is  $w = \phi_0 \times \rho_0$ .

### Derivation of Green's function in cylindrical coordinates

Figure 76 shows a point source placed at  $(\rho', \phi', z')$  exterior to a cylindrical dielectric-coated conductor. This configuration is used in the following Green's function derivation. The outer radius of the cylindrical test-piece is  $b$  and the radius of the inner conductor is  $a$ . The complex permittivities of the dielectric coating and the background medium are  $\varepsilon_2^* = \varepsilon_2' - j\varepsilon_2''$  and  $\varepsilon_1^* = \varepsilon_1' - j\varepsilon_1''$ , respectively, where  $j = \sqrt{-1}$ . Considering the canonical shapes of the sensor electrodes and the test-piece, the electroquasistatic Green's function is derived in cylindrical coordinates. The electric potential at an observation point  $(\rho, \phi, z)$  due to the point source in Figure 76 satisfies the Laplace equation in each homogeneous region exterior to the conductor:

$$\left[ \frac{1}{\rho} \frac{\partial}{\partial \rho} \left( \rho \frac{\partial}{\partial \rho} \right) + \frac{1}{\rho^2} \frac{\partial^2}{\partial \phi^2} + \frac{\partial^2}{\partial z^2} \right] \Psi^{(i)}(\rho, \phi, z) = -\frac{1}{\rho} \delta(\rho - \rho') \delta(\phi - \phi') \delta(z - z') \quad i = 1, 2, \quad (76)$$

and is subject to a Dirichlet boundary condition at the surface defined by  $\rho = a$ :

$$\Psi^{(2)}(\rho = a, \phi, z) = 0, \quad (77)$$

and the interface conditions at the surface defined by  $\rho = b$ :

$$\begin{aligned} \Psi^{(1)}(\rho = b, \phi, z) &= \Psi^{(2)}(\rho = b, \phi, z) \\ \varepsilon_1^* \frac{\partial}{\partial \rho} \Psi^{(1)}(\rho, \phi, z) \Big|_{\rho=b} &= \varepsilon_2^* \frac{\partial}{\partial \rho} \Psi^{(2)}(\rho, \phi, z) \Big|_{\rho=b} \end{aligned} \quad (78)$$

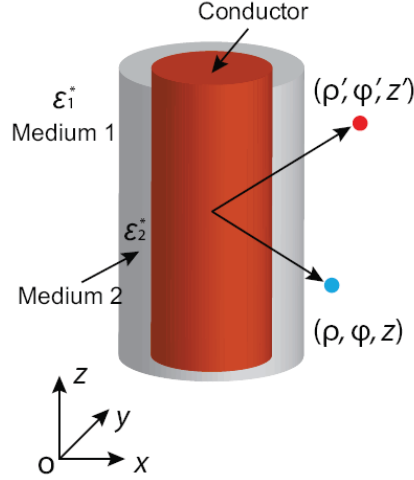


**Figure 76** Point source outside of an infinitely long dielectric-coated conductor.

where superscripts (1) and (2) correspond to the regions defined by  $\rho \geq b$  and  $a \leq \rho < b$ , respectively. Solution to the potential Green's function can be found by following similar procedures in Section 2.2 Chapter V, in which the Green's function due to a point source exterior to a homogeneous dielectric cylinder is derived. Steps taken to derive the electroquasistatic Green's function are summarized as follows.

Begin with the free space Green's function in cylindrical coordinates due to a point charge at the origin. The potential at an observation point  $(\rho, \phi, z)$  is [120]

$$G_0(\rho, z) = \frac{1}{4\pi r} = \frac{1}{2\pi^2} \int_0^\infty K_0(\kappa\rho) \cos(\kappa z) d\kappa, \quad (79)$$

where  $r = \sqrt{\rho^2 + z^2}$  and  $K_0(\kappa\rho)$  is the modified Bessel function of the second kind of order zero. The potential due to a source point at arbitrary location  $(\rho', \phi', z')$  can be obtained by applying the addition theorem given in (80) [120]

$$K_0(\kappa\zeta) = I_0(\kappa\rho_<)K_0(\kappa\rho_>) + 2 \sum_{m=1}^{\infty} \cos[m(\phi - \phi')] I_m(\kappa\rho_<) K_m(\kappa\rho_>), \quad (80)$$

to  $K_0(\kappa\rho)$  in (79) and replacing  $z$  by  $z-z'$ , where  $\zeta = \sqrt{\rho^2 + \rho'^2 - 2\rho\rho' \cos(\phi - \phi')}$ ,  $\rho_<$  is the lesser of  $\rho$  and  $\rho'$ , and  $\rho_>$  is the greater. Now the Green's function in free space is rewritten as

$$G_0(\rho, \phi, z | \rho', \phi', z') = \frac{1}{2\pi^2} \times \left\{ \int_0^\infty \tilde{G}_0(\rho, \rho', \kappa) \cos[\kappa(z-z')] d\kappa + 2 \sum_{m=1}^{\infty} \cos[m(\phi - \phi')] \int_0^\infty \tilde{G}_m(\rho, \rho', \kappa) \cos[\kappa(z-z')] d\kappa \right\}, \quad (81)$$

where  $\tilde{G}_p(\rho, \rho', \kappa) = I_p(\kappa\rho_<)K_p(\kappa\rho_>)$   $p = 0, 1, 2, \dots$ , and  $I_p(\kappa\rho_<)$  is the modified Bessel function of the first kind. As pointed out in [125], the difference between the Green's function due to a point charge in free space and that due to a point charge exterior to an infinitely long dielectric-coated conductor Figure 76 is due to interface conditions that are applied at surfaces of constant  $\rho$ , corresponding to the physical interfaces of the test-piece. To find the Green's function for this case, one needs only to modify the integral kernel  $\tilde{G}_p(\rho, \rho', \kappa)$  in (81) so that the interface conditions in (77) and (78) are satisfied:

$$G_p^{(2)}(\rho = a, \rho', \kappa) = 0 \quad (82)$$

$$\tilde{G}_p^{(1)}(\rho, \rho', \kappa) = \tilde{G}_p^{(2)}(\rho, \rho', \kappa) \quad (83)$$

$$\varepsilon_1 \frac{\partial}{\partial \rho} \tilde{G}_p^{(1)}(\rho, \rho', \kappa) = \varepsilon_2 \frac{\partial}{\partial \rho} \tilde{G}_p^{(2)}(\rho, \rho', \kappa) \quad (84)$$

Following the same steps as in [125], the Green's function  $G(\rho, \phi, z | \rho', \phi', z')$  at an observation point  $(\rho, \phi, z)$  due to a point charge at  $(\rho', \phi', z')$  that is also exterior to the dielectric-coated conductor is derived as:

$$G(\mathbf{r} | \mathbf{r}') = \frac{1}{2\pi^2 \varepsilon_0} \left\{ \int_0^\infty \tilde{G}_0(\rho, \rho', \kappa) \cos[\kappa(z - z')] d\kappa + 2 \sum_{t=1}^\infty \cos[t(\phi - \phi')] \int_0^\infty \tilde{G}_p(\rho, \rho', \kappa) \cos[\kappa(z - z')] d\kappa \right\}, \quad (85)$$

where

$$\tilde{G}_p(\rho, \rho', \kappa) = I_p(\kappa\rho_<)K_p(\kappa\rho_>) + A_p(\kappa)K_p(\kappa\rho)K_p(\kappa\rho') \quad p = 0, 1, \dots, \quad (86)$$

$$A_p(\kappa) = - \frac{(\varepsilon_2^* - \varepsilon_1^*)I_p(\kappa b)I_p'(\kappa b) - \alpha_p(\kappa)[\varepsilon_2^*I_p(\kappa b)K_p'(\kappa b) - \varepsilon_1^*I_p'(\kappa b)K_p(\kappa b)]}{\varepsilon_2^*I_p'(\kappa b)K_p(\kappa b) - \varepsilon_1^*I_p(\kappa b)K_p'(\kappa b) - \alpha_p(\kappa)(\varepsilon_2^* - \varepsilon_1^*)K_p(\kappa b)K_p'(\kappa b)}, \quad (87)$$

$\alpha_p(\kappa) = I_p(\kappa a) / K_p(\kappa a)$ ,  $I_p'(\kappa b) = dI_p(\kappa\rho) / d(\kappa\rho)|_{\rho \rightarrow b}$  and similarly for  $K_p'(\kappa b)$ . The Green's function in the form of modified Bessel functions, (85), is used in the following calculations of the sensor output capacitance. The sensor capacitance is computed later using the derived test-piece geometry and permittivity dependent Green's function.

Note that (85) can be simplified to the case of a homogeneous dielectric rod, described in [125], by assigning  $a = 0$ . The Green's function (85) can also be expressed in the form of Bessel functions of the first and second kind. However, the denominator of the integrand in the Green's function contains an infinite number of zeros and increases the complexity in the numerical implementations.

## Numerical implementation

### Calculation method

The sensor output capacitance  $C$  is calculated numerically using the method of moments (MoM). Calculation procedures used here are similar to those in [125]. In summary, the following steps are taken to compute the sensor capacitance.

First, the Green's function (85) is used to set up the integral equation that relates the unknown sensor surface charge density  $\sigma_s(\phi', z')$  to the imposed potential  $\Psi(\phi, z)$  on the sensor electrodes

$$\begin{aligned} \Psi(\phi, z) = & \int \int_{\text{Left electrode}} G(\rho, \phi, z | \rho', \phi', z') \sigma_s(\phi', z') \rho_0 d\phi' dz' \\ & - \int \int_{\text{Right electrode}} G(\rho, \phi, z | \rho', \phi', z') \sigma_s(\phi' + \pi, z') \rho_0 d\phi' dz'. \end{aligned} \quad (88)$$

In order to solve for the sensor surface charge density numerically, i.e., to use discrete functions approximating the continuous function  $\sigma_s(\phi', z')$ , each electrode in Figure 77 is discretized into  $M \times N$  rectangular elements. The charge density on each element is assumed to be constant and can be different from others. Mathematically, this approximation is expressed as

$$\sigma_s(\phi', z') \approx \sum_{j=1}^{MN} \sigma_j b_j(\phi', z'), \quad (89)$$

where  $b_j(\phi', z')$  is the selected pulse basis function and  $\sigma_j$  is the unknown coefficient to be determined. Note the axisymmetry of the problem, it is only necessary to calculate the surface charge density on one of the electrodes.

To solve for the  $MN$  unknown coefficients  $\sigma_j$ , weighting functions  $w_i(\phi, z)$  are introduced to force the integral equation (88) to be satisfied for each element on the sensor surface. The point-matching method is used in this process, in which the weighting functions are Dirac delta functions. Expressions for  $b_j(\phi', z')$  and  $w_i(\phi, z)$  can be found in [125]. Discretizing the integral equation using weighting functions in each of the  $MN$  elements, (88) is expressed as the following matrix equation:

$$\begin{pmatrix} G_{11} & G_{12} & \cdots & G_{1L} \\ G_{21} & G_{22} & \cdots & G_{2L} \\ \vdots & \vdots & \ddots & \vdots \\ G_{L1} & G_{L2} & \cdots & G_{LL} \end{pmatrix} \times \begin{pmatrix} \sigma_1 \\ \sigma_2 \\ \vdots \\ \sigma_L \end{pmatrix} = \bar{\mathbf{V}}, \quad (90)$$

where

$$G_{ij} = \int \int_{\text{element } j} G(\rho_i, \phi_i, z_i | \rho'_j, \phi'_j, z'_j) b_j(\phi', z') \rho_0 d\phi' dz', \quad (91)$$

$L = MN$  and all the elements in  $\overline{\mathbf{V}}$  share the same potential that is applied to the electrode. The unknown coefficients  $\sigma_j$  are obtained by solving the matrix equation, and the total charge  $Q$  on each electrode is calculated by integrating the surface charge density over the electrode surface. The capacitance  $C$  between the two electrodes is obtained using the relationship  $C=Q/V$ .

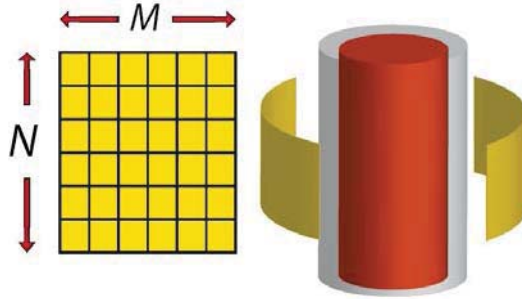


**Figure 77** Curved patch capacitive sensor is divided into  $M \times N$  elements on each electrode, each with assumed constant surface charge density.

#### Example calculations

The dielectric-coated conductor is assumed to be in free space in the following calculations, i.e.,  $\epsilon_{r1}^* = 1$ . When numerically evaluating elements in the  $\overline{\mathbf{G}}$  matrix, the zero to infinity summation and integral in  $G(\rho, \phi, z | \rho', \phi', z')$  (see (85)) need to be truncated. The convergence of the Green's function depends on values of  $\epsilon_2$ ,  $\tan \delta = \epsilon_2 / \epsilon_1$ ,  $a/b$ ,  $b/\rho$  and  $\phi_0$ . When these values are large, large truncation ranges for the summation and integral in (85) are needed. It is found that, for the case  $\epsilon_{r2}' = 5$ ,  $\tan \delta = 0.02$ ,  $a/b = 0.9$ ,  $b/\rho = 1$ ,  $\phi_0 = 178^\circ$  and  $l = 4$  cm, if one truncates the summation in  $G(\rho, \phi, z | \rho', \phi', z')$  to 80 terms and the integral with the range from 0 to 6000 for the off-diagonal components in  $\overline{\mathbf{G}}$  matrix, and the summation to 400 terms and the integral with the range from 0 to 6000 for the diagonal components, accuracy to three significant figures can be achieved in the final calculated complex sensor output capacitance  $C$ , for both real and imaginary parts. The cases calculated in Figure 78 to Figure 80 and Section 2.4 have smaller  $\epsilon_{r2}'$ ,  $\tan \delta$ ,  $a/b$ ,  $b/\rho$  and  $\phi_0$  values than those in the case calculated above. The truncation standard used here is adopted in all of the following numerical calculations, which guarantees convergence to three significant figure accuracy is achieved for all the numerically calculated capacitance values in this section.

The dependence of sensor capacitance on the electrode configuration is shown in Figure 78. The sensor output capacitance is plotted as a function of the electrode length  $l$  and the arc-angle  $\phi_0$ . The dielectric coating has a relative permittivity  $\epsilon_{r2}' = 2.5$ . The radius of the core conductor  $a = 8$  mm and the outer

radius of the dielectric-coated conductor  $b = 9$  mm. The sensor electrodes are assumed to be right on the cylindrical test-piece:  $\rho_0 = b$ . In Figure 78, a linear relationship between the sensor capacitance  $C$  and the electrode length  $l$  is observed for any fixed electrode arc-angle  $\phi_0$ . On the other hand, the sensor output capacitance  $C$  increases as the electrode arc-angle  $\phi_0$  increases for any given electrode length  $l$ , and tends to infinity as  $\phi_0$  tends to  $180^\circ$ . This is explained by the fact that as  $\phi_0$  tends to  $180^\circ$ , the gaps between the two electrodes become infinitesimally small and the resulting capacitance tends to infinity. Figure 78 shows that the sensor output capacitance changes dramatically when  $\phi_0$  and  $l$  have large values. When performing dielectric measurements in practice, it is usually helpful to have large sensor output signal and therefore to have large  $\phi_0$  and  $l$  values. However, when  $l$  and  $\phi_0$  are large,  $C$  changes rapidly, and it is important to have accurate sensor configuration information to infer accurately material dielectric properties from measured  $C$ .

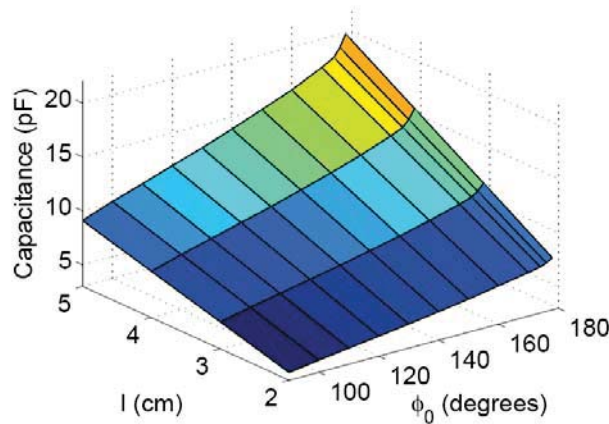


**Figure 78** Calculated sensor output capacitance as a function of electrode length  $l$  and arc-angle  $\phi_0$ . The rod is in free space with conductor radius  $a = 8$  mm, dielectric radius  $b = \rho_0 = 9$  mm and dielectric permittivity  $\epsilon_{r2}' = 2.5$ .

The dependence of sensor capacitance on the test-piece geometry is shown in Figure 79. The sensor output capacitance  $C$  is plotted as a function of the ratio  $b/\rho_0$  and the ratio  $a/b$  (see Figure 75). The dielectric coating permittivity  $\epsilon_{r2}'$  is as for Figure 78. The sensor electrodes have fixed radius  $\rho_0 = 9$  mm, arc-angle  $\phi_0 = 174^\circ$  and length  $l = 4$  cm. It is observed that for fixed  $b/\rho_0$  values, the sensor capacitance increases as the ratio  $a/b$  increases. Such a trend is more obvious when the ratio  $b/\rho_0$  tends to 1. This is because the calculated capacitance  $C$  is actually the series capacitance of the capacitance between one electrode and the core conductor and the capacitance between the core conductor and the other electrode. When the ratio  $a/b$  increases, the distance between the sensor electrodes and the core conductor decreases

and the resulting total capacitance increases. In particular, when  $b/\rho_0 = 1$ , the output capacitance tends to infinity as  $a/b$  tends to 1, in which case the gaps between the sensor electrodes and the core conductor approaches zero. This also explains why the sensor capacitance increases as the ratio  $b/\rho_0$  increases for given  $a/b$  values, and why such changes in capacitance are more rapid for large  $a/b$  values. The fact that the overall permittivity of the region between the electrodes and the conductive core increases as  $b/\rho_0$  increases also contribute to increases in the sensor output signal. In summary, the existence of the conductive core in the test-piece increases the output capacitance for given sensor configurations, and as the conductive core radius  $a$  approaches zero, the test-piece reduces to a homogeneous dielectric rod.

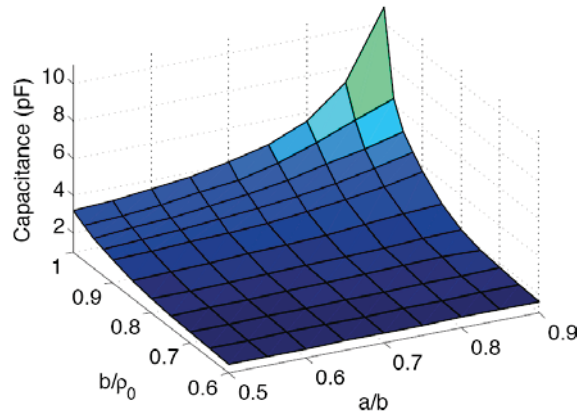


**Figure 79** Calculated sensor output capacitance  $C$  as a function of the ratio of cylindrical test-piece outer radius  $b$  to electrode radius  $\rho_0$  and the ratio of conductive core  $a$  to cylindrical test-piece outer radius  $b$ . The electrode radius, arc-angle and length are 9 mm,  $174^\circ$  and 4 cm, respectively.

Figure 80 shows the sensor capacitance  $C$  and dissipation factor  $D$  as functions of the dielectric coating real permittivity  $\epsilon_{r2}'$  and imaginary permittivity  $\epsilon_{r2}''$ , respectively. Different sensor configurations are considered. In Figure 80a), a linear relationship between  $C$  and  $\epsilon_{r2}'$  is observed for all sensor configurations. It is seen that the slope of sensor capacitance versus dielectric coating real permittivity, i.e., the sensor sensitivity, depends on both the sensor configuration and the geometry of the cylindrical test-piece. The largest slope in Figure 80 occurs when  $a/b$ ,  $b/\rho_0$ , electrode length  $l$  and electrode arc-angle  $\phi_0$  are the largest of the values considered. However, it is worth pointing out that although increasing electrode length  $l$  increases the value of the slope, relative changes in capacitance stay the same, because of the linear relationship between the sensor output capacitance  $C$  and electrode length  $l$  (see Figure 78. For practical inspection of wires,  $a/b$  is fixed, and it is therefore important to keep  $b/\rho_0$  close to 1 to achieve the highest sensitivity. In the selection of  $\phi_0$ , a trade-off exists. Larger  $\phi_0$  gives rise

to larger sensitivity as well as capacitance. On the other hand, larger  $\phi_0$  means that the inter-electrode gap decreases and the penetration of the field into the insulation decreases as a consequence.

Similar relationships between  $D$  and  $\varepsilon_{r2}''$  are observed in Figure 80b). The major difference between the response of  $C$  and  $D$  to the investigated factors is that  $D$  is less sensitive than  $C$  to changes in  $l$ ,  $\phi_0$  and  $a/b$ .

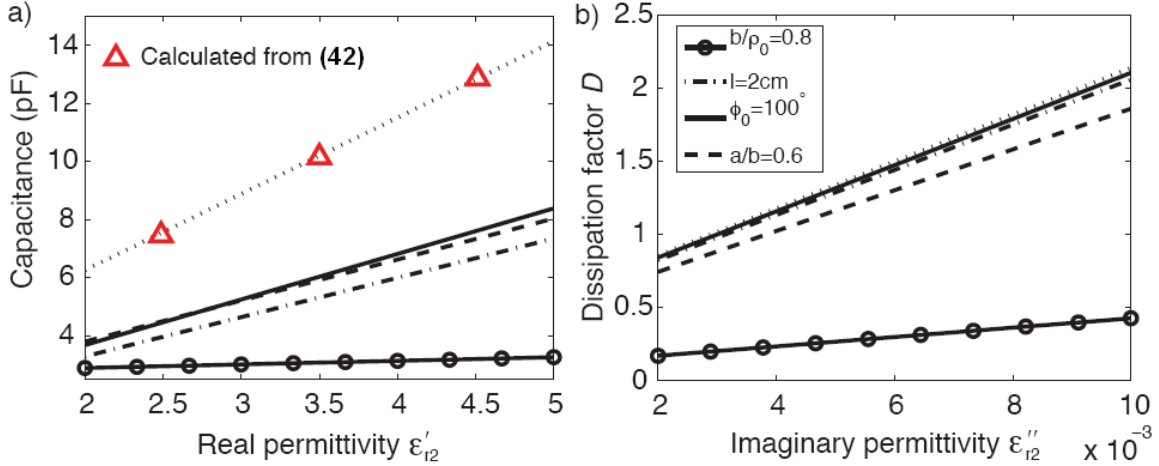


**Figure 80** Calculated sensor capacitance and dissipation factor as a function of the dielectric coating real permittivity  $\varepsilon_{r2}'$  and imaginary permittivity  $\varepsilon_{r2}''$ . Sensor configuration:  $\rho_0 = 9$  mm,  $a/b = 0.8$ ,  $b/\rho_0 = 1$ ,  $l = 4$  cm and  $\phi_0 = 170^\circ$  except where indicated in other lines.  $\varepsilon_{r2}''$  and the material dissipation factor are assumed to be zero in a).  $\varepsilon_{r2}' = 2$  in b).

#### Dependence of capacitance on test-piece permittivity and sensor configuration

If  $l \rightarrow \infty$ ,  $a \rightarrow 0$  and  $b/\rho_0 = 1$ , the case of Figure 75 becomes a two-dimensional problem. An analytical expression for the capacitance per unit length between the two curved patches has been derived in [127] and takes the following general form

$$C = F_s(\varepsilon_1 + \varepsilon_2), \quad (92)$$

where  $F_s$  is a shape factor that depends solely on the capacitor geometry. Considering the linear plots of Figure 80a), the following relationship is found to hold in general for the problem discussed in this section (Figure 77):

$$C = F_s(\varepsilon_1 + \alpha \varepsilon_2), \quad (93)$$

where  $\alpha$  is a constant showing the dependence of  $C$  on  $\varepsilon_1$  and  $\varepsilon_2$ .  $\alpha > 1$  means  $C$  is more dependent on  $\varepsilon_2$  than  $\varepsilon_1$ , and vice versa.  $\alpha = 1$  means  $C$  depends equally on  $\varepsilon_1$  and  $\varepsilon_2$ . The factors  $\alpha$  and  $F_s$  in (93) may be determined by selecting two data points on any of the lines in Figure 80a). It is found that  $\alpha$  and  $F_s$  are constant for any given sensor configuration, independent of the particular data points selected for the calculation.

As an example shown in Figure 80a),  $C$  obtained based on (93) fits nicely on the dashed line for  $\alpha = 2.61$  and  $F_s = 1.01$  m. Similar results are observed for all the other sensor configurations as well. It is found that  $\alpha$  increases as  $b/\rho_0$ ,  $a/b$  and  $l$  increase, and as  $\phi_0$  decreases. The latter relationship can be explained by the fact that as  $\phi_0$  decreases, more electric field penetrates the dielectric coating, and  $\epsilon_2$  will therefore have larger impact on  $C$ . The product  $\alpha F_s$  is the slope in the  $C$  versus  $\epsilon_2$  plot and shows the sensor sensitivity, whose dependency on the sensor configuration has been discussed earlier.

## Experiment

### *Experimental setup and measurement procedures*

Benchmark experiments comparing the measured sensor capacitance with numerically-predicted values were performed to verify the validity of the developed theory. Experiments were conducted at frequency 1 MHz. Note that although the numerical model is developed in the electroquasistatic regime, i.e., the wave length  $\lambda$  (approximately 300 m at 1 MHz) is much greater than the dimension of the test-pieces in the experiment, the dielectric coatings still have complex permittivities. This is due to losses arising in the materials due to the polarization response of the polymers lagging behind the switching of the applied electric field at 1 MHz. For this reason, complex permittivities are considered in the following benchmark experiments.

Two sets of rectangular planar electrodes (shown in Figure 81) were fabricated using photolithography by selectively etching a 18- $\mu\text{m}$ -thick copper cladding (14 mL standard) off a flat 25.4- $\mu\text{m}$ -thick Kapton<sup>®</sup> type 100 CR polyimide film. These flexible electrodes were attached to different cylindrical test-pieces later to form the capacitance sensors. The sensor dimensions are  $w = 29$  mm and  $l = 20$  mm for one set and  $w = 29$  mm and  $l = 40$  mm for the other (see Figure 75). A Nikon EPIPHOT 200 microscope was used to measure the fabricated sensor dimensions, for the purpose of checking the difference between the fabricated dimensions and the nominal ones, and therefore the accuracy of the fabrication process. The “traveling microscope” measurement method, with accuracy of  $\pm 0.01$  mm, was used to measure the dimensions of the relatively large sensor electrodes. It was found that the measured dimensions of the fabricated electrodes are the same as the nominal ones under such measurement accuracy.

Three cylindrical test-pieces, each being a dielectric tube coated copper rod, were used in the measurements to simulate the infinitely long dielectric-coated conductors in theory (see Figure 75). The dielectric tube materials were Acetal Copolymer (Tecaform<sup>™</sup>), Acrylic, and Virgin Electrical Grade Teflon<sup>®</sup> PTFE, respectively. The dielectric tubes were hollowed from homogeneous rods so that the inner diameter of the tube matched the diameter of the copper rod as closely as possible. All the three dielectric tubes were in tight surface contact with the central copper rods. The cylindrical test-pieces used are 152.4

mm in length. These test-pieces are long compared with the electrode lengths (factors of approximately 4 and 7 longer). The edge effect due to finite rod length can be neglected if the sensor electrodes are placed sufficiently far from the ends of the test-piece. Prior to being hollowed out, the permittivity of each dielectric tube was measured, by cutting a disc from the end of each rod and measuring its permittivity using a Novocontrol Alpha Dielectric Spectrometer at  $f = 1$  MHz and room temperature. The measured test-piece permittivity values, together with uncertainty, are provided in Table 20. In the Novocontrol measurements, both sides of each disc (around 19 mm in diameter) were brushed with silver paint to form the measuring electrodes. The capacitance values resulting from these discs were between 2 and 5 pF. The impedance measurement accuracy of the Novocontrol at 1 MHz and room temperature for such capacitance values is 0.1% for the magnitude and  $0.06^\circ$  for the absolute phase accuracy. Note since Teflon<sup>®</sup> are low loss materials (loss tangent below  $10^{-4}$  in the frequency range 20 kHz to 1 MHz at room temperature [128]), accurate measurements of their imaginary permittivities were not achieved using either the Novocontrol or the Agilent E4980A LCR meter with the Agilent 16451B dielectric test fixture.

The diameter of the copper rods, the outer diameter of the dielectric-coated conductors and the thickness of the dielectric coatings were measured using a digital caliper with accuracy of  $\pm 0.01$  mm. Each of these values was measured at ten different locations on the test-piece. An average value and the corresponding deviation were obtained, in which the deviation is defined as the maximum absolute difference between the average value and the ten measured values.

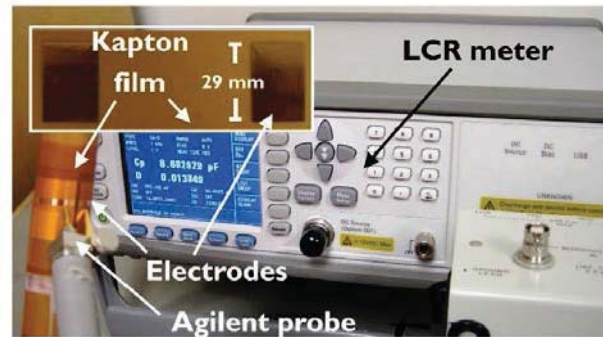


**Figure 81** Agilent E4980A precision LCR meter and Agilent probe test fixture 16095A used for sensor capacitance measurements. Subfigure: photography of the flexible rectangular planar electrodes fabricated using photolithography.

The experimental arrangement for the capacitance measurements is shown in Figure 81. The rectangular patch electrodes were conformed to each cylindrical test-piece by taping the thin Kapton<sup>®</sup> sensor substrate tightly against the dielectric material. The thickness of the film ( $25.4 \mu\text{m}$ ) is accounted for in the numerical modeling while effects of its permittivity are neglected. This is because the sensor capacitance is much more sensitive to small variations in  $b/\rho_0$ , when this ratio is very close to 1, than

those in the test-piece permittivity. The permittivity of the substrate was hence assumed to be that of the test-piece, an assumption that introduces negligible uncertainty. The electrodes were aligned carefully in order to achieve the sensor configuration in the theoretical model as closely as possible. The goal in the alignment was to keep the upper and lower edges of the two electrodes at the same height, the vertical edges of both electrodes in parallel, and the two vertical gaps between the two electrodes of the same size. Another layer of 25.4- $\mu\text{m}$ -thick Kapton<sup>®</sup> film was wrapped tightly onto the outsides of the electrodes to further minimize the air gap between the electrodes and the cylindrical test-piece, leaving part of each electrode exposed to make electrical contact with the probe test fixture later.

In the experimental verifications, two groups of capacitance measurements were performed for each cylindrical test-piece: one group using the 20-mm-long electrodes and the other using the 40-mm-long electrodes. For each cylindrical test-piece, the tube material, brass rod diameter, outer diameter of the dielectric-coated brass, variation in the dielectric tube thickness, electrode radius  $\rho_0$  and electrode arc-angle  $\rho_0$  are provided in Table 21, with uncertainties. Because the two types of electrodes were attached at different locations on each test-piece, the outer diameters of the test-pieces in Table 21 were measured at those individual locations and vary slightly. The electrode radius  $\rho_0$  for each cylindrical test-piece is obtained by summing the outer radius of the dielectric-coated brass rod and the Kapton<sup>®</sup> substrate thickness. The electrode arc-angle  $\rho_0$  and its uncertainty in Table 21 are calculated from the electrode width  $w$ , electrode radius  $\rho_0$  and its uncertainty. Each test-piece has its own electrode arc-angle  $\phi_0$  because the fabricated electrodes share a fixed width  $w$  while the cylindrical test-pieces have different radii. The parameters shown in Table 20 and Table 21 were used as the inputs in the numerical calculations.

An Agilent E4980A precision LCR meter was used to measure the sensor output capacitance at room temperature. The LCR meter operating frequency was set at 1 MHz to approximate the electroquasistatic assumption in the numerical model. Under these conditions, the measurement accuracy of the LCR meter for a 4 pF capacitance is 0.15% and the absolute accuracy for the dissipation factor is 0.0015, whereas those for a 13 pF capacitance are 0.13% and 0.0013, respectively. The measured capacitance values in this section are all within 4 and 13 pF. If a lower operating frequency is desired in capacitance measurements, an impedance measurement instrument with higher accuracy when measuring large impedance values should be used. (According to the relationship  $Z = 1 / j2\pi fC$ , the impedance  $Z$  resulting from measuring a given capacitance  $C$  under a lower frequency  $f$  will be larger). The sensor capacitance  $C$  was measured by placing an Agilent probe test fixture 16095A across the two sensor electrodes, as shown in Figure 81. This probe test fixture was connected to the LCR meter and the

measured capacitance was read from the LCR meter screen. Note that in the modeling the two electrodes are assumed oppositely charged and the conductive core of the test-piece is kept at ground potential. The calculated capacitance is the series capacitance of the capacitance between one electrode and the conductive core and the capacitance between the conductive core and the other electrode. When performing capacitance measurements, however, one needs only to place the probe test fixture across the two sensor electrodes, as shown in Figure 81. The potential on the conductive core is the average of the potentials on the two sensor electrodes, due to the symmetry of the problem, and the capacitance picked up by the probe is the series capacitance calculated in the numerical model.

**Table 20** Measured complex permittivity values of the dielectric coating materials.

Dielectric tube material	Measured dielectric tube real permittivity $\epsilon_{r2}'$	Measured dielectric tube imaginary permittivity $\epsilon_{r2}''$
Tecaform <sup>TM</sup>	$3.77 \pm 0.05$	$0.014 \pm 0.002$
Acrylic	$3.02 \pm 0.05$	$0.055 \pm 0.009$
Teflon <sup>®</sup>	$2.21 \pm 0.04$	Below instrument capability

**Table 21** Parameters of the test-pieces and the capacitive sensors used in benchmark experiments. The three copper rods used as the conductive cores in the cylindrical test-pieces had a uniform diameter of  $15.90 \pm 0.01$  mm.

Dielectric material	$l$ (mm)	$2b$ (mm)	Variation in $(b-a)$ (mm)	$\rho_0$ (mm)	$\phi_0$ (°)
Tecaform <sup>TM</sup>	20	$19.28 \pm 0.03$	0.06	$9.64 \pm 0.02$	$172.4 \pm 0.3$
	40	$19.22 \pm 0.05$	0.06	$9.61 \pm 0.03$	$172.9 \pm 0.5$
Acrylic	20	$19.18 \pm 0.04$	0.03	$9.59 \pm 0.02$	$173.3 \pm 0.4$
	40	$19.17 \pm 0.07$	0.03	$9.59 \pm 0.04$	$173.4 \pm 0.6$
Teflon <sup>®</sup>	20	$19.31 \pm 0.02$	0.07	$9.65 \pm 0.01$	$172.1 \pm 0.2$
	40	$19.3 \pm 0.1$	0.07	$9.67 \pm 0.07$	$171.9 \pm 1.2$

### Results and discussion

Comparison between calculated and measured sensor capacitance  $C$  and dissipation factor  $D$  for each cylindrical test-piece and the two different electrode configurations is made in Table 22. Because of material complex permittivity, complex sensor output capacitance is expected. The sensor dissipation factor is defined as the ratio of the imaginary part of the capacitance to its real part. Since accurately measured imaginary permittivity was not achieved and Teflon<sup>®</sup>, the sensor dissipation factor cannot be calculated and comparison between its calculated and measured  $D$  is not made in Table 22.

**Table 22** Measured and calculated capacitance for various sensor configurations in contact with different cylindrical test-pieces.

Dielectric tube material	Electrode length (mm)	Calculated $C$ (pF)	Measured $C$ (pF)	Relative difference in $C$ (%)	Calculated $D$	Measured $D$	Relative difference in $D$
Tecaform™	20	6.58	6.09 ± 0.12	-7.5	0.003	0.002 ± 0.002	0.002
	40	12.34	11.47 ± 0.19	-7.1	0.003	0.002 ± 0.002	0.001
Acrylic	20	5.64	5.30 ± 0.11	-6.0	0.015	0.014 ± 0.006	0.001
	40	10.36	9.47 ± 0.17	-8.6	0.015	0.015 ± 0.007	0.000
Teflon®	20	4.20	3.92 ± 0.13	-6.7	-	-	-
	40	7.63	6.98 ± 0.16	-8.5	-	-	-

Measured and calculated capacitance  $C$  agree to within an average of 7.4% in Table 22. All the measurement results are smaller than the numerically-predicted ones, by between 0.3 to 0.9 pF. Two factors contributing to lower measured  $C$  are identified. First, during sample preparation, the brass rods were inserted into hollowed dielectric rods to achieve tight surface contact. After insertion, the dielectric coatings were subjected to normal stress exerted by the brass rods and circumferential strain was introduced in the dielectrics. In an independent study, it is found that the real permittivity of Teflon® (PTFE) decreases as its strain increases [129]. This means the actual permittivity of the Teflon® coating the brass rod is likely to be lower than the value used in the numerical calculations, which was measured on a sample slice cut from the rods prior to their being hollowed out, i.e., before strain was introduced. Consequently, measured  $C$  will be smaller than that predicted numerically for dielectrics with strain-induced reduction in permittivity. Second, although Kapton® films are tightly wrapped around the electrodes to attempt to eliminate air gaps between the electrodes and the test-piece, small gaps still exist due to the nonuniform diameters (surface roughness) of the cylindrical test-pieces. For example, the two largest percentage differences between calculated and measured capacitance values in Table 20 are observed for the cases of Acrylic and Teflon® coated test-pieces with 40-mm-long electrodes, which also show the largest variations in test-piece outer diameter (Table 20). It is seen from Figure 79 that the sensor output capacitance changes rapidly when the ratios  $b/\rho_0$  and  $a/b$  are close to one. This indicates that for  $a/b \approx 0.8$  as in these measurements, the existence of air gaps can affect measurement results significantly.

Apart from the above two factors, two sources contributing to measurement uncertainty (not necessarily lower  $C$ ) exist. One is the misalignment of sensor electrodes. For example, the vertical edges of the electrodes tend to bend up, giving rise to small air gaps in the vicinity of inter-electrode gaps, where the sensor is most sensitive. This points to the fact that the ideal way to achieve best agreement between

theory and measurements is to deposit the sensor electrodes directly onto the cylindrical test-pieces, and errors coming from the misalignment of sensor electrodes and the existence of air gaps will be eliminated. However, deposition of electrodes directly onto the test-piece is costly, time-consuming and undesirable in some cases although may be useful for real-time monitoring of structures by in-situ sensors. The other source of uncertainty is variation in the dielectric tube thickness, Table 20. These variations can be traced to surface roughness of the dielectric tubes and/or non-concentricity between the conductive core and the dielectric tube. The effects of rough test-piece surfaces have been discussed above. The effects of eccentricity are discussed here. For the ideal case that the conductor and the dielectric are concentric, as shown in Figure 75, the total sensor capacitance may be approximated by a relationship of the following form:

$$C = \frac{C_0^2}{C_0 + C_0} = C_0 / 2, \quad (94)$$

where  $C_0$  is the capacitance between the conductive core and either electrode. When the conductor and the dielectric become non-concentric, the capacitance between one electrode and the conductor changes to  $C_0 + mC_0$  while the capacitance between the conductor and the other electrode changes to  $C_0 - nC_0$ , where  $m, n > 0$ . The total capacitance  $C'$  changes to

$$C' = \frac{(C_0 + mC_0)(C_0 - nC_0)}{C_0 + mC_0 + C_0 - nC_0} = C_0 \frac{1 + m - n + mn}{2 + m - n}. \quad (95)$$

It is found that when  $m \leq n$ ,  $C'$  is always smaller than  $C$ . However, when  $m > n$ ,  $C'$  is not necessarily smaller than  $C$ . In other words, non-concentricity between the copper rods and the dielectric coatings does not necessarily result in smaller sensor output capacitance values, but does introduce uncertainty to the capacitance measurement.

As shown in Table 22, the absolute difference between the numerically predicted and the measured sensor dissipation factor  $D$  is found to be 0.002 or less. This is close to the LCR meter measurement accuracy, e.g., the measurement accuracy of the dissipation factor of a 5 pF capacitance is  $\pm 0.001$  at 1 MHz and room temperature. Large variation in measured  $D$  is observed, however. One important reason for this is that large variation ( $\pm 16\%$ ) in the measured test-piece  $\ddot{Q}_{r,2}$  is observed, Table 20, due to the measurement accuracy of the instrument. This fact also introduces uncertainty into the calculated  $D$  and contributes to the difference between numerically-predicted and measured results, given in Table 22.

**Summary**

The electroquasistatic Green's function due to a point source exterior to a dielectric-coated conductor has been derived in cylindrical coordinates. The capacitance of the curved patch capacitive sensor has been calculated numerically using the method of moments based on the Green's function. The quantitative dependence of the sensor capacitance on test-piece geometry and the dielectric coating permittivity has been demonstrated numerically and verified experimentally. A discussion of measurement uncertainty is provided. The curved patch capacitive sensor developed in this section has the potential to evaluate effectively the condition of wiring insulation and is complementary to other inspection methods that are focused on evaluating the conductor's condition.

### 3. *A Capacitive Probe for Quantitative Nondestructive Evaluation of Wiring Insulation*

In this section, a capacitive probe is presented that has been developed for quantitative evaluation of wiring insulation permittivity. The probe consists of two patch electrodes that conform to the curvature of the wire under test. A previously-developed numerical model is utilized for inverse determination of insulation complex permittivity from measured probe response. Experimental studies on thermally and hydrolytically exposed wire samples show that the resulting insulation degradation is successfully detected using the described capacitive probe, for the wire type MIL-W-81381/12, which is predominantly Kapton<sup>®</sup> coated. Permittivity changes in the wiring insulation detected by the capacitive probe are shown to be in accordance with results of research conducted previously on thermally and hydrolytically exposed Kapton<sup>®</sup> film samples. Thus the feasibility of quantitative evaluation of wiring insulation permittivity using capacitive techniques is demonstrated, which is of particular interest to the aerospace industry.

#### **Introduction**

Efforts have been made for years to guarantee the functionality of key electrical systems on aircraft. However, the performance of the wiring that connects these key systems was not a strong focus of attention until the crashes of TWA 800 and Swissair 111 [88], attributed to aging wiring. In [89], causes and modes of failure in legacy aircraft wiring have been categorized. These causes include chemical degradation such as corrosion of current carriers and hydrolytic scission of polymer chains in the insulation; electrical degradation of the insulation that may be due to concentrated electric fields at sites of electrical stress; and mechanical degradation due to vibration, over-bending and other kinds of mechanical stress.

Visual inspection is the most widely used method for aircraft wiring inspection. It is highly laborious while giving little quantitative information about the condition of the wires. Different physics-based wire inspection techniques have been developed over the past decade to replace this traditional inspection method, of which a summary is given here.

One of the most commonly used physics-based techniques for the inspection of the conductor in aircraft wiring is reflectometry. A high frequency electrical signal is transmitted along the wire and any impedance discontinuities in the conductor result in reflected signals. The location of the fault can be determined from the time and/or phase delay between the incident and reflected signals. An excellent review paper that compares different reflectometry methods is [91]. Reflectometry methods are distinguished by the types of incident voltage applied. Time domain reflectometry (TDR) uses a short rise time voltage step as the incident voltage. This method is susceptible to noise and is not optimal for live wire testing [92] [93] [94]. Frequency domain reflectometry (FDR) uses a set of stepped-frequency sine

waves as the incident voltage. A conceptual design of a smart wiring system based on FDR methods that can be used for on-board testing of aging aircraft wiring has been described in [90]. Phase-detection frequency-domain reflectometry (PD-FDR) has also been applied for locating open and short circuits in a Navy F-18 flight control harness [95]. Sequence time domain reflectometry (STDTR) and spread spectrum time domain reflectometry (SSTDTR) use pseudo noise sequence and sine wave modulated pseudo noise code as the incident voltage, respectively. Testing systems based on these two techniques are capable of testing live wires and therefore have the potential to be used on energized aircraft to locate intermittent faults. Parameters that control the accuracy, latency, and signal to noise ratio for SSTDTR in locating defects on live cables have been examined in [96], and the feasibility of spread-spectrum sensors for locating arcs on realistic aircraft cables and live wire networks has been demonstrated in [97] and [98]. Aside from reflectometry methods, capacitive and inductive methods have also been applied for assessment of wiring conductor condition. In [99], linear relationships between the capacitance/inductance of open-/short- circuited wires (parallel insulated round wires, twisted-pair wires, and coaxial cables) and their conductor length have been demonstrated. This relationship enables the inverse determination of wire length from measured capacitance/inductance values. These techniques all inspect for so-called 'hard' faults in the metal wire conductor itself and are not capable of inspecting the insulation conditions.

Techniques have also been developed for the evaluation of wiring insulation condition. Infrared thermography and pulsed X-ray systems have been developed for nondestructive testing of wiring insulation [100]. Infrared thermography offers the advantage of rapidly examining large areas of wiring and can serve as a global testing method, whereas a portable pulsed X-ray system can be used to obtain a radiographic image of a portion of the wire or cable. Ultrasonic methods have also been developed for quantitative assessment of degradation in wiring insulation condition caused by heat damage, by modeling insulated wires as cylindrical waveguides [101]. Moreover, acoustic and impedance testing methods aimed at locating intermittent faults in aircraft wires have been reported in [102]. Partial discharge (PD) analysis methods for diagnosing aircraft wiring faults are explored in [104], in which a simulation of PD signal based on a high-voltage insulation testing standard [105] has been detailed, followed by wavelet-based analysis to de-noise the PD signals. Deficiencies of the above methods include the need of complex instruments in the measurement and not being able to provide quantitative information about the insulation condition at specific locations. A favorable solution to these deficiencies is the capacitive method, from which quantitative measurements of the permittivity of wiring insulation at specific locations can be made, from which its condition can be inferred, using relatively simple equipment.

This section describes a prototype capacitive probe that has been fabricated and applied for the inspection of wiring insulation condition of type MIL-W-81381/12 but in principle can be extended to any single-conductor wire. The probe is designed based on a previously developed physical model, in which a curved patch capacitor is exterior to and coaxial with a cylindrical dielectric that coats a conductive core cylinder (Chapter V Section 2). In the model, a quantitative relationship between the complex permittivity of the dielectric coating material and the capacitance and dissipation factor of the capacitor is described. This relationship is utilized here for quantitative assessment of wiring insulation permittivity, based on measured probe capacitance. To demonstrate the feasibility of this proposed technique, groups of wire samples have been thermally and hydrolytically exposed, under different conditions, to induce dielectric property changes in the insulation. Capacitance measurements were performed on the samples, and complex permittivity values of their insulation determined inversely by means of the numerical model. Comparisons made between the complex permittivity of the damaged wires and the control wires show that both the real and imaginary parts of the insulation permittivity of the damaged wires increase as the thermal exposure temperature/time and hydrolytic exposure time increase, and are higher than those of the control wires. Especially, changes in the imaginary permittivity are more significant than those in the real part. For example, following thermal exposure, the imaginary permittivity was observed to increase by up to 39% while the real part by up to 17%, for exposures at temperatures between 400 and 475 °C for various times up to 5 hours. In the hydrolytic exposure experiment, the imaginary permittivity was observed to increase by up to 60% and the real part by up to 12%, for exposure in water for various times up to 4 days. Permittivity changes in the wire insulation detected by the capacitive probe are in accordance with results of independent measurements conducted previously on planar thermally and hydrolytically exposed Kapton<sup>®</sup> film (Chapter II). These proof-of-concept experiments have demonstrated the excellent capability of the capacitive probe for quantitative evaluation of insulation condition for wires of type MIL-W-81381/12, and in principle can be applied to any single-conductor wire.

Apart from the capacitive probe discussed in this research, many other capacitive techniques have been developed and applied for NDE of dielectric materials [130]. For example, capacitive arrays have been developed for robotic sensing using 'scanning' and 'staring' modes, [131]. Detailed literature surveys of capacitive NDE methods can be found in [116] and [125].

### **Summary of the physical model**

The capacitive probe is designed based on the sensor model described in (Chapter V Section 2). The curved patch capacitive sensor consists of two identical and symmetric electrodes, Figure 75. The wire under test is modeled as an infinitely long dielectric-coated perfect conductor. A relationship between the

complex permittivity  $\varepsilon^*$  of the dielectric coating, the sensor capacitance  $C$  and dissipation factor  $D$  is established in the electroquasistatic regime, in which  $\varepsilon^* = \varepsilon' - j\varepsilon''$ ;  $\varepsilon'$  being the real permittivity,  $\varepsilon''$  being the imaginary permittivity, and  $j = \sqrt{-1}$ . It is worth pointing out that, by adopting this model, the multilayer wire insulation Figure 84 is modeled as a one-layer structure. This means the insulation status assessed by the capacitive probe will be the overall condition of all the insulation layers.

In the numerical model described in Section 2.2, the insulation real permittivity  $\varepsilon'$  is in linear relationship with the sensor capacitance  $C$ , and the insulation loss tangent  $\tan\delta = \varepsilon''/\varepsilon'$  is linearly related to the sensor dissipation factor  $D$ . In this section, complex permittivity values of wire samples are inferred from measured probe capacitance and dissipation factor values, based on this numerical model.

In the model, the conductor is kept at ground potential and potentials on the two electrodes are kept at 1 V and -1 V respectively. The calculated capacitance is the series capacitance of the capacitance between one electrode and the conductive core, with the capacitance between the conductive core and the other electrode. In the measurements, however, the conductive core does not have to be grounded. This is because the potential on the conductive core will be the average of that on the two electrodes, and the measured capacitance under this circumstance is the series capacitance calculated through the model.

The validity of this physics-based model has been verified by good agreement between numerical calculations and results of benchmark experiments (Chapter V Section 2). A detailed description of numerical modeling and experimental verification can be found in (Chapter V Section 2).

## **Probe and measurement system**

### *Probe fabrication*

Figure 82 shows the capacitive probe. The probe consists of two 2 x 4 cm<sup>2</sup> acrylic plates and an acrylic rod on which the two plates are mounted so that their surfaces remain parallel. The lower plate is attached to the acrylic rod using a plastic screw, whereas the upper plate can glide up and down by adjusting another plastic screw perpendicular to the two plates. The curved sensor electrodes are formed by brushing a layer of silver paint onto the symmetric grooves in the two plates. The two electrodes are connected to two pins, which are then connected to an LCR meter for capacitance measurements. In order to ensure that the two plates are in parallel, two acrylic dowels are attached to the upper plate using epoxy glue, and inserted into the lower plate. These two acrylic dowels, together with the plastic screw, assure that the two acrylic plates remain parallel during measurements. The subfigure in Figure 82 shows the probe holding a wire under test. The probe and the wire are in tight surface contact with each other.

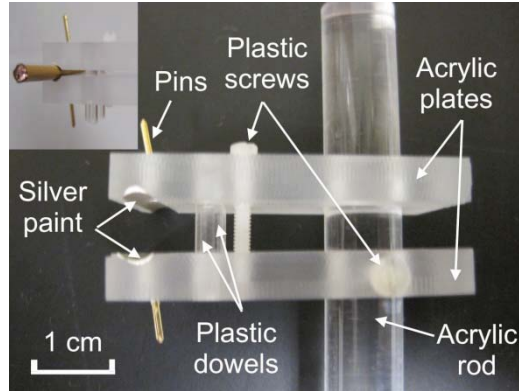


**Figure 82** Photograph of fabricated capacitive probe with curved patch electrodes. Subfigure: capacitive probe holding a wire sample under test.

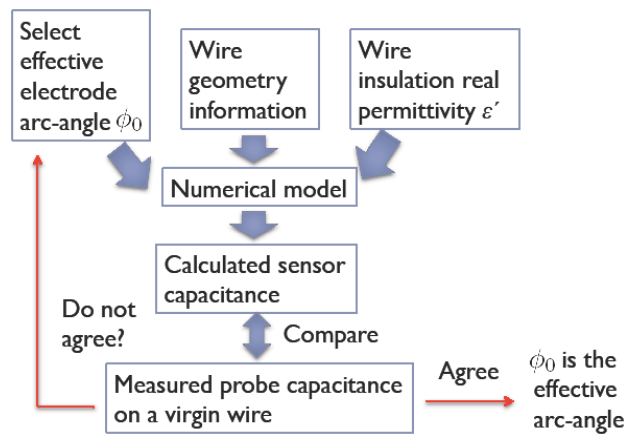
### Parameters

Parameters of the probe are (see Figure 75): electrode radius  $\rho_0 = 2.50$  mm and electrode length  $l = 20$  mm. The electrode radius is taken to be the same as the specified wire sample outer radius. The electrode length is measured directly from the probe.

The region exterior to the curved electrodes in Figure 75 is assumed in the model to be homogeneous, e.g., air. This assumption is not satisfied, however, for the probe depicted in Figure 82 due to the existence of the acrylic plates exterior to the electrodes. To account for this effect, along with possible air gaps between the electrodes and the testing wire due to surface roughness, an effective electrode arc-angle  $\phi_0$  is introduced for the capacitive probe. Steps taken to determine  $\phi_0$  are shown in Figure 83. First, an assumed electrode arc-angle  $\phi_0$ , the wire sample geometry information, and the assumed wire insulation real permittivity ( $\epsilon_r' = 2.7$ ) are input into the numerical model, from which a computed probe capacitance  $C_{model}$  is obtained. Second, capacitance measurements are performed on the virgin wire samples. Third,  $C_{model}$  is compared to the measured probe capacitance  $C_{meas}$ . If  $C_{model}$  and  $C_{meas}$  agree to three significant figures,  $\phi_0$  is considered as the effective electrode arc-angle. Otherwise, a different value is assumed for the effective electrode arc-angle and the above steps are repeated until the stop criterion is satisfied. For testing wires of type MIL-W-81381/12, the effective arc-angle is determined as  $\phi_0 = 80.1 \pm 0.5^\circ$ . This inferred  $\phi_0$  is quite close to the physical electrode arc-angle, which is in the range 80 to 90°. Uncertainty in  $\phi_0$  is due to variations in the measured capacitance ( $2.11 \pm 0.01$  pF). Probe parameters are tabulated in Table 23.

**Table 23** Probe parameters, Figure 82.

$l$ (mm)	$20.0 \pm 0.06$
$\rho_0$ (mm)	$2.50 \pm 0.13$
$\phi_0$ (degrees)	$80.1 \pm 0.5$

**Figure 83** Algorithm for determination of the effective electrode arc-angle  $\phi_0$ .

### Measurement system and uncertainty analysis

For capacitance measurements, the probe was connected to an Agilent LCR meter 4980A by an Agilent probe test fixture 16095A, whose probe pins were connected to the curved patch electrodes of the prototype probe. Capacitance measurements in this section were performed at 1 MHz and room temperature. Detailed discussion on the selection of operating frequency is provided in (Chapter V Section 2).

Uncertainties in the measurement procedure are attributed to achievable precision in the measurement equipment, uncertainty in  $\phi_0$ , and variation in the geometry of the wires under test. These uncertainties contribute to uncertainty in the insulation complex permittivity determined inversely utilizing the numerical model.

The achievable precision of the LCR meter depends on the magnitude of the capacitance measured. In the LCR meter operation manual, relative uncertainty is provided for the measured capacitance whereas absolute uncertainty is provided for the measured dissipation factor. Measured capacitance values in this paper are within the range 2 to 3 pF and for these values the corresponding uncertainty is 0.18% for the

capacitance and 0.0018 for the dissipation factor. This means that, in order to detect insulation degradation by capacitive measurements, the degradation-induced changes in the measured probe capacitance and dissipation factor must be that greater than these values.

As seen in Table 23, the uncertainty in  $\rho_0$  and  $l$  are approximately 5%. When the arc-angle of the curved patch electrodes is far from  $180^\circ$ , i.e., the distance between the edges of the oppositely-charged electrodes is relatively large, the capacitance and dissipation factor change slowly as  $\phi_0$  varies (Chapter V Section 2). This is because the interaction between the electrodes is not intense under this circumstance. For the degradation cases studied in this paper, the uncertainty in the inferred insulation real permittivity  $\epsilon_r'$  resulting from the uncertainty in  $\phi_0$  is within 0.01, i.e., less than 0.5%, whereas that in  $\epsilon_r''$  is 0.0002, i.e., less than 0.2%.

Real wires exhibit variations in their dimensions, surface roughness, roundness and curvature even when they may appear macroscopically similar. For this reason, in the experiments that follow, capacitance measurements were performed on three samples, for each degradation condition. Error bars are included in all the following measurement results. It is worth pointing out that the outer diameters of the thermally and hydrolytically exposed wire samples still lie in the range between 2.41 and 2.63 mm. As will be seen in Section 3.6, the standard deviation in the measurements deriving from these sources is the dominant source of uncertainty in the measurements, larger than that due to the other sources discussed above. Nonetheless, changes in the insulation complex permittivity, due to thermal and hydrolytic exposure, are clearly observed even when uncertainty is taken into account.

### **Parameters of the wire under test**

Capacitance measurements throughout this paper are performed on aircraft wire samples of type MIL-W-81381/12. The wire is composed of a nickel-coated copper conductor, wrapped with two layers of polyimide 150FW-N019 film and one layer of aromatic polyimide coating. Each layer of the polyimide 150FWN019 film is constructed by attaching a 13- $\mu$  m-thick fluorinated ethylene propylene (FEP) fluoropolymer film to a 25- $\mu$  m-thick polyimide FN film, Figure 84. Nominal conductor and outer diameters of the wire are 2.09 and 2.50 mm, respectively. Actual measured wire outer diameters for wires examined in this study range between 2.41 and 2.63 mm.

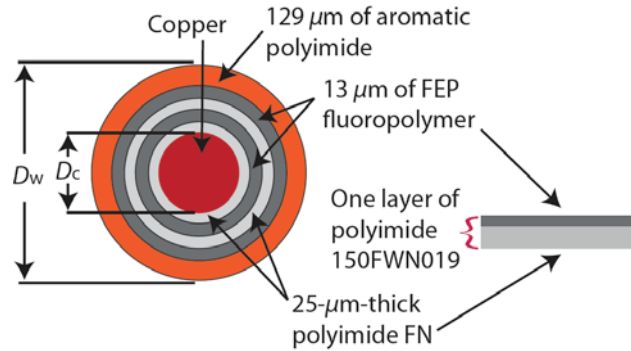


**Figure 84** Schematic diagram of fluorinated ethylene propylene (FEP)-coated polyimide 150FWN019 film. Nominal thicknesses of each layer of polyimide 150FWN019 film, FEP fluoropolymer film, and the liquid H lacquer film are 25  $\mu\text{m}$ , 13  $\mu\text{m}$ , and 129  $\mu\text{m}$ , respectively. The FEP provides adhesion between the layers of polyimide.  $D_c=2.09$  mm,  $D_w=2.50$  mm (nominal).

### Real permittivity

In order to compare the inferred permittivity of the thermally/hydrolytically exposed wires to that of the control wires and therefore provide quantitative assessment of the condition of the insulation, an initial value for the permittivity of the control wires must be assigned.

The real part of the undamaged wire insulation permittivity is assumed to be 2.7 at 1 MHz and room temperature, the condition under which capacitance measurements were performed. Reasons for this assumption are as follows. Considering the schematic shown in Figure 84, we note that there are two main components: polyimide 150FWN019 and an aromatic polyimide outer layer. The manufacturer, DuPont, does not provide a specific permittivity value for polyimide 150FWN019 films, mentioning only that it is less than 3 at 1 kHz and room temperature. According to DuPont, the processing conditions of polyimide 150FWN019 film is, however, very similar to those of the standard polyimide FN films, whose real permittivity is 2.7 at 1 kHz and room temperature. Therefore, we assume the real permittivity of polyimide 150FWN019 to be 2.7 at 1 MHz and room temperature, taking into account the fact that the real permittivity of polyimide does not change significantly over the frequency range from 1 kHz to 1 MHz. Regarding the aromatic polyimide portion of the insulation, the dielectric behavior of aromatic polyimide, types *a* through *f*, is presented in [132]. As will be seen in Section 3.6, degradation of the wire insulation initiates between 400 °C and 450 °C. Only type *f* of the aromatic polyimides studied in [132] presents a thermal degradation initiation temperature ( $T_i = 430$  °C) within this range, whereas  $T_i$  of the other types are greater than 450 °C. The aromatic polyimide coating used in the wire insulation is therefore inferred to be type *f*, whose measured real permittivity is 2.7 at 1 MHz and room temperature [132], the same as that assumed for the polyimide 150FWN019 films. Finally, since the FEP adhesive layer is a relatively minor constituent of the insulation, accounting for approximately 13% of the thickness, and exhibits no unusual dielectric properties ( $\epsilon' = 2.01$  at 1 MHz and room temperature

according to DuPont), it is reasonable to assume that overall real permittivity of the undamaged insulation is 2.7 at 1 MHz and room temperature.

### *Imaginary permittivity*

In order to compare the complex permittivity of thermally and hydrolytically exposed wires to the control/virgin wires, imaginary permittivity  $\epsilon''$  for the control wires has to be determined. Figure 85 shows the steps taken to determine the imaginary permittivity  $\epsilon''$  for the virgin wires. These steps are similar to those described in Figure 85, except that the quantity compared here is the probe dissipation factor  $D$ , instead of the capacitance  $C$ . The inversely determined  $\epsilon_r''$  for the control wires is  $0.016 \pm 0.002$ . Uncertainty in  $\epsilon_r''$  is due to variations in the measured dissipation factor of the control wires ( $0.0055 \pm 0.0006$ ) and  $\phi_0$ . The inferred  $\epsilon_r''$  is in accordance with the results for type *f* aromatic polyimide given in [132] ( $\epsilon_r'' \approx 0.01$  at 1 kHz and room temperature), with the value for polyimide 150FWN019 given by DuPont ( $\epsilon_r'' \approx 0.006$  at 1 kHz and room temperature), and with the value for FEP adhesive given by DuPont ( $\epsilon_r'' \approx 0.004$  at 1 MHz and room temperature).

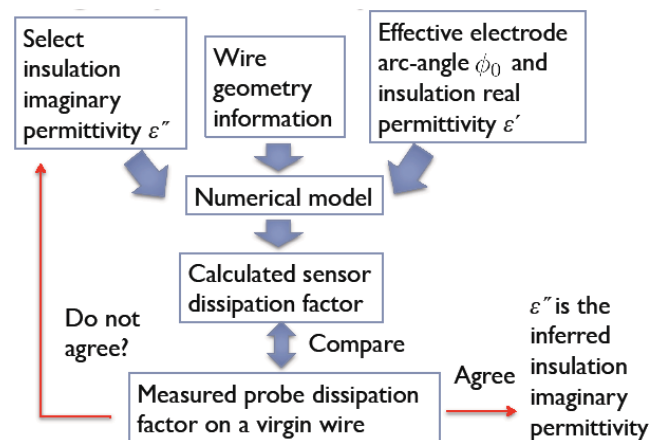


**Figure 85** Algorithm for determination of the imaginary permittivity  $\epsilon''$  for the virgin wires.

### **Case study: evaluation of polyimide-coated wires after thermal and hydrolytic exposure**

The influence of thermal degradation and saline exposure on the complex permittivity of polyimide HN films has been studied in (Chapter II). The samples studied were 125- $\mu\text{m}$ -thick. Explanations of how thermal degradation and saline exposure affect the complex permittivity of polyimide are provided. The work of (Chapter II) guided the choice of experimental parameters for this study.

For the thermal exposure experiment, the exposure temperatures were selected as 400, 425, 450 and 475 °C. For each exposure temperature, five groups of wires, each with three 4-cm-long samples, were isothermally heated in a muffle furnace, Figure 86, for 1, 2, 3, 4 and 5 hours.

Note, the temperature distribution in the furnace is not uniform. To ensure that all the samples are heated at the selected temperature in each experiment, a small ceramic bowl was used to accommodate the wires, and the temperature in the ceramic bowl was measured independently using a thermometer. The upper right figure in Figure 86 shows some of the heat-damaged wire samples in comparison with a control wire. Thermally exposed wires were sealed in plastic bags immediately after being taken out of the furnace to avoid moisture absorption. These samples were then cooled down to room temperature.

The lower right figure in Figure 86 shows a wire sample used in the hydrolytic experiment. Both ends of the wire were sealed with wax to prevent water from migrating into the samples from its ends and via the conductor insulator interface. Five groups of wires, each having three 4-cm-long samples, were immersed in water at room temperature for 0.5, 1, 2, 3, and 4 days, respectively. Capacitance measurements were performed immediately after the samples were removed from the water. Sample surfaces were wiped dry with a soft cloth before capacitance measurements.

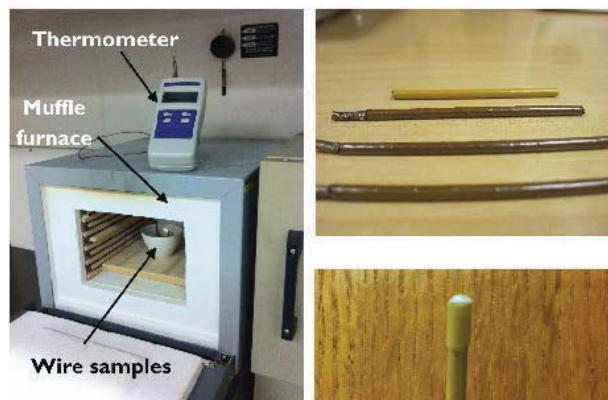


**Figure 86** Left: muffle furnace used for thermal exposure. Upper right: wire samples after heat exposure (brown) and a control wire (yellow). The samples are 4 cm long. Lower right: For hydrolytic exposure, both ends of the sample are sealed with wax.

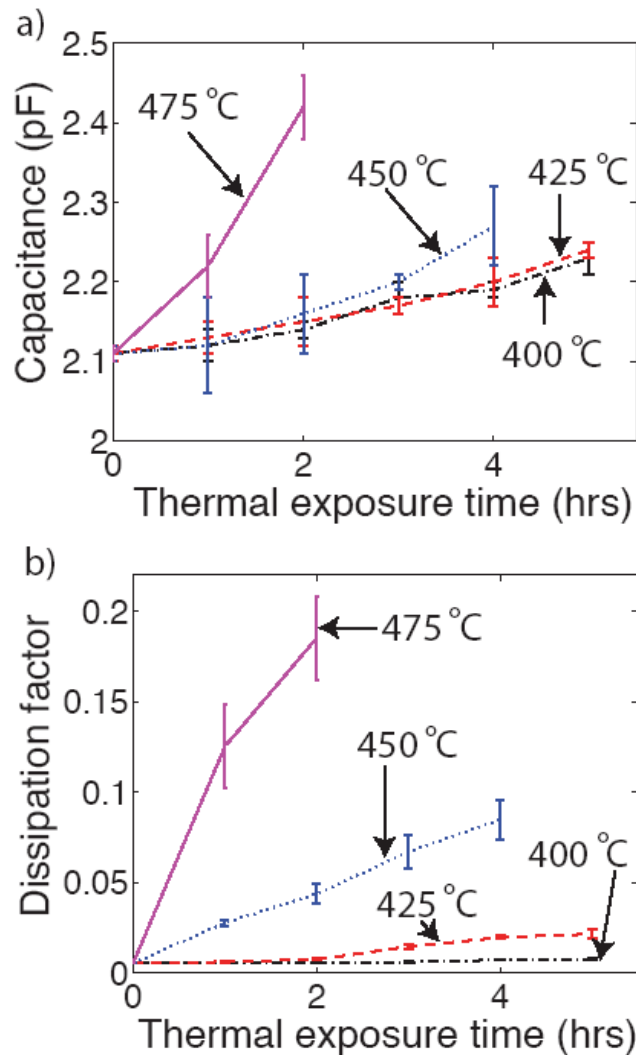
## Results and discussion

### *Thermal exposure*

Figure 87 shows probe capacitance and dissipation factor measured on the thermally exposed wires, as a function of exposure temperature and time. Measurements were performed on the three normally identical wire samples in each group and the mean value and standard deviation obtained.

As can be seen in Figure 87, measured capacitance increases as exposure time and temperature increase. A similar behavior was observed in the measured dissipation factor. In Chapter II, it was found that the dissipation factor of polyimide HN films did not change significantly unless exposed at 475 °C for more than 3 hours. This suggests that increases in the dissipation factor of the thermally degraded wires

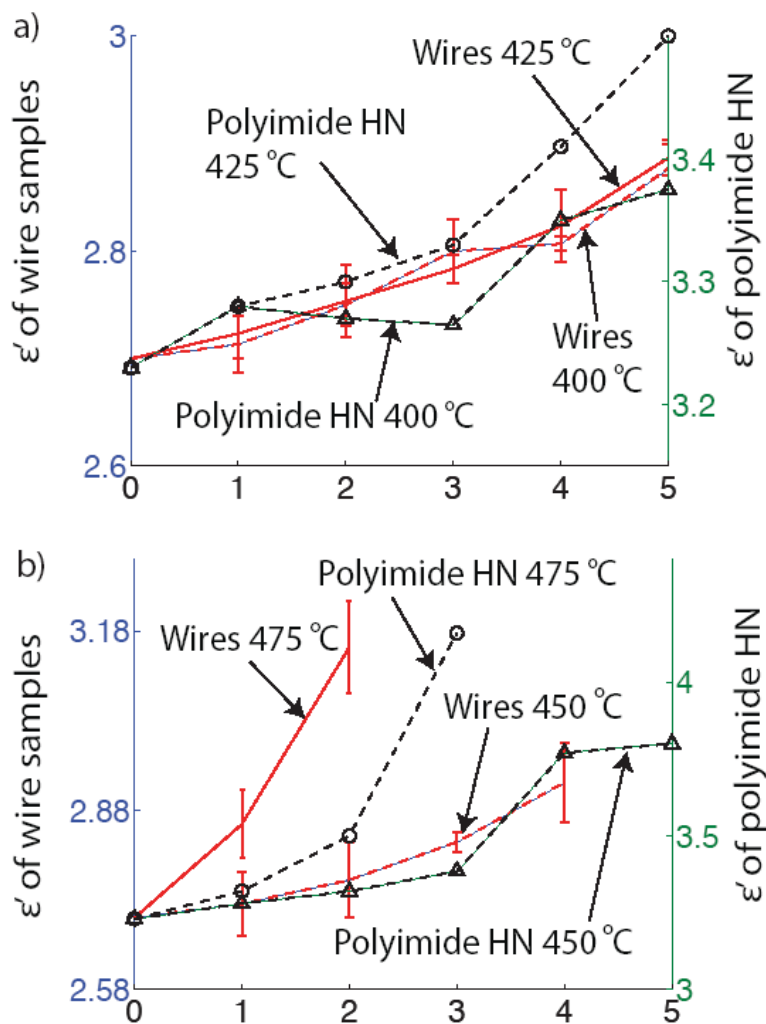
observed here results largely from degradation of the aromatic polyimide coating, rather than the polyimide 150FWN019 layers.



**Figure 87** a) measured capacitance and b) dissipation factor for heat exposed wires. Uncertainties derive from the standard deviation of measurements on three separate samples. Physical degradation of the sample heated beyond 2 hours at 475 °C prevented accurate capacitance measurement for those conditions.

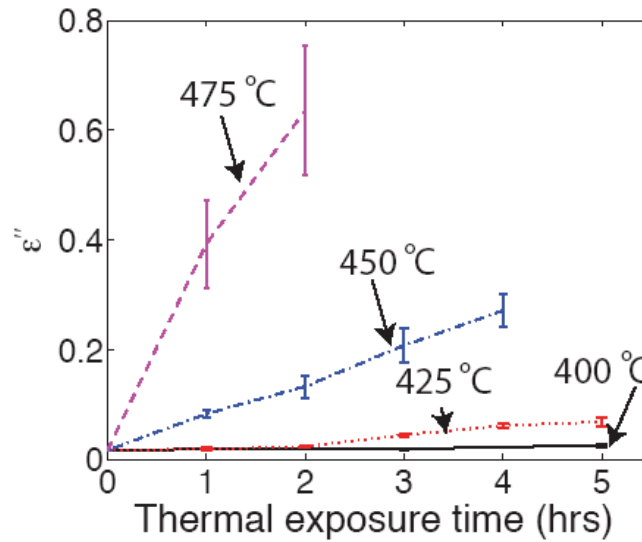
Complex permittivity of the wire samples was inferred from the measured probe capacitance and dissipation factor in the following way. First, an initial guess of the sample complex permittivity  $\epsilon^*$  is input into the numerical model, from which particular values of probe capacitance  $C_{calc}$  and dissipation factor  $D_{calc}$  are obtained. These values are compared with the measured values  $C_{meas}$  and  $D_{meas}$  and  $\epsilon^*$  adjusted until  $C_{calc}$  ( $D_{calc}$ ) and  $C_{meas}$  ( $D_{meas}$ ) agree to within three significant figures. Then,  $\epsilon^*$  is considered as the inferred sample complex permittivity.

Figure 88 shows the inferred insulation real permittivity values in comparison with results presented in Chapter II. The way in which  $\epsilon'$  increases with time and temperature of heat exposure, Figure 88, is in very good agreement with results presented in Chapter II. The inferred imaginary permittivity values of the wires are presented in Figure 89, in which the existence of aromatic polyimide coating contributes predominately to the observed increases in the insulation imaginary permittivity. As can be seen from these two figures, both the real and imaginary parts of the insulation increase as heat exposure temperature and time increase. Especially, the relative change in the insulation imaginary permittivity is greater than that in the real permittivity; the imaginary part increases by up to 39% and the real part by up to 17% compared to the control wires.



**Figure 88** Inferred real permittivity  $\epsilon'$  of the thermally exposed wires in comparison with that of polyimide HN film (Chapter II).

a) 400 and 425 °C; b) 450 and 475 °C.



**Figure 89** Inferred imaginary permittivity  $\epsilon''$  of the thermally exposed wires.

#### *Hydrolytic exposure*

The capacitance and dissipation factor for hydrolytically exposed wires are shown in Figure 90. In accordance with results of previous studies [53] [133], it is observed that both the measured capacitance and dissipation factor increase as water immersion time increase in the first three days, and do not change significantly afterwards. Inferred wire insulation complex permittivity is shown in Figure 91 along with measurement results presented in Chapter II for 125- $\mu\text{m}$ -thick polyimide HN film. The real part of the wire insulation permittivity increased by up to 12% and the imaginary part by up to 60% compared to the control wires. As can be seen from Figure 91 permittivity change in wire insulation as a function of hydrolytic exposure time is in accordance with the results of independent measurements conducted previously on hydrolytically exposed planar polymer insulation samples.

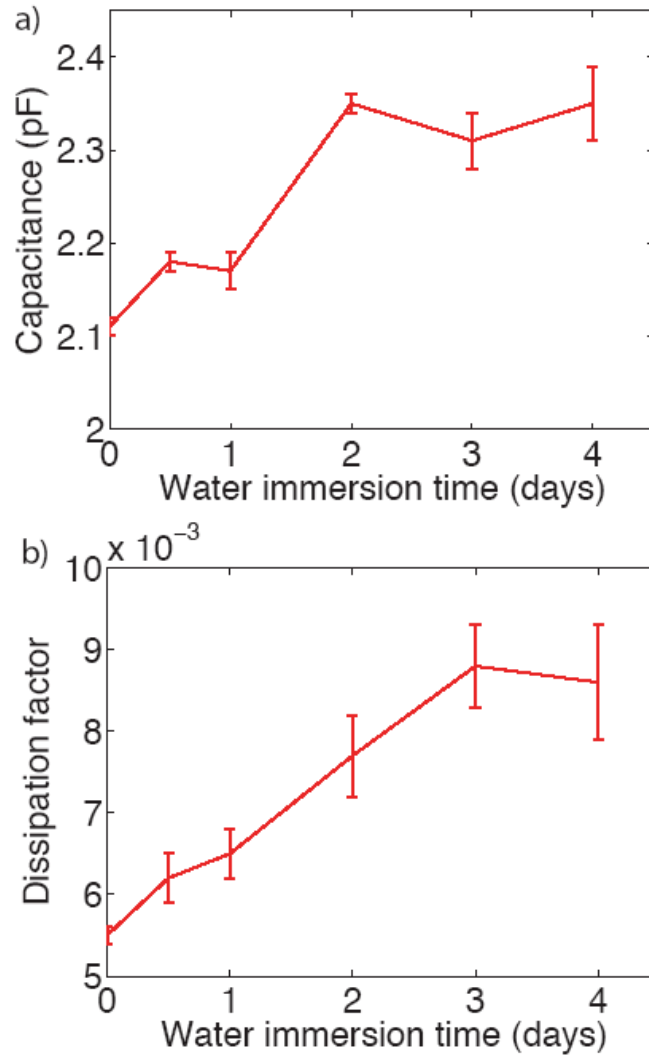


**Figure 90** As for Figure 87 but for hydrolytically exposed wires.

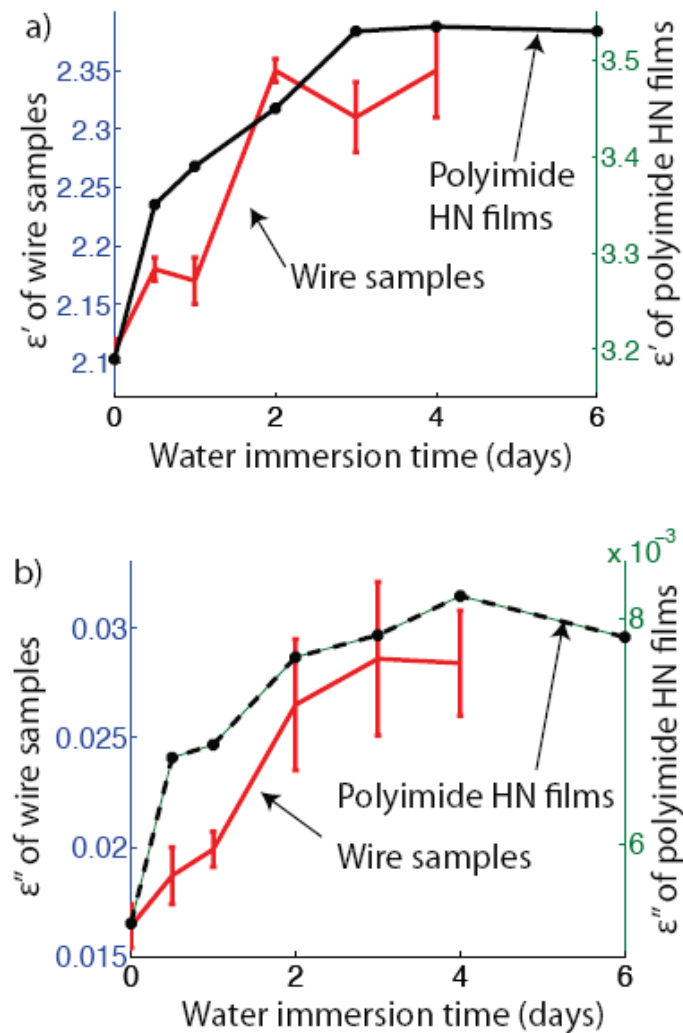


**Figure 91** Inferred complex permittivity, a) real part and b) imaginary part, of the hydrolytically exposed wires in comparison with that of polyimide HN film (Chapter II).

#### 4. Summary

Complex permittivity is an effective indicator of wiring insulation condition. Changes in wiring insulation permittivity, induced by thermal degradation and hydrolytic exposure, have been successfully detected using the capacitive probe presented here, and observations are in accordance with results of previous research (Chapter II). Furthermore, the one-to-one correspondence that exists between the insulation permittivity and measured capacitance justifies the monitoring of changes in insulation status by detecting changes in insulation permittivity, even though the absolute value of the control wire permittivity is assumed from the literature rather than directly measured.

This section focuses on quantitative evaluation of the insulation permittivity after degradation. In practice, it may be more convenient under some circumstances to make comparative measurements of the

capacitance measured on a reference wire and that on the wire under test. The probe presented here is capable of both tasks. Additionally, prior knowledge of the locations at which wiring insulation degradation is most common in any particular aircraft is usually available. The capacitive approach described in this section can therefore be applied for accurate characterization of localized insulation degradation.

For practical measurements, a capacitive device similar to this one can be mounted on a mechanical clip which can be simply applied to an exposed wire. This is the subject of future work.

## Chapter VI. Conclusion

The research presented in this report is motivated by current concerns for aging of electrical wiring insulation materials used in space/air-craft. The influence of various environmental aging processes on insulation capabilities of three insulation polymers has been investigated. Also, a capacitive nondestructive sensor is developed to detect flaws in wiring insulation.

Chapters II, III and IV of the report present the investigation of the deterioration of insulating function of three insulation polymers in association with changes in their material characteristics during various environmental aging processes. The findings of these investigations have successfully answered questions related to how electrical signatures of insulation material change over time with respect to environmental aging, and can be used to develop a library containing relationships between material characteristics and insulation performances. Thermal degradation process of the three polymers has been verified by kinetic reaction models.

Thermal exposure in air and immersion in water/saline of PI has been found to lead to significant deterioration of insulating performance of PI, Chapter II. After either the heating process or immersion in water/saline, the real permittivity and loss factor of PI are increased substantially, there is a significant decrease in dielectric breakdown strength and a higher density of electrically weak points is observed. These observations are explained in terms of chemical degradation due to pyrolysis of imide groups during thermal exposure and formation of ionic side groups during the hydrolysis process of PI while immersed in water. However, dissolved sodium chloride shows no significant influence on dielectric properties of PI immersed in saline solutions.

Results of a study on the influence of thermal exposure and tensile strain on permittivity of PTFE are presented in Chapter III. An increase of approximately 2% in the real permittivity of PTFE is observed following isothermal heating at 340 °C for 96 hr, due to associated increase in crystallinity that enhances the interfacial polarization between the amorphous and crystal phases of the polymer. On the other hand, the real permittivity of PTFE was observed to decrease by approximately 19% as a consequence of 150% mechanical strain. The observation is attributed to the more ordered structure which arises due to alignment of the polymer chains along the direction of loading, which limits motion of polar groups and weakens the interfacial polarization. An increase in the degree of crystallinity was also observed in this case, but it should be noted that value of crystallinity is not the primary factor in determining interfacial polarization relaxation intensity (and therefore permittivity). Rather, the nature and degree of perfection in the crystallized regions play a more dominant role in determining the dielectric properties of the polymer. The degradation mechanisms studied here (thermal exposure and mechanical stress) give rise to crystallizations that are significantly different from each other in nature and degree of perfection. Thus,

the trends in the measured values of crystallinity and in the permittivity for each of the degradation mechanisms described above are not in conflict but rather explained by significant differences in the crystal nature of those samples.

Results of a study on the effect of thermal exposure at 160 °C for 96 hr in air on permittivity of ETFE are presented in Chapter IV. The 2% increase in the real permittivity and 11% decrease in the loss factor of ETFE are associated with oxidation and dehydrofluorination of ETFE during heating, which give rise to formation of polar groups and enhance polarization in the polymer in the presence of an electric field.

Chapter V described the development of a prototype capacitive probe for quantitative NDE of wiring insulation. A numerical model, based on the electrostatic Green's function due to a point source exterior to an infinitely long cylindrical dielectric, and exterior to a dielectric-coated cylindrical conductor, was developed to evaluate quantitatively the permittivity of the dielectric in these cases. The capacitance of a capacitive sensor with two opposing curved patch electrodes was calculated numerically using the method of moments based on the Green's function. The quantitative dependence of the sensor output capacitance on the test-piece permittivity and radius was demonstrated numerically and verified experimentally. The permittivity of various cylindrical test-pieces was inferred from measured capacitance to within 1% accuracy for pure dielectric cylinders. For dielectric-coated conductors, numerical calculations of capacitance and measured agreed to within 7%, on average.

A prototype capacitive probe for quantitative NDE of wiring insulation was designed and fabricated, based on the numerical model, and the insulation complex permittivity was determined inversely from measured probe response. Thermal and hydrolytic exposures were used to induce changes in insulation status for groups of wire samples. Experimental studies on both the damaged and undamaged wire samples demonstrate that insulation status changes for wire type MIL-W-81381/12 can be successfully detected and quantified using the capacitive probe described in this research. In principle, the same technique can be applied to evaluate other wires composed of dielectric-coated conductors.

## Bibliography

- [1] J. H. Collins, "The challenges facing U.S. navy aircraft electrical wiring systems," 2006, 9th Joint FAA/DoD/NASA Aging Aircraft Conference.
- [2] A. Hammoud, M. Staven, J. Suthar and J. Laghari, "Effects of thermal and electric stressing on the breakdown behavior of space wiring," in *IEEE Conf. Electr. Insul. Dielectr. Phenomena (CEIDP)*, 1995.
- [3] 2010. [Online]. Available:  
[http://www2.dupont.com/Kapton/en\\_US/assets/downloads/pdf/HN\\_datasheet.pdf](http://www2.dupont.com/Kapton/en_US/assets/downloads/pdf/HN_datasheet.pdf).
- [4] A. K. Brewer, R. J. Orr and T. A. Janicke, "Hydrolytic deterioration of polyimide insulation on naval aircraft wiring," in *Conference on Electrical Insulation and Dielectric Phenomena*, 1988.
- [5] J. Melcher, Y. Daben and G. Arlt, "Dielectric effects of moisture in polyimide," *IEEE Transactions on Electrical Insulation*, vol. 24, pp. 31-38, 1989.
- [6] D. W. van Krevelen, *Properties of Polymers*, Oxford: Elsevier, 1976.
- [7] M. Tsukiji and W. Bitoh, "Thermal degradation and endurance of polyimide films," in *IEEE International Symposium on Electric Insulation*, 1990.
- [8] J. P. Bellomo, T. Lebey, J. M. Oraison and F. Peltier, "Study of the aging of the different dielectrics materials under specific electrical constraints," in *Proceeding of the 4th international conference on properties and applications of dielectric material*, 1994.
- [9] S. Diahm, M. L. Locattelli and T. Lebey, "Improvement of polyimide electrical properties during short-term of thermal aging," in *Conference on Electrical Insulation and Dielectric Phenomena*, 2008.
- [10] H. M. Banford, W. Yufen, D. J. Tedford and M. J. Given, "The dielectric response of polyimide to combined radiation, vacuum and thermal aging," in *Conference on Electrical Insulation and Dielectric Phenomena*, 1995.
- [11] J. E. Mark, *Physical Properties of Polymers*, Washington, DC: American Chemical Society, 1993.
- [12] H. Ohya, V. V. Kudryavsev and S. I. Semenova, *Polymer Membranes: Applications, Fabrications and Properties*, Kodansha, 1996.
- [13] C. C. Ku and R. Liepins, *Electrical Properties of Polymers*, New York: Hanser, 1987.
- [14] V. Adamec, "Electrode polarization in electrode dielectrics," *IEEE Transactions on Electrical*

- Insulation*, vol. 24, pp. 205-214, 1989.
- [15] D. W. Levi, L. Reich and H. T. Lee, "Degradation of polymers by thermal gravimetric techniques," *Polymer Engineering and Science*, vol. 5, pp. 135-141, 1965.
- [16] M. E. Brown, D. Dollimore and A. K. Galewey, "Reactions in the solid state," *Chemical Kinetics*, vol. 22.
- [17] S. Vyazovkin, "Kinetic concepts of thermally stimulated reactions in solids: a view from a historical perspective," *International Review in Physical Chemistry*, vol. 19, pp. 45-60, 2000.
- [18] H. Friedman, "Kinetics of thermal degradation of char-forming plastics from thermo-gravimetry. Applications to a phenol plastic," *Journal of Polymer Science*, vol. 6c, pp. 183-195, 1963.
- [19] T. Ozawa, "A new method of analyzing thermogravimetric data," *Bull Chem Soc Jpn*, vol. 38, pp. 1881-1886, 1965.
- [20] J. H. Flynn and L. A. Wall, "General treatment of the thermogravimetry of polymers," *J Res Natl Bur Stand*, vol. 70a, pp. 487-453, 1966.
- [21] P. Hondred, S. Yoon, N. Bowler, E. Moukhina and M. R. Kessler, "Degradation Kinetics of Polyimide Film," *High Performance Polymers*, pp. 335-342, 2011.
- [22] J. Opfermann, "Kinetic analysis using multivariate non-linear regression. I. Basic concepts," *J Therm Anal Calorim*, vol. 60, pp. 641-658, 2000.
- [23] D. Farrelly, "DuPont employee, personal communications," March 2010.
- [24] R. A. Dine-Hart, D. B. V. Parker and W. W. Wright, "Oxidative degradation of a polyimide film I initial studies," *Br. Polym. J.*, vol. 3, pp. 222-225, 1971.
- [25] H. Z. Ding and B. R. Varlow, "A new model for propagation of electrical tree structures in polymeric insulation," in *Conference on Electrical Insulation and Dielectric Phenomena*, 2002.
- [26] H. J. Borchardt and F. Daniels, "The application of differential thermal analysis to the study of reaction kinetics," *J Am Chem Soc*, vol. 79, pp. 41-46, 1957.
- [27] S. Vyazovkin and C. A. Wight, "Isothermal and non-isothermal kinetics of thermally stimulated reactions of solids," *International Reviews in Physical Chemistry*, vol. 17, pp. 407-433, 1998.
- [28] E. Pretsch, P. Buhlmann and C. Affolter, *Structure Determination of Organic Compounds*, 4th ed. ed., Springer Berlin Heidelberg, 2000.
- [29] R. A. Dine-Hart, D. B. V. Parker and W. W. Wright, "Oxidative degradation of a polyimide film II studies using hydrazine hydrate," *Br. Polym. J.*, vol. 3, pp. 226-236, 1971.

- [30] A. B. Blumenfeld and A. L. Wdovina, "Thermal behavior and heat stabilization of polyimides and related polymers," in *Polyimides and other High-Temperature Polymers*, 1991, pp. 183-188.
- [31] M. Gupta, Sangita, M. Mathur and J. Shukla, "Relaxation intensity in some polyacrylates," *Pramana-Journal of Physics*, vol. 36, pp. 179-183, 1991.
- [32] E. Butta, S. D. Petris and M. Pasquini, "Young's modulus and secondary mechanical dispersions in polypyromellitimide," *Journal of applied polymer science*, vol. 13, p. 1073, 1969.
- [33] T. Lim, V. Frosini and V. Zaleckas, "Mechanical relaxation phenomena in polyimide and poly(2,6-dimethyl-p-phenylene oxide)," *Polymer Engineering and Science*, vol. 13, pp. 51-58, 1973.
- [34] A. N. Hammound, E. D. Baumann and E. Overton, "High temperature dielectric properties of Apical, Kapton, PEEK, Teflon and Upilex polymers," in *IEEE Conference on Electrical Insulation and Dielectric Phenomena (CEIDP)*, 1992.
- [35] S. Diahm, S. Zelmat, M. L. Locatelli, S. Dinculescu, M. Decup and T. Lebey, "Dielectric breakdown of polyimide films: area, thickness and temperature dependence," *IEEE Trans. Dielectr. Electr. Insul.*, vol. 17, pp. 18-27, 2010.
- [36] M. Nagao, G. Sawa, M. Fukui and M. Ieda, "Dielectric breakdown of polyimide film in high temperature region," *Japanese Journal of Applied Physics*, vol. 15, pp. 1813-1814, 1976.
- [37] S. Zelmat, S. Diahm, M. Decup, M. Locatelli and T. Lebey, "Weibull statistical dielectric breakdown in polyimide up to 400 °C," in *IEEE Conference on Electrical Insulation and Dielectric Phenomena (CEIDP)*, 2008.
- [38] "IEEE guide for the statistical analysis of electrical insulation breakdown data," New York, 2005.
- [39] E. Tuncer, D. R. James, I. Sauers and A. R. Ellis, "On dielectric breakdown statistics," *J. Phys. D: Appl. Phys.*, vol. 39, pp. 4257-4268, 2006.
- [40] R. B. Abernethy, *The New Weibull Handbook*, 5th Edition ed., North Palm Beach : Abernethy, R. B., 2006.
- [41] W. Weibull, "A statistical distribution of wide applicability," *Journal of Applied Mechanics*, vol. 18, pp. 293-297, 1951.
- [42] "Standard Test Method for Dielectric Breakdown Voltage and Dielectric Strength of Solid Electrical Insulating Materials at Commercial Power Frequencies," West Conshohocken, PA, Oct 1, 2009.
- [43] Y. Muramoto, M. Nagao, F. Mizuno and M. Kosaki, "Self-healing breakdown and electrical conduction of polyimide thin films," in *Proceeding of 30th International Symposium on Electrical Insulating Materials*, 1998.

- [44] K. Iida, S. Nakamura and G. Sawa, "Dielectric breakdown and molecular orientation of Poly(4,4'-Oxydiphenylene Pyromellitimide)," *Japanese Journal of Applied Physics*, vol. 33, pp. 6235-6239, 1994.
- [45] L. A. Dissado and J. C. Fothergill, *Electrical degradation and breakdown in polymers*, The Redwood Press, 1988.
- [46] L. Reich and S. A. Stivala, *Elements of polymer degradation*, New York: McGraw-Hill, 1971.
- [47] D. Toop, "Theory of life testing and use of thermogravimetric analysis to predict the thermal life of wire enamels," *IEEE Transactions on Electrical Insulation*, vol. 6, pp. 2-14, 1971.
- [48] T. W. Dakin, "Electrical insulation deterioration treated as a chemical rate phenomenon," *AIEE Transactions*, Vols. 113-118, p. 67, 1948.
- [49] G. Montanari, G. Mazzanti and L. Simoni, "Progress in electrothermal life modeling of electrical insulation during the last decades," *IEEE Transactions on Dielectrics and Electrical Insulation*, vol. 9, pp. 730-745, 2002.
- [50] G. Montanari, "Thermal degradation of electrical insulating materials and the thermokinetic background," *IEEE Transactions on Electrical Insulation*, vol. 25, pp. 1029-1036, 1990.
- [51] G. Montanari and L. Simoni, "Aging phenomenology and modeling," *IEEE Transactions on Electrical Insulation*, vol. 28, pp. 755-776, 1993.
- [52] IEEE Standard Techniques for High Voltage Testing, 1978.
- [53] R. Deiasi and J. Russell, "Aqueous degradation of polyimides," *J. Appl. Polym. Sci.*, vol. 15, pp. 2965-2974, 1971.
- [54] F. J. Campbell, A. K. Brewer, R. J. Orr and T. A. Janicke, "Hydrolytic deterioration of polyimide insulation on naval," in *Conference on Electrical Insulation and Dielectric Phenomena*, 1988.
- [55] M. K. V. K. L. L. M.I. Bessonov, *Polymides: Thermally Stable Polymers*, New York: Plenum Press, 1987.
- [56] S. Wu and D. Denton, "Dielectric modeling of polyimide exposed to environmental stress," *IEEE Transactions on Electrical Insulation*, vol. 26, pp. 362-373, 1992.
- [57] S. Ebnesajjad, *Fluoroplastics, melt processible fluoro-polymers, volume 2: melt processible fluoropolymers*, New York: Norwich, 2003.
- [58] R. Hosemann, "Crystallinity in high polymers, especially fibers," *Polymer*, vol. 3, pp. 349-392, 1966.

- [59] E. N. Brown, C. P. Trujillo, G. T. Gray III and P. J. Rae, "Soft recovery of polytetrafluoroethylene shocked through the crystalline phase II-III transition," *Journal of Applied Physics*, vol. 101, pp. 024916-1-10, 2007.
- [60] E. N. Brown, P. J. Rae, D. M. Dattelbaum, B. Clausen and D. W. Brown, "In-situ measurement of crystalline lattice strains in polytetrafluoroethylene," *Experimental Mechanics*, vol. 48, pp. 119-131, 2008.
- [61] C. W. Bunn and E. R. Howells, "Structure of molecules and crystals of fluoro-carbons," *Nature*, vol. 174, pp. 549-551, 1954.
- [62] C. A. Sperati and H. W. Starkweather, "Fluorine-containing polymers II: polytetrafluoroethylene," *Fortschritte Der Hochpolymeren-Forschung*, pp. 465-495, 1961.
- [63] C. A. Sperati, "Fluorine-containing polymers II: polytetrafluoroethylene," *Fortschr Hochpolym-Forsch Bd*, vol. 2, pp. 465-495, 1961.
- [64] C. W. Bunn, A. J. Cobbold and R. P. Palmer, "The fine structure of polytetrafluoroethylene," *J. Polym. Sci*, vol. 28, pp. 365-370, 1958.
- [65] E. S. Clark, "Molecular conformations of polytetrafluoroethylene: form II and IV," *Polymer*, vol. 40, pp. 4659-4665, 1999.
- [66] J. J. Weeks, I. C. Sanchez and R. K. Eby, "Order-disorder transitions in polytetrafluoroethylene," *Polymer*, vol. 21, pp. 325-331, 1980.
- [67] J. M. Cox and B. A. Wright, "Thermal degradation of fluorine-containing polymers-1,2," *J. Appl. PolymSci*, Vols. 82935-2961, 1964.
- [68] H. D. Flack, "High-pressure phase of polytetrafluoroethylene," *J. Polym. Sci*, vol. 10, pp. 1799-1809, 1972.
- [69] M. Baucchio, ASM Engineering Material Reference, Materials Park, Ohio: ASM International, 1994.
- [70] C. T. Lynch, Handbook of Materials Science, Vol III: Nonmetallic Materials and Applications, Cleveland, Ohio: CRC Press, 1975.
- [71] B. Riddle and J. Baker-Jarvis, "Complex permittivity measurements of common plastic over variable temperatures," *IEEE Transactions on Microwave Theory and Techniques*, vol. 51, pp. 727-733, 2003.
- [72] R. Schwodiauer, J. Heitz, E. Arenholz, S. Bauer-Gogonea, S. Bauer and W. Wirges, "Pulsed-laser-deposited and plasma-polymerized polytetrafluoroethylene (PTFE)-like thin film: a comparative study on PTFE-specific properties," *J. Polym. Sci. B: Polym. Phys*, vol. 37, pp. 2115-2125, 1999.

- [73] H. J. Cho, D. J. Byun and K. Y. Choi, "Investigation into the thermal stability of fluoropolymer coating for heat-resistant application," *Polymer-Korea*, vol. 29, pp. 96-101, 2005.
- [74] S. O. Kasap, *Principles of electrical engineering materials and devices*, McGraw-Hill, 1997.
- [75] I. Alig, S. M. Dudkin, W. Jenninger and M. Marzantowicz, "AC conductivity and dielectric permittivity of poly (ethylene glycol) during crystallization: Percolation picture," *Polymer*, vol. 47, pp. 1722-1731, 2006.
- [76] S. L. Rosen, *Fundamental Principles of Polymeric Materials*, 2nd Edition ed., New York: Wiley, 1993.
- [77] M. Arous, I. Ben Amor, A. Kallel, Z. Fakhfakh and G. Perrier, "Crystallinity and dielectric relaxations in semi-crystalline poly(ether ether ketone)," *J. Phys. Chem. Solids*, pp. 1405-1414, 2007.
- [78] S. V. Gangal, "Tetrafluoroethylene-ethylene copolymer," in *Kirk-Othmer Encyclopedia of Chemical Technology*, New York, John Wiley & Sons, 1994, pp. 657-671.
- [79] D. L. Kerbow, "Ethylene/tetrafluoroethylene copolymer resins," in *Modern fluoropolymers science*, New York, John Wiley & Sons, 1994, pp. 480-491.
- [80] Z. Dang, D. Xie, Y. Yu, H. Xu and Y. Hou, "Enhancement of dielectric permittivity in the ZnO/PZT ceramic matrix nanocomposites," *Materials Chemistry and Physics*, vol. 109, pp. 1-4, 2008.
- [81] P. Avakian and H. W. Starkweather, "Dielectric properties of fluoropolymers," in *Modern Fluoropolymer Science*, New York, John Wiley & Sons, 1997, pp. 91-102.
- [82] J. Opfermann and E. Kaisersberer, "An advantageous variant of the Ozawa-Flynn-Wall analysis," *Thermochim. Acta.*, vol. 203, pp. 167-175, 1992.
- [83] J. Flynn, *Thermal Methods in Polymer Analysis*, p. 163, 1978.
- [84] G. Guerra, C. Rosa, M. Iuliano, V. Petraccone and P. Corradini, "Structural variations as a function of temperature and dynamic mechanical relaxations for ethylene-tetrafluoroethylene and ethylene-chlorotrifluoroethylene alternating copolymers," *Makromol. Chem*, vol. 194, pp. 389-396, 1993.
- [85] J. J. Morelli, C. G. Fry, M. A. Grayson, A. C. Lind and C. J. Wolf, "The thermal oxidative degradation of an ethylene-tetrafluoroethylene-copolymer-based electrical wiring insulation," *J. Appl. Polym. Sci*, vol. 43, pp. 601-611, 1991.
- [86] Y. Mecheri, L. Boukezzi, A. Boubakeur and M. Lallouani, "Dielectric and mechanical behavior of cross-linked polyethylen under thermal aging," in *IEEE Conference on Electrical Insulation and Dielectric Phenomena*, 2000.

- [87] M. Ehsani, H. Borsi, E. Gockenbach, J. Morshedean, G. R. Bakhshandeh and A. A. Shayegani, "Effect of aging on dielectric behavior of outdoor polymeric insulators," in *Conference on Solid Dielectrics*, 2004.
- [88] C. Furse and R. Haupt, "Down to the wire: The hidden hazard of aging aircraft wiring," *IEEE Spectrum*, pp. 35-39, 2001.
- [89] B. G. Moffat, E. Abraham, M. Desmulliez, D. Koltsov and A. Richardson, "Failure mechanisms of legacy aircraft wiring and interconnects," *IEEE Trans. Dielectr. Electr. Insul.*, pp. 808-822, 2008.
- [90] C. Furse, Y. C. Chung, R. Dangol, M. Nielsen, G. Mabey and R. Woodward, "Frequency domain reflectometry for on board testing of aging aircraft wiring," *IEEE Trans. Electromagn. Compat.*, vol. 45, pp. 306-315, 2003.
- [91] C. Furse, Y. C. Chung, C. Lo and P. Pendayala, "A critical comparison of reflectometry methods for location of wiring faults," *Smart Struct. Syst.*, vol. 2, pp. 25-46, 2006.
- [92] B. Waddoups, "Analysis of reflectometry for detection of chafed aircraft wiring insulation," Logan, UT, 2001.
- [93] M. Schmidt, "Use of TDR for cable testing," Logan, UT, 2002.
- [94] A. Jani, "Location of small frays using TDR," Logan, UT, 2003.
- [95] Y. C. Chung, C. Furse and J. Pruitt, "Application of phase detection frequency domain reflectometry for locating faults in an F-18 flight control harness," *IEEE Trans. Electromagn. Compat.*, vol. 47, pp. 327-334, 2005.
- [96] P. Smith, C. Furse and J. Gunther, "Analysis of spread spectrum time domain reflectometry for wire fault location," *IEEE Sensors J.*, vol. 5, pp. 1469-1478, 2005.
- [97] C. Furse, P. Smith and M. Safavi, "Feasibility of spread spectrum reflectometry for location of arcs on live wires," *IEEE Sensors J.*, vol. 5, pp. 1445-1450, 2005.
- [98] C. Furse, P. Smith, C. Lo, Y. C. Chung and P. Pendayala, "Spread spectrum sensors for critical fault location on live wire networks," *Struct. Control Health Monit.*, vol. 12, pp. 257-267, 2005.
- [99] Y. C. Chung, N. N. Amarnath and C. Furse, "Capacitance and inductance sensor circuits for detecting the lengths of open- and short-circuited wires," *IEEE Trans. Instrum. Meas.*, vol. 58, pp. 2495-2502, 2009.
- [100] J. White, E. J. Tucholski and R. E. Green, "Nondestructive testing of aircraft and spacecraft wiring," *Materials Evaluation*, vol. 61, pp. 1315-1320, 2003.
- [101] R. F. Anastasi and E. I. Madaras, "Application of ultrasonic guided waves for aging wire insulation

- assessment," *Materials Evaluation*, vol. 63, pp. 143-147, 2005.
- [102] Z. Xu, S. Saha, D. Koltsov, A. Richardson, B. Honary, J. Hannu, A. Sutherland, B. G. Moffat and M. Desmulliez, "Embedded health monitoring strategies for aircraft wiring systems," in *2nd Electronics system-integration technology conference*, Greenwich, England, 2008.
- [103] B. G. Moffat, M. Desmulliez, K. Brown, C. Desai, D. Flynn and A. Sutherland, "A micro-fabricated current sensor for arc fault detection of aircraft wiring," in *2nd Electronics system-integration technology conference*, Greenwich, England, 2008.
- [104] C. Desai, K. Brown, M. Desmulliez and A. Sutherland, "Selection of wavelet for de-noising PD waveforms for prognostics and diagnostics of aircraft wiring," in *Annual report conference on electrical insulation dielectric phenomena*, Quebec, Canada, 2008.
- [105] "High-voltage test techniques - partial discharge measurement," in *British standard guide-IEC60270*, 2001.
- [106] I. N. Sneddon, *Mixed boundary value problems in potential theory*, Amsterdam: North-Holland Publishing Company, 1966.
- [107] S. S. Vinogradov, P. D. Smith and E. D. Vinogradova, *Canonical problems in scattering and potential theory part I: canonical structures in potential theory*, Boca Raton Florida: Chapman and Hall/CRC Press, 2001.
- [108] V. I. Fabrikant, *Mixed boundary value problems of potential theory and their applications in engineering (mathematics and its applications)*, Kluwer Academic Publishers, 1991.
- [109] A. V. Mamishev, K. Sundara-Rajan, F. Yang, Y. Du and M. Zahn, "Interdigital sensors and transducers," *Proc. IEEE*, vol. 92, pp. 808-845, 2004.
- [110] M. Zaretsky, "Parameter estimation using microdielectrometry with application to transformer monitoring," Cambridge, MA, 1987.
- [111] R. Igreja and C. J. Dias, "Analytical evaluation of the interdigital electrodes capacitance for a multi-layered structure," *Sensor Actuat. A-Phys.*, vol. 12, pp. 291-301, 2004.
- [112] S. C. Mukhopadhyay and C. P. Gooneratne, "A novel planar-type biosensor for noninvasive meat inspection," *IEEE Sensors J.*, vol. 7, pp. 1340-1346, 2007.
- [113] R. H. Bhuiyan, R. A. Dougal and M. Ali, "Proximity coupled interdigitated sensors to detect insulation damage in power system cables," *IEEE Sensors J.*, vol. 7, pp. 1589-1596, 2008.
- [114] X. B. Li, S. D. Larson, A. S. Zyuzin and A. V. Mamishev, "Design principles for multichannel fringing electric field sensors," *IEEE Sensors J.*, vol. 6, pp. 434-440, 2006.

- [115] I. C. Shay and M. Zahn, "Cylindrical geometry electroquasistatic dielectrometry sensors," *IEEE Trans. Dielectr. Electr. Insul.*, vol. 12, pp. 41-49, 2005.
- [116] T. Chen and N. Bowler, "Analysis of a concentric coplanar capacitive sensor for nondestructive evaluation of multi-layered dielectric structures," *IEEE Trans. Dielectr. Electr. Insul.*, vol. 17, pp. 1307-1318, 2010.
- [117] A. A. Nassr, W. H. Ahmed and W. W. El-Dakhakhni, "Coplanar capacitance sensors for detecting water intrusion in composite structures," *Meas. Sci. Technol.*, vol. 19, p. 075702(7pp), 2008.
- [118] A. A. Nassr and W. W. El-Dakhakhni, "Non-destructive evaluation of laminated composite plates using dielectrometry sensors," *Smart Mater. Struct.*, vol. 18, p. 055014 (8pp), 2009.
- [119] P. J. Shull, A. V. Clark, P. R. Heyliger, J. C. Moulder and B. A. Auld, "Characterization of capacitive array for NDE applications," *Res. Nondestr. Eval.*, vol. 2, pp. 11-27, 1990.
- [120] J. D. Jackson, *Classical electrodynamics*, John Wiley & Sons, Inc., 1999.
- [121] A. Gray and G. B. Mathews, *A treatise on Bessel functions and their applications to physics*, Dover, New York, 1966.
- [122] X. Derobert, J. Iaquina, G. Klysz and J. Balayssac, "Use of capacitive and GPR techniques for the non-destructive evaluation of cover concrete," *NDT&E International*, vol. 41, pp. 44-52, 2008.
- [123] I. Bord, P. Tardy and F. Menil, "Influence of the electrodes configuration on a differential capacitive rain sensor performances," *Sens. Actuators B*, vol. 114, pp. 640-645, 2005.
- [124] P. M. Gammell and M. A. Adams, "Detection of strength limiting defects in cellular glasses by dielectric measurements," *Journal of Nondestructive Evaluation*, vol. 2, pp. 113-118, 1981.
- [125] T. Chen and N. Bowler, "Analysis of arc-electrode capacitive sensors for characterization of dielectric cylindrical rods," *IEEE Trans. Instrum. Meas.*, DOI:10.1109/TIM.2011.2157573, 2011.
- [126] T. Chen and N. Bowler, "A capacitive probe for quantitative nondestructive evaluation of wiring insulation," *NDT&E International*, to be submitted, 2011.
- [127] T. Chen and N. Bowler, "Analytical solution for capacitance calculation of a curved patch capacitor that conforms to the curvature of a homogeneous dielectric rod," *App. Phys. Lett.*, to be submitted, 2012.
- [128] E. S. C. Stochmil and J. L. Bessede, "Dielectric properties of polyer-based," *J. Alloys Compd.*, vol. 310, pp. 368-373, 2000.
- [129] L. Li, J. Klavon and N. Bowler, "Reduction in permittivity of polytetrafluoroethylene due to tensile strain," *Mater. Lett.*, to be submitted, 2011.

- [130] L. K. Baxter, *Capacitive sensors: design and applications*, Piscataway, NJ: IEEE Press, 1997.
- [131] M. Gimple and B. A. Auld, "Capacitive arrays for robotic sensing," *Review of progress in quantitative nondestructive evaluation*, vol. 6A, pp. 737-743, 1987.
- [132] S. Chisca, V. E. Musteata, I. Sava and M. Bruma, "Dielectric behavior of some aromatic polyimide films," *Eur. Polym. J.*, vol. 47, pp. 1186-1197, 2011.
- [133] M. M. Koton, V. V. Kudryavtsev, L. A. Laius and M. I. Bessonov, *Polymides: thermally stable polymers*, New York: Plenum Press, 1987.

**REPORT DOCUMENTATION PAGE**

*Form Approved  
OMB No. 0704-0188*

The public reporting burden for this collection of information is estimated to average 1 hour per response, including the time for reviewing instructions, searching existing data sources, gathering and maintaining the data needed, and completing and reviewing the collection of information. Send comments regarding this burden estimate or any other aspect of this collection of information, including suggestions for reducing this burden, to Department of Defense, Washington Headquarters Services, Directorate for Information Operations and Reports (0704-0188), 1215 Jefferson Davis Highway, Suite 1204, Arlington, VA 22202-4302. Respondents should be aware that notwithstanding any other provision of law, no person shall be subject to any penalty for failing to comply with a collection of information if it does not display a currently valid OMB control number.  
**PLEASE DO NOT RETURN YOUR FORM TO THE ABOVE ADDRESS.**

<b>1. REPORT DATE (DD-MM-YYYY)</b> 01-01-2012		<b>2. REPORT TYPE</b> Contractor Report		<b>3. DATES COVERED (From - To)</b>	
<b>4. TITLE AND SUBTITLE</b>  Electromagnetic Nondestructive Evaluation of Wire Insulation and Models of Insulation Material Properties				<b>5a. CONTRACT NUMBER</b> NNX07AU54A	
				<b>5b. GRANT NUMBER</b>	
				<b>5c. PROGRAM ELEMENT NUMBER</b>	
<b>6. AUTHOR(S)</b> Bowler, Nicola; Kessler, Michael R.; Li, Li; Hondred, Peter R.; Chen, Tianming				<b>5d. PROJECT NUMBER</b>	
				<b>5e. TASK NUMBER</b>	
				<b>5f. WORK UNIT NUMBER</b> 284848.02.02.07.02.03	
<b>7. PERFORMING ORGANIZATION NAME(S) AND ADDRESS(ES)</b> NASA Langley Research Center Hampton, Virginia 23681-2199				<b>8. PERFORMING ORGANIZATION REPORT NUMBER</b>	
<b>9. SPONSORING/MONITORING AGENCY NAME(S) AND ADDRESS(ES)</b> National Aeronautics and Space Administration Washington, DC 20546-0001				<b>10. SPONSOR/MONITOR'S ACRONYM(S)</b>  NASA	
				<b>11. SPONSOR/MONITOR'S REPORT NUMBER(S)</b>  NASA/CR-2012-217330	
<b>12. DISTRIBUTION/AVAILABILITY STATEMENT</b> Unclassified - Unlimited Subject Category 23 Availability: NASA CASI (443) 757-5802					
<b>13. SUPPLEMENTARY NOTES</b>  Langley Technical Monitor: K. Elliott Cramer					
<b>14. ABSTRACT</b> Polymers have been widely used as wiring electrical insulation materials in space/air-craft. The dielectric properties of insulation polymers can change over time, however, due to various aging processes such as exposure to heat, humidity and mechanical stress. Therefore, the study of polymers used in electrical insulation of wiring is important to the aerospace industry due to potential loss of life and aircraft in the event of an electrical fire caused by breakdown of wiring insulation. Part of this research is focused on studying the mechanisms of various environmental aging process of the polymers used in electrical wiring insulation and the ways in which their dielectric properties change as the material is subject to the aging processes. The other part of the project is to determine the feasibility of a new capacitive nondestructive testing method to indicate degradation in the wiring insulation, by measuring its permittivity.					
<b>15. SUBJECT TERMS</b>  Degradation; Dielectric; Electrical insulation; Electromagnetic field frequency; Permittivity; Wiring					
<b>16. SECURITY CLASSIFICATION OF:</b>			<b>17. LIMITATION OF ABSTRACT</b>	<b>18. NUMBER OF PAGES</b>	<b>19a. NAME OF RESPONSIBLE PERSON</b>
<b>a. REPORT</b>	<b>b. ABSTRACT</b>	<b>c. THIS PAGE</b>			STI Help Desk (email: help@sti.nasa.gov)
U	U	U	UU	168	<b>19b. TELEPHONE NUMBER (Include area code)</b> (443) 757-5802